TOPICS IN GEOPHYSICAL FLUID DYNAMICS:

I. NATURAL CONVECTION IN SHALLOW CAVITIES

II. STUDIES OF A PHENOMENOLOGICAL TURBULENCE MODEL

Thesis by

Donald Edward Cormack

In Partial Fulfillment of the Requirements

for the Degree of

Doctor of Philosophy

California Institute of Technology

Pasadena, California

1975

(Submitted December 13, 1974)

To Nancy and Kristeen

ACKNOWLEDGMENTS

I would like to express my sincere appreciation to my research advisors, Professors L. G. Leal and J. H. Seinfeld for their guidance and encouragement throughout the course of this work, and for their personal interest in my future career.

During these studies, I have received financial support from the California Institute of Technology in the form of a Graduate Teaching Assistantship and a Graduate Research Assistantship, and from Union Oil in the form of a fellowship.

The numerical computations, reported in this thesis, were made possible, in part, through National Science Foundation Grant No. GK-35476, and, in part, through free computing time made available by the Institute.

PREFACE

As the annual production of waste by-products such as heat and chemical species has increased, so too has the rate of discharge of these pollutants into the atmosphere and bodies of water. To understand fully the consequences of such dumping, it is necessary to predict accurately the rate of dispersion and decay of these pollutants in the environment. For this purpose, one must have available an accurate description of the dynamical behavior of the atmosphere or body of water of interest. Of particular significance in establishing the complex flow patterns which dominate these systems is the interaction of ambient density stratification and buoyancy induced convection caused by spatial inhomogeneities in density (temperature). Although such spatial inhomogeneities can arise from a number of sources, perhaps the most common is differential surface heating. For example, the temperature discontinuity at the shoreline between a large body of cold water and land significantly influences and, indeed, often dominates the local circulation pattern to produce the land-sea breeze phenomenon. On a somewhat larger scale, significant differences in surface temperature and roughness in an urban area produce a local wind and temperature structure which is considerably disturbed relative to the prevailing conditions far upstream or downstream of the city. This has been called the urban heat island phenomenon. Similar, fairly localized phenomena also result in bodies of water where spatial inhomogeneities in density can arise from power plant or

sewage discharges, or from evaporation and fresh water inflow in the case of salt water estuaries.

A second factor which further complicates the accurate prediction of such geophysical flows is their turbulent nature. Since many factors, such as the density structure, surface boundary conditions and past history, affect the turbulence characteristics, the successful solution of the turbulence problem requires the development of a model which is able to represent accurately not only the production, redistribution and dissipation of turbulent stresses, but also the fluxes of all dynamically active scalar quantities such as heat.

In an effort to better understand both of the above aspects of geophysical flows, this thesis deals with two apparently independent problems. The first (Part I) deals with *laminar, natural convection in a shallow cavity with differentially heated end walls,* and is an attempt to understand the physics governing the slow gravitational circulation which is characteristic of shallow bodies of fluid, such as coastal estuaries, cooling ponds, or atmospheres which are vertically constrained by an elevated inversion layer. This laminar problem is treated exactly (subject only to the Boussinesq approximation.)

In Part II, the *development of a suitable turbulence model* is undertaken. The evaluation of existing turbulence models by direct comparison with available experimental data indicates that many of the models in current use are completely inadequate. As a partial remedy, a new model for isothermal flows is proposed.

ABSTRACT

Part I

The problem of natural convection in a cavity of small aspect ratio with differentially heated end walls is considered. It is shown by use of matched asymptotic expansions that the flow consists of two distinct regimes: a parallel flow in the core region and a second, non-parallel flow near the ends of the cavity. An analytical solution valid at all orders in the aspect ratio, A, is found for the core region, while the first several terms of the appropriate asymptotic expansion are obtained for the end regions. Parametric limits of validity for the parallel flow structure are discussed. Asymptotic expressions for the Nusselt number and the single free parameter of the parallel flow solution, valid in the limit as $A \to 0$, are derived.

Also presented are numerical solutions of the full Navier-Stokes equations, which cover the parameter range Pr = 6.983, $10 \leq Gr \leq 2 \times 10^4$ and $0.05 \leq A \leq 1$. A comparison with the asymptotic theory shows excellent agreement between the analytical and numerical solutions provided that $A \lesssim 0.1$ and $Gr^2 Pr^2 A^3 \lesssim 10^5$. In addition, the numerical solutions demonstrate the transition between the shallow-cavity limit and the boundary-layer limit, A fixed $Gr \to \infty$.

Finally, the effect of upper surface boundary conditions on the flow structure within differentially heated shallow cavities is examined. Matched asymptotic solutions, valid for small cavity aspect ratios are presented for the cases of uniform shear stress with zero heat flux, uniform heat flux with zero shear stress, and a heat flux

linearly dependent on surface temperature with zero shear stress. It is shown that these changes in surface boundary conditions have an important influence on temperature and flow structure within the cavity.

Part II

The rational closure technique proposed by Lumley and Khajeh-Nouri (1974), in which each unknown correlation is represented as an expansion about the homogeneous, isotropic state, is applied to the approximate closure of the mean Reynolds stress tensor, and rate of dissipation equations for turbulent flows. The high Reynolds number turbulence model which results is similar in many respects to that presented by Lumley et al. However, a more detailed effort is made to evaluate systematically the numerous parameters. Particular emphasis is placed on the suitability and quality of the experimental data which is used for the estimation of model parameters and on the uniqueness and universality of the resulting parameters.

A quantitative comparison of the present turbulence model to those proposed by Daly and Harlow (1970), Hanjalic and Launder (1972b), Shir (1973) and Wyngaard, Coté and Rao (1973), indicates that the present model gives the best overall prediction of the dynamic response for the homogeneous flows of Uberoi (1956, 1957), Champagne, Harris and Corrsin (1970) and Tucker and Reynolds (1968). A further comparison, which evaluates the ability of these turbulence models to predict profiles of the triple-velocity correlation, the rate of inter-component transfer and the rate of turbulence energy dissipation for inhomogeneous flows indicates that, *of the previous turbulence models,*

that of Hanjalic and Launder is most consistent with the data examined. However, the present model shows promise to yield an even better approximation to the experimental data.

TABLE OF CONTENTS

Part I: NATURAL CONVECTION IN SHALLOW CAVITIES

J. Fluid Mech. (1974), *vol.* 65, *part* 2, *pp.* 209–229
Printed in Great Britain

A. Natural convection in a shallow cavity with differentially heated end walls. Part 1. Asymptotic theory

By D. E. CORMACK, L. G. LEAL
Chemical Engineering, California Institute of Technology, Pasadena
AND J. IMBERGER
Department of Mathematics and Mechanical Engineering, University of Western Australia, Nedlands

(Received 23 March 1973 and in revised form 15 February 1974)

The problem of natural convection in a cavity of small aspect ratio with differentially heated end walls is considered. It is shown by use of matched asymptotic expansions that the flow consists of two distinct regimes: a parallel flow in the core region and a second, non-parallel flow near the ends of the cavity. A solution valid at all orders in the aspect ratio A is found for the core region, while the first several terms of the appropriate asymptotic expansion are obtained for the end regions. Parametric limits of validity for the parallel flow structure are discussed. Asymptotic expressions for the Nusselt number and the single free parameter of the parallel flow solution, valid in the limit as $A \to 0$, are derived.

1. Introduction

Convection due to buoyancy forces is an important and often dominant mode of heat and mass transport. Of particular significance to the dispersion of pollutants and heat waste in estuaries are the buoyancy-driven convective motions induced by gradients in salt concentration or temperature.

Unfortunately the direct modelling of these natural systems is very complex, mainly because the flow is turbulent. However, the idealized problem of laminar flow in an enclosed rectangular cavity with differentially heated ends does provide some insight into these more difficult problems, and has been studied extensively in other contexts by prior investigators. The majority of these studies have used finite-difference numerical solutions of the full equations of motion, subject to the Boussinesq approximation, to consider cavities which were either square or had height h larger than their length l (cf. Quon 1972; Wilkes & Churchill 1966; Newell & Schmidt 1970; Szekely & Todd (1971); De Vahl Davis 1968). However, Batchelor (1954), Elder (1965) and Gill (1966) have shown that analytical progress is possible when the cavity aspect ratio h/l is large.

Batchelor (1954) considered both large and small Grashof numbers Gr. In the latter case, he obtained an asymptotic solution about the pure conduction

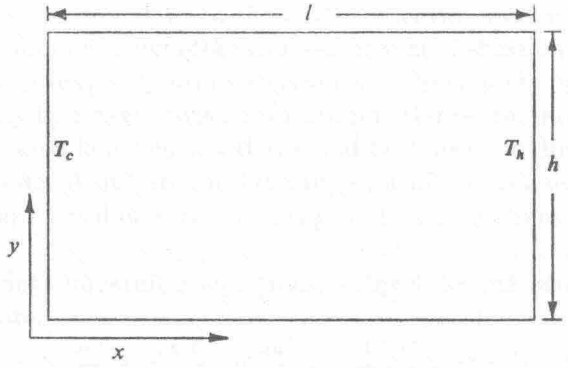

FIGURE 1. Schematic diagram of system.

mode of heat transfer. For large Gr, Batchelor envisaged a flow with thin boundary layers on all solid surfaces and a closed-streamline isothermal core of constant vorticity. Motivated by the experimental measurements of Elder (1965), Gill (1966) proposed an alternative structure for the case $h/l \gg 1$ and $Gr \gg 1$. In Gill's model the flow is decomposed into boundary layers adjacent to the end walls in which the horizontal temperature gradients are large, and a core region in which the temperature is assumed to be a function only of the vertical coordinate. In spite of the approximations necessary to solve the resulting equations Gill reported moderate agreement with the experimental measurements of Elder (1965). A key feature of the case $h/l \gg 1$, which is implicit in Gill's model, is that the core dynamics play only a secondary role in establishing the overall flow structure, which is dominated by the buoyancy-driven boundary layers. A natural question is whether this qualitative feature persists as the aspect ratio h/l is varied. In particular, in the limit as $h/l \to 0$, which is most relevant for the naturally occurring flows of interest in the present investigation, one might anticipate that viscous effects in the core would play an increasingly important role in establishing the flow structure for all fixed (though large) values of Gr.

In the present paper, we use the standard methods of matched asymptotic expansions to consider the cavity flow problem in this limiting case $h/l \ll 1$, Gr fixed. We shall show that the flow structure consists of two parts: a parallel-flow core region in which essentially all of the horizontal temperature drop occurs and which is dominated by viscous effects; and end regions which serve primarily to turn the core flow through 180° as required by the solid end walls. The numerical and experimental results reported in parts 2 and 3 of the present study show excellent agreement with this asymptotic theory for large, though finite values of of $(h/l)^{-1}$.

2. Mathematical formulation of the problem

We consider a closed rectangular two-dimensional cavity of length l and height h which contains a Newtonian fluid, and is shown schematically in figure 1. The end walls are held at different but uniform temperatures T_c and T_h, with $T_c < T_h$.

The top and bottom are insulated, and all surfaces are rigid no-slip boundaries. Actually, the upper boundary of the environmental systems mentioned in the introduction is more closely approximated as a zero-shear surface. However, it was found that the experimental measurements, to be presented in part 3, could be obtained only in a cavity with a no-slip lid. Hence, the present analysis was undertaken to provide a solution that could be compared directly with the experimental results. A systematic investigation of the influence of the upper surface conditions on flow structure may be found in Cormack, Stone & Leal (1974).

The appropriate governing equations, subject to the usual Boussinesq approximations, are

$$\frac{\partial u'}{\partial t'}+u'\frac{\partial u'}{\partial x'}+v'\frac{\partial u'}{\partial y'}=-\frac{1}{\rho_0}\frac{\partial P}{\partial x'}+\nu(\nabla^2 u'), \tag{1}$$

$$\frac{\partial v'}{\partial t'}+u'\frac{\partial v'}{\partial x'}+v'\frac{\partial v'}{\partial y'}=-\frac{1}{\rho_0}\frac{\partial P}{\partial y'}+\nu(\nabla^2 v')+g\beta(T-T_c), \tag{2}$$

$$\partial u'/\partial x'+\partial v'/\partial y'=0, \tag{3}$$

$$\frac{\partial T}{\partial t'}+u'\frac{\partial T}{\partial x'}+v'\frac{\partial T}{\partial y'}=\frac{k}{C_p\rho_0}(\nabla^2 T), \tag{4}$$

with corresponding boundary conditions

$$\begin{aligned} u' = v' = 0 \quad &\text{on all solid boundaries,}\\ \partial T/\partial y' = 0 \quad &\text{on} \quad y' = 0, h,\\ T = T_c, T_h \quad &\text{on} \quad x' = 0, l. \end{aligned} \tag{5}$$

Here, u' and v' are the horizontal and vertical velocity components; ν, ρ_0, C_p, k and β are the kinematic viscosity, density, heat capacity, thermal conductivity and coefficient of thermal expansion, all referred to some mean temperature of the fluid.

Non-dimensionalizing, using the definitions

$$x=\frac{x'}{h}, \quad y=\frac{y'}{h}, \quad u=\frac{u'}{g\beta h^3(T_h-T_c)/\nu l}, \quad v=\frac{v'}{g\beta h^3(T_h-T_c)/\nu l},$$

$$\theta=(T-T_c)/(T_h-T_c), \quad t=t'g\beta h^2(T_h-T_c)/\nu l,$$

and introducing a stream function ψ such that

$$u=\partial\psi/\partial y, \quad v=-\partial\psi/\partial x,$$

one can reduce (1)–(4) to

$$GrA^2\left(\frac{\partial\omega}{\partial t}+\frac{\partial(\omega,\psi)}{\partial(x,y)}\right)=A\nabla^2\omega+\frac{\partial\theta}{\partial x}, \tag{6}$$

$$\nabla^2\psi=-\omega. \tag{7}$$

$$GrPrA\left(\frac{\partial\theta}{\partial t}+\frac{\partial(\theta,\psi)}{\partial(x,y)}\right)=\nabla^2\theta, \tag{8}$$

with boundary conditions

$$\psi=\partial\psi/\partial x=0, \quad \theta=Ax \quad \text{at} \quad x=0, A^{-1} \tag{9a}$$

and

$$\psi=\partial\psi/\partial y=\partial\theta/\partial y=0 \quad \text{at} \quad y=0,1. \tag{9b}$$

Although the characteristic velocity scaling may at first appear an arbitrary choice, it is consistent with the physical picture of a buoyancy- driven parallel flow which is moderated by viscous effects over a length l, and may in fact be justified *a posteriori* by the theory which is presented in this paper. The dimensionless parameters are

$$Gr \equiv g\beta(T_h - T_c)\,h^3/\nu^2 \quad \text{(Grashof number)},$$

$$Pr \equiv C_p\,\mu/k \quad \text{(Prandtl number)}$$

and

$$A \equiv h/l \quad \text{(aspect ratio)}.$$

In what follows, we consider the asymptotic problem in which $A \to 0$ with Pr and Gr held fixed.

3. The core flow

The key to a proper asymptotic solution, in the present case, is a proper resolution of the central or core region of the cavity. Fortunately, the flow structure in this region is surprisingly simple and amenable to direct analytical solution of the governing equations. Both the numerical and experimental evidence which we shall present in parts 2 and 3 in fact indicate that the streamlines in the core region become more nearly parallel as the aspect ratio is decreased, with substantial deviations from this structure only occurring in the immediate vicinity of the end walls. Acceptance of a parallel flow structure as a first approximation in the core would imply that the appropriate characteristic scale length in the x direction must be $O(A^{-1})$.

With introduction of the characteristic horizontal scale $\hat{x} = O(A^{-1})$, equations (6)–(8) become

$$Gr\,A^2\frac{\partial(\omega,\psi)}{\partial(\hat{x},y)} = A^2\frac{\partial^2\omega}{\partial\hat{x}^2} + \frac{\partial^2\omega}{\partial y^2} + \frac{\partial\theta}{\partial\hat{x}}, \tag{10}$$

$$A^2\partial^2\psi/\partial\hat{x}^2 + \partial^2\psi/\partial y^2 = -\omega, \tag{11}$$

$$Pr\,Gr\,A^2\frac{\partial(\theta,\psi)}{\partial(\hat{x},y)} = A^2\frac{\partial^2\theta}{\partial\hat{x}^2} + \frac{\partial^2\theta}{\partial y^2}, \tag{12}$$

where $\hat{x} = Ax$.

Using (10)–(12), one may now obtain the full asymptotic solution for the core temperature and velocity fields, as a regular expansion in the small parameter A. Although the precise forms of the gauge functions in this expansion are strictly obtainable only from the requirements for a proper asymptotic match with the corresponding solutions in the end regions, we anticipate the simple form (which will be verified *a posteriori*)

$$\left.\begin{aligned}\theta &= \theta_0 + A\theta_1 + A^2\theta_2 + \ldots,\\ \psi &= \psi_0 + A\psi_1 + A^2\psi_2 + \ldots,\\ \omega &= \omega_0 + A\omega_1 + A^2\omega_2 + \ldots.\end{aligned}\right\} \tag{13}$$

The systematic solution, valid for $A \ll 1$, which results on substituting these

expansions into (10)–(12) and equating terms of like order in A has the same form at all orders in A, i.e.

$$\psi = K_1(\tfrac{1}{24}y^4 - \tfrac{1}{12}y^3 + \tfrac{1}{24}y^2), \tag{14}$$

$$\theta = K_1\hat{x} + K_1^2 Gr\,Pr\,A^2(\tfrac{1}{120}y^5 - \tfrac{1}{48}y^4 + \tfrac{1}{72}y^3) + K_2, \tag{15}$$

where

$$K_1 = c_1 + c_2 A + c_3 A^2 + \ldots,$$

$$K_2 = c_1^* + c_2^* A + c_3^* A^2 \ldots$$

and $c_1, c_2, \ldots, c_1^*, c_2^*, \ldots, c_n^*$ are constants which depend on Gr and Pr.

The velocity field corresponding to (14) is strictly parallel to the top and bottom walls of the cavity, and cannot, therefore, satisfy the boundary conditions (9a) at the end walls. These conditions must be satisfied by solutions valid in the end regions, and in general, the two parameters K_1 and K_2 are evaluated by matching the core solution with these two end-region solutions. In the present case, however, the problem simplifies somewhat owing to the centro-symmetry property of the equations and boundary conditions (discussed by Gill 1966). This property imposes the requirement on the solutions that

$$\psi(\hat{x}, y) = \psi(1-\hat{x}, 1-y), \quad \omega(\hat{x}, y) = \omega(1-\hat{x}, 1-y)$$

and

$$\theta(\hat{x}, y) = 1 - \theta(1-\hat{x}, 1-y).$$

Hence, one half of the cavity is an inverted mirror image of the other. Moreover, it is apparent that

$$\theta(\tfrac{1}{2}, \tfrac{1}{2}) = \tfrac{1}{2},$$

so that, according to (15),

$$\tfrac{1}{2}K_1 + \tfrac{1}{1440}K_1^2 Gr\,Pr\,A^2 + K_2 = \tfrac{1}{2}.$$

This relationship allows the constants c_i^* (and hence K_2) to be entirely eliminated in favour of the single set $\{c_i\}, i = 1, 2, \ldots, \infty$, e.g.

$$c_1^* = \tfrac{1}{2} - \tfrac{1}{2}c_1, \quad c_2^* = -\tfrac{1}{2}c_2, \quad c_3^* = -\tfrac{1}{2}c_3 - \tfrac{1}{1440}c_1^2 Gr\,Pr. \tag{16a,b,c}$$

With the constant K_2 thus eliminated, it is possible to evaluate K_1 completely (and hence the $c_i, i = 1, 2, \ldots, \infty$, which depend on Gr and Pr) by matching the core solution with a proper solution that is valid in either of the two end regions. This matching process is, of course, considerably simplified by the fact that the basic form of the core solution is preserved at all orders in the small parameter A.

Before proceeding to a resolution of the flow in the end regions, it is useful to note the key structural features of the basic core solution for Gr fixed, $A \to 0$ [equations (14) and (15)] and to contrast these with the structure in the previously noted conduction and boundary-layer limits A fixed, $Gr \to 0$ and A fixed, $Gr \to \infty$ of Batchelor and Gill. The solution (14) and (15) exhibits two key features. First, the velocity field in the core is parallel to all orders in the small parameter A. Second, to a first approximation, θ is independent of vertical position, and varies linearly between the end walls. The primary driving force for motion is the horizontal temperature gradient in the core. In fact, we shall show in the next section that $c_1 = 1$, so that effectively all of the temperature drop

occurs across the core. The end regions are thus dynamically passive, in the sense that they serve simply to turn the flow through 180° as required by the condition of zero volume flux through the end walls. In contrast, for the boundary-layer limit A fixed, $Gr \to \infty$ considered by Gill, nearly all of the temperature drop occurs in thin layers at the two ends, and these provide the driving force for flow. In this case, it is the *core* region which is passive. Flow exists there only as a result of entrainment–detrainment from the end-wall boundary layers. Clearly, the flow structure for A fixed (perhaps small), $Gr \to \infty$ is fundamentally different from that for Gr fixed (perhaps large), $A \to 0$.

It is obvious from the first-order temperature distribution that the heat transfer process is dominated by conduction. Thus, it is important to note that the present theory is definitely distinct from the pure conduction limit A fixed, $Gr \to 0$ considered by Batchelor. Physically, the dominance of conduction for asymptotically small values of A (with Gr large) is a result of the cumulative effect of locally small viscous effects acting over a sufficiently long distance. This reasoning is also consistent with the velocity scaling, which indicates that the length of the cavity plays a role that is identical with that played by viscosity. That is, by either doubling the length or doubling the viscosity, while keeping all other variables constant, one achieves the same effect, to cut the core velocity in half. Hence, when A is small enough, the core velocity is actually 'throttled' to small magnitude by viscosity for any arbitrarily large value of Gr.

4. The flow in the end regions

We turn now to a consideration of the end regions of the cavity where the core flow described in the previous section is not valid. Although we are primarily interested in determining the coefficients c_i of the parameter K_1, and hence the quantitative details of the core region, it is nevertheless of some interest to develop the full asymptotic solution in this region of the flow. In view of the centrosymmetry of the problem, we explicitly consider only the end $x = 0$. As we shall see, it is necessary to proceed to third order in the end flow solution in order to obtain the first non-trivial correction for the core region.

In the end regions, the characteristic length scales in each of the co-ordinate directions are $O(h)$. In this sense, the structure for $A \to 0$, Gr fixed (and large) is fundamentally different from the expected structure for $Gr \to \infty$, with A fixed (and small), since there exist no boundary-layer-like regions in the present case. Furthermore, since the parallel structure of the core requires that *all* streamlines eventually enter the end region, it is clear that the scaling used for the horizontal velocity in the core must be maintained in the analysis of the end regions. Hence, (6)–(8) must be solved subject to the boundary conditions

$$\psi = \partial\psi/\partial y = \partial\theta/\partial y = 0 \quad \text{on} \quad y = 0, 1, \tag{17a}$$

$$\psi = \partial\psi/\partial x = \theta = 0 \quad \text{on} \quad x = 0 \tag{17b}$$

and the matching condition

$$\lim_{x\to\infty} \psi_{\text{end}}(x, y) \Leftrightarrow \lim_{\hat{x}\to 0} \psi_{\text{core}}(\hat{x}, y) \quad \text{as} \quad A \to 0. \tag{18}$$

As in the core region, the solution can be obtained as a regular perturbation expansion in the small parameter A of the form

$$\theta = \theta_0 + A\theta_1 + A^2\theta_2 + \ldots,$$
$$\psi = \psi_0 + A\psi_1 + A^2\psi_2 + \ldots,$$
$$\omega = \omega_0 + A\omega_1 + A^2\omega_2 + \ldots.$$

Substituting these expansions into (6)–(8) and equating terms of like order in A, we obtain an infinite sequence of coupled linear differential equations for the unknown functions θ_i, ψ_i and ω_i. In order to clarify the discussion to follow, we list these together with the explicit matching conditions which must be satisfied for large x, up to $O(A^3)$.

(i) At $O(1)$

$$\partial\theta_0/\partial x = 0,$$
$$\nabla^2\theta_0 = 0, \quad \lim_{x\to\infty}\theta_0 = c_1^*. \tag{19}$$

(ii) At $O(A)$

$$\nabla^2\omega_0 = -\partial\theta_1/\partial x, \quad \nabla^2\psi_0 = -\omega_0, \tag{20}$$
$$\nabla^2\theta_1 = Pr\,Gr\,\partial(\theta_0,\psi_0)/\partial(x,y), \tag{21}$$
$$\lim_{x\to\infty}\psi_0 = c_1(\tfrac{1}{24}y^4 - \tfrac{1}{12}y^3 + \tfrac{1}{24}y^2),$$
$$\lim_{x\to\infty}\partial\psi_0/\partial x = 0, \quad \lim_{x\to\infty}\theta_1 - c_1 x + c_2^*.$$

(iii) At $O(A^2)$

$$\nabla^2\omega_1 + \partial\theta_2/\partial x = Gr\,\partial(\omega_0,\psi_0)/\partial(x,y), \tag{22}$$
$$\nabla^2\psi_1 = -\omega_1,$$
$$\nabla^2\theta_2 = Pr\,Gr\left(\frac{\partial(\theta_1,\psi_0)}{\partial(x,y)} + \frac{\partial(\theta_0,\psi_1)}{\partial(x,y)}\right), \tag{23}$$
$$\lim_{x\to\infty}\psi_1 = c_2(\tfrac{1}{24}y^4 - \tfrac{1}{12}y^3 + \tfrac{1}{24}y^2),$$
$$\lim_{x\to\infty}\partial\psi_1/\partial x = 0, \quad \lim_{x\to\infty}\theta_2 = c_2 x + c_1^2 Gr\,Pr\,(\tfrac{1}{120}y^5 - \tfrac{1}{48}y^4 + \tfrac{1}{72}y^3) + c_3^*.$$

(iv) At $O(A^3)$

$$\nabla^2\omega_2 + \frac{\partial\theta_3}{\partial x} = Gr\left(\frac{\partial(\omega_0,\psi_1)}{\partial(x,y)} + \frac{\partial(\omega_1,\psi_0)}{\partial(x,y)}\right), \tag{24}$$
$$\nabla^2\psi_2 = -\omega_2,$$
$$\nabla^2\theta_3 = Pr\,Gr\left(\frac{\partial(\theta_1,\psi_1)}{\partial(x,y)} + \frac{\partial(\theta_2,\psi_0)}{\partial(x,y)} + \frac{\partial(\theta_0,\psi_2)}{\partial(x,y)}\right), \tag{25}$$
$$\lim_{x\to\infty}\psi_2 = c_3(\tfrac{1}{24}y^4 - \tfrac{1}{12}y^3 + \tfrac{1}{24}y^2),$$
$$\lim_{x\to\infty}\partial\psi_2/\partial x = 0, \quad \lim_{x\to\infty}\theta_3 = c_3 x + 2c_1 c_2\,Gr\,Pr\,(\tfrac{1}{120}y^5 - \tfrac{1}{48}y^4 + \tfrac{1}{72}y^3) + c_4^*.$$

The boundary conditions (17a, b) at each order become simply

$$\psi_i = \partial\psi_i/\partial y = \partial\theta_i/\partial y = 0 \quad \text{on} \quad y = 0, 1, \tag{26a}$$
$$\psi_i = \partial\psi_i/\partial x = \theta_i = 0 \quad \text{on} \quad x = 0. \tag{26b}$$

The temperature and velocity fields θ_0, θ_1, ψ_0 and ω_0

We begin by considering the $O(1)$ and $O(A)$ fields using (19)–(21). The solution at $O(1)$ for θ_0 is trivial, since the only solution of $\partial\theta_0/\partial x = 0$ which satisfies the boundary conditions (26) is $\theta_0 \equiv 0$. It follows from the matching condition

and (16a) that $c_1^* = 0$ and $c_1 = 1$. Moreover, substitution of this solution into (21) gives $\nabla^2\theta_1 = 0$. With the appropriate boundary and matching conditions, this leads to the solution $\theta_1 = x$, from which it follows that $c_2^* = c_2 = 0$. Hence to first order, the temperature distribution everywhere in the cavity is strictly linear in x and the dominant mode of heat transfer is pure conduction. In this limited sense the present solution resembles the earlier work of Batchelor for $Gr \ll 1$ and A fixed, though it should be re-emphasized that the present analysis is valid for any Gr provided only that A is sufficiently small.†

In the light of the above results, (20) may be rewritten as

$$\nabla^2\omega_0 = -1, \quad \nabla^2\psi_0 = -\omega_0. \tag{27}$$

In view of the previously stated matching conditions for ψ_0, it is convenient to introduce the transformation

$$\psi_0 = \phi + (\tfrac{1}{24}y^4 - \tfrac{1}{12}y^3 + \tfrac{1}{24}y^2)$$

into (27), which may then be combined to give

$$\nabla^4\phi = 0, \tag{28}$$

with the boundary conditions

$$\phi = \partial\phi/\partial y = 0 \quad \text{on} \quad y = 0, 1,$$
$$\phi = -(\tfrac{1}{24}y^4 - \tfrac{1}{12}y^3 + \tfrac{1}{24}y^2), \quad \partial\phi/\partial x = 0 \quad \text{on} \quad x = 0.$$

The required matching with the core solution yields the final boundary condition on ϕ,

$$\lim_{x\to\infty}\phi = \lim_{x\to\infty}\partial\phi/\partial x = 0.$$

The distribution of ϕ is identical with the displacement of an elastic semi-infinite strip clamped at the edges and subjected to a small displacement at $x = 0$. The difficulties inherent in obtaining an analytic solution to problems of this general nature are well known. On the other hand, numerical solution can be rather straightforward and would be sufficient in the present case for generating an accurate approximation to the stream-function field in the end region. Nevertheless, we feel that it is worthwhile to pursue the analytical representation since the method of solution is interesting in its own right. Furthermore, it provides a useful check on the numerical solution for ψ_0 that is to be used in subsequent stages of the asymptotic theory.

To obtain an analytical expression for ϕ, we extend a method developed by Benthem (1963) that largely follows the well-known lines of Laplace transform theory. If new independent variables are defined as

$$y' = 2y - 1, \quad x' = 2x,$$

so that ϕ is even in y', then the boundary function $\phi(0, y')$ may be expanded as a cosine series

$$\phi(0, y') = \sum_{n=1}^{\infty} d_n \cos\left(\frac{n\pi}{2}y'\right), \tag{29}$$

with

$$d_n = 2\sin\left(\frac{n\pi}{2}\right)(1-(-1)^n)\left(\frac{1}{12n^3\pi^3} - \frac{1}{n^5\pi^5}\right). \tag{30}$$

† A more explicit condition for validity of the present theory will appear in §5.

k	$2s_k$
1	$4{\cdot}2124 + i\ 2{\cdot}2507$
2	$10{\cdot}7125 + i\ 3{\cdot}1032$
3	$17{\cdot}0734 + i\ 3{\cdot}5511$
4	$23{\cdot}3984 + i\ 3{\cdot}8588$

TABLE 1. First four roots of $\sin 2s_i + 2s_i = 0$ in first quadrant

The key to obtaining an analytical solution is the assumption that the second- and third-order derivatives of ϕ on the boundary may also be expressed as cosine series of the similar form

$$\left.\frac{\partial^2\phi}{\partial x'^2}\right|_{x'=0} = \sum_{n=1}^{\infty} a_n \cos\left(\frac{n\pi}{2}y'\right) \tag{31}$$

and

$$\left.\frac{\partial^3\phi}{\partial x'^3}\right|_{x'=0} = \sum_{n=1}^{\infty} b_n \cos\left(\frac{n\pi}{2}y'\right), \tag{32}$$

where a_n and b_n are unknown coefficients to be determined. Following the familiar procedures of Laplace transform theory and after considerable manipulation, the solution may ultimately be expressed as an expansion in Papkowich–Fadle eigenfunctions (cf. Fadle 1941)

$$\phi(x', y') = \sum_{k=1}^{\infty}\sum_{n=1}^{\infty}\left[\frac{d_n(-s_k^3 + \frac{1}{2}n\pi s_k) - a_n s_k + b_n}{(s_k^2 - (\frac{1}{2}n\pi)^2)^2} - \frac{d_n}{s_k}\right]\frac{n\pi \sin\frac{1}{2}n\pi}{4\cos^2 s_k} \times (\sin s_k \cos s_k y' - y' \cos s_k \sin s_k y')\, e^{-s_k x'}, \tag{33}$$

where $s_k, k = 1, 2, \ldots, \infty$, are the complex roots (with positive real part) of the transcendental equation

$$\sin 2s_k + 2s_k = 0 \tag{34}$$

and a_n and b_n satisfy the set of algebraic equations

$$\sum_{n=1}^{\infty}\left\{\frac{d_n(s_k^3 - \frac{1}{2}n\pi s_k) + a_n s_k + b_n}{(s_k^2 - (\frac{1}{2}n\pi)^2)^2} - \frac{d_n}{s_k}\right\} n\pi \sin\tfrac{1}{2}n\pi = 0, \quad k = 1, 2, \ldots, \infty. \tag{35}$$

In theory, the determination of a_n and b_n requires the inversion of a matrix of infinite dimension. Hence, in practice one must truncate the series after a finite number of terms (assume that the rest are zero) and obtain an approximate solution.

The first four roots of the transcendental equation (34) that occur in the first quadrant of the imaginary plane have been tabulated by Mittleman & Hillman (1946) and are listed in table 1. Furthermore, if $q + ir$ is an eigenvalue, then so is $q - ir$ since the roots of (34) are symmetrically placed about both the real and imaginary axes. This symmetry ensures that the imaginary part of (33) is identically zero.

We were unable to prove analytically that the truncated approximation of (33) converges to the correct solution of (28). However, a qualitative indication of such convergence is provided by a comparison of truncated versions of (33) with a full numerical solution of the governing equations plus associated

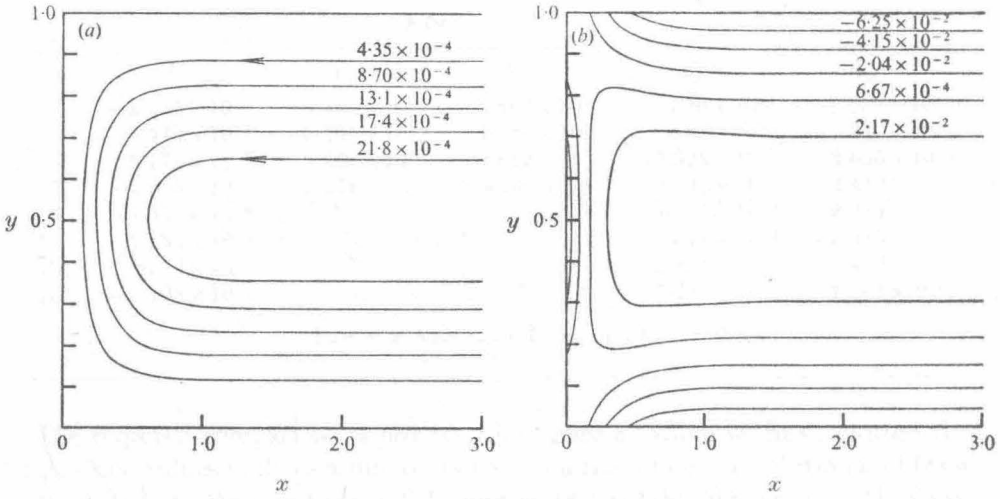

FIGURE 2. (*a*) First-order stream function ψ_0 (streamlines) and (*b*) first-order vorticity ω_0 (lines of constant vorticity).

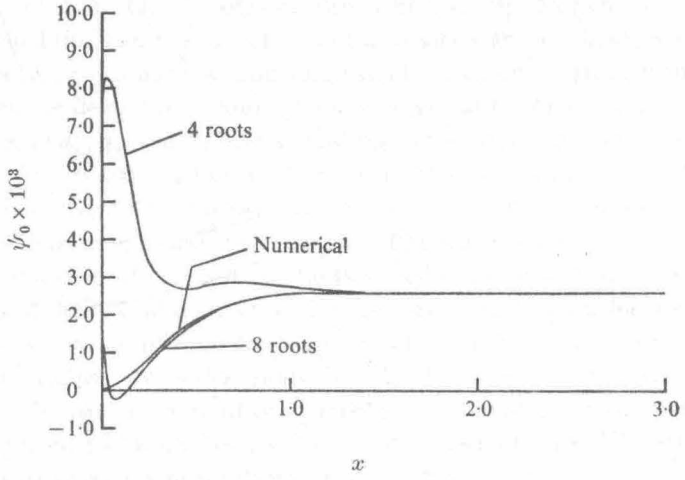

FIGURE 3. Comparison of numerical and analytical solutions for ψ_0.

boundary conditions. A numerical solution of (27) was therefore obtained for ψ_0 and ω_0 by means of an explicit Gauss–Seidel iteration scheme. The equations were approximated by a central difference representation on a geometrically expanding grid of 21 points in the x direction and a sine-transformed grid of 21 points in the y direction (a similar sine-transformed grid will be described in part 2). The boundary conditions at $x = \infty$ were applied at the finite distance $x = 3$. All of these numerical parameters were systematically varied to demonstrate their adequacy for the present purposes. The numerically determined streamlines and equi-vorticity lines are plotted in figures 2 (*a*) and (*b*). Although we shall subsequently discuss some qualitative features of these plots, we first return to the comparison of the numerical and analytical solutions.

		4 roots		8 roots	
n	d_n	a_n	b_n	a_n	b_n
1	$-2{\cdot}307\times10^{-3}$	$5{\cdot}267\times10^{-2}$	$4{\cdot}482\times10^{-1}$	$5{\cdot}620\times10^{-3}$	$1{\cdot}039\times10^{-2}$
3	$-3{\cdot}440\times10^{-4}$	$-5{\cdot}295\times10^{-1}$	$1{\cdot}934\times10^{-1}$	$5{\cdot}842\times10^{-2}$	$-1{\cdot}886\times10^{-1}$
5	$8{\cdot}173\times10^{-5}$	$9{\cdot}866\times10^{-1}$	$3{\cdot}642$	$-7{\cdot}322\times10^{-2}$	$2{\cdot}565\times10^{-1}$
7	$-3{\cdot}053\times10^{-5}$	$5{\cdot}258$	$-3{\cdot}309\times10^{1}$	$3{\cdot}017\times10^{-1}$	$-2{\cdot}451$
9	$1{\cdot}451\times10^{-5}$	—	—	$-1{\cdot}279\times10^{-1}$	$-2{\cdot}254$
11	$-7{\cdot}986\times10^{-6}$	—	—	$-1{\cdot}671\times10^{-1}$	$-6{\cdot}813$
13	$4{\cdot}852\times10^{-6}$	—	—	$2{\cdot}429$	$7{\cdot}409$
15	$-3{\cdot}164\times10^{-6}$	—	—	$7{\cdot}152$	$1{\cdot}581\times10^{1}$

TABLE 2. Values of d_n, a_n and b_n

The required comparison is provided by figure 3, where we have plotted the centre-line values of ψ_0 as a function of x, from the numerical solution and from (33), using both the first four and the first eight available eigenvalues. The solution obtained by using only the first two eigenvalues from each of the first and fourth quadrants represents a rather poor approximation to the 'exact' (numerical) solution. On the other hand, when all eight of the available eigenvalues are used (i.e. eight terms of the infinite series are retained), the correspondence between the numerical and analytical solutions is greatly improved. In fact, appreciable deviations from the numerical solution persist only for $x < 0{\cdot}3$. The coefficients d_n, a_n and b_n corresponding to the four- and eight-term approximations to (33) are listed in table 2. Presumably, inclusion of more terms in the series would improve the comparison of the analytical and numerical solutions. We shall not, however, carry the analysis further in this paper.

The chief feature of interest in the flow field, evident from figure 2, is that both the streamlines and equi-vorticity lines are nearly parallel for $x \geqslant 1$. This observation is consistent with the initial assumption that the horizontal length scale characterizing the end regions is $O(h)$. In addition, it is of some interest to note that the linear gradient of θ_1 acts as a source of positive vorticity in the region away from the walls (figure 2*b*), while the motion of the fluid past the walls produces vorticity of opposite (negative) sign.

The temperature and velocity fields at higher orders of approximation

To obtain the coefficients c_3, c_4, etc. corresponding to higher-order approximations in the core flow, it is necessary to continue to higher orders in the end regions as well. The remainder of this section is concerned with the solution of (22)–(25) for the functions ψ_1, ω_1 and θ_2 and ψ_2, ω_2 and θ_3, which, when combined with the results of the previous section, yield the coefficients c_3 and c_4, respectively.

Although, in theory, it is relatively straightforward to obtain an analytical solution for θ_2, it is impractical in view of the complexity of the solution for ψ_0 to use this or higher-order solutions to evaluate the stream function, vorticity or temperature at any given point. Hence, to determine θ_2, ψ_1 and ω_1, we proceed numerically, using the numerical solutions for ψ_0 and ω_0 in conjunction with

(22) and (23). The explicit dependence on Pr and Gr is eliminated by applying the transformations

$$\theta_2 = Gr\,Pr\,\theta_2', \quad \psi_1 = Pr\,Gr\,\psi_1' + Gr\,\psi_1'', \quad \omega_1 = Pr\,Gr\,\omega_1' + Gr\,\omega_1''$$

to (22) and (23), which become

$$\nabla^4\psi_1' = \partial\theta_2/\partial x, \tag{36a}$$

$$\nabla^4\psi_1'' = -\partial(\omega_0, \psi_0)/\partial(x, y), \tag{36b}$$

$$\nabla^2\theta_2' = \partial\psi_0/\partial y. \tag{37}$$

These equations are to be solved together with the homogeneous boundary conditions (26) and the matching conditions

$$\lim_{x\to\infty}\psi_1' = \lim_{x\to\infty}\partial\psi_1'/\partial x = 0, \tag{38a}$$

$$\lim_{x\to\infty}\psi_1'' = \lim_{x\to\infty}\partial\psi_1''/\partial x = 0 \tag{38b}$$

and

$$\lim_{x\to\infty}\theta_2' = f(y) - \tfrac{1}{2}c_3', \tag{39}$$

where $c_3' = c_3/Pr\,Gr$ and $f(y) = \frac{1}{120}y^5 - \frac{1}{48}y^4 + \frac{1}{72}y^3 - \frac{1}{1440}$.

The coefficient c_3' is easily evaluated by noting that (37), integrated over the depth of the cavity, may be combined with the boundary conditions at $y = 0$, 1 to yield

$$\frac{d^2}{dx^2}\left[\int_0^1 \theta_2'\,dy\right] = 0. \tag{40}$$

The only solution of (40) satisfying the relevant boundary condition

$$\int_0^1 \theta_2'\,dy = 0 \quad \text{at} \quad x = 0$$

and the matching condition $\lim_{x\to\infty}\int_0^1 \theta_2'\,dy = -\frac{c_3'}{2}$

is the trivial solution $\int_0^1 \theta_2'\,dy \equiv 0,$

with the important implication that

$$c_3' \equiv 0. \tag{41}$$

A numerical solution for θ_2' was obtained using the same grid and iterative procedure that were previously used for the determination of ψ_0. The result is shown in figure 4, where lines of constant θ_2' are plotted. The main feature is the strong y dependence of θ_2', which clearly represents a sharp departure from the pure conduction temperature profile obtained for θ_1. While $\partial\theta_2'/\partial x$ is negative for $y < 0{\cdot}5$, it is positive for $y > 0{\cdot}5$. In addition, this solution is consistent with the asymptotic boundary condition since $\partial\theta_2'/\partial x \to 0$ as $x \to \infty$.

Using the numerical solutions for θ_2' and ψ_0, we proceed to the solution for ψ_1 and ω_1. Since ψ_1 is subject only to homogeneous boundary conditions, it

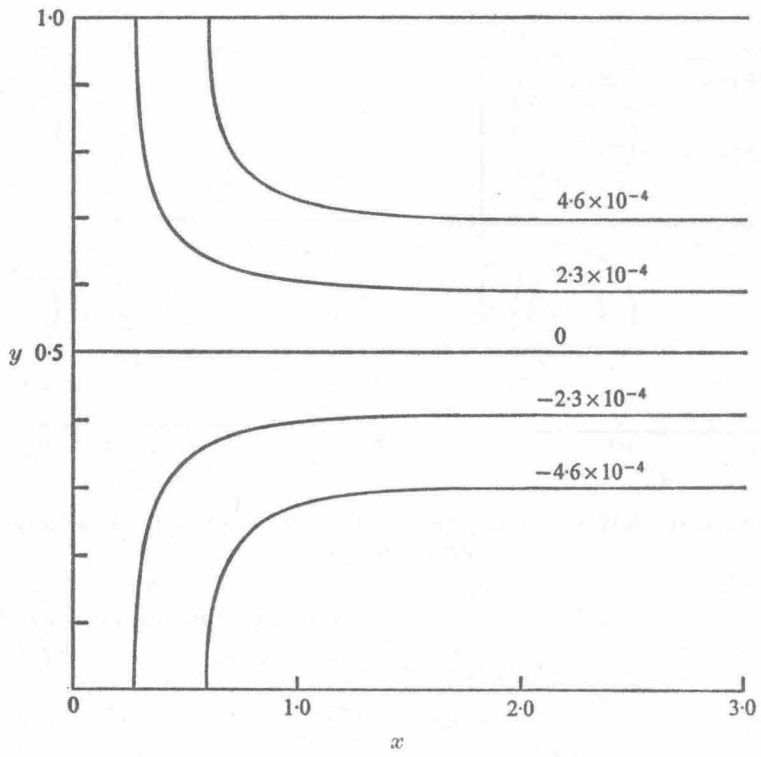

FIGURE 4. $O(A^2)$ temperature correction θ_2': isotherms.

follows that the associated flow is confined to the end region and hence interacts only indirectly with the core flow. Equations (36a, b) were again solved numerically using the previously described numerical solutions to generate the inhomogeneous terms. The resultant solutions for ψ_1' and ψ_1'' are presented in figures 5(a) and (b), respectively. As expected, both corrections are characterized by closed streamlines. In the upper half of the end region the contours of positive ψ_1' indicate that the positive gradient of θ_2' induces a counterclockwise flow, whereas in the lower half the converse is true. The streamlines of ψ_1'' are similar to those of ψ_1', but are of opposite sign, and smaller magnitude. The vorticity functions ω_1' and ω_1'' which we have *not* plotted are similar, with closed contours of positive (negative) vorticity in the upper half and of negative (positive) vorticity in the lower half.

We shall return, after first describing the solution for the velocity and temperature fields ψ_2, ω_2 and θ_3, to consider the qualitative influence of ψ_1 on the flow characteristics in the end region.

The $O(A^3)$ problem for ψ_2, ω_2 and θ_3 is simplified considerably by the previous results. Turning first to the temperature equation (25), we note that $\partial(\theta_0, \psi_2)/\partial(x, y)$ is identically zero, while $\partial(\theta_1, \psi_1)/\partial(x, y)$ reduces to $\partial\psi_1/\partial y$. Moreover, one can eliminate the Pr, Gr dependence of the equation by introducing the change of variables

$$\theta_3 = Pr^2\,Gr^2\theta_3' + Pr\,Gr^2\theta_3''$$

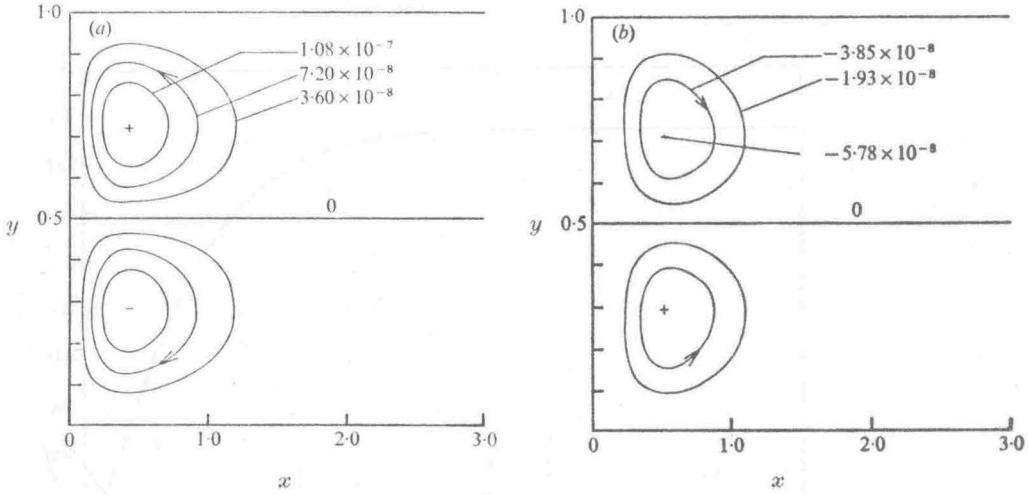

FIGURE 5. (*a*) $O(Gr\ Pr\ A)$ stream function ψ_1' and (*b*) $O(Gr\ A)$ stream function ψ_1'': streamlines.

to yield the independent equations

$$\nabla^2\theta_3' = \partial\psi_1'/\partial y + \partial(\theta_2', \psi_0)/\partial(x, y) \tag{42a}$$

and

$$\nabla^2\theta_3'' = \partial\psi_1''/\partial y, \tag{42b}$$

which must be solved subject to the boundary conditions

$$\theta_3' = \theta_3'' = 0 \quad \text{on} \quad x = 0,$$

$$\partial\theta_3'/\partial y = \partial\theta_3''/\partial y = 0 \quad \text{on} \quad y = 0, 1$$

and the matching conditions

$$\lim_{x\to\infty}\theta_3' = -\tfrac{1}{2}c_4', \quad \lim_{x\to\infty}\theta_3'' = -\tfrac{1}{2}c_4'', \tag{43a, b}$$

where

$$c_4 = Pr^2\,Gr^2\,c_4' + Pr\,Gr^2 c_4''.$$

The integral of (42*b*) over the depth of the cavity indicates that, like c_3', c_4'' is identically zero. However, the same is not true for c_4'. Hence, this constant must be determined during the course of the numerical solution for θ_3'. This is accomplished by noting that (43*a*) also implies

$$\lim_{x\to\infty}\partial\theta_3'/\partial x = 0. \tag{44}$$

Since the solution of (42*a*) subject to either of the conditions (43*a*) or (44) is unique, the numerical solution of the latter problem not only yields θ_3', but also c_4'. A surprising feature of this solution is that θ_3' appears to depend only on x to within the available numerical accuracy. Hence, in figure 6 we have plotted only the centre-line value for θ_3' as a function of x. It is evident that θ_3' does asymptotically approach a constant value of approximately $1{\cdot}74 \times 10^{-6}$, so that

$$c_4' = -3{\cdot}48 \times 10^{-6}.$$

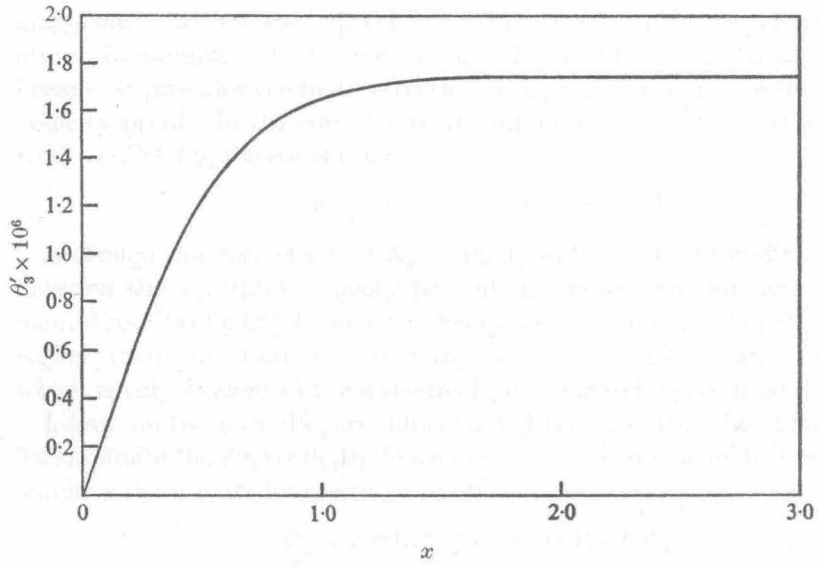

FIGURE 6. $O(Pr^2\, Gr^2\, A^3)$ temperature correction θ_3' *vs.* x.

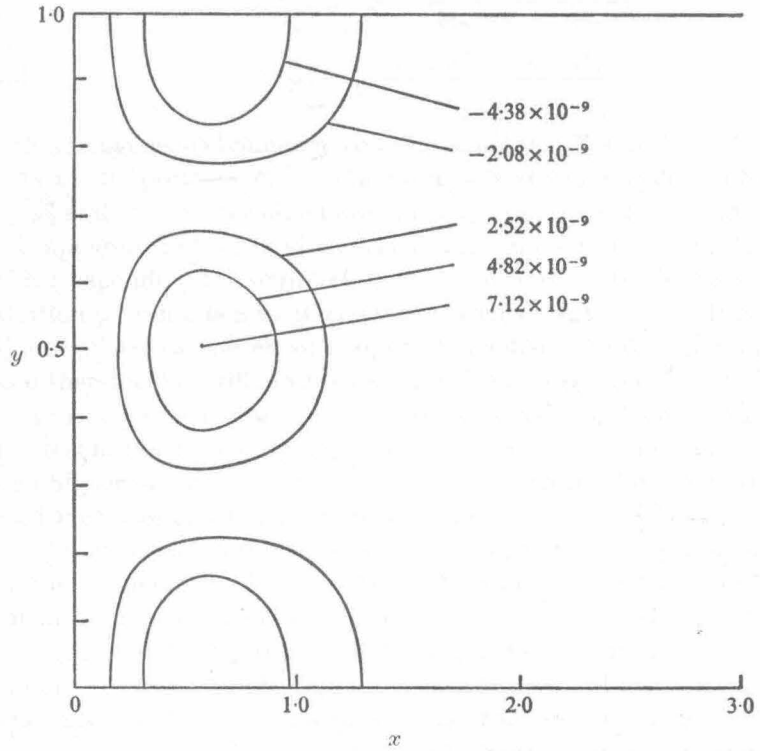

FIGURE 7. $O(Pr\, Gr^2\, A^3)$ temperature correction θ_3'': isotherms.

In contrast to θ_3', the numerical solution for θ_3'', as shown by the contours in figure 7, is a strong function of y. However, since θ_3'' is approximately two orders of magnitude smaller than θ_3', the $O(A^3)$ correction to the temperature field will always be dominated by θ_3' unless $Pr \ll 1$. The fact that c_4' is non-zero is significant because it provides the first correction to K_1 and hence, to the temperature and velocity profiles in the core due to the interaction with the end region. Correct to $O(Gr^2 Pr^2 A^3)$, the constant K_1 is

$$K_1 = 1 - 3{\cdot}48 \times 10^{-6} Gr^2 Pr^2 A^3. \tag{45}$$

Although this correction for K_1 is largely sufficient for providing a comparison between the asymptotic theory presented here and the numerical and experimental results of parts 2 and 3, it is beneficial to obtain one more term of the end-region stream-function expansion, ψ_2, since it provides a detailed flow correction which is very evident in the numerical solutions to be presented in part 2.

Like ψ_1 and ω_1, ψ_2 and ω_2 are subject only to homogeneous boundary conditions. To eliminate the Pr, Gr dependence in (24), it is convenient to break this problem into three parts by means of the transformations

$$\psi_2 = Pr^2 Gr^2 \psi_2' + Pr\, Gr^2 \psi_2'' + Gr^2 \psi_2''',$$
$$\omega_2 = Pr^2 Gr^2 \omega_2' + Pr\, Gr^2 \omega_2'' + Gr^2 \omega_2''',$$

such that

$$\nabla^4 \psi_2' = \partial \theta_3'/\partial x, \tag{46a}$$

$$\nabla^4 \psi_2'' = \frac{\partial \theta_3''}{\partial x} - \frac{\partial(\omega_0, \psi_1')}{\partial(x,y)} - \frac{\partial(\omega_1', \psi_0)}{\partial(x,y)} \tag{46b}$$

and

$$\nabla^4 \psi_2''' = -\frac{\partial(\omega_0, \psi_1'')}{\partial(x,y)} - \frac{\partial(\omega_1'', \psi_0)}{\partial(x,y)}, \tag{46c}$$

with homogeneous boundary conditions for ψ_2', ψ_2'' and ψ_2'''.

As in the previous cases, (46) were solved numerically and the streamlines ψ_2', ψ_2'' and ψ_2''' so determined are plotted in figures 8(a), (b) and (c), respectively. It is apparent that each mode has a dominant set of closed streamlines, ψ_2' and ψ_2'' corresponding to counterclockwise flow and ψ_2''' to clockwise circulation. In addition ψ_2'' exhibits a weak clockwise circulation for $x > 1$. It is significant that ψ_2'' and ψ_2''' are two orders of magnitude smaller than ψ_2', since, unless $Pr \ll 1$, ψ_2 (and therefore ω_2) will always be dominated by ψ_2' (and ω_2').

In principle, it is possible to continue generating higher-order corrections to the stream-function and temperature profiles in the end region. However, with each higher-order term, the number of numerical solutions that must be calculated increases substantially. In fact, for the $O(A^n)$ problem, one must obtain $2n-1$ numerical solutions. Because of the symmetry properties of the previously obtained numerical solutions, the $O(A^4)$ problem (which has not been specifically outlined) does not contribute to K_1 (i.e. $c_5 \equiv 0$). Hence, in order to obtain the next non-trivial correction to the temperature gradient in the core ($O(Gr^4 Pr^4 A^5)$), one must proceed to the $O(A^5)$ problem in the end region. Since 13 additional solutions would be required fully to determine c_6, we have elected to terminate the asymptotic expansion at $O(A^3)$. The implications of the results to this order are discussed in the next section.

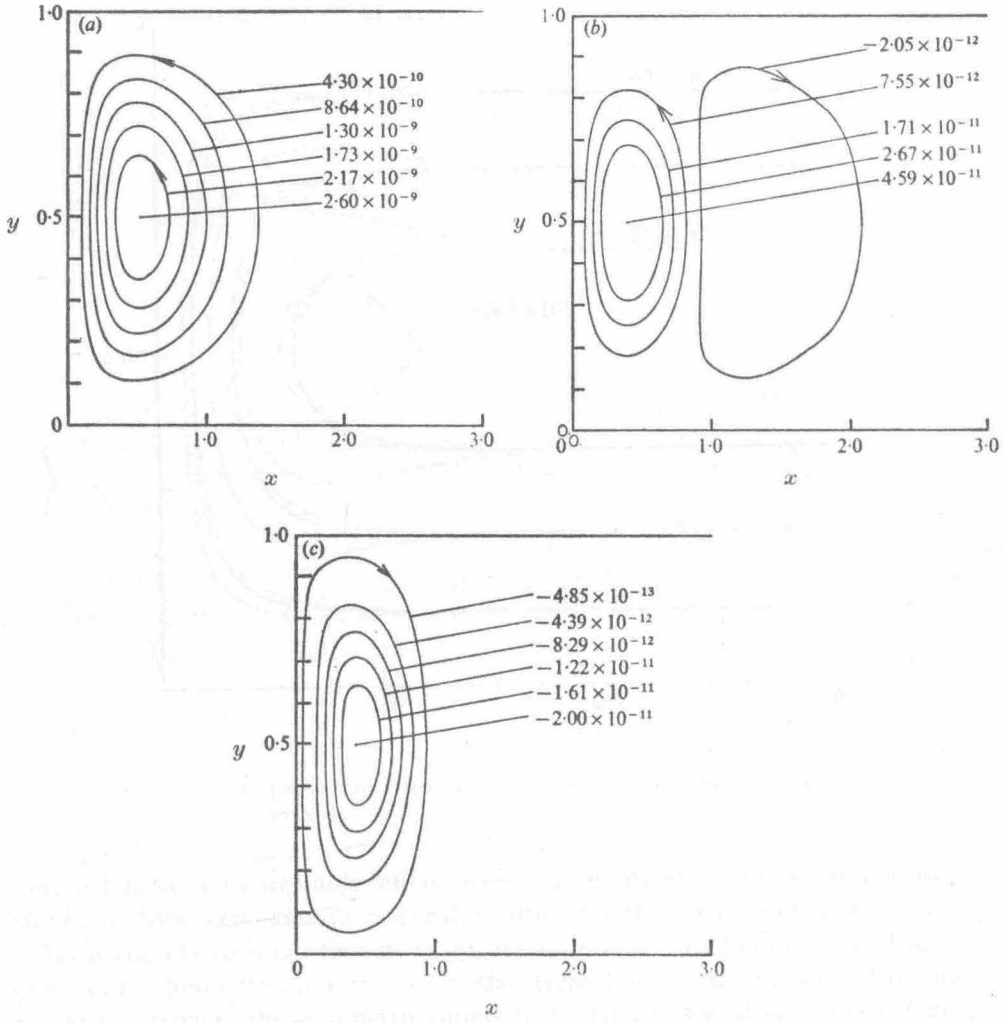

FIGURE 8. (*a*) $O(Pr^2\,Gr^2\,A^2)$ stream function correction ψ_2', (*b*) $O(Pr\,Gr^2\,A^2)$ stream function correction ψ_2'' and (*c*) $O(Gr^2\,A^2)$ stream function correction ψ_2'''.

The composite expansion for the end region

To obtain a qualitative appreciation of the influence of the higher-order corrections ψ_1 and ψ_2 on the flow characteristics in the end region, we have plotted ψ_0 as well as the composite functions

$$\Psi_1 = \psi_0 + Pr\,Gr\,A\psi_1' + Gr\,A\psi_1'', \tag{47a}$$

$$\Psi_2 = \Psi_1 + Pr^2 Gr^2 A^2 \psi_2' + Pr\,Gr^2 A^3 \psi_2'' + Gr^2 A^3 \psi_2''' \tag{47b}$$

in figure 9 for the representative parameter values $Gr = 8 \times 10^3$, $Pr = 6{\cdot}983$ and $A = 0{\cdot}01$. For these values, the correction terms in (47) are approximately one order of magnitude smaller than ψ_0. Hence, a good qualitative idea of the influence of each correction can be deduced, although higher-order terms

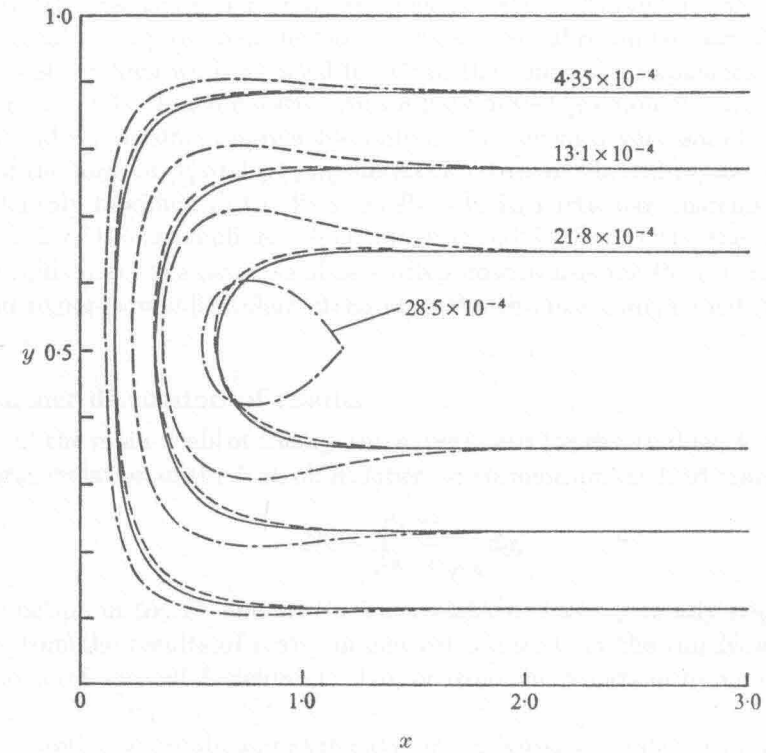

FIGURE 9. Comparison of streamlines of composite functions Ψ_1 and Ψ_2 with ψ_0. ——, ψ_0; – – – –, Ψ_1; — — —, Ψ_2.

may still have an appreciable influence on any quantitative comparison between the asymptotic and exact (numerical) solution for this parameter range.

With the above limitation in mind, we note that the dominant qualitative effect of the first correction is to skew the streamlines in the cold end of the box upward relative to the symmetric function ψ_0. That is, the streamlines entering the cold end region advance further into the upper corner and are then deflected outwards to a more gently rounded corner at the bottom by the action of the end wall.

This shift in the streamlines represents the first effects of the stable stratification on the flow in the end region. A possible physical explanation is that the stratification retards vertical motion so that the fluid starts its downward flow nearer the end wall where the stratification is weakest owing to the end-wall cooling.

For particular values of the parameters considered, the second correction ψ_2 has an even more pronounced influence on the contour lines than does the first correction. (In the asymptotic limit as $A \to 0$, of course, the first corrections will be larger than the second corrections.) The influence of ψ_2 on the flow is to increase the net local mass flux. Figure 9 indicates that this increased mass flux may result in closed streamlines in the end region. The parallel streamlines that leave the core are diverted towards the upper wall and away from the lower wall

as they traverse the end region. The characteristic 'bump' in the streamlines which results is a prominent feature of the numerical results of part 2.

The value which we have used for Pr in the composite expansion of figure 9 is approximately that for water. As we have noted previously, the corrections ψ_1'', ψ_2'' and ψ_2''' become appreciable only as Pr becomes very small. Clearly, in view of the form of ψ_1'' and ψ_2''', the detailed nature of the end-region flow will be considerably modified in the limit as $Pr \to 0$. In particular, instead of the upward shift of the streamlines which we observed for $Pr = O(1)$, the streamlines in the cold end of the cavity will be shifted downwards for $Pr \ll 1$. In addition, the end-region flow will be characterized by the absence of any closed streamlines.

5. Further discussion of results

One of the main goals of theory and experiment for cavity flows is the prediction or correlation of the Nusselt number, the dimensionless heat transfer rate

$$Nu = \int_0^1 \left.\frac{\partial \theta}{\partial x}\right|_{x=0} dy, \tag{48}$$

as a function of Gr, Pr and A. Such correlations have generally been deduced either from the results of many numerical solutions of the full Navier–Stokes equations (cf. Newell & Schmidt 1970) or from the results of numerous experiments.

It is possible to obtain an expression for the Nusselt number from the present asymptotic approach for the limit $A \to 0$ with Pr and Gr fixed. To obtain the relationship, we must evaluate (48) using the temperature profile in the cold end of the cavity, correct to $O(Gr^2 Pr^2 A^3)$, e.g.

$$\theta = Ax + Gr\,Pr\,A^2\theta_2' + Gr^2 Pr^2 A^3 \theta_3' + Gr^2 Pr\,A^3\theta_3''. \tag{49}$$

Owing to the antisymmetry of θ_2' about $y = 0{\cdot}5$ evident in figure 4, θ_2' does not contribute to the integral (48). Similarly, θ_3'' does not contribute to the integral. The contribution of θ_3', on the other hand, must be determined by numerical integration of the previously calculated distribution of θ_3'. Correct to $O(Gr^2 Pr^2 A^3)$ the result is

$$Nu = A(1 + 2{\cdot}86 \times 10^{-6} Gr^2 Pr^2 A^2).\dagger \tag{50}$$

The Nusselt number, as defined by (48), is equivalent to the longitudinal dispersion rate which is frequently used to characterize real estuaries. It is, therefore, significant that the first convective contribution to Nu is precisely the Taylor dispersion coefficient, calculated using the first-order core velocity profile (cf. equation (12) of the recent review paper of Fischer (1973)).

At the present time, there exist no experimentally or numerically determined correlations for Nu, that are valid for $A \ll 1$, with which (50) may be compared. However, it will be shown in part 2 that values of Nu calculated from numerical solutions of the full Navier–Stokes equations for $0{\cdot}1 < A < 0{\cdot}05$

† The next correction to Nu arises from the $O(A^4)$ problem and can be shown to be $c_4' Gr^2 Pr^2 A^4$.

agree with (50) provided only that $Gr^2 Pr^2 A^3$ is suitably restricted in magnitude. A point of some interest with regard to (50) is the graphic illustration it provides of the fundamental difference between the limiting processes $A \to 0$, $Gr \gg 1$ (fixed) and $A \ll 1$ (fixed), $Gr \to \infty$. In the latter circumstance we have previously suggested (and our numerical and experimental results of parts 2 and 3 provide further evidence in corroboration) that the flow structure will be dominated by natural-convection boundary layers at the side walls, with all of the horizontal temperature drop occurring in these regions and the interior core flow driven primarily by the entrainment–detrainment process associated with these layers. In this case, the Nusselt number (48) must clearly be proportional to Gr^m, with $m > 0$. In contrast, however, the expression (50) shows that, if Gr is held fixed and A is decreased without limit, the Nusselt number must ultimately become independent of Gr to first order, no matter how large Gr may be!

Finally, although the asymptotic analysis which we have considered is strictly valid only in the limit $A \to 0$ with Gr and Pr fixed, it is useful to consider the range of values of these parameters where the results may be of practical use. Such an undertaking is, perhaps, particularly desirable in the present circumstance since (14) and (15) indicate the existence of a parallel flow structure to all orders of magnitude in A. Certainly the asymptotic treatment does not explicitly indicate an upper limit of A. However, the numerical solution for ω_0, figure 2(*b*), indicates that the equi-vorticity lines are graphically parallel only for $x > 2$. Thus, before parallel flow can exist, the cavity must be at least four times as long as it is deep, or $A \lesssim 0{\cdot}25$. The form found for K_1, e.g.

$$K_1 = 1 + c_4' Gr^2 Pr^2 A^3 + O(Gr^4 Pr^4 A^5),$$

indicates that the actual value of A necessary for the core solution (14) and (15) to be valid must depend explicitly upon the fixed values of Gr and Pr. Although a rigorous convergence criterion is not possible with the limited results presented here, an approximate criterion can be obtained by requiring only that the second term in the expansion for K_1 be small relative to the first. If we take 0·1 to be small, then it is found that

$$Gr^2 Pr^2 A^3 \lesssim 10^5. \tag{51}$$

Even if the 'small' correction were allowed to be $O(1)$, the range of values of Gr, Pr and A encompassed by (51) would not be changed substantially. It is, of course, necessary to examine experimental results and/or numerical solutions of the full Navier–Stokes equations in order to substantiate the estimate embodied in (51). This we do in parts 2 and 3 of the present work.

This work was done, in part, while J. Imberger was a visitor to the Keck Laboratory of Environmental Engineering at the California Institute of Technology, with the support of a National Science Foundation Grant GK-35774X.

REFERENCES

BATCHELOR, G. K. 1954 *Quart. Appl. Math.* **12**, 209.

BENTHEM, J. P. 1963 *Quart. J. Mech. Appl. Math.* **16**, 413.

CORMACK, D. E., STONE, G. P. & LEAL, L. G. 1974 *Int. J. Mass Heat Transfer*, to appear.

DE VAHL DAVIS, G. 1968 *Int. J. Heat Mass Transfer*, **11**, 1675.

ELDER, J. W. 1965 *J. Fluid Mech.* **23**, 77.

FADLE, J. 1941 *Ing. Archiv.* **11**, 125.

FISCHER, H. B. 1973 *Ann. Rev. Fluid Mech.* **5**, 59.

GILL, A. E. 1966 *J. Fluid Mech.* **26**, 515.

MITTLEMAN, B. S. & HILLMAN, A. P. 1946 *Math. Tables & Other Aids to Comp.* **2**, 61.

NEWELL, M. E. & SCHMIDT, F. W. 1970 *J. Heat. Transfer*, **92**, 159.

QUON, C. 1972 *Phys. Fluids*, **15**, 12.

SZEKELY, J. & TODD, M. R. 1971 *Int. Heat Mass Transfer*, **14**, 467.

WILKES, J. O. & CHURCHILL, S. W. 1966 *A.I.Ch.E. J.* **12**, 161.

J. Fluid Mech. (1974), *vol.* 65, *part* 2, *pp.* 231–246
Printed in Great Britain

B. Natural convection in a shallow cavity with differentially heated end walls. Part 2. Numerical solutions

By D. E. CORMACK, L. G. LEAL AND J. H. SEINFELD
Chemical Engineering, California Institute of Technology, Pasadena

(Received 23 March 1973 and in revised form 15 February 1974)

Numerical solutions of the full Navier–Stokes equations are obtained for the problem of natural convection in closed cavities of *small* aspect ratio with differentially heated end walls. These solutions cover the parameter range $Pr = 6{\cdot}983$, $10 \leqslant Gr \leqslant 2 \times 10^4$ and $0{\cdot}05 \leqslant A \leqslant 1$. A comparison with the asymptotic theory of part 1 shows excellent agreement between the analytical and numerical solutions provided that $A \lesssim 0{\cdot}1$ and $Gr^2A^3Pr^2 \lesssim 10^5$. In addition, the numerical solutions demonstrate the transition between the shallow-cavity limit of part 1 and the boundary-layer limit; A fixed, $Gr \to \infty$.

1. Introduction

This paper reports numerical solutions of the full Navier–Stokes equations, subject to the Boussinesq approximation, for buoyancy-driven convection in a shallow rectangular cavity of height h and length l ($h \ll l$) with insulated top and bottom, and differentially heated end walls. In part 1, hereafter denoted as I†, Cormack, Leal & Imberger (1974) presented an asymptotic solution to the problem, valid in the limit as the cavity aspect ratio $A \equiv h/l \to 0$, for fixed, though arbitrary, values of the Grashof and Prandtl numbers Gr and Pr. It was shown that the flow structure in this limit consists of two distinct regimes: a parallel flow in the central core and a non-parallel flow which is confined to within an $O(h)$ distance of the end walls. The present investigation considers the domain of small but finite A with Gr ranging from 10 to 2×10^4. Strong evidence is found to support the asymptotic theory of I. More important, however, the numerical solutions also illustrate the role of Gr in establishing the flow structure when A is small, but not vanishingly so. In particular, the transition from the parallel flow regime of I to the boundary-layer limit of Gill (1966) is clearly demonstrated.

Numerical investigations of buoyancy-induced convection in rectangular cavities with differentially heated side walls have been numerous. The first extensive investigation was contributed by Wilkes & Churchill (1966), who studied the steady-state and transient fluid behaviour for $Gr < 10^5$ and aspect ratios of 1, 2 and 3. However, a more thorough numerical study was reported

† Equations and figures from I will be denoted as IX, where X refers to the original equation or figure number.

almost simultaneously by Elder (1966), which encompassed the conduction-dominated regime of Batchelor's (1954) theoretical analysis, as well as Rayleigh numbers ($Ra = GrPr$) up to 10^5, for aspect ratios varying from 1 to 4. More recent investigations have been reported by De Vahl Davis (1968) and Newell & Schmidt (1970). All of these studies have dealt primarily with the dependence of the flow structure and overall Nusselt number on Rayleigh number for $A \geqslant 1$ and large Ra. The chief qualitative feature evident from these studies, and of interest in the present context, is the existence of end-wall boundary layers, and the corresponding lack of any appreciable horizontal temperature gradients in the core for large values of Ra (or Gr).

Most recently Quon (1972) studied the effect of changing the dynamical boundary conditions for large Rayleigh numbers, $Ra > 10^5$, and $A = 1$. Changes in the horizontal boundary conditions from free shear to no slip were found to have little influence on the main flow. Furthermore, for one of the cases, the basic assumptions of Gill's (1966) boundary-layer analysis were apparently satisfied. However, Quon's solutions show only modest quantitative agreement with Gill's approximate analysis of the boundary-layer model. On the other hand, his results are in good agreement with the experiments of Elder (1965).

It is surprising that the previous numerical work has been concerned exclusively with aspect ratios $A \geqslant 1$, in spite of the frequent relevance of small aspect ratios to problems of environmental fluid mechanics (see I). In this respect, the present study not only represents a substantial departure from the previous work, but provides a base from which more detailed investigations of the small aspect ratio problem may be undertaken.

2. Formulation of the numerical problem

We consider here an enclosed cavity of aspect ratio $A \leqslant 1$, which is filled with a Newtonian fluid. The top and bottom of the cavity are rigid no-slip boundaries which are perfectly insulating, while the side walls are similarly rigid and no-slip,but are maintained at different uniform temperatures T_h and T_c. A schematic diagram of the system was presented in figure I1. The governing equations, non-dimensionalized and subject to the Boussinesq approximation, were shown in I to be

$$GrA^2\left(\frac{\partial\omega}{\partial t}+\frac{\partial(\omega,\psi)}{\partial(x,y)}\right) = A\nabla^2\omega+\frac{\partial\theta}{\partial x}, \tag{1}$$

$$\nabla^2\psi = -\omega \tag{2}$$

and

$$Gr\,PrA\left(\frac{\partial\theta}{\partial t}+\frac{\partial(\theta,\psi)}{\partial(x,y)}\right) = \nabla^2\theta. \tag{3}$$

Here, ψ is the stream function defined in terms of the horizontal and vertical velocity components by $u = \partial\psi/\partial y$, $v = -\partial\psi/\partial x$,

ω is the vorticity and θ is the dimensionless temperature. The relevant boundary conditions are

$$\left.\begin{aligned}\psi = \partial\psi/\partial x = 0, \quad \theta = xA \quad \text{on} \quad x = 0, 1/A,\\ \psi = \partial\psi/\partial y = 0, \quad \partial\theta/\partial y = 0 \quad \text{on} \quad y = 0, 1.\end{aligned}\right\} \tag{4}$$

In the remainder of this paper we consider the solution of (1)–(3) subject to the conditions (4) using a finite-difference numerical scheme. It is well known that such a treatment introduces errors that depend explicitly on the grid spacing. To minimize this truncation error, it is desirable to use the smallest grid spacing possible throughout the domain of integration. However, since the computation time increases markedly as the number of grid points is increased, one must reach a compromise between the accuracy of the solution and the computation time necessary to reach that solution.

Square cavities have received thorough consideration in this regard. Elder (1966) found that solutions obtained with an 11×11 grid were qualitatively acceptable, that a marked improvement occurred when the mesh size was halved to 21×21, but that little further change resulted when a finer mesh was used. The idea of using a scaled grid to reduce the number of mesh points was introduced by Newell & Schmidt (1970). In this scheme, the smallest grid spacing is maintained in the wall regions of the cavity, where gradients of the field variables are largest, whereas a coarser grid is used to yield comparable accuracy in the central region of the cavity, where gradients are small. Newell & Schmidt varied the grid spacing in their calculations by applying a nonlinear (polynomial) co-ordinate transformation to (1)–(3), which were then finite differenced using a uniform square mesh. An alternative is to impose the graded mesh directly on the original equations (1)–(3).

The scaled-grid approach of Newell & Schmidt was adopted for the present work. Several different transformations including the Newell–Schmidt polynomials were tried, as well as various mesh sizes in the transformed planes. For square cavities the most satisfactory choices appeared to be the sine transformations

$$x = \frac{1}{2A}\left[1 + \frac{\sin X}{\sin 0{\cdot}45\pi}\right] \quad \text{with} \quad -0{\cdot}45\pi \leqslant X \leqslant 0{\cdot}45\pi, \tag{5}$$

$$y = \frac{1}{2}\left[1 + \frac{\sin Y}{\sin 0{\cdot}45\pi}\right] \quad \text{with} \quad -0{\cdot}45\pi \leqslant Y \leqslant 0{\cdot}45\pi, \tag{6}$$

with 21 equally spaced grid points in each co-ordinate direction (X and Y) in the transformed plane. For $A \leqslant 0{\cdot}2$, the transformation (5) required far too many grid points in the X direction to provide the necessary resolution in the end regions. Hence, while the transformation (6) was retained for the vertical co-ordinate, we resorted to what we shall refer to as an arbitrarily discretized grid for the horizontal direction in these cases. With this approach, the discrete step size Δx_i was chosen to be a function of the co-ordinate position i. Although the spacing of the arbitrary grid was different for each case studied, the choice was made in a consistent manner, based primarily on the observation from I that the overall flow is composed of a core region in which the horizontal derivatives scale as $1/A$ and two end regions whose extent is independent of A (for $A \ll 1$). The same resolution of the fluid motion in each of these three regions was obtained by splitting the grid points up evenly with one third of the points in each region. With the final requirement that the grid spacing vary smoothly

from a minimum near the end walls to a maximum in the core, an adequate grid was obtained using a 21×45 mesh system.

Once converged solutions had been obtained on the 21×45 grid, they were recomputed using a 21×55 grid, the extra ten points being split evenly between the two end regions. In all cases, the new values of the stream function differed from the results using the coarser grid only in the fourth significant figure. Furthermore, the integral properties, such as the overall Nusselt number, differed by 1% or less. The addition of grid points in the core had no effect on the final solution. This degree of consistency was deemed acceptable in view of the very large increase in computer costs required to obtain the minor benefits of any further increase in accuracy. As we shall see, a quantitative indication of the error introduced by this finite-difference scheme is provided by comparison of the numerical results with the asymptotic theory of I.

The difference equations which result from either the transformation (5) and (6) or the transformation (6) with the arbitrarily discretized horizontal grid may be expressed in a similar form and were derived in the present work by replacing time derivatives in (1) and (2) with forward differences, by representing the Jacobian (or convective) terms in the conservative form suggested by Arakawa (1966) and by replacing all other spatial derivatives with two-point central differences. The general form of the difference equations which result is well known and hence, in the interest of brevity, we shall not repeat them here†.

To incorporate the boundary conditions into the difference scheme, we have transformed the two boundary conditions on ψ to an explicit representation for both ψ and ω on the cavity walls. An appropriate relationship for ω, accurate to $O(\Delta x)^2$ or $O(\Delta y)^2$, may be obtained from Taylor series expansions of ψ at the internal rows or columns nearest the wall, combined with the boundary conditions (4) and equation (2) evaluated at the boundary.

3. The numerical algorithm

Although we were interested only in the steady-state solution, we chose to integrate the transient difference equations from an initial guess at the steady flow configuration to the final steady state by means of the two-step, alternating direction, implicit method (A.D.I.) developed by Peaceman & Rachford (1955). The systems of tridiagonal linear equations that resulted at each step of the integration were solved by means of the Thomas algorithm (Von Rosenberg 1969, p. 113). The A.D.I. technique has the advantage over explicit methods that it is numerically more stable and hence allows the use of a larger time step Δt. It has the disadvantage, however, that each iteration requires more computation than does an iteration with the explicit techniques.

We found also that a larger discrete time step could be used for the integration of the temperature equation than could be used for the vorticity equation. Hence, to reduce the computation time required to reach the final solution, a different time step was used in each equation. For the cases which we investigated, the

† A copy of these may be obtained from the authors, or the editor, upon request.

Case	Gr	A	Pr	Gr^2A^3	Nu	K_1	ψ_{max}
I	2×10^4	1·0	0·733	—	2·64	—	$3·92\times10^{-4}$
II	2×10^4	1·0	6·983	4×10^8	5·55	—	$8·91\times10^{-5}$
III	2×10^4	0·2	6·983	$3·2\times10^6$	4·07	0·166	$5·16\times10^{-4}$
IV	2×10^4	0·1	6·983	4×10^5	3·10	0·336	$1·01\times10^{-3}$
V	2×10^4	0·05	6·983	5×10^4	1·68	0·603	$1·65\times10^{-3}$
VI	2×10^3	0·1	6·983	4×10^3	0·417	0·840	$2·33\times10^{-3}$
VII	500	0·1	6·983	$2·5\times10^2$	0·130	0·968	$2·70\times10^{-3}$
VIII	10	0·1	6·983	0·1	0·1006	0·996	$2·75\times10^{-3}$

TABLE 1. Parameter values considered

temperature time step was chosen as much as 1000 times larger than the vorticity time step.

Computation time was further minimized by making use of the centro-symmetry property of the combined equations and boundary conditions. In particular, if there are n_x grid points in the x direction and n_y grid points in the y direction, then symmetry requires

$$\left.\begin{aligned}\psi(i,j) &= \psi(n_x-i, n_y-j),\\ \omega(i,j) &= \omega(n_x-i, n_y-j),\\ \theta(i,j) &= 1-\theta(n_x-i, n_y-j).\end{aligned}\right\} \tag{7}$$

Hence, only half of the grid points need be scanned at each iteration, leading to at least a 50 % cut in computation time.

Excellent indications of the progress of the integration were provided by an integral of the vorticity over one end of the cavity (essentially, a drag coefficient) and by the Nusselt number as defined in equation (I48). Once the variations in both of these integral parameters between iterations were of the same magnitude as the computer truncation error, the integration was stopped. For the IBM 370-155 which was used, this occurred when changes were taking place in the fifth or sixth significant figure. Typical computation times using the approach outlined above were 20–30 min with the variations due primarily to changes in the Grashof number and to variations in the accuracy of the starting values assumed for θ, ψ and ω.

4. Numerical results

Square box

As a preliminary test to establish the overall consistency of the numerical results produced by our algorithm, we considered a square cavity with

$$Gr = 2\times10^4 \quad \text{and} \quad Pr = 0·733,$$

listed as case I in table 1. Wilkes & Churchill (1966) had previously considered the same system. With a 21×21 grid in the Cartesian co-ordinate system, they obtained a Nusselt number of 2·52, whereas using (5) and (6), with 21 points in each co-ordinate direction, we obtained $Nu = 2·64$. We consider the difference

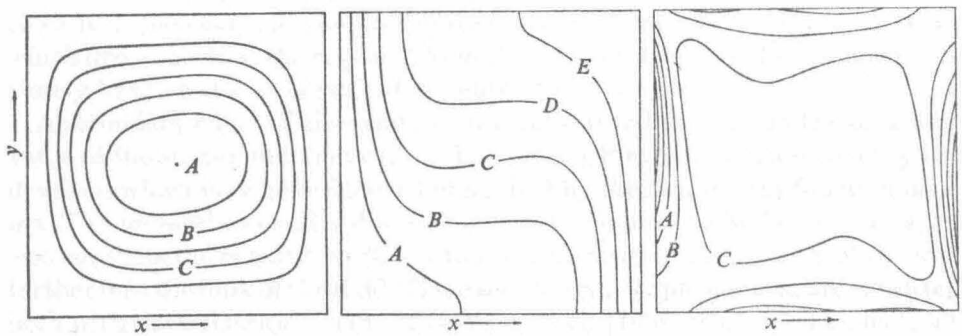

FIGURE 1. Case I; $Gr = 2 \times 10^4$, $A = 1$, $Pr = 0{\cdot}733$. (*a*) Streamlines; $A = 3{\cdot}92 \times 10^{-4}$, $B = 2{\cdot}62 \times 10^{-4}$, $C = 1{\cdot}31 \times 10^{-4}$. (*b*) Isotherms; $A = 0{\cdot}167$, $B = 0{\cdot}333$, $C = 0{\cdot}5$, $D = 0{\cdot}667$, $E = 0{\cdot}833$. (*c*) Vorticity contours; $A = -1{\cdot}41 \times 10^{-2}$, $B = -5{\cdot}77 \times 10^{-3}$, $C = 2{\cdot}55 \times 10^{-3}$.

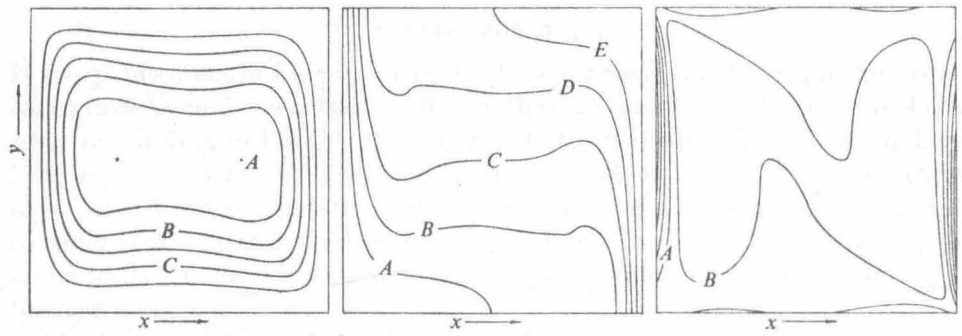

FIGURE 2. Case II; $Gr = 2 \times 10^4$, $A = 1$, $Pr = 6{\cdot}983$. (*a*) Streamlines; $A = 8{\cdot}91 \times 10^{-4}$, $B = 5{\cdot}90 \times 10^{-4}$, $C = 2{\cdot}96 \times 10^{-4}$. (*b*) Isotherms; $A = 0{\cdot}167$, $B = 0{\cdot}333$, $C = 0{\cdot}5$, $D = 0{\cdot}667$, $E = 0{\cdot}833$. (*c*) Vorticity contours; $A = -4{\cdot}24 \times 10^{-3}$, $B = 7{\cdot}6 \times 10^{-4}$.

between these values to be largely insignificant, particularly in view of the large scatter of the numerically determined values for Nu as a function of Ra that have been collected by Quon (1972) from various authors (cf. his figure 9).

In figure 1 the flow configuration is presented for this case. The structure of the isotherms indicates that the only substantial horizontal temperature gradients occur in the lower right and upper left ends of the cavity. Since the buoyancy forces are proportional to the temperature gradients [cf. equation (1)], the overall flow must be driven by these essentially boundary-layer-like regions, with the flow in the core maintained by the requirements of continuity as suggested by the model of Gill (1966).

A change in the Prandtl number from 0·733 to 6·983 (the Prandtl number of water at 20 °C) with all other parameters held constant produced a considerable change in flow structure, as indicated by comparing figures 1 and 2. The chief change is a thinning of the thermal boundary layer, which is to be expected

on the basis of standard boundary-layer arguments (Gill 1966). Furthermore, since it is the buoyancy-induced forces in the thermal boundary-layer region which drive the flow, the region of largest vertical velocity is also confined more closely to the walls, as is evident in figure 2(*a*).

A secondary effect of increasing Pr is a substantial decrease in the maximum value of the stream function within the cavity.† Furthermore, a secondary flow develops which may be recognized in figure 2 by the two stream-function maxima. This induced secondary flow not only causes inflexions in the isotherms, but also convects the negative vorticity that is generated in the vicinity of the walls further into the bulk of the fluid. These secondary flow phenomena are consistent both with the numerical results of De Vahl Davis (1968), Rubel & Landis (1969) and Quon (1972) and with the experimental results of Elder (1965), who found that such a flow results for $Ra > 10^5$. For the present case $Ra = 1{\cdot}4 \times 10^5$. This strong dependence of the flow characteristics on Pr for $A = 1$ is in contrast to the conclusion in I that the stream-function and vorticity fields should be independent of Pr to first order for $A \ll 1$.

Cavities with $A < 1$

It was pointed out in I [equation (I51)], that, for constant Pr, a significant parameter in determining whether the flow in the core complies with the parallel flow structure derived in I is $Gr^2 A^3$. To illustrate the transition from the boundary-layer regime of large Gr^2A^3 to the parallel flow structure of 'small' Gr^2A^3, we have carried out computations at several values of this parameter. The cases considered are shown in table 1, in order of decreasing Gr^2A^3. Also listed are the numerically calculated Nusselt numbers and maximum stream function $\psi_{\max}$ for each case.

All of the results for $A < 1$ deal only with $Pr = 6{\cdot}983$, primarily so that the results can be directly compared with experimental observations in water (see part 3), but also to take advantage of the observation of De Vahl Davis (1968) that the stability of the numerical algorithm increases with increasing Pr.

In figures 3–8, we have plotted the streamlines, isotherms and contours of constant vorticity for each case, also arranged in order of decreasing Gr^2A^3 so that the trends of the numerical solution can easily be identified. It should be noted that all of the results are plotted as square figures; hence, for cavities with small aspect ratios the horizontal length scale is substantially compressed.

An examination of the results for the cavities with $Gr = 2 \times 10^4$, $Pr = 6{\cdot}983$ and various aspect ratios (figures 2–5) reveals that the streamlines and vorticity lines become more nearly parallel as A decreases, as was anticipated in the analysis of I. It is perhaps worth emphasizing that this transition to parallel flow is not simply a consequence of decreasing the overall temperature gradient $(T_h - T_c)/l$, as the aspect ratio is made smaller. In fact, one can change A in such a manner that the overall temperature difference must actually be increased in

† The apparent difference between this result and that of De Vahl Davis (1968) is due both to different scaling and to the fact that we held Gr fixed while De Vahl Davis used Ra ($= Gr\,Pr$) as the fixed parameter.

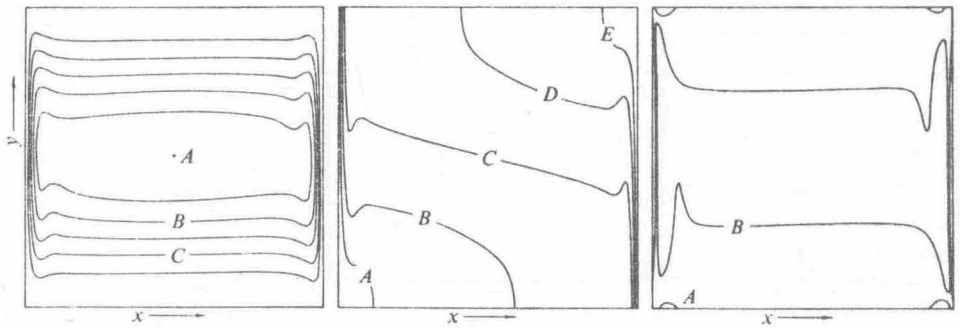

FIGURE 3. Case III; $Gr = 2 \times 10^4$, $A = 0{\cdot}2$, $Pr = 6{\cdot}983$. (*a*) Streamlines; $A = 5{\cdot}16 \times 10^{-4}$, $B = 3{\cdot}45 \times 10^{-4}$, $C = 1{\cdot}73 \times 10^{-4}$. (*b*) Isotherms; $A = 0{\cdot}167$, $B = 0{\cdot}333$, $C = 0{\cdot}5$, $D = 0{\cdot}667$, $E = 0{\cdot}833$. (*c*) Vorticity contours; $A = -1{\cdot}88 \times 10^{-2}$, $B = 3{\cdot}48 \times 10^{-3}$.

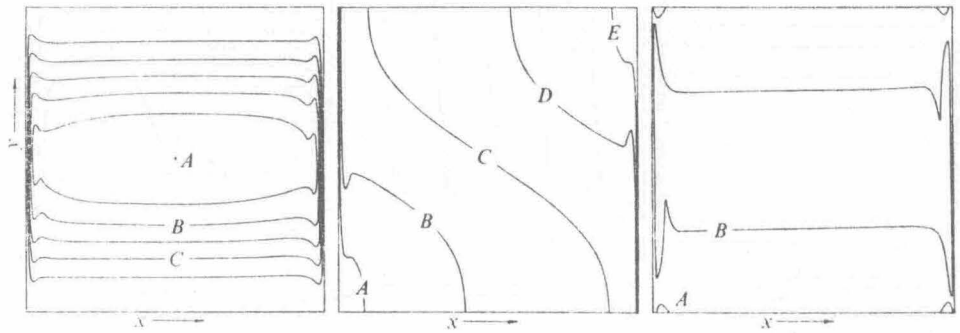

FIGURE 4. Case IV; $Gr = 2 \times 10^4$, $A = 0{\cdot}1$, $Pr = 6{\cdot}983$. (*a*) Streamlines; $A = 1{\cdot}01 \times 10^{-3}$, $B = 6{\cdot}72 \times 10^{-4}$, $C = 3{\cdot}36 \times 10^{-4}$. (*b*) Isotherms; $A = 0{\cdot}167$, $B = 0{\cdot}333$, $C = 0{\cdot}5$, $D = 0{\cdot}667$, $E = 0{\cdot}833$. (*c*) Vorticity contours; $A = -3{\cdot}18 \times 10^{-2}$, $B = 6{\cdot}28 \times 10^{-3}$.

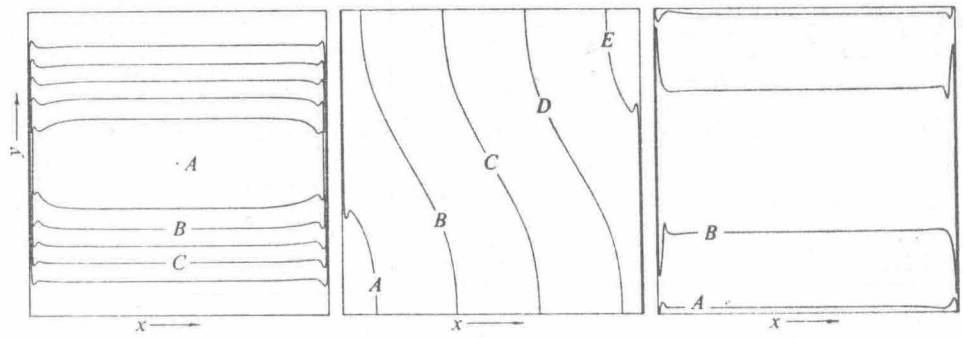

FIGURE 5. Case V; $Gr = 2 \times 10^4$, $A = 0{\cdot}05$, $Pr = 6{\cdot}983$. (*a*) Streamlines; $A = 1{\cdot}65 \times 10^{-3}$, $B = 1{\cdot}11 \times 10^{-3}$, $C = 5{\cdot}53 \times 10^{-4}$. (*b*) Isotherms; $A = 0{\cdot}167$, $B = 0{\cdot}333$, $C = 0{\cdot}5$, $D = 0{\cdot}667$, $E = 0{\cdot}833$. (*c*) Vorticity contours; $A = -4{\cdot}43 \times 10^{-2}$, $B = 9{\cdot}09 \times 10^{-3}$.

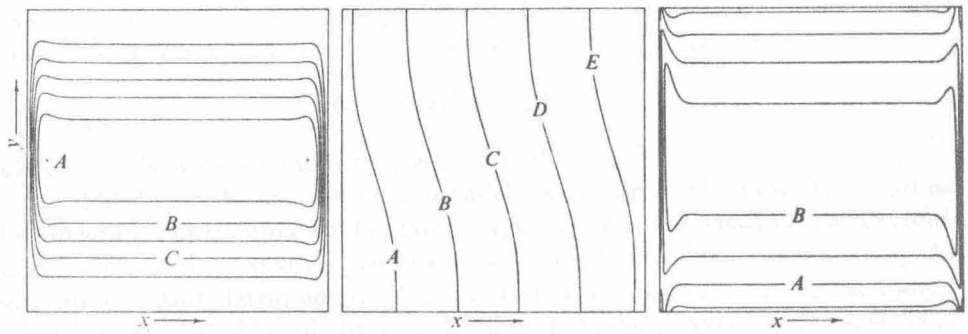

(*a*) (*b*) (*c*)

FIGURE 6. Case VI; $Gr = 2 \times 10^3$, $A = 0{\cdot}1$, $Pr = 6{\cdot}983$. (*a*) Streamlines; $A = 2{\cdot}33 \times 10^{-3}$, $B = 1{\cdot}55 \times 10^{-3}$, $C = 7{\cdot}74 \times 10^{-4}$. (*b*) Isotherms; $A = 0{\cdot}167$, $B = 0{\cdot}333$, $C = 0{\cdot}5$, $D = 0{\cdot}667$, $E = 0{\cdot}833$. (*c*) Vorticity contours; $A = -2{\cdot}60 \times 10^{-1}$, $B = 2{\cdot}20 \times 10^{-2}$.

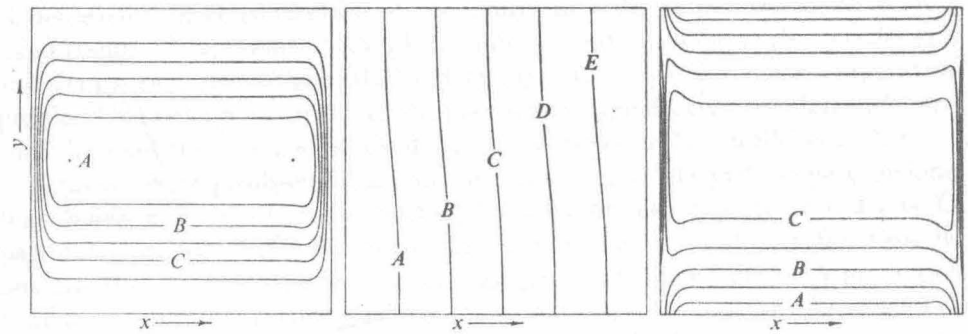

(*a*) (*b*) (*c*)

FIGURE 7. Case VII; $Gr = 500$, $A = 0{\cdot}1$, $Pr = 6{\cdot}983$. (*a*) Streamlines; $A = 2{\cdot}70 \times 10^{-3}$, $B = 1{\cdot}80 \times 10^{-3}$, $C = 8{\cdot}99 \times 10^{-4}$. (*b*) Isotherms; $A = 0{\cdot}167$, $B = 0{\cdot}333$, $C = 0{\cdot}5$, $D = 0{\cdot}667$, $E = 0{\cdot}833$. (*c*) Vorticity contours; $A = -6{\cdot}31 \times 10^{-2}$, $B = -1{\cdot}96 \times 10^{-2}$, $C = 2{\cdot}40 \times 10^{-2}$.

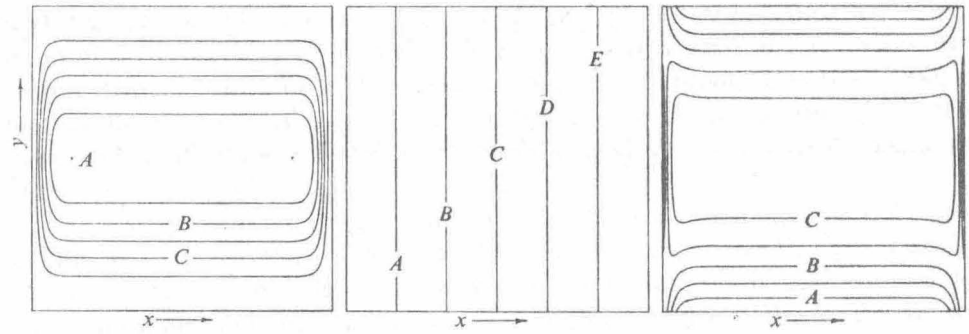

(*a*) (*b*) (*c*)

FIGURE 8. Case VIII; $Gr = 10$, $A = 0{\cdot}1$, $Pr = 6{\cdot}983$. (*a*) Streamlines; $A = 2{\cdot}75 \times 10^{-3}$, $B = 1{\cdot}84 \times 10^{-3}$, $C = 9{\cdot}17 \times 10^{-4}$. (*b*) Isotherms; $A = 0{\cdot}167$, $B = 0{\cdot}333$, $C = 0{\cdot}5$, $D = 0{\cdot}667$, $E = 0{\cdot}833$. (*c*) Vorticity contours; $A = -6{\cdot}26 \times 10^{-2}$, $B = -1{\cdot}99 \times 10^{-2}$, $C = 2{\cdot}28 \times 10^{-2}$.

order to hold Gr fixed. For example, A may be decreased by simply decreasing h while holding l constant. Then, to maintain a specified constant

$$Gr\ (\equiv \beta g(T_h - T_c)\, h^3/\nu^2),$$

it is obviously necessary to increase $(T_h - T_c)/l$.

In addition to the increasingly parallel character of the flow, the gradual disappearance of the thermal boundary layers as A is decreased is also a prominent feature of the transition. In case II, the core flow is driven primarily by the entrainment and detrainment of fluid from the buoyancy-driven boundary layers. On the other hand, by case V these boundary layers have essentially disappeared. The major portion of the temperature drop occurs across the core, so that the overall flow is necessarily driven by the buoyancy forces in the core. This transition to a core-driven flow, with decreasing A, was suggested in I and is completely consistent with the asymptotic theory.

The above tendencies are not restricted to the situation with Gr fixed and A decreasing. A consideration of the figures in order of decreasing Gr with A fixed (figures 4, 6, 7 and 8) reveals a similar trend of increasingly parallel flow and a transition from a thermal boundary-layer structure to a linear temperature profile. This behaviour provides support for the qualitative conclusion from I that the condition (I51) is sufficient for the existence of the parallel core flow.

Figures 3–8, when observed in order of decreasing $Gr^2 A^3$, yield some additional tendencies, most of which fall within the scope of the asymptotic analysis. Of particular prominence is the decreasing magnitude of the stream-function deflexions that occur as the fluid enters and leaves the end regions. A prediction from the asymptotic theory was that these deflexions, for constant Pr, should be $O(Gr^2 A^2)$, provided that A is sufficiently small. Since the arrangement in order of decreasing $Gr^2 A^3$ also produces an arrangement in order of decreasing GrA, this phenomenon is again compatible with the asymptotic theory.

One characteristic of the stream-function deflexions at the larger values of GrA which is not predicted by the first four terms of the asymptotic expansion is the 'necking down' of the streamlines before they again diverge.† Closely associated with the necking phenomenon is the occurrence of the stream-function maximum in the *core* rather than in the end regions as predicted in the asymptotic theory. Only in cases VI–VIII, for which necking is absent, does the absolute maximum of ψ occur in the end regions. However, a closer examination of the numerical results does indicate that there always exists at least a *local* maximum of ψ in each end region.

Some additional interesting trends are also displayed by the plots of the isotherms and equi-vorticity lines. For the larger values of $Gr^2 A^3$, the vorticity gradients are extremely large in the vicinity of the end walls, and, in relative terms, are almost non-existent in the bulk of the fluid. Hence, in this limited sense, Batchelor's (1954) conjecture of a uniform-vorticity core at large Gr (A fixed, $Gr \to \infty$) is basically confirmed. It is important to note, however, that the basic

† There is, however, a strong indication that this phenomenon would be realized with a subsequent (higher-order) correction to the solution in the end region.

flow structure in this limit is otherwise completely unlike that suggested by Batchelor and in qualitative accord with that proposed by Gill. In particular, because of the strong horizontal advection due to entrainment–detrainment from the boundary layers, the temperature distribution in the core at large Gr^2A^3 shows only a weak dependence on horizontal position, while still retaining reasonably strong vertical gradients. The vorticity generated at the end walls does not effectively diffuse to the core, because the buoyancy forces in the region adjacent to the walls provide an effective sink for this vorticity (they appear as source terms for vorticity of opposite sign) which greatly decreases its magnitude before it can reach the core. A lucid explanation of the transient development of this (large Gr^2A^3) physical structure has recently been provided by Quon (1972). As either A or Gr is decreased, the magnitude of the vorticity gradients in the end regions is decreased, and the temperature distribution shows a gradual transition from the strong vertical dependence of the boundary-layer regime towards the totally horizontal dependence corresponding to the linear profile of I. Ultimately, in cases VI–VIII, the vorticity gradients are of comparable magnitude throughout the cavity. In addition, as expected from the asymptotic analysis, the vorticity distribution becomes increasingly symmetric with decreasing A or Gr.

A more quantitative comparison of the numerical solutions with the asymptotic theory is possible particularly for the flow in the core. Equation (I14) indicates that, if the flow is parallel, then

$$u/K_1 = \partial^2 f(y)/\partial y^2, \tag{8}$$

where

$$f(y) = \tfrac{1}{120}y^5 - \tfrac{1}{48}y^4 + \tfrac{1}{72}y^3$$

and K_1 is the parallel-flow parameter. Any deviation of numerically determined values of u/K_1 from the relationship in (8) will give a good indication of deviations of the numerical solutions from the parallel flow structure. Hence, the problem of quantitatively comparing the numerical and analytical velocity profiles reduces to one of finding a value for K_1 from each numerical solution. This is easily done since, according to equation (I15), the core temperature can be separated into two parts when A is sufficiently small. One part is a linear function of x and the other is the fifth-order polynomial $f(y)$. Hence, a value for K_1 can be determined from each numerical solution (whether or not the flow is identically parallel in the core) by fitting the numerically determined temperature θ_{ij}, in a least-squares manner, to the equation

$$\theta = K_1 Ax + K_2$$

at the five central grid points, on the line $y = 0{\cdot}5$. The resulting values of K_1 are presented in table 1. As expected in view of the transition from the boundary-layer regime to the 'conduction' regime of the I, the coefficient K_1 increases as Gr^2A^3 decreases.

Figure 9 is a plot of the theoretically and numerically determined velocity profiles u/K_1 on the centre-line $x = 1/2A$ as a function of y. It is apparent that as Gr^2A^3 decreases the velocity profile approaches more closely the parallel structure. However, for values of $Gr^2A^3 < 10^4$, cases VI–VIII, the numerical

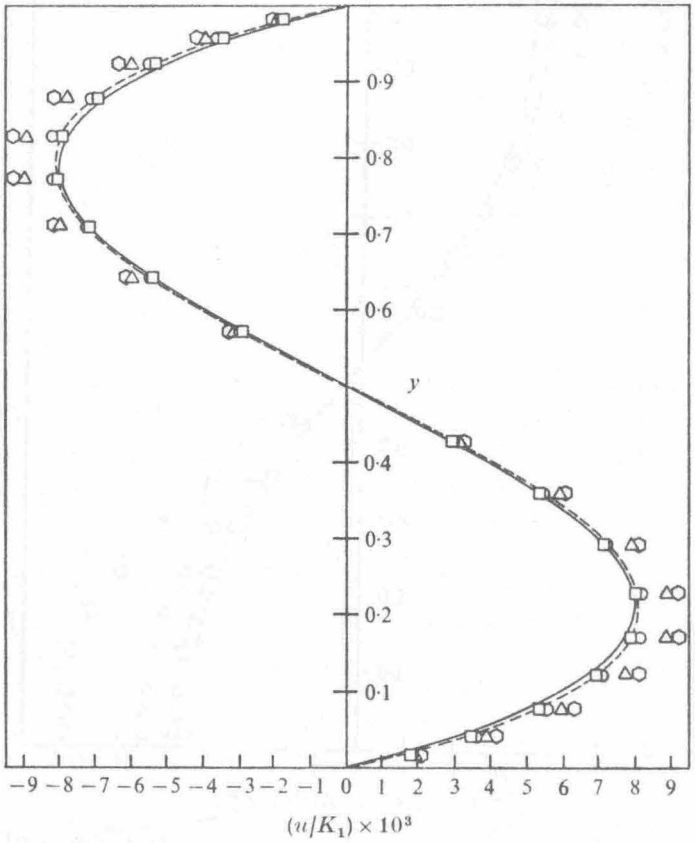

FIGURE 9. Comparison of normalized horizontal velocity at $x = 1/2A$ with theoretical parallel-flow profile (solid line). ○, $Gr = 2 \times 10^4$, $A = 0{\cdot}2$; △, $Gr = 2 \times 10^4$, $A = 0{\cdot}1$; ○, $Gr = 2 \times 10^4$, $A = 0{\cdot}05$; □, $Gr = 2 \times 10^3$, $A = 0{\cdot}1$; – – –, $Gr = 5 \times 10^2$, $A = 0{\cdot}1$.

data fall on a single curve (the broken line) that is somewhat different from the theoretical profile. Because of its consistency, we attribute this discrepancy to the numerical error introduced by the finite-difference scheme and grid network used. Since this error constitutes only a very small fraction of $\hat{u}/K_1$, the correspondence between the analytical theory and the limiting form of the numerical velocity profiles would appear to be quite satisfactory.

It is significant that cases III–V, in which Gr^2A^3 is largest, have horizontal velocities larger than those predicted by the parallel-flow theory with K_1 evaluated from the numerical solutions. As the transition from the asymptotic limit of I to the boundary-layer regime of Gill is encountered, the driving force for fluid motion must gradually change over from one totally dominated by the horizontal temperature gradient in the core to one controlled by entrainment–detrainment from the boundary layers at the end walls. Hence, as Gr^2A^3 is increased, the theoretical prediction from I must increasingly underestimate the actual horizontal velocities, since it is based entirely on the core-gradient mechanism. This is evident in the results of figure 9.

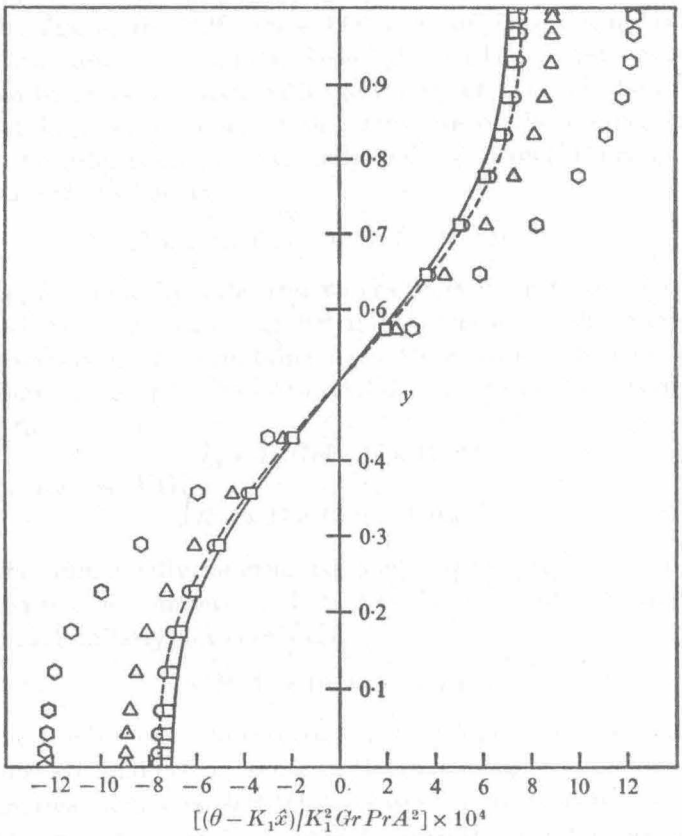

FIGURE 10. Comparison of numerically determined θ at $x = 1/2A$ with theoretical core temperature (solid line). Notation as in figure 9.

It is also possible to obtain a quantitative estimate for the value of $Gr^2Pr^2A^3$ at which the core flow changes from parallel to non-parallel from the results presented in figure 9, and hence to verify condition (I51). The velocity profile of case V deviates only slightly from the limiting profile of the numerical solutions, whereas that for case VI falls directly on the limiting curve. Hence, the appropriate limit for validity of the parallel flow structure (for $A \sim 0{\cdot}1$) must occur at a $Gr^2Pr^2A^3$ between $2{\cdot}5 \times 10^6$ (case V) and 2×10^5 (case VI). This observation lends strong support to the speculation of I that the parallel flow structure will apply for $Gr^2Pr^2A^3 \lesssim 10^5$, provided that A is sufficiently small.

Further consideration of the core solution of I indicates that a plot of

$$(\theta - K_1 Ax)/K_1^2 GrPrA^2$$

as a function of y should also yield the fifth-order polynomial $f(y)$, provided that A and $Gr^2Pr^2A^3$ are such that the parallel-flow theory is relevant. Figure 10 is a plot of this function evaluated at the centre-line $x = 1/2A$. For cases III–VI, with decreasing Gr^2A^3, the numerical profiles approach the theoretical curve as would be expected. On the other hand, for case VII the difference between the

numerical and theoretical curves increases slightly and for case VIII, which is not shown on the figure, the differences between the theoretical and numerical data points are large and random. Although this latter trend would, at first glance, appear to be inconsistent with the theory of I, it is in fact a numerical artifact which is a consequence of the structure of the temperature field as $Pr\,GrA^2 \to 0$. An order-of-magnitude analysis of equation (I15) reveals that both $K_1 Ax$ and θ are $O(1)$ whereas

$$K_1^2 Gr\,Pr\,A^2 f(y) = O(Gr\,Pr\,A^2 \times 10^{-3}).$$

If we assume, for some hypothetical values of the parameters Gr, Pr and A, that the core flow is identically parallel and, furthermore, that the numerically determined temperature field contains a consistent error ξ_1, then a simple calculation shows that the error in the numerical data corresponding to figure 10 will be amplified to

$$\xi_2 = \xi_1 / GrPrA^2 \times 10^{-3}.$$

To be specific, for case VII,

$$GrPrA^2 \times 10^{-3} = 0{\cdot}035,$$

so that, if the numerically determined temperature profile contains an error of 0·5 %, then it is not unreasonable to have an error of 15 % in the reduced numerical data. Similarly, for case VIII,

$$GrPrA^2 \times 10^{-3} = 7 \times 10^{-4},$$

so that even a small numerical error would be amplified to substantial proportions. We must conclude that, owing to the increasing prominence of even the smallest numerical errors as $GrPrA^2$ decreases, figure 10 is of limited value in establishing the region of Gr, Pr, A space in which the core-flow solution is valid.

In the previous discussion, it has been emphasized that the numerical results effectively display the transition from the parallel flow regime of small Gr^2A^3 to the boundary-layer regime of large Gr^2A^3. Perhaps the most graphic demonstration of this transition is provided by figure 11, a plot of $\log(1-K_1)$ as a function of $\log(Gr^2A^3)$. The asymptotic expression for K_1, equation (I45), indicates that for constant Pr such a plot should yield a curve that is asymptotic to the straight line

$$\log(1-K_1) = \log(3{\cdot}48 \times 10^{-6} Pr^2) + \log(Gr^2A^3) \tag{9}$$

in the limit as $A \to 0$. On the other hand, the boundary-layer theory suggests that for large Gr^2A^3 the horizontal gradient of temperature in the core should be zero. Hence for large Gr^2A^3 the curve should be asymptotic to the line

$$1 - K_1 = 1.$$

The numerically determined values of K_1 display the expected trends in both limits.

A further demonstration of the transition from the parallel to the boundary-layer regime is provided by figure 12, a plot of $\log(Nu - A)$ as a function of $\log(Gr^2A^3)$. We emphasize that it is the *deviation* of the actual Nu from the asymptotic value A that is plotted here. For small values of Gr^2A^3, the

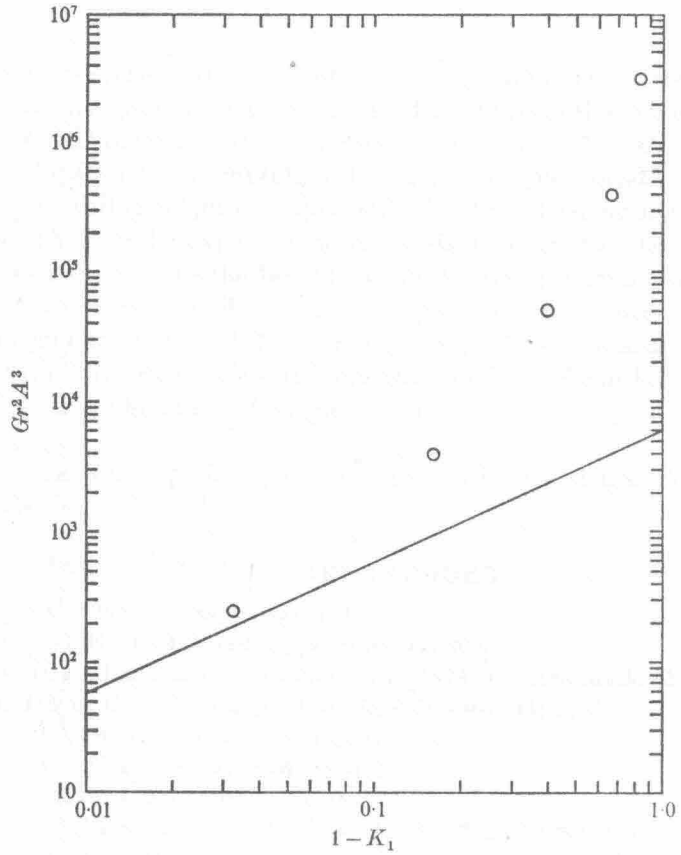

FIGURE 11. Variation of K_1 with Gr^2A^3. ○, numerical data; ——, asymptotic theory.

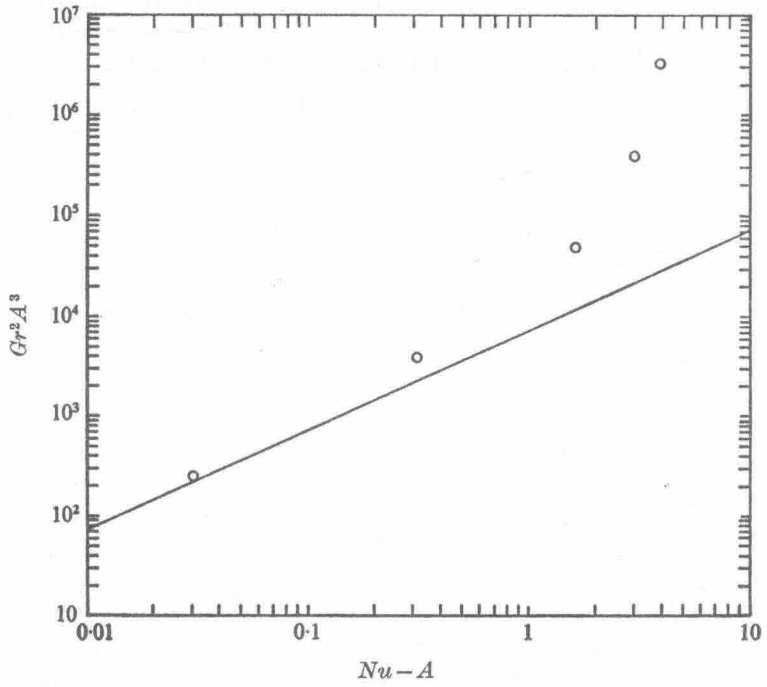

FIGURE 12. Variation of $Nu-A$ with Gr^2A^3. ○, numerical data; ——, asymptotic theory.

numerically determined values of the Nusselt number are asymptotic to the theoretical straight line which was derived in I. On the other hand, it is also evident that, as Gr^2A^3 increases, the numerically determined Nusselt numbers deviate considerably from the asymptotic value. In fact, for the largest values of Gr^2A^3 considered, the scaling of figure 12 apparently has little bearing on the actual Nusselt number. This is to be expected, however, since at large values of Gr^2A^3 the flow resembles more closely the boundary-layer structure than it does the parallel flow structure. Since Gill's boundary-layer analysis showed that Nu should be independent of A, and vary directly as $(GrPr)^{\frac{1}{4}}$, the sharp increase in the slope of the numerical curve at large values of Gr^2A^3 can be attributed to the transition to the boundary-layer structure.

This work was supported, in part, by National Science Foundation Grant GK-35476.

REFERENCES

Arakawa, A. 1966 *J. Comp. Phys.* **1**, 119.

Batchelor, G. K. 1954 *Quart. Appl. Math.* **12**, 209.

Cormack, D. E., Leal, L. G. & Imberger, J. 1974 *J. Fluid Mech.* **65**, 209.

De Vahl Davis, G. 1968 *Int. J. Heat Mass Transfer*, **11**, 1675.

Elder, J. W. 1965 *J. Fluid Mech.* **23**, 77.

Elder, J. W. 1966 *J. Fluid Mech.* **24**, 823.

Gill, A. E. 1966 *J. Fluid Mech.* **26**, 515.

Newell, M. E. & Schmidt, F. W. 1970 *J. Heat Transfer*, **92**, 159.

Peaceman, D. W. & Rachford, H. H. 1955 *J. Soc. Ind. Appl. Math.* **3**, 28.

Quon, C. 1972 *Phys. Fluids*, **15**, 12.

Rubel, A. & Landis, F. 1969 *Phys. Fluids Suppl.* II, **12**, II-208.

Von Rosenberg, D. U. 1969 *Methods for the Numerical Solution of Partial Differential Equations*. Elsevier.

Wilkes, J. O. & Churchill, S. W. 1966 *A.I.Ch.E. J.* **12**, 161.

C. THE EFFECT OF UPPER SURFACE BOUNDARY CONDITIONS ON CONVECTION IN A SHALLOW CAVITY WITH DIFFERENTIALLY HEATED END-WALLS[†]

By D. E. Cormack, G. P. Stone and L. G. Leal

The effect of upper surface boundary conditions on the flow structure in shallow cavities with differentially heated end-walls is examined. Matched asymptotic solutions, valid for small cavity aspect ratios are presented for the following cases: uniform shear stress with zero heat flux, uniform heat flux with zero shear stress, and heat flux linearly dependent on surface temperature with zero shear stress. It is shown that these changes in surface boundary conditions have an important influence on the temperature and flow structure within the cavity.

[†]This manuscript has been accepted for publication in the International Journal of Heat and Mass Transfer.

NOMENCLATURE

A,	aspect ratio = h/ℓ;
B,	dimensionless shear parameter = $\ell\tau_o/h^2(T_h - T_c)\beta g$;
c_i, c_i',	coefficients which are functions of Gr and Pr;
c_p	heat capacity;
$F(y)$	$y^5/120 - 5y^4/192 + y^3/48$
$f(T)$	surface heat flux;
Gr	Grashof number = $\beta g(T_h - T_c)h^3/\nu^2$;
H	scaled thermal exchange coefficient = Kh/kA^2;
h	cavity depth;
K	effective thermal exchange coefficient;
K_1, K_2	core solution parameters;
k	thermal conductivity;
ℓ	cavity length;
ℓ'	characteristic length for surface heat transfer;
Nu	Nusselt number = $\int_o^{'} \frac{\partial\theta}{\partial x}\Big|_{x=0} dy$;
Pr	Prandtl number = $c_p\mu/k$;
Q	scaled surface heat flux = $qh/kA^2(T_h - T_c)$;
q	surface heat flux;
T_c, T_h	cold- and hot-end wall temperatures;
T_e	equilibrium temperature for surface heat transfer;
u^*	slip velocity;
x,y	cartesian coordinates nondimensionalized by h;
$\hat{x}$	Ax;
β	coefficient of thermal expansion;

ε $\sqrt{Kh/k}$;

η $(1 - y)$;

Θ $(1 - \theta)$;

θ $(T - T_c)/(T_h - T_c)$;

μ viscosity;

ν kinematic viscosity;

ξ horizontal distance from hot end of cavity = $A^{-1} - x$;

$\bar{\xi}$ core variable for semi-infinite cavity = $\varepsilon\xi$;

τ_o surface kinematic shear stress;

Ω hot end vorticity;

ω vorticity;

Ψ hot end stream function;

ψ stream function;

1. INTRODUCTION

It has become a common practice to use estuaries and other bodies of water for the disposal of the waste heat that arises as a by-product of fossil and atomic fuel electric power generation. Similarly, sewage treatment plants often discharge high concentrations of organic pollutants directly into estuaries and coastal waters. Although such dumping may be safely carried out, it is important to take proper consideration of its impact on the biochemical processes that depend critically on the water temperature and purity. As a first step toward understanding the biological impact, laboratory and field experiments have established practical temperature and toxicity limits, beyond which the biological processes are impaired. However, before outfall systems can be designed so that these limits are not exceeded, it is necessary to understand more fully the mechanisms by which these wastes are dispersed within the body of water.

Estuaries which are shallow (depth much smaller than length) and have strong enough vertical mixing to prevent the formation of density wedges, often exhibit a density distribution which is vertically uniform but which varies approximately linearly in the horizontal direction. An excellent naturally occurring example is Shark Bay on the West Australian coast (Logan and Cebulski [1]). More commonly, perhaps, the horizontal gradient may be established as a result of man-related heat input near the end of the estuary. In either case, the slow gravitational circulation, induced by the horizontal density gradient, can contribute significantly to the longitudinal dispersion of pollutants, mainly by the mechanism of Taylor diffusion (Fischer [2]).

A complete dynamic model of an estuary such as Shark Bay would, of course, be very complex. The geometry of the estuary is complicated, and the flow

is turbulent and generally coupled with the tidal cycle. Furthermore, various regions of the flow field are controlled by processes occurring on very different length scales. In the immediate vicinity of the source (for example, near the discharge of heated fluid from a power plant) the problem is dominated by the details of the source geometry, and the local mixing processes (cf. Harleman and Stolzenbach [3]). Covering a much wider area beyond this so-called "near-field" region, is the region of interest in the present work, namely the "far-field," where the primary transport mechanisms are bulk diffusion and convection. In this region, the detailed velocity and density fields are relatively insensitive to the source configuration. In addition, since the time scale of the gravitational circulation in the far-field is large, the influence of the tidal cycle and other unsteady variations of velocity on the mean circulation in the estuary may be taken into account by the use of effective eddy exchange coefficients (Imberger [4]). Thus, considerable insight into the basic far-field flow structure can be obtained from the idealized problem of laminar flow in a shallow two-dimensional cavity with differentially heated end walls.

Investigations into the problem of natural convection in two-dimensional cavities have been extensive. Most theoretical studies have focused on numerical solutions of the full equations of motion, subject to the Boussinesq approximation, for cavities which are either square or have a depth, h, larger than their length, ℓ (cf. Quon [5], Wilkes and Churchill [6], Newell and Schmidt [7], and DeVahl Davis [8]). Notably, these studies have not dealt specifically with the case of *small* aspect ratio ($A \equiv h/\ell \ll 1$) which is relevant to the estuary circulation problem. In a recent paper, Cormack, Leal and Imberger [9] (henceforth denoted as "I") provided an

analytical description of the convective motion of a Newtonian fluid in a two-dimensional enclosed cavity with a rigid, no-slip, insulating lid for the limiting case $A \to 0$, with fixed values of the Grashof number, Gr. The basic features of shallow cavity flow, as predicted by this theory, were subsequently verified both by numerical solutions of the full equations of motion (Cormack, Leal and Seinfeld [10]), and by experimental measurements (Imberger[4]).

As explained by Imberger [4], the no-slip insulating boundary was the only surface condition for which reliable laboratory data could be obtained, and this motivated its use in our previous analytical investigation. Clearly, this condition is quite different from that relevant to an open surface estuary, and the effect of this difference upon the circulation dynamics is not obvious. It is the purpose of the present study to investigate this question for the more realistic conditions of an imposed surface shear stress (due, for example, to a surface wind stress) and surface heat transfer. The analysis will show that these modifications of the boundary conditions can have a very significant effect on the Nusselt number (and hence on the longitudinal dispersive capacity of the cavity) as well as on the form of the velocity and temperature profiles for $A \to 0$, with other parameters held fixed.[†]

[†] In contrast, for $Gr \to \infty$, A fixed, the recent numerical solutions of Quon [5] indicate that the upper surface condition for the velocity plays a less important role, at least in determining Nu.

2. MATHEMATICAL FORMULATION OF THE PROBLEM

The system that we consider is shown schematically in Figure 1. It consists of a cavity of length, ℓ, and height, h, that contains a Newtonian fluid. The end walls are held at different, but uniform temperatures, T_c and T_h, with $T_c < T_h$. The bottom of the box is insulated and the end walls and bottom are rigid, no-slip boundaries. At the upper surface, the kinematic shear stress is assumed to have some uniform value, τ_o, and the heat flux is given as a function of the surface temperature, f(T).

Subject to the usual Boussinesq approximation, the steady-state equations governing this system may be expressed (see I) as

$$GrA^2 \frac{\partial(\omega,\psi)}{\partial(x,y)} = A\nabla^2\omega + \frac{\partial\theta}{\partial x} \tag{1}$$

$$\nabla^2\psi = -\omega \tag{2}$$

$$PrGrA \frac{\partial(\theta,\psi)}{\partial(x,y)} = \nabla^2\theta \tag{3}$$

with boundary conditions

$$\left.\begin{aligned} &\psi = 0,\ \frac{\partial\psi}{\partial x} = 0,\quad \theta = Ax \quad \text{on } x = 0, A^{-1} \\ &\psi = 0,\ \frac{\partial\psi}{\partial y} = 0,\quad \frac{\partial\theta}{\partial y} = 0 \quad \text{on } y = 0 \end{aligned}\right\} \tag{4}$$

and

$$\frac{\partial\psi}{\partial x} = 0,\ \frac{\partial^2\psi}{\partial y^2} = \frac{\ell\tau_o}{h^2(T_h - T_c)\beta g},\ \frac{\partial\theta}{\partial y} = \frac{hf(T)}{k(T_h - T_c)} \quad \text{on } y = 1 \tag{5}$$

To nondimensionalize these equations, we have used h as the characteristic length scale, and $\beta g(T_h - T_c)h^3/\nu\ell$ as the characteristic velocity. Although perhaps not obvious, this velocity scaling is the most convenient choice for the present problem, where the basic flow structure is found to consist of a buoyancy driven parallel flow which is moderated by viscous effects over a length ℓ. At any rate, it may be justified a posteriori by the theory which

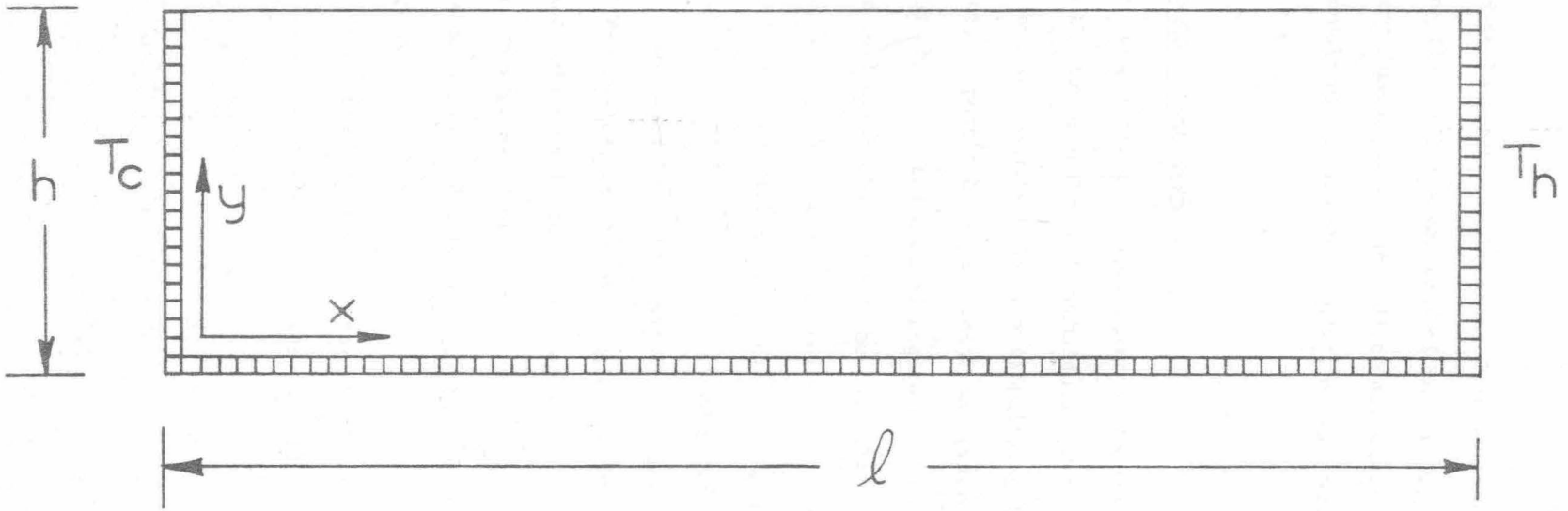

FIGURE 1: SCHEMATIC DIAGRAM OF THE CAVITY.

is presented in this paper. The dimensionless parameters which appear in the equations (1) - (3) are the Grashof number Gr, the Prandtl number Pr, and the cavity aspect ratio. The additional dimensionless parameters introduced as a result of the surface conditions (5), will be discussed in the body of the paper.

3. THE NO-SLIP, INSULATED CAVITY

Before the general case represented by (5) is considered, it is useful to summarize the basic analytical techniques and results obtained in I, for the no-slip insulated cavity. The key simplifying feature in this case is the assumption, supported by experimental observation, that the length scale for horizontal change in the central region of the cavity is $O(A)^{-1}$, while the scale for horizontal change near the end walls is only O(1). Because this disparity in length scales increases as $A \to 0$, an analytic solution to (1) - (5) may be obtained using the standard methods of matched asymptotic expansions, in the limit $A \to 0$ with the other parameters held fixed. Analytically, the cavity is decomposed into three parts, a core region of extent $O(A^{-1})$ in the center of the cavity, and two end regions within an O(1) distance of the end walls. The solutions in the three regions are coupled by the matching requirements in the regions of overlap.

The core solution is easily obtained by introducing the scaling

$$\hat{x} = Ax \tag{6}$$

into the governing equations and boundary conditions (1) - (5), and expanding the streamfunction and temperature as regular series in the small parameter A

$$\left.\begin{aligned} \psi &= \psi_o + A\psi_1 + A^2\psi_2 + \ldots \\ \theta &= \theta_o + A\theta_1 + A^2\theta_2 + \ldots \end{aligned}\right\} \tag{7}$$

The resulting solution is

$$\psi = K_1(y^4/24 - y^3/12 + y^2/24) \tag{8}$$

$$\theta = K_1\hat{x} + K_1^2 GrPrA^2(y^5/120 - y^4/48 + y^3/72) + K_2 \tag{9}$$

where

$$\left.\begin{aligned} K_1 &= c_1 + Ac_2 + A^2c_3 + \ldots \\ K_2 &= c_1' + Ac_2' + A^2c_3' + \ldots \end{aligned}\right\} \tag{10}$$

The coefficients $c_1, c_2, \ldots, c_1', c_2', \ldots$ are determined by matching the core solution with solutions valid in the end regions. Because of the symmetry of equations (1) - (4) and the no-slip, insulated boundary conditions, the coefficients c_i' can be eliminated in favor of the single set c_i, so that the matching operation reduces to a consideration of solutions valid in the cold end of the cavity. Upon calculating the end region solutions and carrying out the matching, the coefficient K_1, governing the magnitude of the horizontal temperature gradient in the core, was found to be

$$K_1 = 1 - 3.48 \times 10^{-6} Gr^2Pr^2A^3 + O(Gr^4Pr^4A^5) \tag{11}$$

while the Nusselt number,

$$Nu \equiv \int_0^1 \frac{\partial\theta}{\partial x}\bigg|_{x=0} dy$$

was shown to be of the form

$$Nu = A + 2.86 \times 10^{-6} Gr^2Pr^2A^3 + O(Gr^2Pr^2A^4). \tag{12}$$

The corresponding stream function representing the first order flow field in the (cold) end region is shown in Figure 2a.

Solutions (8) and (9) indicate that the core flow for a no-slip insulated surface is parallel to all orders of magnitude in A, while, to first order in

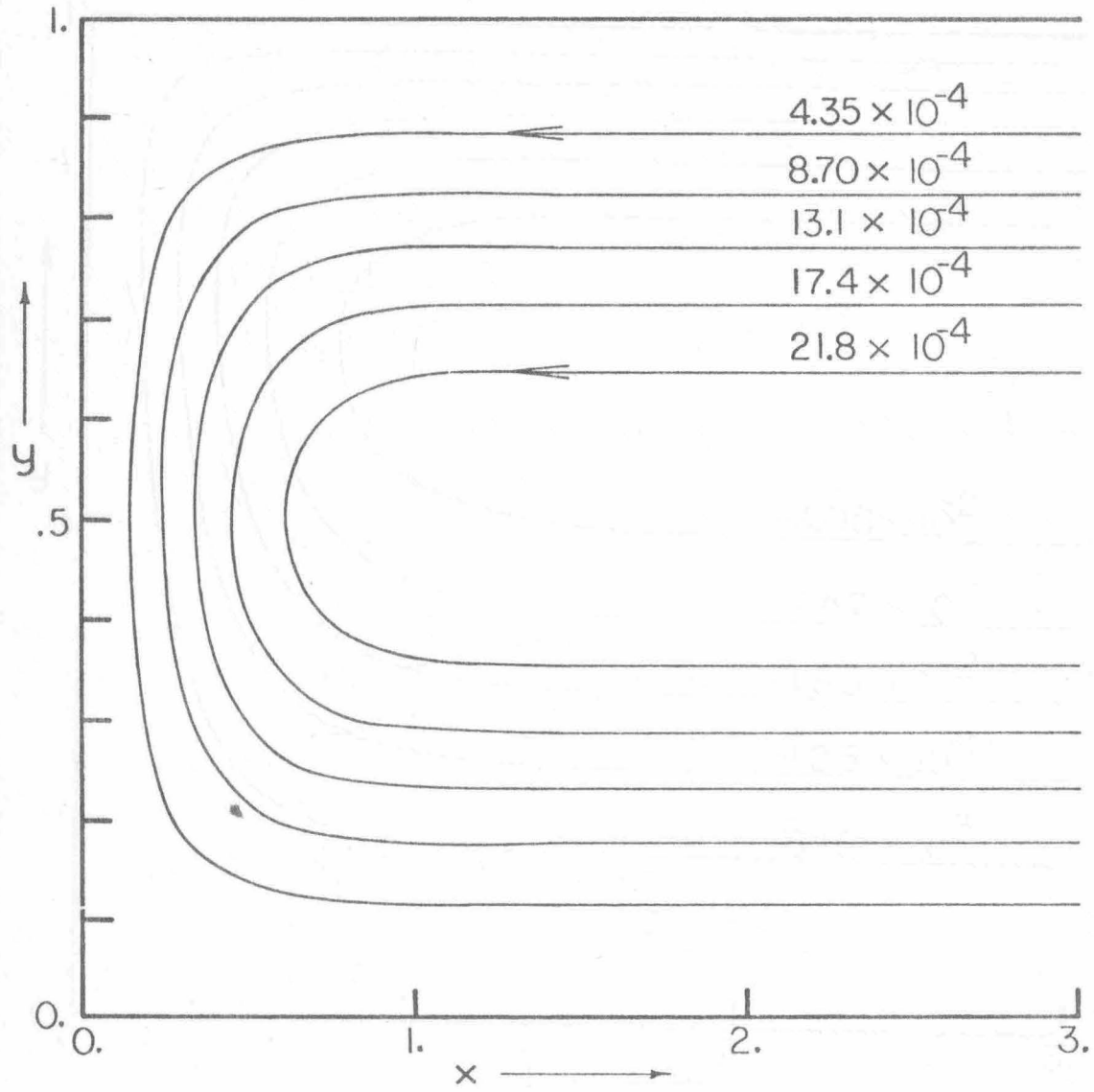

FIGURE 2a: STREAMLINES IN COLD END; FIXED LID.

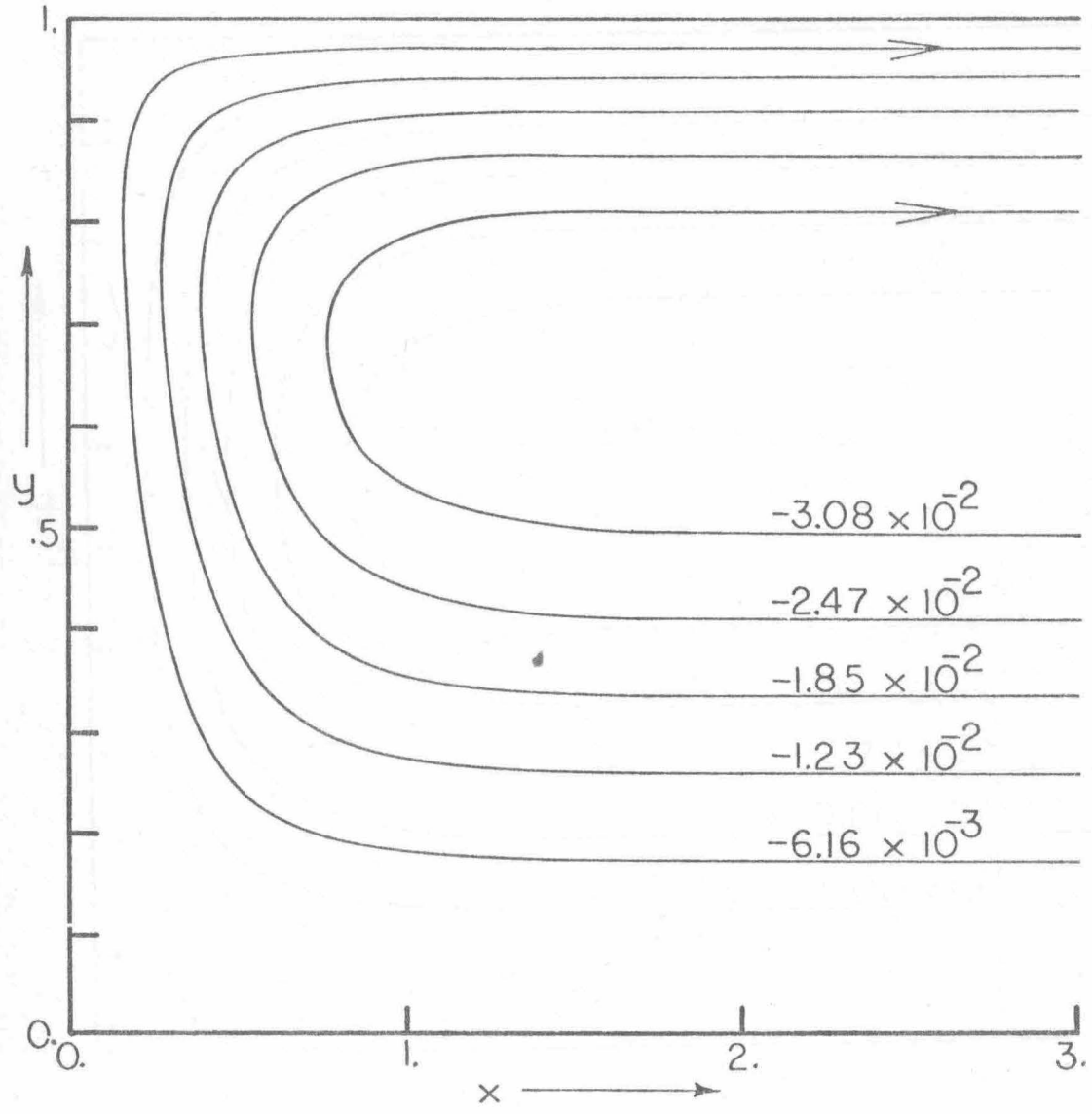

FIGURE 2b: STREAMLINES IN COLD END; IMPOSED SHEAR STRESS.

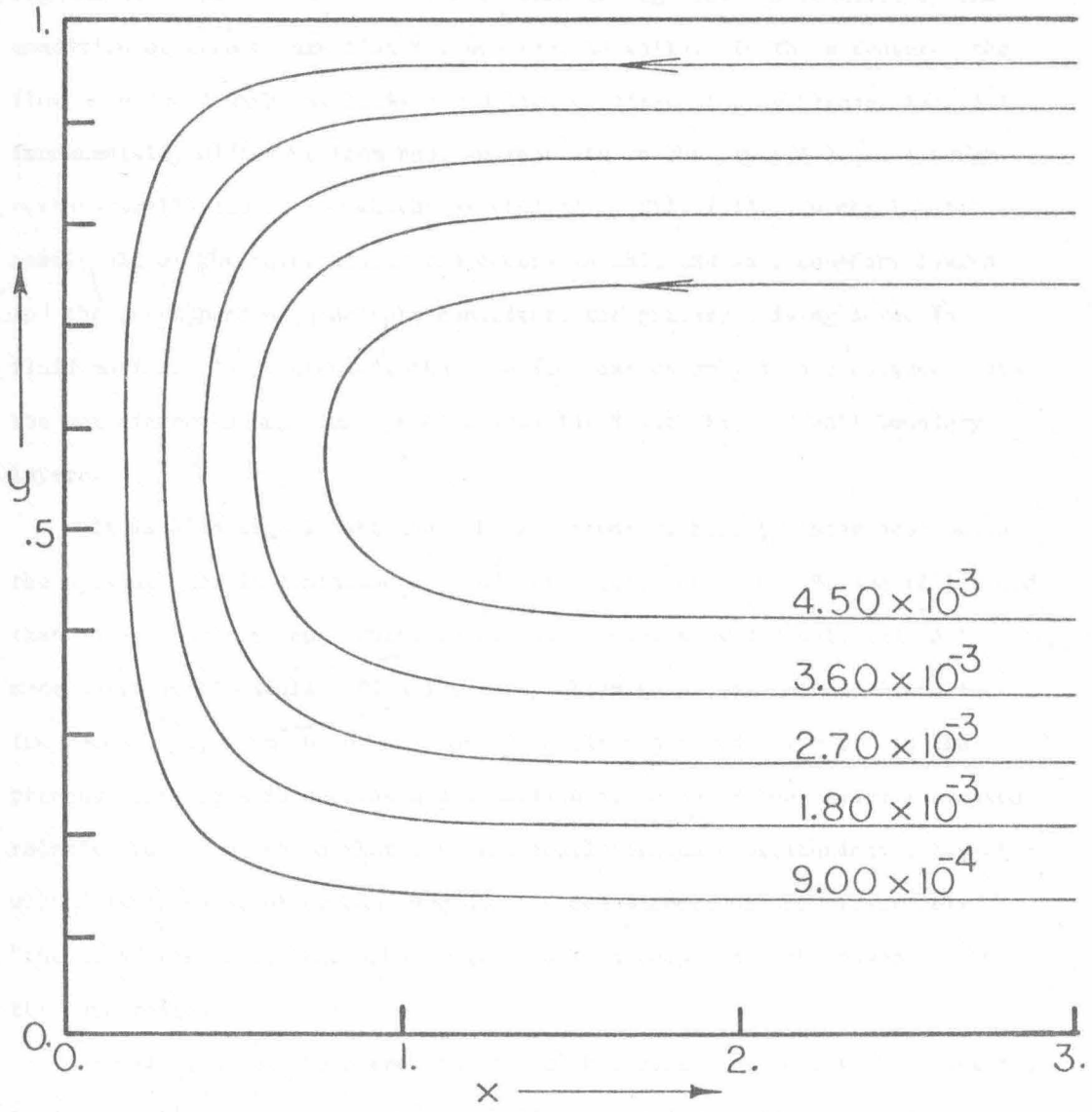

FIGURE 2c: STREAMLINES IN COLD END; ZERO SHEAR STRESS

A, the temperature is linear in $\hat{x}$ and independent of y. Thus, to a first approximation, the end regions are isothermal and the driving force for convection is associated with the horizontal gradient of θ in the core. The end regions serve mainly to turn the core flow through 180° as required by the condition of zero volume flux through the end walls. In these features the flow associated with the limit $A \to 0$ with Gr fixed (though perhaps large) is fundamentally different from that appropriate to the limit A fixed (though perhaps small) and $Gr \to \infty$ which was studied by Gill [11]. In the latter case, nearly all of the temperature drop occurs in thin end wall boundary layers and the corresponding gradients constitute the primary driving force for fluid motion. In particular, the core flow exists *only* as a consequence of the entrainment-detrainment process associated with the end wall boundary layers.

It is also significant that the longitudinal heat transfer process in the present case is dominated by conduction (cf. equations (9) and (12)), and that this occurs for any arbitrary Grashof number provided only that A is made sufficiently small. Clearly, the problem considered here differs in a fundamental way from the usual conduction limit A fixed, $Gr \to 0$. In the present case, as A is decreased the horizontal scale of the cavity increases relative to its depth so that even the small viscous contributions associated with a large value of Gr can eventually become important and effectively "throttle" the flow, thus enhancing conduction compared with convection in the core region.

Finally, it may be noted that the higher order *convective* contributions to (9) and (12) are a result of the Taylor diffusion mechanism which has been recently reviewed in the context of cavity and estuary flows, by Fischer [12].†

†The convective terms in these equations can, in fact, be reproduced using the general equations (10) and (12) of Fischer's paper.

In the following sections we consider the changes in flow structure which occur as the no-slip, insulated upper surface conditions are replaced by the conditions (5).

4. ASYMPTOTIC VELOCITY AND TEMPERATURE FIELDS WITH AN IMPOSED SURFACE SHEAR STRESS AND ZERO HEAT FLUX

The logical extension of the no-slip upper surface, which was discussed in I and summarized in the previous section, is the case of an imposed, uniform shear stress, τ_o. The problem differs from the previous one only in the condition

$$\frac{\partial^2\psi}{\partial y^2} = \frac{\ell\tau_o}{h^2(T_h - T_c)\beta g} = B \text{ on } y = 1 \tag{13}$$

which replaces the no-slip condition, $\partial\psi/\partial y = 0$. In natural estuaries, τ_o could be interpreted as the time- and space-averaged value of the surface wind shear stress. In that case, a typical range for τ_o would be $0 - 10\text{cm}^2/\text{sec}^2$ (cf. Lumley and Panofsky [13]), which leads to the estimate $0 \lesssim |B| \lesssim 2$ in Shark Bay. The dimensionless parameter B provides a measure of the relative magnitudes of the surface shear force and the characteristic buoyancy force in the cavity. When $B \ll 1$, the buoyancy forces are dominant and the problem is equivalent to the case $\tau_o = 0$. On the other hand, for $B \gg 1$, the shear forces are dominant and the problem is a forced convection flow to first approximation. It is the intermediate case, $B \sim O(1)$, which we will pursue here. The analysis follows that in I fairly closely. Thus, in the interest of brevity, we omit the details of the end region solutions and of the matching. The relevant techniques are demonstrated in the Appendix for the somewhat simpler but representative case of $B = 0$. Here, we shall concentrate

on the solutions themselves rather than on the methods used to obtain them.

In the core region,

$$\psi = K_1\left(\frac{y^4}{24} - \frac{5y^3}{48} + \frac{y^2}{16}\right) + \frac{B}{4}(y^3 - y^2) \tag{14}$$

$$\theta = K_1\hat{x} + PrGr\ A^2\left\{K_1^2\left(\frac{y^5}{120} - \frac{5y^4}{192} + \frac{y^3}{48}\right) + K_1 B\left(\frac{y^4}{16} - \frac{y^3}{12}\right)\right\} + K_2 \tag{15}$$

where K_1 and K_2 are polynomials in A. The coefficients of K_1 and K_2 depend on Gr, Pr, A and B, and are determined by matching (14) and (15) with the solutions in the two end regions. The principal feature of interest in the latter (end region solutions) is the fact that the surface shear stress yields only a simple additive contribution at first order in A.

$$\psi = \psi_o + B\hat{\psi}_o + O(A)$$

The first term, ψ_o, is simply the $\tau_o = 0$ solution outlined in the Appendix. The second term, $\hat{\psi}_o$, which is directly attributable to the imposed surface shear stress, was obtained numerically. The governing equation and boundary conditions are

$$\nabla^4\hat{\psi}_o = 0 \tag{16}$$

$$\left.\begin{aligned} &\hat{\psi}_o = 0 \qquad \text{on } x = 0 \quad \text{on } y = 0,1 \\ &\frac{\partial\hat{\psi}_o}{\partial y} = 0 \qquad \text{on } y = 0; \qquad \frac{\partial\hat{\psi}_o}{\partial x} = 0 \qquad \text{on } x = 0,\infty \\ &\frac{\partial^2\hat{\psi}_o}{\partial y^2} = 1 \qquad \text{on } y = 1\ . \end{aligned}\right\} \tag{17}$$

The numerical scheme closely resembled that described in the Appendix for ψ_o. Typical streamlines for $\hat{\psi}_o$ are presented in Figure 2b.

To determine K_1 and Nu to $O(A^3)$, in addition to the five end region temperature corrections obtained in the Appendix for $\tau_o = 0$, three additional corrections had to be calculated; one at $O(A^2)$ and two at $O(A^3)$. The resulting expression for K_1, correct to $O(A^3)$, is

$$K_1 = 1 - Pr^2Gr^2A^3(19.16 \times 10^{-6} - 2.536 \times 10^{-4}B + 8.550 \times 10^{-4}B^2) + O(A^4) \quad (18)$$

Similariy, the Nusselt number (12) is modified to

$$Nu_{\tau_o} = A + Pr^2Gr^2A^3(13.10 \times 10^{-6} - 1.736 \times 10^{-4}B + 5.952 \times 10^{-4}B^2) + O(A^4) \quad (19)$$

Our primary interest in the results of the preceding analysis is with the qualitative variations in flow structure which are induced by changes in boundary conditions at the upper surface. Most relevant to the far-field aspects of estuary flows are the structure of the core flow and the magnitude of the first correction ($O(A^3)$) to the Nusselt number, since the latter is a measure of the rate of longitudinal convective transport in the cavity. In this regard, the most important conclusion from the solutions (14) - (19) is the absence of any fundamental change in the flow structure for nonzero B. The parallel flow in the core region is preserved for any fixed value of B in the limit as $A \to 0$. In addition, the temperature field, which is dominated at first order by the basic conduction mechanism, remains linear in the horizontal coordinate in all cases with the y-dependence of the temperature field (and therefore the vertical density stratification) entering only as a higher order, $O(A^2)$, term. Finally, the fundamental Taylor diffusion mechanism which dominates the convective heat transfer process in the core is again reflected in the basic forms of the temperature gradient, K_1, and the Nusselt number. In spite of these basic similarities, however,

the detailed temperature and velocity distributions vary substantially with changes in B, and these changes are accompanied by important variations in the capacity for longitudinal convective transport of heat.

The most obvious variations in the core flow are those associated with the velocity profile. In Figure 3 we compare the normalized velocity profiles for the no-slip boundary condition, $(y^3/6 - y^2/4 + y/12)$ and the free shear condition, $(y^3/6 - 5y^2/16 + y/8)$. Also plotted is the linearly additive shear induced velocity component $(3y^2/4 - y/2)$. Most significant are the variations in magnitude. Clearly, the free shear condition allows uniformly larger values of the horizontal velocity than does the no-slip condition. The normalized shear-induced velocity component is larger by an order of magnitude than even the corresponding free-shear component. Thus even for relatively small values of B, an imposed shear stress may have a significant influence on the circulation rate within the cavity. A comparison of equations (11) and (12) with equations (18) and (19) (with $B = 0$) reveals that the increased magnitude of the core velocity in the free surface problem, as compared to the no-slip problem, results in a smaller core temperature gradient (K_1), and an enhanced capacity for longitudinal transport of heat (Nu). In addition, the flow associated with a finite shear stress at the surface produces an additional correction to both K_1 and Nu whose sign depends on the magnitude and sign of B. It is especially significant that the convective contribution to Nu for the free surface case is approximately *five* times larger than the corresponding contribution for the no-slip problem, while the coefficients at $O(B)$ and $O(B^2)$ are both larger than the $O(1)$ coefficient by approximately an order of magnitude! Hence, even for small values of B, the convective transport of heat by Taylor

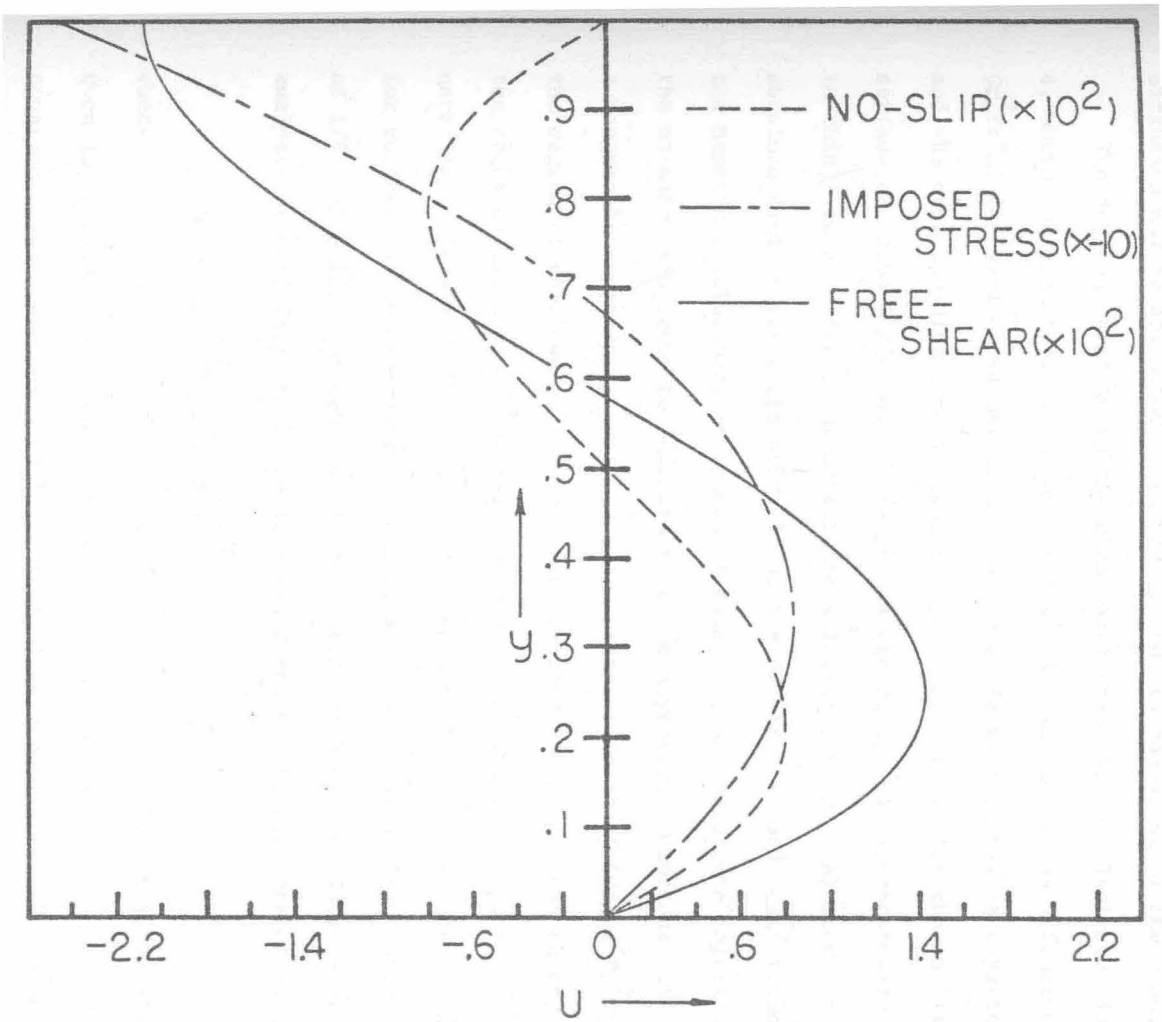

FIGURE 3: VELOCITY PROFILES.

diffusion may be *dominated* by the shear induced component of the flow.

The dependence of Nu on the shear parameter, B, is illustrated in Figure 4, where the asymptotic solution for (Nu - A) is plotted as a function of $Gr^2Pr^2A^3$ for various values of B. For comparison, the small A asymptote and the corresponding experimental data of Imberger [4] for the no-slip upper surface are also included. Three points are of special interest with regard to this figure. First, the asymptotic solution for (Nu - A) shows an absolute minimum for fixed $Gr^2Pr^2A^3$, at B = 0.1458. Second, comparison of the numerical solutions, experimental data and the asymptotic solution for the no-slip case seems to indicate that the asymptotic solutions will provide a reasonable approximation of the exact behavior for $A^3 < 10^5/Gr^2Pr^2$. Thus, the degree of shallowness required for validity of the present theory (i.e. the required value of A) decreases with decreasing Gr. Third, in the alternate limit, $Gr \to \infty$ with A held fixed (though small) the experimental data for various values of A approach one of a set of straight lines with slope of 1/8. This large Gr behavior is consistent with the boundary-layer analysis of Gill [11] which predicts (in terms of the ordinate of Figure 4)

$$Nu = (cA^{-3/8})(Pr^2Gr^2A^3)^{1/8} \tag{20}$$

where c is a constant, independent of Gr, Pr and A. The numerical data of Quon [5] provide substantial evidence that the Nusselt number (and thus the constant, c) in this boundary layer limit is the same for either a no-slip or free shear upper surface, in distinct contrast to the behavior in the present shallow cavity limit. Presumably, this difference reflects the fundamentally different physical processes governing the two limiting cases.

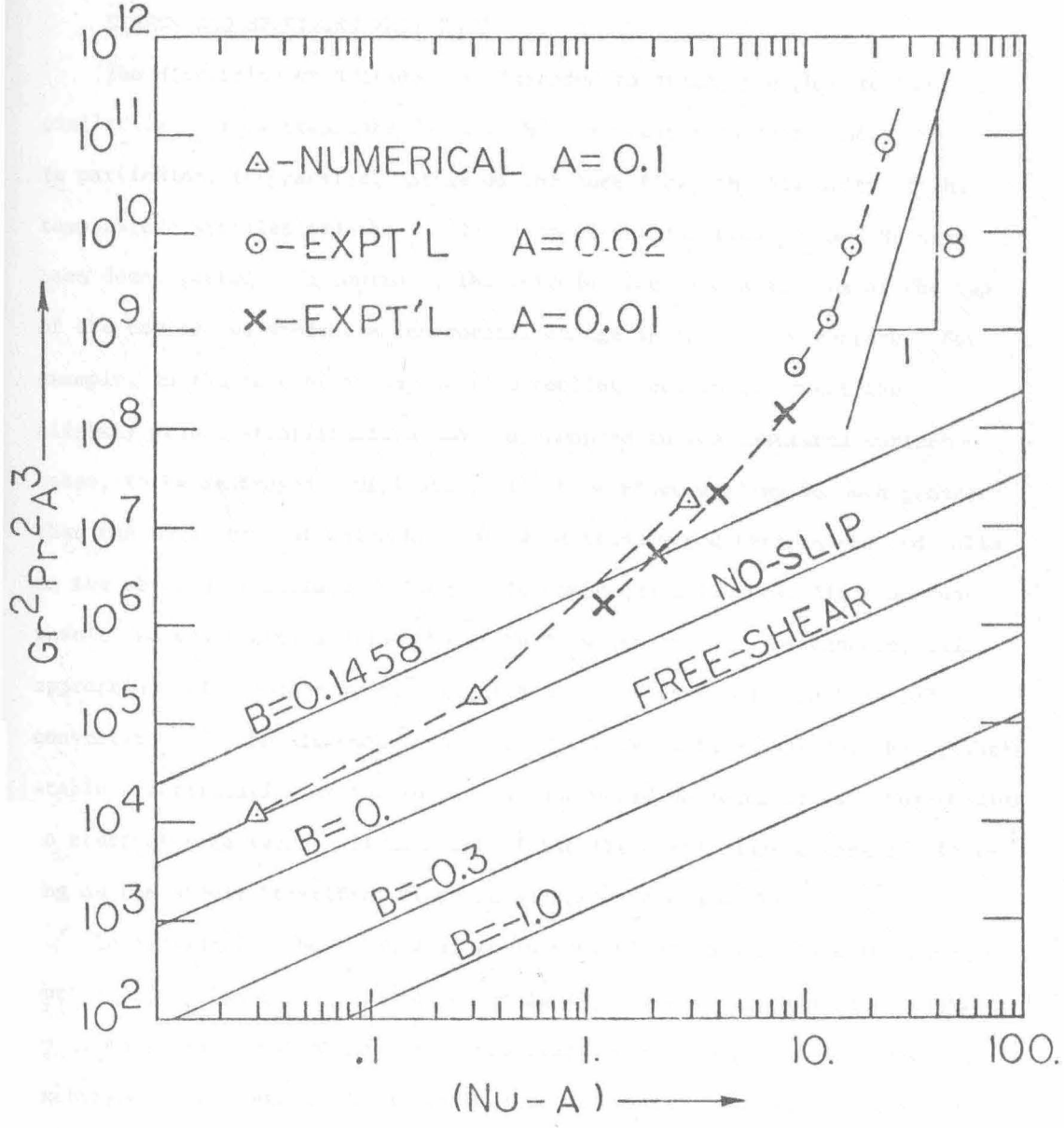

FIGURE 4: HEAT TRANSFER CHARACTERISTICS,(Nu-A) vs. $Gr^2Pr^2A^3$.

5. ASYMPTOTIC VELOCITY AND TEMPERATURE FIELDS WITH ZERO SURFACE SHEAR STRESS AND SPECIFIED HEAT FLUX

The discussion of section 4 is intended to strongly emphasize the similarity in flow structure for the three kinematic surface conditions. In particular, the parallel nature of the core flow, the linearity of the temperature profiles and the similar form of the functions K_1 and Nu have been demonstrated. In contrast, the introduction of a heat flux at the top of the cavity can produce a fundamental change in the flow structure. For example, in the case of *strong* surface cooling, one would expect the slightly stable stratification that is produced in the insulated surface cases, to be destroyed. Ultimately, if the surface cooling is much greater than the total rate at which heat would be transferred through the end walls in the absence of surface cooling, a strongly unstable stratification must result, necessitating a major change in flow structure. For example, under appropriate circumstances, such cooling may lead to a modified "Benard" convection. In the alternate instance of strong surface *heating*, the slightly stable stratification of the insulated case would be intensified, thus tending to restrict free (vertical) movement of the fluid and cause a form of blocking as the stably stratified fluid encounters the end walls.

In considering these changes, it is convenient to associate the nonzero surface heat flux with a new length scale ℓ', which is the distance required to transfer an amount of heat per unit time equal in magnitude to that exchanged at the end walls in the absence of surface heating. In general, it may be anticipated that, as an upper limit, the parallel flow structure discussed previously cannot be preserved over distances greater than ℓ'. A comparison of ℓ' with the physical length scale ℓ of the cavity thus

yields three limiting regimes, $\ell' \ll \ell$, $\ell' \sim \ell$ and $\ell' \gg \ell$ corresponding to the cases of large, moderate and small surface heat transfer. The case $\ell' \gg \ell$ is of only modest interest since it reduces, at first order, to the case of an insulated surface which we have previously considered. On the other hand, the case $\ell' \ll \ell$ leads to velocity and temperature distributions quite unlike those observed in the usual estuary flows. Hence, in the present discussion, we limit our considerations to the case $\ell' \sim \ell$ where the contributions of surface and end wall heat transfer are comparable.

a. Uniform Surface Heat Flux

In this section we consider the special case of constant, uniform surface heat transfer and zero surface shear stress. Thus, in (5), we put $\tau_o = 0$ and $f(T) = q$ (constant), where q is the magnitude of the outwardly directed heat flux. In order that $\ell \sim \ell'$, as assumed, we require that the total heat flux per unit time through the upper surface of the cavity be of the same order of magnitude as the rate of heat exchange which would occur at the end walls in the absence of surface heating. Since the dimensionless heat flux through the end walls in the latter case is $O(A)$ (see equation (12)), it thus follows that the dimensionless heat flux at the upper surface must be restricted to be of $O(A^2)$, i.e.

$$\left.\frac{\partial\theta}{\partial y}\right|_{y=1} = - A^2 Q \tag{21}$$

where

$$Q \equiv \frac{qh}{kA^2(T_n - T_c)}$$

is an arbitrary constant which is independent of A.

With the heat flux through the surface constrained, the scaling arguments that were outlined in section 3 are still relevant and the core

temperature and velocity fields are

$$\psi = \left\{ Q\hat{x} + c_1 + A^2 PrGrQ \left[\frac{Q(1-2\hat{x})}{1920} - \frac{1}{360} + PrGr \left\{ \left(\frac{Q^2}{24} - \frac{Q}{6} + \frac{1}{2} \right) 1.309 \times 10^{-5} \right.\right.\right.$$

$$\left.\left.\left. - \left(\frac{Q^2\hat{x}^3}{3} + c_1 Q\hat{x}^2 + c_1^2\hat{x} \right) 3.927 \times 10^{-5} \right\} \right] \right\} F'(y) + A^2 GrQ(Q\hat{x} + c_1)$$

$$\left[\frac{y^9}{72576} - \frac{5y^8}{64512} + \frac{29y^7}{161280} - \frac{y^6}{4608} + \frac{y^5}{7680} - 5.977 \times 10^{-5} y^3 \right.$$

$$+ 3.049 \times 10^{-5} y^2 + Pr \left(\frac{y^9}{181440} - \frac{y^8}{32256} + \frac{y^7}{20160} - 1.740 \times 10^{-4} y^3 \right.$$

$$\left.\left. + 1.498 \times 10^{-4} y^2 \right) \right] + O(A^3) \qquad (22a)$$

$$\theta = K_1\hat{x} + GrPrA^2K_1^2 F(y) + K_2 + \frac{Q\hat{x}^2}{2} - A^2Q\frac{y^2}{2} + PrGrA^2\left(Q^2\hat{x}^2 + 2Qc_1\hat{x}\right)F(y)$$

$$- \frac{PrGrQ^2A^2\hat{x}^2}{1920} - Pr^2Gr^2A^2Q \left(\frac{Q^2\hat{x}^4}{12} + \frac{Q\hat{x}^3c_1}{3} + \frac{c_1^2\hat{x}^2}{2} \right) 3.927 \times 10^{-5}$$

$$+ O(A^4) \qquad (22b)$$

As before, the coefficients of K_1 and K_2 were determined by matching with the relevant solutions in the end regions in a manner which proceeds as outlined in the Appendix. One important result is that the first order stream function in the end region is identical to the free-surface solution, ψ_o. However, in order to obtain K_1 and Nu correct to $O(A^3)$, it was necessary to obtain two *new* end region temperature solutions in addition to those outlined in the Appendix; one at $O(A^2)$ which can be expressed analytically, and one at $O(A^3)$ which must be determined numerically. The result for K_1[†] is

[†] Note, $c_1 = 1 - Q/2$.

$$K_1 = 1 - \frac{Q}{2} + PrGrA^2\left(\frac{Q^2}{1920} - \frac{2Q}{720} + PrGr\left(\frac{Q^3}{24} - \frac{Q^2}{6} + \frac{Q}{2} \right) 3.927 \times 10^{-5} \right)$$

$$+ PrGrA^3\left(Q\left(1 - \frac{Q}{2}\right) 2.00 \times 10^{-3} - PrGr\left(1 - \frac{Q}{2}\right)^3 1.916 \times 10^{-5} \right) + O(A^4) \quad (23)$$

As expected, equation (23) reduces to the insulated surface form, (equation (18) with B = 0), in the limit as $Q \to 0$. However, for nonzero Q, K_1 is changed substantially even at O(1). In addition, there is a correction to K_1 at $O(A^2)$, where previously there was no correction, as well as additional changes at $O(A^3)$. Unfortunately, the complex dependence of K_1 on Q prevents a more detailed comparison with previous results.

In all of the cases considered previously, the Nusselt number, as defined in section 3 has provided a direct measure of the flux of heat between the end walls of the cavity. In contrast, however, the introduction of a flux of heat through the top of the cavity leads to a horizontal flux of heat that is a function of horizontal position. Nevertheless, either the hot or cold end Nusselt number does provide a measure of the overall dispersive capacity of the cavity for heat (the choice depends on whether the "source" is located at the hot or cold end of the cavity). The result in the cold end is

$$Nu_{cold} = \left(1 - \frac{Q}{2}\right)A + A^3 PrGr\left\{ - Q^2 8.68 \times 10^{-4} + Q\left(1 - \frac{Q}{2}\right) 1.75 \times 10^{-2} \right.$$

$$\left. + PrGr\left(\frac{Q^3}{4} - \frac{5Q^2}{4} + 3Q - 1 \right) 1.31 \times 10^{-5} \right\} + O(A^4) \quad (24)$$

and

$$Nu_{hot} = Nu_{cold} + QA \ .$$

Upon comparing Nu_{cold} and Nu_{hot} with the Nusselt number for an insulated surface (equation (18) with B = 0), it may be observed that the heat enters through the hot end at a rate (Q/2)A *slower* than it does for the insulated boundary case and leaves through the cold end at a rate (Q/2)A *faster* than previously. Hence the heat added through the upper surface is "discharged" equally by the two ends of the cavity.

With the undetermined constants specified, it is possible to examine in detail the core streamfunction and temperature distributions. Notably the parallel flow structure that was so evident in the previous cases is no longer present. Even at first order in A, the streamlines are not parallel in the core

$$\psi^* = \left(Q\hat{x} + 1 - \frac{Q}{2}\right)F'(y) + O(A^2) \ .$$

More surprising, however, for $|Q| > 2$, the asymptotic theory predicts that the first order stream function vanishes at

$$\hat{x}_o = \frac{1}{2} - \frac{1}{Q}$$

When $Q > 2$, ψ^* is negative (clockwise circulation) for $\hat{x} < \hat{x}_o$ and positive (counterclockwise circulation) for $\hat{x} > \hat{x}_o$. On the other hand, when $Q < -2$, the opposite situation exists with counterclockwise circulation for $\hat{x} < \hat{x}_o$, and clockwise for $\hat{x} > \hat{x}_o$. This behavior of the first order velocity field, is intimately coupled with the first order temperature distribution

$$\theta^* = \left(1 - \frac{Q}{2}\right)\hat{x} + Q\,\frac{\hat{x}^2}{2} + O(A^2) \ .$$

A graphical comparison of the present temperature distribution and the previous insulated surface profile is shown in Figure 5 where the first order temperature profiles are plotted for selected values of the surface heat flux. The

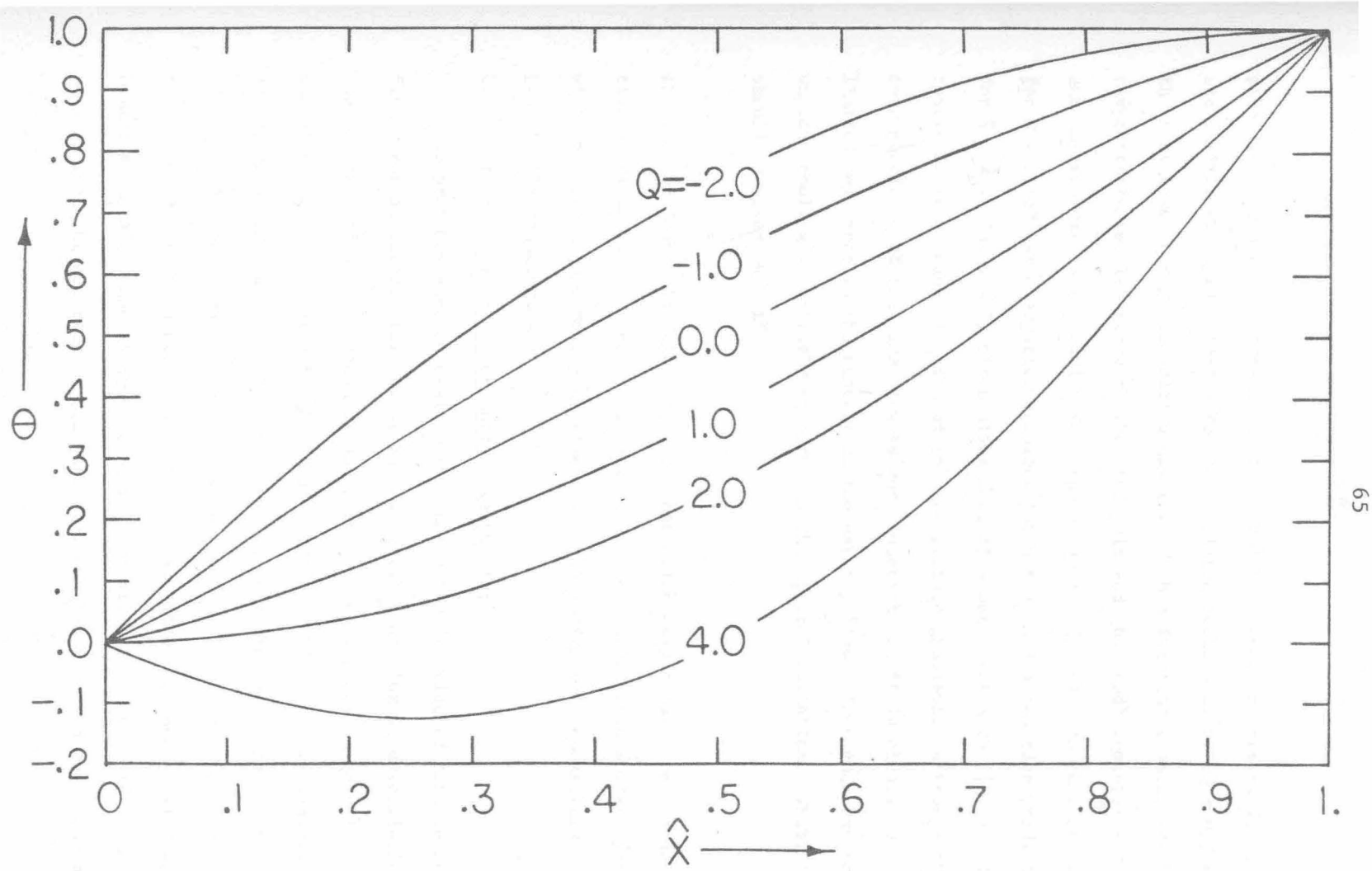

FIGURE 5: FIRST ORDER TEMPERATURE PROFILE FOR UNIFORM SURFACE HEAT FLUX.

positive values of Q represent surface cooling, hence the curves for $Q > 0$ are shifted downward relative to the insulated surface curve ($Q = 0$), while the curves for $Q < 0$ are shifted upward. With sufficient cooling (or heating), temperatures smaller (larger) than the cold end (hot end) temperatures are encountered within the cavity (cf. the curve for $Q = 4$). In particular, for $Q > 2$, θ^* has a negative gradient for $\hat{x} < \hat{x}_o$ and a positive gradient for $\hat{x} > \hat{x}_o$. The doubly circulating core flow encountered for $|Q| > 2$ is a result of this change in sign of the temperature gradient. Although this characteristic of the core flow is very interesting, it is clearly of limited relevance in the context of the estuary flows since such extreme surface cooling is unlikely to occur in the natural situation. Thus, it should be noted that if

$$Q \lesssim 1$$

then, as indicated in Figure 5, the first order temperature and stream function profiles in the core are very similar to the insulated surface profiles, with the streamlines nearly parallel, and the horizontal temperature gradient practically constant.

b. Heat Flux a Function of Surface Temperature

The previous section dealt with a uniformly distributed surface heat flux. For an estuary this distribution of the heat flux is unrealistic since the net rate of heat exchange at any point on the surface is actually the sum of the rates at which heat is transferred by radiation, by evaporation, and by conduction between the water and the overlying air. Hence, the rate of heat transfer at each point on the surface must be specified as a function of the surface temperature as well as ambient variables such as wind speed, humidity and air temperature. Edinger, Duttweiler and Geyer [14] demonstrated that the net rate of heat transfer can be expressed most conveniently

in terms of an effective thermal exchange coefficient K and an equilibrium temperature, T_e, both of which depend on observable meteorological variables and change continuously in response to varying meteorological conditions. The interested reader is referred to Edinger et al. [14] for details concerning the evaluation of K and T_e. The net heat transfer rate becomes

$$q_{net} = - K(T_s - T_e)$$

where T_s is the surface temperature. For our present purposes we take T_e equal to the cold end temperature so that the surface heat flux is a maximum at $\hat{x} = 1$ and is a minimum (zero) at $\hat{x} = 0$, and assume that the surface shear stress is zero. As in the previous example, we consider only the case in which the total surface heat transfer is constrained to be of the same magnitude (with respect to A) as that which would occur at the end walls with $K \equiv 0$. Hence, we consider the boundary condition

$$\frac{\partial \theta}{\partial y} = - HA^2\theta \quad \text{on } y = 1 \tag{25}$$

where

$$H \equiv \frac{Kh}{kA^2}$$

is an arbitrary constant which is independent of A.

To obtain an asymptotic solution for the core region, which is valid in the limit $A \to 0$ with Gr, Pr and H held fixed, we utilized the scaling arguments and formal expansion in A outlined previously. The core solution, after matching, is

$$\psi = \left[\frac{\sqrt{H}\cosh(\sqrt{H}\hat{x})}{\sinh(\sqrt{H})} + A^2C_3'(\hat{x})\right]F'(y) + A^2\left[\frac{\sinh(\sqrt{H}\hat{x})\cosh(\sqrt{H}\hat{x})}{\sinh^2(\sqrt{H})}\, H^{3/2}Gr\left\{\frac{y^9}{72576}\right.\right.$$

$$- \frac{5y^8}{64512} + \frac{29y^7}{161280} - \frac{y^6}{4608} + \frac{y^5}{7680} - 5.98 \times 10^{-5} y^3 + 3.05 \times 10^{-5} y^2$$

$$+ \Pr\left(\frac{y^9}{181440} - \frac{y^8}{32256} + \frac{y^7}{20160} - 1.74 \times 10^{-5} y^3 + 1.50 \times 10^{-4} y^2 \right) \Bigg\}$$

$$- H^{3/2} \frac{\cosh(\sqrt{H}\hat{x})}{\sinh(\sqrt{H})} \left\{ \frac{y^6}{240} - \frac{y^5}{96} + \frac{y^4}{96} - \frac{y^3}{120} + \frac{y^2}{240} \right\} \Bigg] + O(A^3) \qquad (26a)$$

$$\theta = \frac{\sinh \sqrt{H}\hat{x})}{\sinh(\sqrt{H})} + A^2 \left[- \frac{H\sinh(\sqrt{H}\hat{x})}{\sinh(\sqrt{H})} \frac{y^2}{2} + \frac{PrGrH\cosh^2(\sqrt{H}\hat{x})}{\sinh^2(\sqrt{H})} F(y) \right.$$

$$\left. + c_3(\hat{x}) \right] + O(A^3) \qquad (26b)$$

where

$$c_3(\hat{x}) = \frac{PrGrH\cosh(2\sqrt{H}\hat{x})}{\sinh^2(\sqrt{H})5760} - \frac{3.93 \times 10^{-5} Pr^2 Gr^2}{\sinh^3(\sqrt{H})} \left\{ \frac{H\sinh(3\sqrt{H}\hat{x})}{32} \right.$$

$$\left. + \frac{H^{3/2}}{8} \hat{x}\cosh(\sqrt{H}\hat{x}) \right\} - \frac{PrGrH}{640\sinh^2(\sqrt{H})} - \frac{H^{3/2}\hat{x}\cosh(\sqrt{H}\hat{x})}{6\sinh(\sqrt{H})}$$

$$+ \frac{\sinh(\sqrt{H}\hat{x})}{\sinh(\sqrt{H})} \left\{ \frac{H}{6} + 3.93 \times 10^{-5} \frac{Pr^2 Gr^2}{\sinh^3(\sqrt{H})} \left(\frac{H\sinh(3\sqrt{H})}{32} + \frac{H^{3/2}\cosh(\sqrt{H})}{8} \right) \right.$$

$$\left. - \frac{PrGrH}{576} + \frac{H^{3/2}\cosh(\sqrt{H})}{6\sinh(\sqrt{H})} \right\}$$

As a result of the matching, it was also shown that the streamfunction for the cold end region is

$$\psi(x,y) = \frac{\sqrt{H}}{\sinh\sqrt{H}} \psi_o(x,y) + O(A^2) \ , \qquad (27)$$

while the hot end streamfunction is

$$\psi(A^{-1} - x,y) = \sqrt{H}\coth(\sqrt{H})\psi_o(x,y) + O(A^2) \tag{28}$$

where ψ_o is the same solution that was calculated for the zero shear case (Figure 2c).

The behavior of the core solution in the limit as $H \to 0$ is, of course, identical to the insulated surface case. An excellent indication of the influence of finite values of H is provided by the first order core solution. To facilitate discussion, we have plotted the first order temperature profile

$$\theta_o = \frac{\sinh(\sqrt{H}\hat{x})}{\sinh(\sqrt{H})}$$

in Figure 6 for selected values of H. In Figure 7 we show

$$\frac{\sqrt{H}\cosh(\sqrt{H}\hat{x})}{\sinh(\sqrt{H})}$$

(as an indication of the core streamfunction magnitude), for the same values of H. Because the surface heat flux is proportional to the difference between surface temperature and T_c, a larger portion of the temperature drop occurs near the hot end of the cavity as H increases, thus causing increased temperature gradients in the hot end and decreased gradients in the cold end. These changes in the temperature profile are also reflected by the distribution of streamfunction in Figure 7. The increased temperature gradient in the hot end increases the driving force for the core flow so that the streamfunction increases as H increases. The converse is true for the cold end. For the extreme case plotted, $H = 100$, ψ is essentially zero for $\hat{x} < .5$. This tendency for ψ to approach zero at some distance far from the hot end wall hints of a limiting form of the solution as $H \to \infty$, in which A

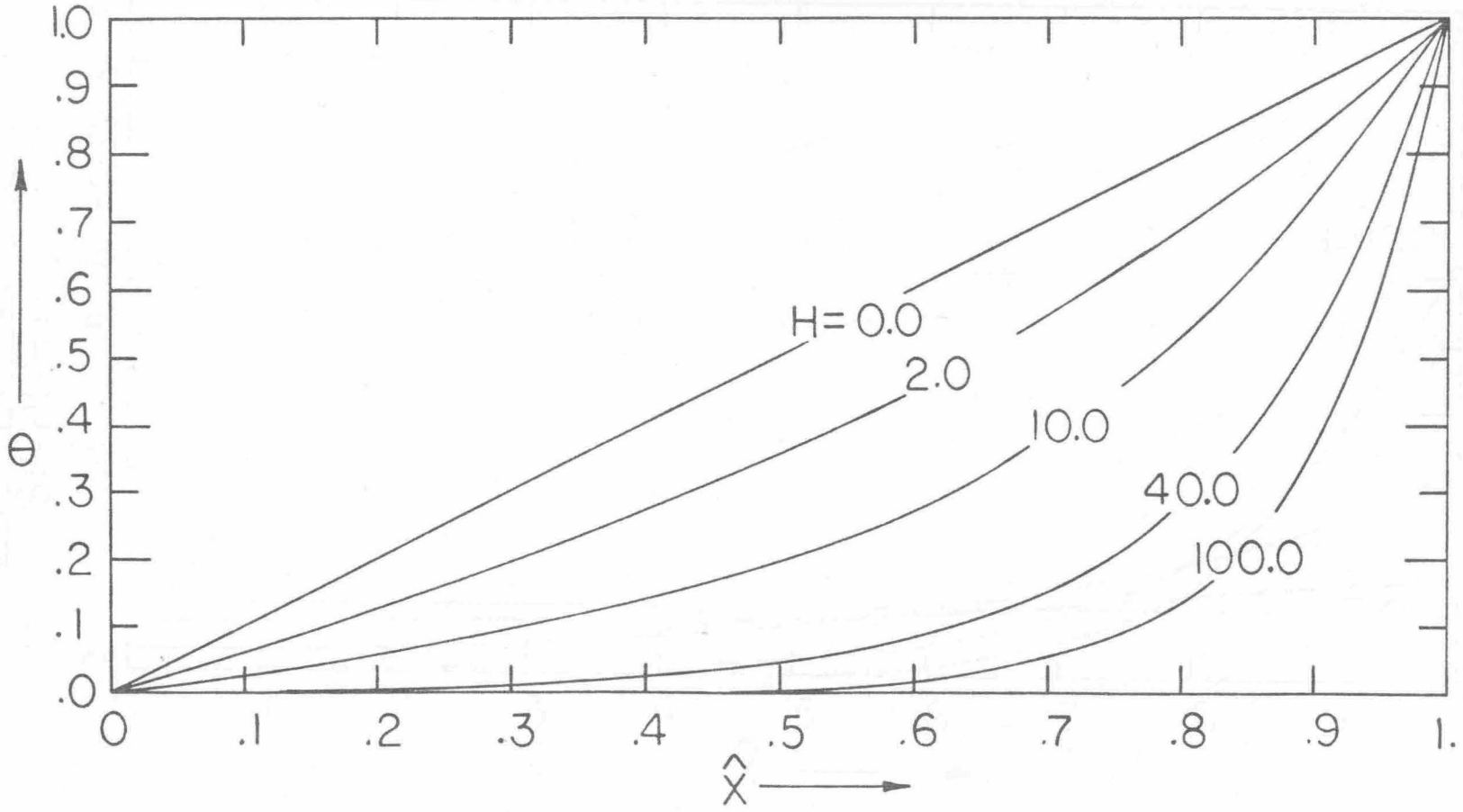

FIGURE 6: FIRST ORDER TEMPERATURE PROFILE FOR HEAT FLUX A FUNCTION OF SURFACE TEMPERATURE.

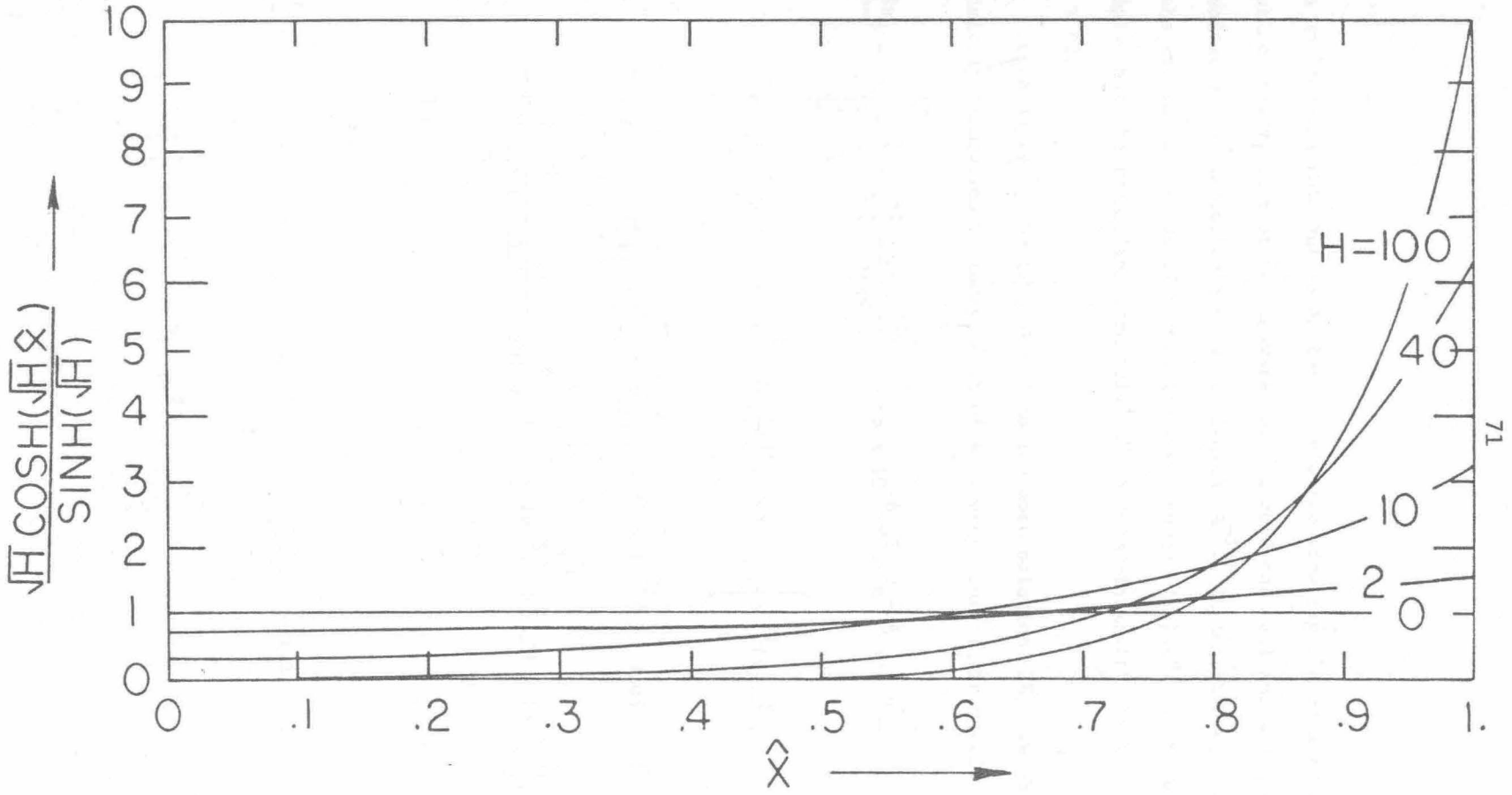

FIGURE 7: MAGNITUDE OF FIRST ORDER STREAM FUNCTION FOR SURFACE HEAT FLUX A FUNCTION OF SURFACE TEMPERATURE.

is no longer a relevant parameter. Since the flow field does not occupy the entire cavity, it must be unaware of the cold end wall and hence independent of the dimensionless cavity length, A^{-1}. In this sense, the flow behaves, for $H \to \infty$, as if the cavity were "semi-infinite". Figures 6 and 7 imply that the transition from "finite" to "semi-infinite" cavity occurs at $H \sim 40$.

Upon applying the limit $H \to \infty$ to the core solution (26), we obtain a limiting form which is independent of A as previously anticipated,

$$\lim_{H\to\infty}\psi = \sqrt{H}\Bigg[\Bigg\{e^{-\bar{\xi}} + \varepsilon^2\Bigg(\frac{2PrGre^{-2\bar{\xi}}}{5760} - 3.68 \times 10^{-6}Pr^2Gr^2e^{-3\bar{\xi}} + \bar{\xi}\,\frac{e^{-\bar{\xi}}}{6}$$

$$+ e^{-\bar{\xi}}\Big(1.23 \times 10^{-6}Pr^2Gr^2 - \frac{PrGr}{576}\Big)\Bigg)\Bigg\}F'(y) + \varepsilon^2\Bigg\{e^{-2\bar{\xi}}Gr\Bigg(\frac{y^9}{72576}$$

$$- \frac{5y^8}{64512} + \frac{29y^7}{161280} - \frac{y^6}{4608} + \frac{y^5}{7680} - 5.98 \times 10^{-4}y^3 + 3.05 \times 10^{-5}y^2$$

$$+ Pr\Bigg(\frac{y^9}{181440} - \frac{y^8}{32256} + \frac{y^7}{20160} - 1.74 \times 10^{-5}y^3 + 1.50 \times 10^{-4}y^2\Bigg)\Bigg)\Bigg\}$$

$$+ O(\varepsilon)^3\Bigg] \qquad (29a)$$

$$\lim_{H\to\infty}\theta = e^{-\bar{\xi}} + \varepsilon^2\Bigg[-e^{-\bar{\xi}}\,\frac{y^2}{2} + PrGre^{-2\bar{\xi}}F(y) + \frac{PrGre^{-2\bar{\xi}}}{5760} - 1.23 \times 10^{-6}Pr^2Gr^2e^{-3\bar{\xi}} + \frac{\bar{\xi}e^{-\bar{\xi}}}{6}$$

$$+ e^{-\bar{\xi}}\Big\{\frac{1}{6} + 1.23 \times 10^{-6}Pr^2Gr^2 - \frac{PrGr}{576}\Big\}\Bigg] + O(\varepsilon^3) \qquad (29b)$$

in which

$$\bar{\xi} = \varepsilon\xi \text{ and } \varepsilon \equiv \sqrt{\frac{Kh}{k}} \quad .$$

For convenience, we have used the independent variable ξ which measures the horizontal distance into the cavity from the hot end, scaled with respect to h.

In view of the expressions (27) - (29), it is apparent that the appropriate velocity and length scales in the limit $H \to \infty$ are

$$u = O\left(\sqrt{\frac{Kh}{k}}\,\frac{\beta g(T_h - T_c)h^3}{\nu}\right)$$

and (30)

$$\ell' = O\left(\frac{h}{\varepsilon}\right) = O\left(\sqrt{\frac{kh}{K}}\right) .$$

The latter is the length scale characterizing the rate of heat transfer through the cavity surface. This spontaneous appearance of a new length scale provides an excellent opportunity to enlarge on the previous discussion relating the horizontal length scale of the core flow to the rate of surface cooling. To this end, Figure 8 shows the fully matched first order streamfunction profiles for the semi-infinite cavity ($H \to \infty$) at two values of ε. It is clear from these figures that as the heat transfer rate (ε^2) increases, the horizontal extent of the core flow is decreased proportionately.

An examination of the semi-infinite cavity solution (equations 29) indicates that to ensure convergence, we must have $\varepsilon << 1$. This in turn suggests that a necessary condition for the validity of the analysis leading to the general solutions (26) is

$$A << 1$$

and

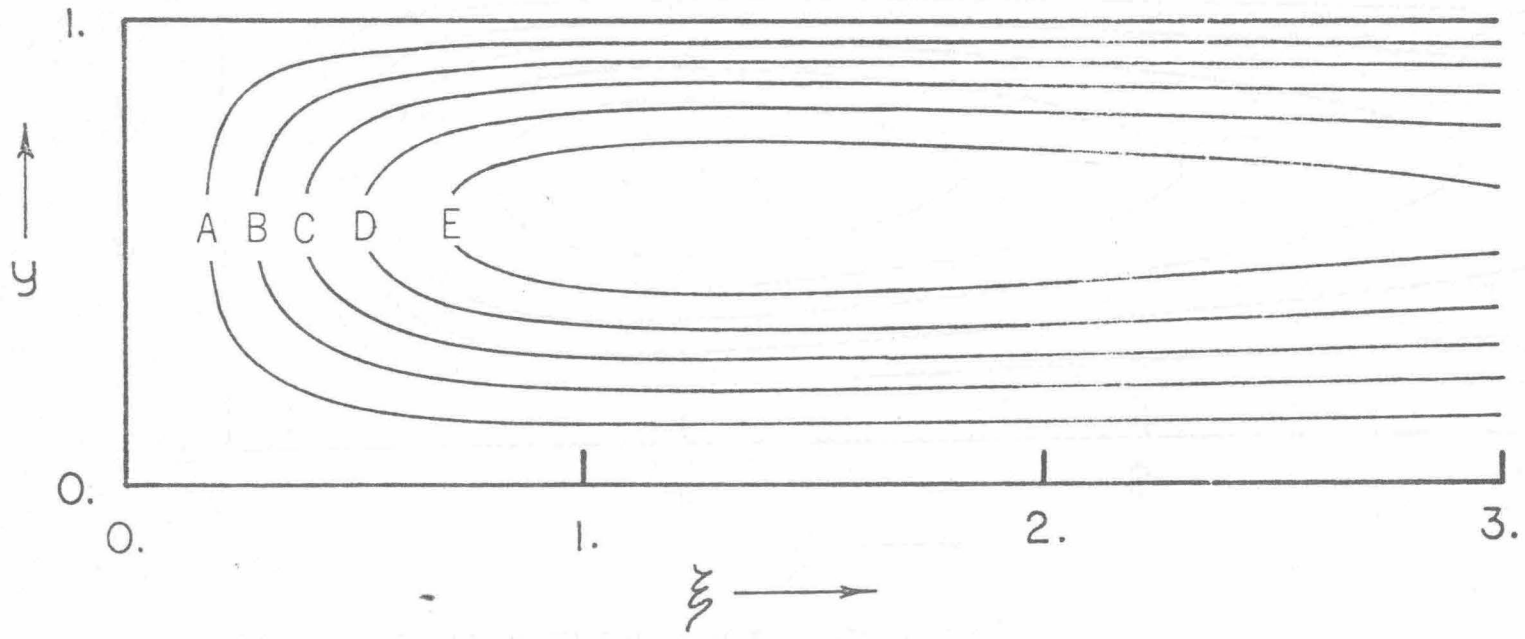

FIGURE 8a: STREAMLINES FOR SEMI-INFINITE CAVITY, ϵ = 0.1 ;
A=7.7×10^{-4}, B=1.5×10^{-3}, C=2.3×10^{-3}, D=3.1×10^{-3}, E=3.8×10^{-3}.

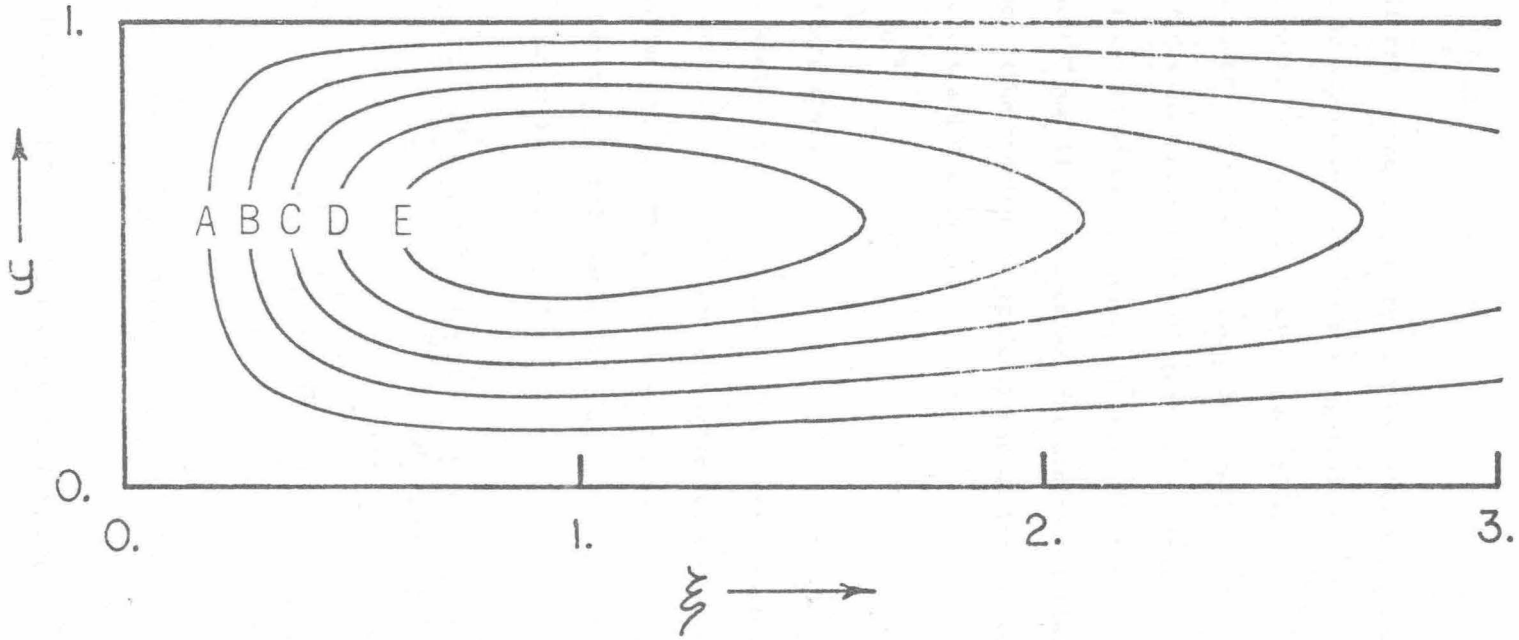

FIGURE 8b: STREAMLINES FOR SEMI-INFINITE CAVITY, ϵ =0.5;
A=4.4x10^{-4}, B=9.3x10^{-4}, C=1.4x10^{-3}, D=1.9x10^{-3}, E=2.4x10^{-3}.

$$HA^2 = \frac{Kh}{k} << 1 .$$

To determine if the second inequality will be satisfied under realistic conditions, it is useful to estimate the magnitude of $\frac{Kh}{k}$. Field measurements indicate that, for an ambient wind speed of from 1 to 5 m/sec, K varies between about 2.5×10^{-4} and 5.0×10^{-3} cal$(c°cm^2sec)^{-1}$. Furthermore, since estuary flows are invariably turbulent, we estimate the effective thermal diffusivity to be of the order u*h[†] (cf. Fischer [12]), where u* is the "slip velocity" and is about 1 cm/sec for horizontal fluid velocities of about 10 cm/sec. (The precise magnitude of the horizontal velocity will depend on Gr, Pr, A and H.) Hence,

$$\frac{Kh}{k} \sim 10^{-4}$$

for typical estuary flows.

The heat transfer characteristics for the present surface boundary condition are quite different from the insulated surface case. Once again, because heat is removed through the surface of the cavity, the horizontal heat flux is a function of horizontal position. The Nusselt number is therefore a maximum at the hot end

$$Nu_{hot} = A\sqrt{H}\coth(\sqrt{H}) + A^3\left[PrGrH^{3/2}\left\{\frac{\coth(\sqrt{H})}{960} + \frac{\sinh(2\sqrt{H})}{2880\sinh(\sqrt{H})}\right\} - \frac{H^{3/2}}{6}\coth(\sqrt{H})\right.$$

$$- 3.927 \times 10^{-5}\frac{Pr^2Gr^2}{\sinh^3(\sqrt{H})}\left\{\frac{H^2}{8}\sinh(\sqrt{H}) - \sqrt{H}\coth(\sqrt{H})\left\{\frac{H}{32}\sinh(3\sqrt{H})\right.\right.$$

$$\left.\left.\left. + \frac{H^{3/2}}{8}\cosh(\sqrt{H})\right\} + \frac{3H^{3/2}}{32}\cosh(3\sqrt{H}) + \frac{H^{3/2}}{8}\cosh(\sqrt{H})\right\} - \frac{H}{6}\left(1 - \coth^2(\sqrt{H})\right)$$

[†] Here we have assumed that the turbulent Prandtl number is ~ 1.

$$+ \mathrm{PrGrH}^{3/2}\left\{1.309 \times 10^{-5}\mathrm{PrGrcoth}^{3}(\sqrt{H}) - 1.74 \times 10^{-3}\coth(\sqrt{H})\right\}\Bigg]$$

$$+ O(A^4) \tag{31}$$

and is a minimum at the cold end

$$\mathrm{Nu}_{\mathrm{cold}} = \frac{A\sqrt{H}}{\sinh(\sqrt{H})} + A^3\left[-\frac{H^{3/2}}{\sinh(\sqrt{H})}\left(\frac{1}{6} + 8.59 \times 10^{-6}\,\frac{\mathrm{Pr}^2\mathrm{Gr}^2}{\sinh^2(\sqrt{H})} + \frac{\mathrm{PrGr}}{576}\right.\right.$$

$$\left. - \frac{\mathrm{Pr}^2\mathrm{Gr}^2(1.309\times10^{-5})}{\sinh^2(\sqrt{H})} - 1.227 \times 10^{-6}\,\frac{\mathrm{Pr}^2\mathrm{Gr}^2}{\sinh^3(\sqrt{H})}\sinh(3\sqrt{H})\right)$$

$$\left. + 4.91 \times 10^{-6}\,\frac{\mathrm{Pr}^2\mathrm{Gr}^2\mathrm{H}^2}{\sinh^4(\sqrt{H})}\cosh(\sqrt{H}) + H^2\,\frac{\coth(\sqrt{H})}{6\sinh(\sqrt{H})}\right] + O(A^4) \tag{32}$$

In the limit as $H \to 0$, these expressions for Nu reduce to that found for the insulated free-shear surface. Unfortunately, the complexity of expressions (31) and (32) precludes a detailed comparison with Nusselt numbers for the previous cases.

References

1. Logan, W. B. and D. E. Cebulski, Carbonate Sedimentation and Environments, Shark Bay, Western Australia, The American Ass. of Pet. Geol., Memoir No. 13 (1970).

2. Fischer, H. B., Mass Transport Mechanisms in Partially Stratified Estuaries, J. of Fluid Mech., 53, 671 (1972).

3. Harleman, D. R. F. and K. D. Stolzenbach, Fluid Mechanics of Heat Disposal From Power Generation, Ann. Rev. of Fluid Mech., 4, 7 (1972).

4. Imberger, J., Natural Convection in a Shallow Cavity with Differentially Heated End Walls. Part 3. Experimental Results, J. of Fluid Mech., 65, 247 (1974).

5. Quon, C., High Rayleigh Number Convection in an Enclosure--A Numerical Study, Phys. Fluids, 15, 12 (1972).

6. Wilkes, J. O. and S. W. Churchill, The Finite Difference Computation of Natural Convection in a Rectangular Enclosure, A.I.Ch.E. J., 12, 161 (1966).

7. Newell, M. E. and F. W. Schmidt, Heat Transfer by Laminar Natural Convection Within Rectangular Enclosures, J. of Heat Trans., 92, 159 (1970).

8. DeVahl Davis, G., Laminar Natural Convection in an Enclosed Rectangular Cavity, Int. J. Heat Mass Transfer, 11, 1675 (1968).

9. Cormack, D. E., L. G. Leal and J. Imberger, Natural Convection in a Shallow Cavity with Differentially Heated End Walls. Part 1. Asymptotic Theory, J. of Fluid Mech., 65, 209 (1974).

10. Cormack, D. E., L. G. Leal and J. H. Seinfeld, Natural Convection in a Shallow Cavity with Differentially Heated End Walls. Part 2. Numerical Solutions, J. of Fluid Mech., 65, 231 (1974).

11. Gill, A. E., The Boundary-layer Regime for Convection in a Rectangular Cavity, J. of Fluid Mech., 26, 515 (1966).

12. Fischer, H. B., Longitudinal Dispersion and Turbulent Mixing in Open Channel Flows, Ann. Rev. of Fluid Mech., 5, 59 (1973).

13. Lumley, J. L. and H. A. Panofsky, The Structure of Atmospheric Turbulence, 1964 Interscience Pub., New York.

14. Edinger, J. E., D. W. Duttweiler and J. C. Geyer, The Response of Water Temperature to Meteorological Conditions, W. Res. Research, 4, 1137 (1968).

Appendix A: Detailed Matching of End and Core Solutions for the Free Surface Problem

To demonstrate the matching procedure used in the paper, we consider the simplest case, that of an insulating, free surface ($\tau_o = 0$) at the top of the cavity. Subject to the assumption that the surface is flat, boundary conditions (5) become

$$\psi = \frac{\partial^2 \psi}{\partial y^2} = \frac{\partial \theta}{\partial y} = 0 \text{ on } y = 1 \tag{A-1}$$

The problem is otherwise the same as that outlined in Section 3, and the horizontal scaling arguments remain valid. Thus, the core solution consistent with the conditions (A-1) may easily be shown to be

$$\psi = K_1\left(\frac{y^4}{24} - \frac{5y^3}{48} + \frac{y^2}{16}\right) \tag{A-2}$$

$$\theta = K_1\hat{x} + K_1^2 \mathrm{GrPrA}^2\left(\frac{y^5}{120} - \frac{5y^4}{192} + \frac{y^3}{48}\right) + K_2 \tag{A-3}$$

Both K_1 and K_2 are polynomials in A, with coefficients which must be determined by matching (A-2) and (A-3) with solutions which are valid in the ends of the cavity. For the no-slip surface, the centro-symmetry property of the equations and boundary conditions allowed K_2 to be eliminated in favor of K_1, so that the matching had to be carried out explicitly only in the cold end of the cavity. In the present example, and, indeed, in all of the problems considered in the present work, this simplification is not possible so that it is necessary, in principle, to carry out the detailed matching explicitly in both ends of the cavity. As we shall see, however, certain symmetry relationships are still useful in simplifying the problem.

In the cold end, the original equations (1), (2) and (3) must be solved, subject to the boundary conditions (4) and (A-1) for $y = 0, 1$ and $x = 0$, so that they match with the core solution according to

$$\lim_{x \to \infty} \psi = (c_1 + Ac_2 + \ldots)\, F'(y) \tag{A-4}$$

$$\lim_{x\to\infty} \theta = (c_1 + Ac_2 + \ldots)\hat{x} + (c_1 + Ac_2 + \ldots)^2 GrPrA^2 F(y) + (c_1' + Ac_2' + \ldots) \tag{A-5}$$

Here

$$F(y) = \frac{y^5}{120} - \frac{5y^4}{192} + \frac{y^3}{48}$$

and the prime in $F'(y)$ denotes differentiation with respect to y.

In the hot end of the cavity, it is convenient to express the equations and matching conditions in terms of the transformed variables

$$\xi = (A^{-1} - x)$$

$$\eta = (1 - y)$$

$$\Phi = 1 - \theta$$

so that the form of the equations remains unchanged

$$GrA^2 \frac{\partial(\Omega,\Psi)}{\partial(\xi,\eta)} = A\nabla^2\Omega + \frac{\partial\Phi}{\partial\xi} \tag{A-6}$$

$$\nabla^2\Psi = -\Omega \tag{A-7}$$

$$PrGrA \frac{\partial(\Phi,\Psi)}{\partial(\xi,\eta)} = \nabla^2\Phi \tag{A-8}$$

but the boundary conditions become

$$\left.\begin{aligned} &\Psi = \frac{\partial\Psi}{\partial\xi} = \Phi = 0 \text{ on } \xi = 0 \\ &\Psi = \frac{\partial\Psi}{\partial\eta} = \frac{\partial\Phi}{\partial\eta} = 0 \text{ on } \eta = 1 \\ &\Psi = \frac{\partial^2\Psi}{\partial\eta^2} = \frac{\partial\Phi}{\partial\eta} = 0 \text{ on } \eta = 0 \end{aligned}\right\} \tag{A-9}$$

Here, Ψ and Ω denote the stream function and vorticity in the hot end. The transformed matching conditions are

$$\lim_{\xi\to\infty} \Psi = (c_1 + Ac_2 + \ldots)F'(1 - \eta)$$

$$\lim_{\xi\to\infty} (1 - \Phi) = (c_1 + Ac_2 + \ldots)(1 - \xi A) + (c_1 + Ac_2 + \ldots)^2 GrPrA^2 F(1 - \eta) + (c_1' + Ac_2' + \ldots).$$

A solution in each of the hot and cold ends can be obtained as a regular expansion in A, i.e.

$$\psi = \psi_o + A\psi_1 + \ldots; \qquad \theta = \theta_o + A\theta_1 + \ldots \qquad \text{(cold)}$$

$$\Psi = \Psi_o + A\Psi_1 + \ldots; \qquad \Theta = \Theta_o + A\Theta_1 + \ldots \qquad \text{(hot)}$$

We have listed the appropriate equations and matching conditions at each order in A in table 1.

To initiate the solution of these equations, we note that the temperature functions θ_o and Θ_o are both identically zero, so that to satisfy the matching constraints (C - 1) and (H - 1) it follows that

$$c_1' = 0$$

$$c_1 = 1$$

Because θ_o is zero, equation (C - 3) reduces to $\nabla^2\theta_1 = 0$ and can be solved independently from (C - 2) to yield

$$\theta_1 = x$$

with the corresponding result from the matching condition (C - 5)

$$c_2' = 0.$$

Similarly, in the hot end,

$$\Theta_1 = \xi$$

and the condition (H - 5) yields

$$c_2 = 0$$

In light of these results, equations (C - 2) and (H - 2) may now be solved to yield the 0(1) contributions to the flow field in the hot and cold end. Substituting the solutions for θ_1 and Θ_1 into these equations, we obtain for the cold end

$$\nabla^4\psi_o = 1 \qquad \text{(A-10)}$$

with matching condition

$$\lim_{x\to\infty} \psi_o \to F'(y),$$

and for the hot end

$$\nabla^4 \Psi_o = 1$$

with

$$\lim_{\xi\to\infty} \Psi_o \to F'(1 - \eta)$$

From these equations, it is clear that the hot end stream function, Ψ_o, can be expressed in terms of the cold end distribution by

$$\psi_o(\alpha,\gamma) = \Psi_o(\alpha,1 - \gamma).$$

It is therefore necessary to obtain only one of the hot or cold end solutions at this level of approximation. We consider the function ψ_o in the cold end.

We have shown in I that it is possible to obtain an analytical solution for ψ_o. However, the resulting solution is extremely cumbersome and becomes completely unwieldy for evaluating higher order solutions. On the other hand, numerical solution of equation (A-10) with appropriate boundary conditions is relatively straightforward and for the present purposes is sufficient. In order to obtain this solution, the equation (A-10) was approximated by a central difference representation on a geometrically expanding grid of 21 points in the x-direction and a uniform grid of 21 points in the y-direction and solved using an explicit Gauss-Seidel iterative scheme. Details of the calculation may be obtained from I. The resulting streamlines of ψ_o are presented in Figure (2c).

We turn now to consider the solution at $O(A^2)$ for θ. Taking the preceding results into account, the governing equation (C - 5) in the cold end becomes

$$\nabla^2\theta_2 = PrGr\,\frac{\partial\psi_o}{\partial y} \tag{A-11}$$

with the matching condition

$$\lim_{x\to\infty}\theta_2 = GrPrF(y) + c_3'.$$

The matching at this order in A can be accomplished most effectively by considering the integral of equation (A-11) over the depth of the cavity. Carrying out this integration, we obtain the ordinary differential equation for

$$H(x) \equiv \int_0^1 \theta_2\,dy$$

$$\frac{d^2H}{dx^2} = 0 \tag{A-12}$$

with the integrated boundary conditions

$$H = 0 \quad \text{on } x = 0 \tag{A-13a}$$

$$\lim_{x\to\infty} H = GrPr\int_0^1 F(y)dy + c_3' \tag{A-13b}$$

The only solution of equation (A-12) consistent with the conditions (A-13) is the trivial solution

$$H = 0$$

for all x. Hence, it follows that

$$c_3' = -GrPr\int_0^1 F(y)dy = -\frac{GrPr}{720}$$

A similar integral analysis of equation (H - 5) indicates that

$$c_3 = 0$$

In order to carry the asymptotic solution to higher orders in A, it is necessary to determine the detailed distribution of θ_2 in the end region. This was done using the same numerical procedure and grid spacing as described previously for ψ_o. It may also appear that an independent numerical solution must be obtained for Θ_2; however, this is not the case. Rather, by considering the relationship between ψ_o and Ψ_o and the relationship between the boundary conditions on θ_2 and Θ_2, it is possible to show that

$$\theta_2(\alpha,\gamma) = -\theta_2(\alpha,1-\gamma)$$

Finally, it would now be possible to obtain a numerical solution for ψ_1. However, our main interest in continuing the expansion to higher order in A is to obtain the first nontrivial corrections to K_1 and Nu. For this purpose, it is sufficient to note that ψ_1 must satisfy the condition

$$\lim_{x\to\infty} \psi_1 = 0$$

The first nonzero correction to K_1 comes from the coefficient c_4 (note $c_2 = c_3 = 0$). To obtain c_4, we must consider the problem (C - 7) and (C - 9) for θ_3. This equation, plus matching condition, is simplified by our preceding results to

$$\nabla^2\theta_3 = \mathrm{PrGr}\left(\frac{\partial\psi_1}{\partial y} + \frac{\partial(\theta_2,\psi_o)}{\partial(x,y)}\right) \tag{A-14}$$

with

$$\lim_{x\to\infty} \theta_3 = c_4'.$$

Utilizing the linearity of this problem, we can conveniently consider θ_3 and c_4' as consisting of two parts

$$\theta_3 = \bar{\theta}_3 + \bar{\bar{\theta}}_3$$

and

$$c_4' = \bar{c}_4' + \bar{\bar{c}}_4'$$

where

$$\nabla^2\bar{\theta}_3 = \mathrm{PrGr}\,\frac{\partial\psi_1}{\partial y} \tag{A-15}$$

with

$$\lim_{x\to\infty} \bar{\theta}_3 = \bar{c}_4'$$

and

$$\nabla^2\bar{\bar{\theta}}_3 = \mathrm{PrGr}\,\frac{\partial(\theta_2,\psi_o)}{\partial(x,y)} \tag{A-16}$$

with

$$\lim_{x\to\infty} \bar{\bar{\theta}}_3 = \bar{\bar{c}}_4'$$

A consideration of the integral of equation (A-15) across the depth of the cavity yields the result

$$\int_0^1 \bar{\theta}_3 dy \equiv 0$$

for all x, so that

$$\bar{c}_4' = 0$$

On the other hand, such an integral analysis of equation (A-16) yields no information concerning $\bar{\bar{c}}_4'$. Instead, $\bar{\bar{c}}_4'$ must be determined by numerically solving equation (A-16) subject to the boundary condition (see I)

$$\lim_{x\to\infty} \frac{\partial \bar{\bar{\theta}}_3}{\partial x} = 0$$

This procedure yields both the unique solution for $\bar{\bar{\theta}}_3$, and the numerical value

$$\bar{\bar{c}}_4' = 9.58 \times 10^{-6} Gr^2 Pr^2.$$

In the same manner that the relationship between θ_2 and Θ_2 was deduced previously, it is also possible to show that

$$\bar{\bar{\theta}}_3(\alpha,\gamma) = \bar{\bar{\Theta}}_3(\alpha,1-\gamma)$$

In particular, therefore, the matching condition for Θ_3 requires

$$c_4 = -2\bar{\bar{c}}_4'$$

This completes the solution to the desired level of approximation.

Table 1: End Region Equations and Matching Conditions for $\tau_o = 0$

	Cold End		Hot End	
O(1)	$\frac{\partial \theta_0}{\partial x} = 0$		$\frac{\partial \Phi_0}{\partial \xi} = 0$	
	$\nabla^2 \theta_0 = 0$ $\quad \lim_{x\to\infty} \theta_0 = C_1'$	(C-1)	$\nabla^2 \Phi_0 = 0$ $\quad \lim_{\xi\to\infty} \Phi_0 = 1 - C_1 - C_1'$	(H-1)
O(A)	$\nabla^4 \psi_0 = \frac{\partial \theta_1}{\partial x}$	(C-2)	$\nabla^4 \psi_0 = \frac{\partial \Phi_1}{\partial \xi}$	(H-2)
	$\nabla^2 \theta_1 = \mathrm{PrGr} \frac{\partial(\theta_0, \psi_0)}{\partial(x,y)}$	(C-3)	$\nabla^2 \Phi_1 = \mathrm{PrGr} \frac{\partial(\Phi_0, \Psi_0)}{\partial(\xi,\eta)}$	(H-3)
	$\lim_{x\to\infty} \psi_0 = C_1 F'(y)$	(C-4)	$\lim_{\xi\to\infty} \Psi_0 = C_1 F'(1-\eta)$	(H-4)
	$\lim_{x\to\infty} \theta_1 = C_1 x + C_2'$	(C-5)	$\lim_{\xi\to\infty} \Phi_1 = C_1 \xi - C_2 - C_2'$	(H-5)
$O(A^2)$	$\nabla^4 \psi_1 = \frac{\partial \theta_2}{\partial x} - \mathrm{Gr} \frac{\partial(\omega_0, \psi_0)}{\partial(x,y)}$	(C-6)	$O(A^2)$ $\nabla^4 \Psi_1 = \frac{\partial \Phi_2}{\partial \xi} - \mathrm{Gr} \frac{\partial(\Omega_0, \Psi_0)}{\partial(\xi,\eta)}$	(H-6)
	$\nabla^2 \theta_2 = \mathrm{PrGr} \left(\frac{\partial(\theta_1, \psi_0)}{\partial(x,y)} + \frac{\partial(\theta_0, \psi_1)}{\partial(x,y)} \right)$	(C-7)	$\nabla^2 \Phi_2 = \mathrm{PrGr} \left(\frac{\partial(\Phi_1, \Psi_0)}{\partial(\xi,\eta)} + \frac{\partial(\Phi_0, \Psi_1)}{\partial(\xi,\eta)} \right)$	(H-7)

Table 1: (continued)

$\lim_{x\to\infty}\psi_1 = C_2F'(y)$ (C-8)	$\lim_{\xi\to\infty}\Psi_1 = C_2F'(1-\eta)$ (H-8)
$\lim_{x\to\infty}\theta_2 = C_2x + C_1^2GrPrF(y) + C_3'$ (C-9)	$\lim_{\xi\to\infty}\Theta_2 = C_2\xi - C_1^2GrPrF(1-\eta) - C_3' - C_3$ (H-9)
$O(A^3)\quad \nabla^4\psi_2 = \frac{\partial\theta_3}{\partial x} - Gr\left(\frac{\partial(\omega_0,\psi_1)}{\partial(x,y)} + \frac{\partial(\omega_1,\psi_0)}{\partial(x,y)}\right)$ (C-10)	$O(A^3)\quad \nabla^4\Psi_2 = \frac{\partial\Theta_3}{\partial\xi} - Gr\left(\frac{\partial(\Omega_0,\Psi_1)}{\partial(\xi,\eta)} + \frac{\partial(\Omega_1,\Psi_0)}{\partial(\xi,\eta)}\right)$ (H-10)
$\nabla^2\theta_3 = PrGr\left(\frac{\partial(\theta_1,\psi_1)}{\partial(x,y)} + \frac{\partial(\theta_2,\psi_0)}{\partial(x,y)} + \frac{\partial(\theta_0,\psi_2)}{\partial(x,y)}\right)$ (C-11)	$\nabla^2\Theta_3 = PrGr\left(\frac{\partial(\Theta_1,\Psi_1)}{\partial(\xi,\eta)} + \frac{\partial(\Theta_2,\Psi_0)}{\partial(\xi,\eta)} + \frac{\partial(\Theta_0,\Psi_2)}{\partial(\xi,\eta)}\right)$ (H-11)
$\lim_{x\to\infty}\psi_2 = C_3F'(y)$ (C-12)	$\lim_{\xi\to\infty}\Psi_2 = C_3F'(1-\eta)$ (H-12)
$\lim_{\to\infty}\theta_3 = C_3x + 2C_1C_2GrPrF(y) + C_4'$ (C-13)	$\lim_{\xi\to\infty}\Theta_3 = C_3\xi - C_4 - 2C_1C_2GrPrF(1-\eta) - C_4'$ (H-13)

Appendix B: Details of the Numerical Methods; Supplementary Notes for Editor's File

I. FINITE DIFFERENCE EQUATIONS

After the spatial derivatives have been replaced with two-point central differences and the time derivatives replaced by forward differences, the finite difference equations become

$$GrPrA\left[\frac{\theta^{n+1}_{i,j} - \theta^{n}_{i,j}}{\Delta t} + X'_i Y'_j J_{i,j}(\theta^n,\psi^n)\right] = B_i\theta^n_{i+1,j} - C_i\theta^n_{i,j} + D_i\theta^n_{i-1,j} + E_j\theta^n_{i,j+1} - F_j\theta^n_{i,j} + G_j\theta^n_{i,j-1} \tag{S-1}$$

$$Gr A^2\left[\frac{\omega^{n+1}_{i,j} - \omega^{n}_{i,j}}{\Delta t} + X'_i Y'_j J_{i,j}(\omega^n,\psi^n)\right] = A\left(B_i\omega^n_{i+1,j} - C_i\omega^n_{i,j} + D_i\omega^n_{i-1,j} + E_j\omega^n_{i,j+1} - F_j\omega^n_{i,j} + G_j\omega^n_{i,j-1}\right) + \frac{Y'_j}{2\Delta Y}\left(\theta^n_{i,j+1} - \theta^n_{i,j-1}\right) \tag{S-2}$$

$$B_i\psi^n_{i+1,j} - C_i\psi^n_{i,j} + D_i\psi^n_{i-1,j} + E_j\psi^n_{i,j+1} - F_j\psi^n_{i,j} + G_j\psi^n_{i,j-1} = -\omega^n_{i,j} \tag{S-3}$$

The coefficients B_i, C_i, D_i, E_j, F_j and G_j and the Jacobian, $J_{i,j}(\omega,\psi)$ depend on the particular scheme used to introduce the graded mesh. If we represent a general nonlinear transformation by the functional form

$$X = X(x) \text{ and } Y = Y(y)$$

with first and second derivatives denoted by single and double primes respectively, the coefficients B through G may be expressed in the form

$$B_i = \left(\frac{X'_i}{\Delta X}\right)^2 + \frac{X''_i}{\Delta X}$$

$$C_i = 2\left(\frac{X'_i}{\Delta X}\right)^2$$

$$D_i = \left(\frac{X'_i}{\Delta X}\right)^2 - \frac{X''_i}{\Delta X}$$

$$E_j = \left(\frac{Y'_j}{\Delta Y}\right)^2 + \frac{Y''_j}{\Delta Y}$$

$$F_j = 2\left(\frac{Y'_j}{\Delta Y}\right)^2$$

$$G_j = \left(\frac{Y'_j}{\Delta Y}\right)^2 - \frac{Y''_j}{\Delta Y}$$

The corresponding expression for the Jacobian is

$$J_{i,j}(\omega,\psi) = -\frac{Y'_j X'_i}{12\Delta X\Delta Y} H_{i,j}$$

where

$$\begin{aligned} H_{i,j} = \Big[& \omega_{i+1,j}(\psi_{i,j-1} + \psi_{i+1,j-1} - \psi_{i,j+1} - \psi_{i+1,j+1}) \\ & + \omega_{i,j+1}(\psi_{i+1,j} + \psi_{i+1,j+1} - \psi_{i-1,j} - \psi_{i-1,j+1}) \\ & + \omega_{i,j-1}(\psi_{i-1,j-1} + \psi_{i-1,j} - \psi_{i+1,j-1} - \psi_{i+1,j}) \\ & + \omega_{i-1,j}(\psi_{i-1,j+1} + \psi_{i,j+1} - \psi_{i-1,j-1} - \psi_{i,j-1}) \\ & + \omega_{i+1,j+1}(\psi_{i+1,j} - \psi_{i,j+1}) + \omega_{i-1,j-1}(\psi_{i-1,j} - \psi_{i,j-1}) \\ & + \omega_{i-1,j+1}(\psi_{i,j+1} - \psi_{i-1,j}) + \omega_{i+1,j-1}(\psi_{i,j-1} - \psi_{i+1,j}) \Big] \end{aligned}$$

Alternatively, when the arbitrarily discretized mesh is used in the horizontal direction ($A \leq 0.2$), the coefficients B_i, C_i and D_i become

$$B_i = \frac{2}{\Delta x_i(\Delta x_i + \Delta x_{i-1})}$$

$$C_i = 2\left(\frac{1}{\Delta x_i} + \frac{1}{\Delta x_{i-1}}\right) / (\Delta x_i + \Delta x_{i-1})$$

$$D_i = \frac{2}{x_{i-1}(x_i + x_{i-1})}$$

and the Jacobian is

$$J_{i,j}(\omega,\psi) = - H_{i,j} \frac{Y'_j}{6(\Delta Y\ (\Delta x_i + \Delta x_{i-1}))}$$

The appropriate boundary condition to be imposed on ω at the lower boundary of the cavity is

$$\omega_{i,1} = \frac{-F_1}{4} (8\psi_{i,2} - \psi_{i,3}) + O(\Delta Y)^2 \qquad \text{(S-4)}$$

Similar expressions may be derived for the vorticity on the other solid boundaries and for the temperature on the insulated surfaces by the method outlined in the paper.

II. NUMERICAL ALGORITHM

A typical iteration (n+1) was carried out as follows:

1. With known values of ψ^n, ω^n and θ^n at time step n, equation (S-1) was integrated ahead in time by one complete time step (two half time steps) to give θ^{n+1}.
2. θ^{n+1} was calculated on the upper and lower boundaries from the finite difference approximation of the insulating boundary condition.
3. Equation (S-2) was integrated for 1/2 time step using θ^{n+1}, ψ^n and ω^n to give $\omega^{n+1/2}$.
4. $\psi^{n+1/2}$ was determined by means of an A.D.I. iteration using an "over relaxation" factor of 1.5. This iteration was continued until equation (S-3) was satisfied at all grid points to within a prespecified error.
5. $\psi^{n+1/2}$ was used to evaluate $\omega^{n+1/2}$ on the boundaries using equation (S-4) and its counterpart on the remaining boundaries.
6. Equation (S-2) was integrated for another 1/2 time step using θ^{n+1}, $\psi^{n+1/2}$ and $\omega^{n+1/2}$ to give ω^{n+1}.

7. ψ^{n+1} was determined as in 4.

8. ω^{n+1} was evaluated on the boundaries from ψ^{n+1}.

9. Steps 1) to 8) were repeated until further iteration no longer changed the solution.

Appendix C: Finite-Difference Grids Used in the Numerical Calculations

The grid spacings used in the numerical solution of the full Navier-Stokes equations are given in table C-1, for the cold half of the cavity. The grid in the hot end is simply a mirror reflection (about the center of the cavity) of that in the cold end.

The horizontal grid spacing used for the asymptotic solutions was

$$\Delta x_j = c \text{ for } j = 1, 2, 3$$

$$\Delta x_j = c\, \alpha^{j-3} \text{ for } j > 3$$

where

$$c = 3.0/(3 + \sum_{j=4}^{20} \alpha^{j-3})$$

and

$$\alpha = 1.2$$

Table C-1: Horizontal Grid Spacing for Full Numerical Solutions

	Δx_i x295.0xA		
Case	III	IV, VI, VII, VIII,	V
j = 1	0.933	0.470	0.2764
2	0.933	0.470	0.2764
3	0.933	0.470	0.2764
4	2.800	1.290	0.3582
5	2.800	1.290	0.3966
6	2.800	1.290	0.4000
7	2.800	1.290	0.5000
8	2.800	1.290	0.6000
9	2.800	1.290	0.7000
10	2.800	1.290	0.8000
11	2.800	1.290	0.9000
12	2.800	1.290	1.000
13	3.100	2.970	1.168
14	8.400	9.830	1.757
15	13.50	15.21	3.000
16	13.50	15.21	4.771
17	13.50	15.21	5.000
18	13.50	15.21	5.000
19	13.50	15.21	8.000
20	13.50	15.21	14.04
21	13.50	15.21	14.04
22	13.50	15.21	14.04
j=23...27	-	-	14.04

Part II: STUDIES OF A PHENOMENOLOGICAL TURBULENCE MODEL

1. INTRODUCTION

Although useful qualitative information can be deduced about flows of geophysical significance by examination of an analogous laminar flow, quantitative information can result *only* if their turbulent character is properly taken into account. In this respect, the development of a realistic model to describe the turbulent transport of momentum, heat and mass is basic to the study of geophysical fluid mechanics. Such a model must be sufficiently complex that it can yield a realistic representation of the time averaged flow, but at the same time, simple enough so that computation times are realistic. This latter consideration is particularly important for numerical simulation of meso-scale, three-dimensional atmospheric and estuarine flows.

A. Models for Computation of Turbulent Flows

i. Direct Solution of the Navier-Stokes Equations

The primary concern in computing turbulent flow fields is to model the mechanism of turbulent transport in a manner that is sufficiently complex to yield realistic representations of the time-averaged flow, while at the same time to maintain computational feasibility. Although the full equations of motion, continuity and energy do provide a complete representation of the system for both laminar *and* turbulent flows, direct numerical (finite-difference) solution of these equations in the turbulent case is not practical at the present time (or for the foreseeable future). The difficulty is that the large scale disturbance flow contains most of the turbulent kinetic energy and is primarily

responsible for the enhanced diffusivity for momentum, heat, and molecular species, while the small scale structure provides essentially all of the energy dissipation. Hence, in order to achieve a satisfactory representation of the flow, it is necessary to resolve fluctuations in the dependent variables over length scales ranging from the macroscopic scale of the overall geometry, to the Kolmogoroff scale, $(\nu^3/\varepsilon)^{1/4}$, characteristic of the dissipative eddies. The ratio of these scales varies as $Re^{-3/4}$, where Re is the Reynolds number based on the macroscopic length scale. Emmons (1970) has suggested that computation times of the order of one hundred (100) years would be required for a problem of even modest complexity using present day computers.

Using a slightly different numerical approach (which still amounts to solving the unaveraged Navier-Stokes equations directly), Orszag (1969, 1971a b, 1972) has demonstrated the computational feasibility of obtaining *exact* individual realizations of *simple* homogeneous turbulent flows by numerically solving the Navier-Stokes equations in a truncated wave number space. Such solutions are made possible by the fast Fourier transform but even with this innovation computation times are still substantial. Orszag himself points out that there are two basic motivations to pursue approximate turbulence models (which seek to quantify the turbulent transport properties without resolving the dissipative scales of the flow).

i. A satisfactory turbulence model implies a much deeper understanding of the physical processes involved than brute-force

computation could ever provide.

ii. The quantities of turbulence models are calculated as *statistically averaged* variables, whereas, the individual realizations of a direct calculation contain a random component and hence can provide useful information concerning the average flow characteristics only after *many* realizations (which constitute an ensemble) have been averaged.

Even in light of these significant advantages of approximate turbulence models, exact spectral solutions of the Navier-Stokes equations can yield important insight into the mechanisms of turbulence transport. In particular, full numerical solutions of this type can provide detailed quantitative information, which is difficult or even impossible to obtain experimentally using current techniques, but which is invaluable for the development and assessment of phenomenological, turbulent transport models.

ii. Approximate Turbulence Models which Employ the Mean Equations of Motion

As an alternative to solving the Navier-Stokes equations in a 'brute-force' manner, and subsequently averaging an ensemble of such solutions to obtain the mean flow characteristics, one can deal directly with the equations which describe the *average* velocity and temperature field, U_i and Θ. If turbulent fluctuations from the mean profiles are denoted by lower case symbols then, subject to the Boussinesq approximation, the averaged equations of motion in index notation are

$$\left.\begin{aligned} &\frac{\partial U_i}{\partial t} + U_j \frac{\partial U_i}{\partial x_j} = -\frac{1}{\rho}\frac{\partial P}{\partial x_i} + \frac{\partial}{\partial x_j}\left(\upsilon \frac{\partial U_i}{\partial x_j} - \overline{u_i u_j}\right) + \\ &\qquad \beta(\Theta - \Theta_o) g \delta_{i_3} \\ &\frac{\partial U_i}{\partial x_i} = 0 \end{aligned}\right\} \quad (1)$$

$$\frac{\partial \Theta}{\partial t} + U_j \frac{\partial \Theta}{\partial x_j} = \frac{1}{Cp\rho}\frac{\partial}{\partial x_j} K \frac{\partial \Theta}{\partial x_j} - \frac{\partial}{\partial x_j}\overline{u_j \theta} \quad (2)$$

Here, Θ_o is an arbitrary reference temperature and P, υ, β, g, Cp and K are, respectively, the pressure, kinematic viscosity, coefficient of thermal expansion, heat capacity and thermal conductivity. The overbar is used to denote ensemble averages of the indicated random quantity.

As they stand, equations (1) and (2) are not closed since $\overline{u_i u_j}$ and $\overline{u_j \theta}$ are additional unknowns. Hence, in addition to the usual numerical difficulties associated with the nonlinearity of these equations, the primary modeling problem is to develop adequate closure approximations for the turbulent momentum and energy flux terms and thereby render the equations solvable.

Although no rigorous method of closure has yet been developed, a number of semiempirical approximations have been proposed, the simplest of which can yield only qualitative results for restricted classes of flows, and the most sophisticated of which show promise of being universally applicable. Arranged in the order of increasing complexity, these techniques fall into three general categories:

i) mean velocity field techniques (MVF) which attempt to express the turbulent fluxes in terms of the mean velocity and local geometric quantities,

ii) mean turbulent energy closure methods (MTE) which employ one or two additional transport equations (usually based on the conservation of turbulence energy) to aid in modeling the turbulent fluxes, and

iii) mean Reynolds stress closure techniques (MRS) which include an additional differential equation for each component of $\overline{u_i u_j}$ and $\overline{u_j \theta}$.

a. Mean Velocity Field Techniques.

The simplest closure approximation dating to Boussinesq (1903), relates the Reynolds stresses and turbulent heat fluxes to the gradients of the mean velocity and temperature in the manner

$$\overline{u_i u_j} = - K_M \left(\frac{\partial U_i}{\partial x_j} + \frac{\partial U_j}{\partial x_i} \right) \tag{3}$$

$$\overline{u_j \theta} = - K_H \frac{\partial \Theta}{\partial x_j} \tag{4}$$

The quantities K_H and K_M are "eddy diffusion" coefficients for heat and momentum, which are assumed to be functions only of local flow and geometric variables. Although appealing because of their simplicity, the applicability of such gradient transport or eddy diffusion models is extremely limited. One fundamental deficiency lies in the implicit

assumption that the momentum and heat fluxes depend linearly on the average, instantaneous gradient of mean velocity and temperature with the principal axes of the Reynolds stress tensor and the bulk rate of strain tensor aligned. Experimental data indicate that such alignment is not the case in general. In addition, the formulae (3) and (4) suffer from the limitation that they are *local* theories, and as such, cannot account for the flow's memory of its past history or for the awareness of the local turbulence structure to nearby turbulence conditions. To account for memory and awareness a successful model must provide for the convection and diffusion of turbulence properties.

The effects of convection and diffusion are unimportant only for equilibrium or near equilibrium flows (i.e. for flows in which the local rate of turbulence energy production balances the local rate of turbulence energy dissipation). For example when variations in either space or time of the bulk flow are slow or nonexistent, advection and diffusion are negligible, and the eddy diffusion models are effective. In contrast however, many features of non-equilibrium flows cannot even be qualitatively predicted by simple gradient transport models. In many flows, the point of zero turbulent momentum flux does not correspond to the point of zero bulk velocity gradient as equation (3) would predict (c.f. the experimental results of Hanjalic and Launder (1972a) for flow in an asymmetric channel as well as the more recent works of Irwin (1973) and Wilson (1974) on wall-jets). Similarly, under certain circumstances, the phenomenon of counter-gradient heat transfer has been observed in the atmosphere (Deardorff (1966), Deissler (1968)) which would imply a

negative eddy diffusivity for heat.

Thermal stratification, present in most atmospheric flows, considerably complicates the dynamics of the turbulence since the associated gradients of potential energy can produce or dissipate turbulent kinetic energy, and will similarly suppress or enhance the transport of momentum and heat. To accommodate the possibility of thermal stratification in a boundary- or surface-layer, equations (3) and (4) are often formulated in the form of a dimensionless wind shear, ϕ_M, and heat flux, ϕ_H (c.f. Blom and Wartena (1969), Taylor (1969, 1970, 1971), Onishi and Estoque (1968) and Nickerson (1968))

$$\phi_M = \frac{ky}{(\overline{uv})^{\frac{1}{2}}} \frac{\partial U}{\partial y} \tag{5}$$

and

$$\phi_H = \frac{\rho Cp}{(\overline{\theta v})^{\frac{1}{2}}} ky \frac{\partial \Theta}{\partial y} \tag{6}$$

where k is von Karman's constant and y is the coordinate normal to the surface. Monin and Obukhov (1954) showed that, in theory, when the flow is in a state of equilibrium, ϕ_M and ϕ_H are *universal* functions of y/L where L is the Monin-Obukhov length scale. Experimental measurements in the laboratory and in the atmosphere verify this universality (c.f. Businger, Wyngaard, Izumi and Bradley (1971) or Monin and Yaglom (1971)). It must be emphasized, however, that equations (5) and (6) are valid only for *equilibrium* flows. There is no justification to assume (as Taylor (1969, 1970, 1971) and Onishi and Estoque (1968) have done) that

these expressions are valid under non-equilibrium conditions. In fact as Peterson (1969a) points out, there is substantial evidence to the contrary.

The primary features of interest for the calculation of micro-mesoscale dispersion in the atmosphere involve continuous changes in boundary conditions (for instance, changes in surface roughness and surface heat flux as an air flow passes through an urban environment) to which the turbulent flow field must adjust by means of the very transport processes which the simple gradient transport theories overlook. Hence, the local theories and similarity arguments which have been commonly used for essentially unchanging flows are unacceptable for the class of problems which characterize mesoscale atmospheric dynamics.

b. Sub-grid Scale Gradient Diffusion Models

Lilly (1967), Deardorff (1970a, b, 1972) and others have developed a numerically based model which is essentially a compromise between the purely local theories of turbulence transport and the brute-force computation method discussed in section 1.A.i. This approach is based on the application of a grid-scale averaging operator to the governing Navier-Stokes equations (with the averaging performed over the grid volume of the calculations, rather than over an ensemble of flows) to filter out the sub-grid scale (SGS) motions. The filtered variables may be computed explicitly after assumptions are made for the SGS Reynolds stresses and energy fluxes, which arise from the averaging process. The larger scale eddies are included directly, without approximation, in the computation and the empirical assumptions are thus limited to the smaller scale motions of the flow. Smagorinsky et al.

(1965), Lilly (1967) and Deardorff (1970a, b) have proposed forms for the SGS Reynolds stresses which suffer from the disadvantage that they too are local in nature. However, the approximation so introduced appears to be less severe than that introduced by the pure gradient-diffusion models since it involves only the smallest scales of the turbulent flow. An advantage of this approach is that certain probability functions which are useful for turbulent mixing calculations, can be determined directly from the numerical solutions (Lamb, 1971, 1974). On the other hand, the local nature of the turbulent transport mechanism at the small scale of the energy spectrum, the necessity to calculate the time averaged flow field from an ensemble of solutions, the inability to simulate stably stratified flows, and the necessity to use a very fine computation mesh lying within the inertial subrange, are major disadvantages of this approach.

c. Mean Turbulent Energy Transport Models

To take into consideration the effects of past history and the surrounding field on the local turbulence characteristics, numerous models, based on transport equations, have been constructed to describe the spatial and temporal variations of turbulence properties. The first widely used turbulent boundary layer prediction method of this type was developed by Bradshaw, Ferris and Atwell (1967). In this model a differential equation, relating the transport, production and dissipation of turbulence energy was used to determine the turbulent momentum flux. The basic hypothesis is that the ability of a turbulent flow to transport momentum and heat is

strongly correlated with the general level of activity of the turbulence and hence is also correlated with the magnitude of the fluctuating portion of the turbulent velocity field. The actual relationship between the turbulence energy (per unit mass), $\frac{1}{2}q^2 = \frac{1}{2}\overline{u_i u_i}$, and the Reynolds stress, $\overline{u_i u_j}$, used by Bradshaw et al. was the structure assumption,

$$\overline{u_i u_j} = C_{ij} q^2$$

where the C_{ij} are experimentally determined constants that depend on the type of strain encountered by the flow.

Nee and Kovasznay(1968) also proposed a turbulence model which entails the solution of one differential equation (in addition to the Navier-Stokes equations) with the effective eddy viscosity, K_M, as dependent variable. Whereas the model of Bradshaw et al. (1967) is based on the approximate closure of the exact turbulence energy equation, that of Nee and Kovasznay is constructed on simple heuristic grounds. Reynolds (1970) presented arguments in favor of, and against each of the above approaches; on balance, neither is to be preferred above the other. Both of these one-equation models have in common the major disadvantage that they employ a turbulence length scale, ℓ, characteristic of the energy containing eddies, that must be specified as a *local* algebraic function of position. Once again, the effects of advection and diffusion of the length scale will certainly be important in highly non-equilibrium flows. In many instances, in fact, as Hanjalic and Launder (1972b) have pointed out, if one neglects the

advection and diffusion of the length scale, one might as well use Prandtl's mixing length hypothesis.

In an attempt to overcome the length scale limitation, and thereby develop a model of more universal applicability, Harlow and Nakayama (1967), Rodi and Spalding (1970) and Jones and Launder (1972) have introduced a second transport equation from which the length scale may be determined. Closure is accomplished by specifying the effective eddy viscosity in equation (3) through the Prandtl-Kolmogoroff relationship

$$K_M = q\ell$$

Rodi and Spalding retain the turbulent energy-length scale product as their second dependent variable, while Harlow and Nakayama, and Jones and Launder employ the energy dissipation rate, which at high turbulence Reynolds numbers ($Re_\ell >> 1$, where $Re_\ell = \frac{q\ell}{\nu}$) is generally acknowledged to be related to q and ℓ in the manner

$$\varepsilon \sim q^3/\ell$$

The constant of proportionality must be determined by experiment.

For a number of flows, the two-equation models have proven acceptable where one-equation and mixing length models have previously failed. For example, Rodi and Spalding predicted the rate of spread of a plane mixing-layer, a plane jet and a radial jet reasonably well. Unfortunately different values of one adjustable parameter had to be used for each jet. With similar accuracy, Jones and Launder predicted one class of wall boundary-layer flows, in which streamwise accelerations cause a partial reversion of the flow toward the laminar condition.

However, even with these apparent successes, the non-universal nature of the models, and the implicit assumption of alignment of the principal axes of the bulk rate of strain tensor and the Reynolds stress tensor limits the applicability of the two equation models. For highly non-equilibrium flows, a higher order closure approximation is required.

d. Mean Reynolds Stress Transport Models

Models which have the potential to achieve a sufficient degree of approximation for the geophysical applications alluded to previously are those which provide a transport equation for *each* Reynolds stress component, in the manner originally proposed by Chou (1945). Such models are based on the approximate closure of the exact equation for the Reynolds stress tensor, which can easily be derived directly from the Navier-Stokes equations (c.f. Tennekes and Lumley, 1972). In index notation, the relevant equation is

$$\frac{D\overline{u_i u_j}}{Dt} = -\overline{u_i u_k}\frac{\partial U_j}{\partial x_k} - \overline{u_j u_k}\frac{\partial U_i}{\partial x_k} - \frac{\partial}{\partial x_k}\overline{u_i u_j u_k} - \left(\overline{u_j \frac{\partial p}{\partial x_i}} + \overline{u_i \frac{\partial p}{\partial x_j}}\right)/\rho + \nu \frac{\partial^2 \overline{u_i u_j}}{\partial x_k^2} - 2D_{ij} + \left(\overline{u_j \theta}\,\delta_{3i} + \overline{u_i \theta}\,\delta_{3j}\right)\frac{g}{T_o} \qquad (7)$$

where $D_{ij} = \nu \overline{\frac{\partial u_i}{\partial x_\ell}\frac{\partial u_j}{\partial x_\ell}}$

Equation (7) now expresses the second order moments of equation (1) in terms of third order moments which are themselves unknown. Although

exact equations can also be derived for each of these new unknowns, it is pointless to pursue this approach since each new equation contains more unknown moments. Instead, Daly and Harlow (1970), Donaldson (1972), Donaldson, Sullivan and Rosenbaum (1972), Hanjalic and Launder (1972b) and Shir (1973) have chosen to consider only the first equation in this infinite sequence, equation (7), and to close this equation with *algebraic* models for the unknown third order correlations, in terms of the known second order moments and mean flow variables.

In addition to the six independent transport equations for the Reynolds stress components, Donaldson et al. employ an algebraic expression for the integral length scale of the flow (ℓ), while Shir employs a differential equation for this length scale. The models of Daly and Harlow, and Hanjalic and Launder incorporate an additional transport equation for the rate of turbulence energy dissipation, ε, where

$$\varepsilon = D_{ii}$$

An exact equation for ε can also be derived from the Navier-Stokes equation as

$$\frac{D\varepsilon}{Dt} = - 2\nu \frac{\partial U_j}{\partial x_k} \overline{\frac{\partial u_j}{\partial x_\ell} \frac{\partial u_k}{\partial x_\ell}} - 2\nu \frac{\partial U_k}{\partial x_\ell} \overline{\frac{\partial u_j}{\partial x_\ell} \frac{\partial u_j}{\partial x_k}} - 2\nu \overline{\frac{\partial u_j}{\partial x_\ell} \frac{\partial u_k}{\partial x_\ell} \frac{\partial u_j}{\partial x_k}}$$

$$- \nu \frac{\partial}{\partial x_k} \overline{u_k \left[\frac{\partial u_j}{\partial x_\ell}\right]^2} - \frac{2\nu}{\rho} \frac{\partial}{\partial x_j} \left(\overline{\frac{\partial u_j}{\partial x_\ell} \frac{\partial p}{\partial x_\ell}} \right) + \nu \frac{\partial^2 \varepsilon}{\partial x_k^2}$$

$$- 2\nu^2 \overline{\left[\frac{\partial^2 u_j}{\partial x_k \partial x_\ell}\right]^2} \qquad (8)$$

As in equation (7), the higher order moments that appear in equation (8) must be expressed in terms of the known lower order moments. With this closure strategy, it is hoped that reasonably simple assumptions for the third order moments will yield adequate predictions of the second order correlations, $\overline{u_i u_j}$ and ε.

The basic philosophy of making closure assumptions at third order, rather than at second order as the MVF and MTE models do, is common to the three models mentioned above, and although substantial variations between the three models do arise since the details of the closure approximations differ in each case, all three models suffer from a fundamental shortcoming. As Lumley and Khajeh-Nouri (1973) point out, none of these models is based on a systematic procedure for generating the closure expressions. In the absence of a systematic approach, these models are constructed on the basis of *ad hoc* approximations which, in general, satisfy only the most elementary requirements of tensor invariance and dimensional consistency. The result is that these models overlook terms that may be significant and retain other terms that are unimportant. This point will be enlarged upon at a later point, during the more detailed discussion of these models.

To remedy the above inadequacy, Lumley and Khajeh-Nouri (1973) proposed a rational closure scheme which is an extension of Lumley's (1967, 1970) quest for a turbulent constitutive relation. In addition, for the thermally coupled problem, a similar closure scheme for the turbulent heat flux terms of equation (2) was proposed. It consists of three transport equations for the heat flux components, a transport

equation for the temperature variance, $\overline{\theta^2}$, and a fifth transport equation for the dissipation of temperature variance, ε_θ.

As the first step in this modeling scheme, the relevant second order moment equations are reduced to their high Reynolds number forms according to the scaling laws set forth by Tennekes and Lumley (1972). This process eliminates a number of terms from each equation. Finally, the mathematical formalism of invariant modeling (Robertson (1940), Lumley (1970)) is used to model each unknown third order moment as a functional expansion about the isotropic, homogeneous state. The resulting high Reynolds number turbulence model is complete in the sense that it incorporates a transport equation for *all* of the second order moments. In addition, it is apparent how one could proceed to generate higher order corrections (i.e. higher order in Re_ℓ) in an asymptotic representation that might be used to predict finite Reynolds number flows better. This latter point is particularly appealing since it is often observed in fluid mechanics that the first term of such an asymptotic representation provides an accurate prediction of flows over a considerably larger parameter range than one would expect on a theoretical basis (c.f. Prandtl's boundary-layer theory).

The systematic closure approach of Lumley and Khajeh-Nouri shows great promise of yielding a turbulence model which will accurately predict a wide variety of flows, including the non-equilibrium flows which are of ultimate interest. Unfortunately, this model contains many more universal constants than do the previous models, which must be established by comparison with simple laboratory and atmospheric flows. For

this parameter determination, it would be desirable to have an independent set of data for each constant to be evaluated. Unfortunately, there are only a limited number of fully documented experimental flows. Hence, in practice, coefficients must be evaluated from a more restricted data base. However, every effort should be made to include a reasonably diverse selection of flows in the parameter estimation. In contrast, Lumley and Khajeh-Nouri have attempted to evaluate *all* of the parameters on the basis of *one* experimental flow; a turbulent wake.

Aware of the difficulty associated with the determination of the many constants, Wyngaard, Coté and Rao (1973) presented a considerably simplified version of Lumley and Khajeh-Nouri's model. Unfortunately, in many instances, the Wyngaard version of the model departs in a fundamental way from the strict rules of the closure theory. In particular, Wyngaard's model violates the principle of tensor invariance in the important "tendency-toward-isotropy" term and resorts to an *ad hoc* eddy diffusion hypothesis for the triple correlations. (These points will be enlarged upon in sections 2.D and 4.B.) Using this model, Wyngaard, Coté and Rao (1973) examined the horizontally homogeneous atmospheric boundary layer under conditions of neutral and unstable stratification, and compared their results with Deardorff's (1972) three-dimensional calculation. Wyngaard and Coté (1974) also simulated the evolution of the one-dimensional atmospheric boundary layer for day 33 of the Wangara experiment in Australia, and compared their predicted profiles of wind, temperature, humidity and Reynolds stresses with those calculated by Deardorff (1974). In both cases, the

distributions of mean velocity, temperature and humidity were in qualitative agreement with Deardorff's results. However, the distributions of Reynolds stress and other second order correlations showed *substantial* deviations from the 3-D calculation. Indeed, it will be shown in section 4.C that Wyngaard's version of Lumley's model cannot predict in an adequate fashion the turbulent dynamics of one of the simplest of laboratory flows; the homogeneous shear flow.

The inability of the Wyngaard model to predict accurately second order correlations is particularly significant for two reasons. First, even though the profiles of mean velocity and temperature are in reasonable agreement with those of the 3-D calculations in this case, one might expect that for accelerating flows, such as those that occur in the vicinity of the urban heat island (c.f. Townsend (1972)), much poorer agreement would be found since errors in the directional distribution of turbulence energy will be amplified by the mechanism of turbulence energy production by vortex stretching. Second, the distributions of second order correlations are also significant when one is interested in the dispersion of chemically reactive species. Donaldson and Hilst (1972) have shown that, for fast chemical reactions of second and higher-order, such as the free-radical reactions of photochemical smog, the rate of reaction may be *controlled* by the second order correlations of concentration, which in turn depend strongly on the second order correlations of velocity and temperature. In view of one of the potential applications of the turbulence modeling efforts (i.e. to predict the dispersion of chemically reacting species in the urban atmosphere boundary layer), it is essential that

the model predict the second order correlations more accurately than is possible using Wyngaard's simplified version of Lumley's model.

To conclude the discussion of existing turbulence models, it should be reemphasized that the basic philosophy behind Lumley and Khajeh-Nouri's closure scheme seems to be a very sound one. Unfortunately, in their *application* of the model and also in Wyngaard's application of his version of the model, *insufficient attention has been directed to the systematic determination of model parameters.* It is essential that the unicity of parameter values which adequately model one particular flow and the universality of these parameters for a broad range of flows, be established on the basis of laboratory studies for which full profiles of the second order correlations have been documented. Of course, numerical experiments of the type done by Wyngaard et al. are useful first steps which have helped to establish the potential of Reynolds stress transport models for predicting atmospheric flows. In addition, certain *qualitative* questions, such as the influence of the Coriolis force on the turbulent energy budget (Wyngaard, Arya and Coté, 1974), may be usefully investigated. However, confident quantitative predictions of flows over the strongly inhomogeneous surface boundary conditions that characterize the urban atmospheric boundary layer can be made only after comprehensive model validation studies have been completed.

In what follows, the rational closure technique proposed by Lumley and Khajeh-Nouri (1973) is applied to equations (7) and (8). The resulting turbulence model is similar in many respects to that

presented by Lumley et al. However, more effort is made to evaluate the parameters in a systematic manner. Particular emphasis is placed on the suitability and quality of experimental data used for the evaluation of model parameters and on the unicity and universality of the resulting parameters.

2. THE RATIONAL CLOSURE TECHNIQUE

A. High Reynolds Number Form of the Equations

Basic to the closure technique is the assumption that the Reynolds stress tensor and the dissipation rate can be expanded as asymptotic series in Re_ℓ of the form

$$\overline{u_i u_j} = (\overline{u_i u_j})_o + Re_\ell^{-\alpha_1} (\overline{u_i u_j})_1 + \ldots + Re_\ell^{-\alpha_k} (\overline{u_i u_j})_k + \ldots \tag{9}$$

and

$$\varepsilon = \varepsilon_o + Re_\ell^{-\beta_1} \varepsilon_1 + \ldots + Re_\ell^{-\beta_k} \varepsilon_k + \ldots \tag{10}$$

If ($\alpha_k > 0$, $\beta_k > 0$; $k = 1, 2, \ldots$) then $\overline{u_i u_j}$ and ε exhibit an asymptotic form in the limit $Re_\ell \to \infty$. To obtain systematically the equations which govern each term in equations (9) and (10), it is necessary to substitute these series into *properly scaled* versions of equations (7)-(8), and then to equate coefficients of equal order in Re_ℓ.

To deduce the proper scaling, Tennekes and Lumley (1972) propose two fundamental scaling concepts.

i. Quantities which appear in correlations can be associated with either the energy containing eddies, which have characteristic velocity u, and characteristic length ℓ, *or* with the dissipative range of eddies which also have characteristic velocity u, but which have a much smaller length scale, the Taylor micro-scale, $\lambda \sim 4\ell\, Re_\ell^{-\frac{1}{2}}$. Derivatives which are outside of correlations correspond to the energy containing range, whereas derivatives within the corre-

lations are associated with the dissipative range.

ii. The correlation coefficient between quantities, each taken from different ranges, is of order

$$\lambda/\ell \sim 4\ Re_\ell^{-\frac{1}{2}}$$

The second scaling law arises since any correlation between the energy containing and dissipative structures results from the interaction of motions at the two scales. The 'effectiveness' of this interaction (i.e. the correlation coefficient) varies as the ratio of the frequencies of the ranges involved, $(u/\ell)/(u/\lambda) = \lambda/\ell$. Since the dissipative structure has a very high frequency at large Re_ℓ, the effectiveness of the interaction is low.

An examination of equation (7) indicates that only one term is of higher order in Re_ℓ,

$$\left\{ \nu \frac{\partial^2 \overline{u_i u_j}}{\partial x_k^2} \right\} / \varepsilon = 0\ (Re_\ell^{-1})$$

On the other hand, an examination of equation (8) indicates that

$$\left\{ \nu \overline{\frac{\partial u_j}{\partial x_\ell} \frac{\partial u_k}{\partial x_\ell} \frac{\partial u_j}{\partial x_k}} \right\} / \frac{D\varepsilon}{Dt} = 0\ (Re_\ell^{\frac{1}{2}})\ ,$$

and

$$\left\{ \nu \frac{\partial^2 \varepsilon}{\partial x_k^2} \right\} / \frac{D\varepsilon}{Dt} = 0\ (Re_\ell^{-1})$$

The previous scaling arguments cannot be blindly applied to the last

term in equation (8), which may be interpreted as the dissipation of dissipation rate. Although the first derivative scales as before ($\partial u_j/\partial x_\ell \sim u/\lambda$), the second derivative scales with respect to the smallest length scale in the turbulent flow, the Kolmogorov length scale, $\eta = \ell Re_\ell^{-3/4}$. (A more detailed discussion of the origin of this scaling is presented in Appendix A.) Hence the correct order of magnitude for this term is

$$\left\{ \nu^2 \overline{\left(\frac{\partial^2 u_j}{\partial x_k \partial x_\ell} \right)^2} \right\} \Big/ \frac{D\varepsilon}{Dt} = 0 \ (Re_\ell^{\frac{1}{2}})$$

Finally, the first and second terms on the right side of equation (8) require additional consideration. At high Re_ℓ, it is generally accepted that the small scale dissipative structure tends to be isotropic. Hence, the dissipation tensor

$$D_{ij} = \nu \overline{\frac{\partial u_i}{\partial x_\ell} \frac{\partial u_j}{\partial x_\ell}}$$

is itself isotropic for large Re_ℓ. Any anisotropy in the dissipative structure must result from interaction between the dissipative structure and the anisotropic energy containing structure. However, the correlation coefficient for interactions between energy containing and dissipative eddies is $0(Re_\ell^{-\frac{1}{2}})$. Hence, the anisotropy of the dissipation tensor will be $0(Re_\ell^{-\frac{1}{2}})$, i.e.

$$D_{ij} = \frac{\varepsilon}{3}\delta_{ij} + b_{ij} Re_\ell^{-\frac{1}{2}} + \ldots \qquad (11)$$

where

$$b_{ij} \sim \nu \frac{u^2}{\lambda^2}$$

The application of equation (11) and the continuity equation to the second term in equation (8) yields

$$\left(\nu \frac{\partial U_i}{\partial x_k} D_{ik} \right) / \frac{D\varepsilon}{Dt} = 0 \ (Re_\ell^{-\frac{1}{2}})$$

Similarly, the tensor $\overline{\frac{\partial u_j}{\partial x_\ell} \frac{\partial u_j}{\partial x_k}}$ is governed by the dissipative structure and so, has an anisotropic component of order $(Re_\ell^{-\frac{1}{2}})$. Hence

$$\left(\nu \frac{\partial U_k}{\partial x_\ell} \overline{\frac{\partial u_j}{\partial x_\ell} \frac{\partial u_j}{\partial x_k}} \right) / \frac{D\varepsilon}{Dt} = 0 \ (Re_\ell^{-\frac{1}{2}})$$

All other terms in equation (8) which have not been specifically mentioned are 0(1) with respect to $D\varepsilon/Dt$.

Now, if only the high Re_ℓ asymptotic solutions, $(\overline{u_j u_i})_o$ and ε_o, are sought, equations (7)-(8) can be simplified to the forms

$$\frac{D\overline{u_i u_j}}{Dt} = - \overline{u_i u_k} \frac{\partial U_j}{\partial x_k} - \overline{u_j u_k} \frac{\partial U_i}{\partial x_k} - \frac{\partial}{\partial x_k} \overline{u_i u_j u_k} - \left(\frac{\partial \overline{U_j p}}{\partial x_i} + \frac{\partial \overline{U_i p}}{\partial x_j} \right) / \rho - \frac{2}{3} \varepsilon \delta_{ij} \qquad (12)$$

and

$$\frac{D\varepsilon}{Dt} = -2\nu \overline{\frac{\partial u_j}{\partial x_\ell}\frac{\partial u_k}{\partial x_\ell}\frac{\partial u_j}{\partial x_k}} - 2\nu^2 \overline{\left(\frac{\partial^2 u_j}{\partial x_k \partial x_k}\right)^2} - \nu \frac{\partial}{\partial x_k}\left[\overline{u_k\left(\frac{\partial u_j}{\partial x_\ell}\right)^2} + \frac{2}{\rho}\overline{\frac{\partial u_k}{\partial x_\ell}\frac{\partial p}{\partial x_\ell}}\right] \qquad (13)$$

The order of magnitude analysis of the first two terms on the right side of equation (13) indicated that each is $O(Re_\ell^{\frac{1}{2}})$ with respect to the other terms. The first term represents 'production of dissipation' through the stretching of vorticity by the energy containing eddies, and the second term represents the 'destruction of dissipation' by the action of viscosity. These processes must nearly balance each other so that the sum of these terms is only $O(1)$ with respect to $D\varepsilon/Dt$. It is interesting to note that Townsend's (1951) analysis of the fine structure of turbulence, which was based on a balance between the opposing effects of vorticity dissipation by molecular viscosity, and vorticity production by turbulent shear, is consistent with (or a consequence of) the above scaling of the dissipation equation, as $Re_\ell \to \infty$. Although Townsend derived a universal law for the three-dimensional energy spectrum (which is in excellent agreement with experimental measurements) at the smallest scales of turbulent motion (i.e. at scales smaller than those which contribute most to the dissipation), this universal law is of no use in establishing models for the higher order Re_ℓ terms which appear in equation (13).

Of course, equations (12) and (13) are only valid in flows (or

regions of flows) where $Re_\ell >> 1$. To understand the limitations that this may place on the applicability of the turbulence model, it is useful to examine an equilibrium turbulent boundary-layer. In such a flow, near the wall the relevant characteristic velocity is the slip- or friction-velocity, $u^* = \sqrt{\tau/\rho}$, where τ is the wall shear stress, and the characteristic length scale is ky where k is von Karman's constant and y is the coordinate normal to the wall. Thus, for this flow,

$$Re_\ell \sim \frac{u^* k y}{\nu}$$

For equations (12)-(13) to be valid,

$$y >> \frac{\nu}{u^* k} \tag{14}$$

This inequality suggests that the high Reynolds number equations are valid only at points far from the solid surface. However, this restriction is not too severe since inequality (14) is identical with that which defines the inner (lower) boundary of the region where the law of the wall is valid. Experimentally, it is observed that the logarithmic velocity profile is valid for yu^*/ν as small as 100. Furthermore, since the law of the wall is essentially an infinite Reynolds number theory, as verified by the lack of Re_ℓ dependence of the relevant coefficients, this suggests that the high Reynolds number equations (12)-(13) are themselves valid for $Re_\ell \gtrsim 100$.

To describe the turbulence for y less than the lower boundary of the logarithmic region, some of the terms in equations (7)-(8) which

are higher order in Re_ℓ at points far from the boundary, must be retained by 'stretching' the y-coordinate with respect to Re_ℓ, in analogy to Prandtl's theory for laminar boundary-layers.

B. Independent Variables

With the high Reynolds number form of the governing equations deduced, the unknown correlations in equations (12) and (13) must be modeled as functions of the known lower order quantities, U_i, $\overline{u_i u_j}$ and ε. The most general functional form for one of these higher order correlations, $Q_{ij\ldots k}(\bar{x},t)$, which is consistent with this requirement is thus

$$Q_{ij\ldots k}(\bar{x},t) = \int_{-\infty}^{t} d\tau \int_{-\infty}^{\infty}\int_{-\infty}^{\infty}\int_{-\infty}^{\infty} d\bar{\xi}\, F_{ij\ldots k}(U_i(\bar{x}+\xi,\tau),$$

$$\overline{u_i u_j}(\bar{x}+\bar{\xi},\tau),\ \varepsilon(\bar{x}+\bar{\xi},\tau)) \qquad (15)$$

Here, $F_{ij\ldots k}$ denotes some generalized functional of its arguments. The limits of integration are intended to signify integration over all points in the fluid, including boundaries, and over all time, from the present backward to some initial instant. Thus, it is presumed in (15), that the turbulence properties at a point exhibit both a perfect memory for previous states and an infinite 'awareness' of (or dependence on) the state of the turbulence at all other points in the fluid.

Due to its extremely general statement of functionality, the

functional relationship (15) is of limited use in its present form. In particular, the presumed dependence on all surrounding points in space and on all preceding instants in time, implies an implicit dependence of the closure model on the specific initial and boundary conditions for each problem. Thus, in its most general form, the expression (15) leads to the hopeless situation of a unique closure model for each turbulent flow to be considered. Fortunately, one can reduce the complexity of the general form by noting the implicit dependence of U_i on $\overline{u_i u_j}$, and by introducing the plausible hypothesis of a turbulence with a 'fading memory' for past history, and a 'limited awareness' of the turbulence characteristics at surrounding points in space (c.f. Lumley, 1970). In particular, it is assumed

i) For a known distribution of Reynolds stress, $\overline{u_i u_j}(\bar{x},t)$, one can determine the mean velocity field, $U_i(\bar{x},t)$, by solving the Navier-Stokes equations, subject to appropriate initial and boundary conditions. Thus, it is assumed that any dependence of $Q_{ij\ldots k}$ on the mean velocity field can be included implicitly through direct dependence on $\overline{u_i u_j}$, so that U_i can be eliminated from the arguments of $F_{ij\ldots k}$ in equation (15).

ii) It is also assumed that the function $Q_{ij\ldots k}$ is dominated by spatially and temporally local values of the 'independent' variables (the hypothesis of fading memory and limited awareness which was originally suggested by Lumley (1970)). Thus, the general *functional* form for

$Q_{ij...k}$ can be expressed as an *ordinary function* of the local values of $\overline{u_i u_j}$, ε and their first few derivatives in space and time. (This is analogous to expanding the spatial and temporal dependence of the functional as a Taylor series about the local point.) If it is further assumed that the characteristic time for change of $Q_{ij...k}$ is sufficiently short relative to the characteristic time scales of $\overline{u_i u_j}$ and ε, then $Q_{ij...k}$ may be approximated, to zero order in the ratio of these time scales, as a function only of the instantaneous (present) values of $\overline{u_i u_j}$, ε and their spatial derivatives. Finally, if $\bar{x}$ is not too near a solid boundary, it is assumed that the detailed character of the boundary conditions will not be important to the general form of $Q_{ij...k}$. Instead, it is anticipated that initial and boundary conditions will serve only to set length and time scales which govern the statistics of the turbulence.

Rather than simply accept these simplifying assumptions, and attempt to establish their validity *a posteriori* by comparison of model calculations which incorporate them with experimental data, it would be desirable to justify them directly. Unfortunately, this is only partially possible for ii) and remains as an unresolved problem for i). Before we proceed with the development of the model equations, we briefly summarize the extent to which we have been able to justify

assumptions i) and ii).

i) Uniqueness of the Mean Velocity Distribution

Consider first assumption i). The key question posed here is: for a *specified* distribution of $\overline{u_i u_j}(\bar{x},t)$, can the mean field equations be solved to yield a unique mean velocity field? The most extensive study of existence and uniqueness of solutions to the Navier-Stokes equations (of which we are aware), is the monograph of Ladyzhenskaya (1969). However, this work is concerned solely with *laminar* flow conditions. Recently, Warsi (1974) extended the work of Ladyzhenskaya to examine the uniqueness of mean *turbulent* flows in a bounded domain. He concluded that a sufficient condition for the existence of unique solutions is that the Reynolds stress be bounded from below by the eddy viscosity relationship in equation (3). However, the question of uniqueness of the mean velocity field for a *specified* Reynolds stress distribution is not answered by Warsi's analysis. Of more relevance to this question is the laminar analysis of flows acted upon by a distributed body force, since $\partial \overline{u_i u_j}/\partial x_j$ can be treated as such a force. With this interpretation, the laminar analysis of flows with vanishingly small viscosity and acted upon by a distributed body force, can be applied directly to the current problem. For *inviscid* two-dimensional flows, past impermeable boundaries, the existence of unique solutions has been demonstrated (c.f. pp. 185 of Ladyzhenskaya, 1969). Unfortunately, in the more relevant circumstance of small but non-zero viscosity, the situation is still

far from clear (for example, see Nickel, 1973). We have not been able to proceed further. Thus, at the present time, the existence of a unique mean velocity distribution is simply accepted as a physically plausible assumption, which remains to be verified either directly or by *a posteriori* comparison of model calculations which incorporate assumption i) with suitable experimental data.

ii) The Local Nature of the Pressure Gradient-Velocity Correlation

The assumptions in ii) of 'fading memory' and 'limited awareness' are better understood after an examination of the exact equations which govern the various unknown correlations of equations (12) and (13), which to this point have been represented symbolically by $Q_{ij\ldots k}$. We begin with the pressure-velocity correlation, which was shown by Chou (1945) to satisfy a Poisson's equation. The appropriate form of the solution for the present purposes is

$$\frac{1}{\rho}\overline{u_i \frac{\partial p}{\partial x_k}} = \frac{1}{2\pi}\iiint \frac{\partial}{\partial \xi_k}\left(\frac{\partial U_m}{\partial x_n}(\bar{x}+\bar{\xi}) \frac{\partial}{\partial \xi_m}\overline{u_i(\bar{x})u_n(\bar{x}+\bar{\xi})}\right)$$

$$\frac{1}{r}\, d\xi_1 d\xi_2 d\xi_3 + \frac{1}{4\pi}\iiint \frac{\partial^3 \overline{u_m(\bar{x}+\bar{\xi})u_n(\bar{x}+\bar{\xi})u_i(\bar{x})}}{\partial \xi_m \partial \xi_n \partial \xi_k}$$

$$\frac{1}{r} d\xi_1 d\xi_2 d\xi_3 + \frac{1}{4\pi\rho}\iint \left[\frac{1}{r}\frac{\partial}{\partial n}\left(\overline{\frac{\partial p(\bar{x}+\bar{\xi})}{\partial \xi_k} u_i(\bar{x})}\right) - \right.$$

$$\left. \overline{\frac{\partial p(\bar{x}+\bar{\xi})u_i(\bar{x})}{\partial \xi_k}} \frac{\partial}{\partial n}\left(\frac{1}{r}\right)\right] ds \qquad (17)$$

where $\partial/\partial n$ denotes the normal derivative to the surface at $\bar{\xi}$ and r is $(\xi_i \xi_i)^{\frac{1}{2}}$. The first two integrals are volume integrals taken over all space and the third integral is taken over all solid boundaries.

Although the limited awareness principle had not been hypothesized at the time, Chou (1945) attempted to establish the spatially local nature of the pressure-velocity correlation. He argued that the factor r^{-1} which appears in each of the integrals of (17) implies that the effects of velocity and pressure fluctuations at points distant from $\bar{x}$ contribute only insignificantly to the single point pressure-velocity correlation. However, since the first two integrals are taken over the total fluid volume, Chou's argument is clearly valid *only* if the two-point double- and triple-velocity correlations themselves go to zero sufficiently rapidly (as $\bar{\xi} \to \infty$) that the integrand is $O(r^{-(3+\delta)})$ for large r, where $\delta > 0$. The rate of decrease of these two-point correlations was not considered in detail by Chou.

To examine the first integral (I_1), it is useful to follow the example of Chou (1945), Rotta (1951) and Hanjalic and Launder (1972b) and to expand the mean velocity gradient as a Taylor series in $\bar{\xi}$, about the point $\bar{x}$, i.e.

$$\frac{\partial U_m}{\partial x_n}(\bar{x} + \bar{\xi}) = \frac{\partial U_m}{\partial x_n}(\bar{x}) + \xi_i \left.\frac{\partial^2 U_m}{\partial x_n \partial x_i}\right|_{\bar{x}} + \ldots \qquad (18)$$

Now, if only points within a radius r_o of $\bar{x}$ contribute to I_1, and if

the characteristic length scale for change of the mean velocity gradient is much larger than r_o, then the velocity gradient in I_1 can be approximated by its value at $\bar{x}$ (i.e. by the first term in (18)). In general, this is probably not a bad approximation except perhaps in the immediate vicinity of a solid boundary where

$$\frac{\partial^2 U_i}{\partial y^2} \sim \frac{1}{y^2}$$

(It should be noted that Hanjalic and Launder have invoked this assumption even in the near-wall region.) Thus, at least for points not too near solid surfaces, the expression for I_1 may be approximated as

$$I_1 \simeq \frac{1}{2\pi} \frac{\partial U_m}{\partial x_n} \iiint \frac{\partial^2 \overline{u_i(\bar{x}) u_n(\bar{x} + \bar{\xi})}}{\partial \xi_k \partial \xi_m} \frac{1}{r} \partial \xi_1 \partial \xi_2 \partial \xi_3 \qquad (19)$$

The convergence of I_1 is now seen to depend solely on the characteristics of $\partial^2(\overline{u_i(\bar{x}) u_n(\bar{x} + \bar{\xi})})/\partial \xi_j \partial \xi_m$. Furthermore, since the second derivatives of $\overline{u_i(\bar{x}) u_n(\bar{x} + \bar{\xi})}$ will approach zero at least as rapidly as the correlation itself, to establish the convergence of I_1, it is sufficient to consider the behavior of the two-point velocity correlation itself.

Many experimental studies (see for example, Champagne, Harris and Corrsin (1970), and Wygnanski and Fiedler (1970)) suggest that the two-point velocity correlation does diminish extremely rapidly with increasing r, as is required for the convergence of (19). In fact,

for isotropic turbulence, the rate of decay of the two-point velocity correlation is exponential (c.f. Batchelor (1953) or Hinze (1959)), and for low Reynolds number isotropic turbulence the longitudinal component of the correlation varies as

$$\overline{u_1(\bar{x})u_1(\bar{x}+\bar{\xi})} \sim \exp(-r^2/2\lambda^2)^{\dagger}$$

Indeed, all experimental evidence (of which we are aware) is consistent with bounded values for I_1. On the other hand, the two-point correlation is non-zero over a finite radius. Therefore, it must be expected that I_1 may depend on turbulence characteristics within about one integral length scale of $\bar{x}$. The integral length scale, ℓ, is chosen here as the radius of influence since this is the size of a typical eddy, within which the two-point correlation is non-zero.

The behavior of the two-point triple-velocity correlation which appears in the second integral (I_2) is very poorly documented for inhomogeneous flows. In general, only measurements of *single-point* triple- and two-point double-velocity correlations are reported. Nevertheless, it is plausible that this correlation diminishes at least as rapidly as the two-point double-velocity correlation with

---

†If the Taylor microscale, λ, persisted as the length scale for spatial decay of the two-point velocity correlation in inhomogeneous flows and for high Reynolds number turbulence, as $Re_{\ell} \to \infty$, the two-point correlation would approach a delta-function distribution. Hence, the assumption of spatially local dependence in this instance would be exact. However, the experimental evidence tends to indicate rather that, for inhomogeneous, high Reynolds number flows, the integral length scale is the appropriate length scale.

increasing r (except possibly for small r where it may increase, c.f. Stewart (1951)). Thus, it appears likely that I_2 is bounded and, furthermore, dependent on turbulence properties within a radius of, at most, one integral length scale of $\bar{x}$.

The third integral (I_3) in equation (17) represents the contributions to the single-point pressure-velocity correlation due to interactions between velocity fluctuations at $\bar{x}$ and pressure fluctuations at the boundaries ($\bar{\xi}$). Although a number of experimental studies have, in principle, had the capability to measure the $\bar{\xi}$-dependence of the two-point surface-pressure velocity correlation (c.f. Gorshkov (1968), Blake (1970) and Elliott (1972)), such data have not appeared in the literature. Thus, once again, one can only proceed with a plausible assumption. Hence, it is supposed that the correlation diminishes with increasing $\bar{\xi}$ in an exponential manner, similar to the two-point velocity correlation discussed above. An implication of this supposition is that the correlation $\overline{p(\bar{x} + \bar{\xi})u_i(\bar{x})}$ is small for points not too close to the boundary. Thus, I_3 and the corresponding boundary dependence of $\overline{u_i \frac{\partial p}{\partial x_k}}$ may be neglected for points, $\bar{x}$, which are not too close to solid boundaries.

In conclusion, then, it is clear that $\overline{u_i \frac{\partial p}{\partial x_k}}$ is not strictly a spatially local function of $\overline{u_i u_j}$ and ε. However, it does appear that the dependence on turbulence properties is restricted to a region within one integral length scale of the point of interest. Furthermore, due to the rapid decay of the two-point correlations as r increases, it appears likely that this spatial dependence is dominated

by the turbulence characteristics in the immediate vicinity of $\bar{x}$ (i.e. over a length *scale* considerably smaller than ℓ). Hence, while we expect $\overline{u_i \frac{\partial p}{\partial x_k}}$ to depend on spatial derivatives of $\overline{u_i u_j}$ and ε at $\bar{x}$ in addition to the local values of these quantities, it may suffice to include only derivatives of first and second order in this functionality. Finally, for points not too near solid surfaces, the boundary dependence of the pressure-velocity correlation may apparently be neglected.

iii) The Triple-Velocity Correlation

The second term in the stress tensor equations, which must be modeled in terms of lower order correlations, is the triple-velocity term, $\overline{u_i u_k u_\ell}$. The exact differential equation governing this third order tensor is

$$\frac{D}{Dt}\overline{u_i u_k u_\ell} + \frac{\partial U_i}{\partial x_j}\overline{u_j u_k u_\ell} + \frac{\partial U_k}{\partial x_j}\overline{u_j u_\ell u_i} + \frac{\partial U_\ell}{\partial x_j}\overline{u_j u_i u_k} +$$

$$\frac{\partial \overline{u_j u_i u_k u_\ell}}{\partial x_j} = -\frac{1}{\rho}\overline{\frac{\partial p}{\partial x_i} u_k u_\ell} - \frac{1}{\rho}\overline{\frac{\partial p}{\partial x_k} u_\ell u_i} - \frac{1}{\rho}\overline{\frac{\partial p}{\partial x_\ell} u_i u_k} +$$

$$\frac{\partial \overline{u_i u_j}}{\partial x_j}\overline{u_k u_\ell} + \frac{\partial \overline{u_j u_k}}{\partial x_j}\overline{u_\ell u_i} + \frac{\partial \overline{u_j u_\ell}}{\partial x_j}\overline{u_i u_k} - 2\nu\left\{\overline{u_\ell \frac{\partial u_i}{\partial x_m}\frac{\partial u_k}{\partial x_m}} + \right.$$

$$\left.\overline{u_i \frac{\partial u_k}{\partial x_m}\frac{\partial u_\ell}{\partial x_m}} + \overline{u_k \frac{\partial u_\ell}{\partial x_m}\frac{\partial u_i}{\partial x_m}}\right\} + \nu \frac{\partial^2 \overline{u_i u_k u_\ell}}{\partial x_n \partial x_n} \qquad (20)$$

An analysis of this equation indicates that the only term of higher order in Reynolds number (and, hence, the only term which is negligible on this basis) is the last term (the 'viscous diffusion' term).

In the discussion of the pressure-velocity correlation term, attention was focused on its spatially local character. In the case of the triple-velocity correlation, the spatial character can be examined, only indirectly, after an examination of the characteristic time scales for the correlation, which are accessible through equation (20). Hence, we will return to a discussion of the spatial character of $\overline{u_i u_j u_k}$ after the discussion of time scales.

To establish that the triple-velocity correlation depends only on *present* values of lower order correlations, it is necessary to examine characteristic times which arise out of equation (20). The three which appear to be most important are:

1) the convective time scale

$$\tau_c = \frac{\left| \overline{u_i u_j u_k} \right|}{\left| U_\ell \frac{\partial \overline{u_i u_j u_k}}{\partial x_\ell} \right|}$$

2) the time scale which characterizes the 'production' by mean flow-turbulence interaction

$$\tau_{p.m.} = \frac{\left| \overline{u_i u_j u_k} \right|}{\left| \frac{\partial U_i}{\partial x_\ell} \overline{u_i u_k u_\ell} \right|}$$

3) the time scale which characterizes the 'production' by

turbulent-turbulent interaction

$$\tau_{p.t.} = \frac{\left| \overline{u_i u_j u_k} \right|}{\left| \overline{u_k u_j} \frac{\partial u_i u_\ell}{\partial x_\ell} \right|}$$

In these expressions $| Q_{ij...k} |$ denotes a suitable norm of the tensor $Q_{ij...k}$. Certainly, additional characteristic times can be constructed from other terms in equation (20). For instance, from the last term on the left side of equation (20) one could construct a 'turbulent diffusion' time, or from the next to the last term on the right side, a 'dissipation' time scale. However, it is not anticipated that these terms could dominate the dynamics of $\overline{u_i u_j u_k}$ in the manner of the 'production' terms. A similar situation is actually found for the dynamics of the Reynolds stress tensor in shear flows: although many time scales can be constructed, it is the production time scale that dominates the evolution of Reynolds stress.

Two of the three characteristic times cited are formed from 'production' terms. To determine which production term dominates, and thereby to establish which time scale dominates the evolution of the triple-velocity correlation, it is useful to examine their ratio,

$$P = \frac{\tau_{p.t.}}{\tau_{p.m.}} = \frac{\left| \frac{\partial U_i}{\partial x_\ell} \overline{u_i u_k u_\ell} \right|}{\left| \overline{u_k u_j} \frac{\partial u_i u}{\partial x_\ell} \right|} \qquad (21)$$

As an estimate of the magnitude and functionality of $\overline{u_i u_j u_k}$, we adopt the model, which is the final result of the work in section 4.B,†

$$\overline{u_i u_j u_k} = \alpha_1 \frac{q^4}{\varepsilon} M_{ijk\ell} \frac{\partial q^2}{\partial x_\ell} + \alpha_5 \frac{q^4}{\varepsilon} \left(\frac{\partial a_{ik}}{\partial x_j} + \frac{\partial a_{ij}}{\partial x_k} + \frac{\partial a_{kj}}{\partial x_i} \right) +$$

$$\alpha_7 \frac{q^2}{\varepsilon} (\delta_{ik} a_{j\ell} + \delta_{ij} a_{k\ell} + \delta_{jk} a_{i\ell}) \frac{\partial q^2}{\partial x_\ell} +$$

$$\alpha_{12} \frac{q^2}{\varepsilon} \left(a_{ik} \frac{\partial a_{j\ell}}{\partial x_\ell} + a_{ij} \frac{\partial a_{k\ell}}{\partial x_\ell} + a_{kj} \frac{\partial a_{i\ell}}{\partial x_\ell} \right) \qquad (22)$$

where

$$M_{ijk\ell} \equiv \delta_{ij}\delta_{k\ell} + \delta_{ik}\delta_{j\ell} + \delta_{kj}\delta_{i\ell}$$

$$a_{ij} \equiv \overline{u_i u_j} - \frac{q^2}{3} \delta_{ij}$$

and the parameters, α_i are given in table 6.

For turbulent wakes and shear-layers, it is observed that the double-velocity correlations take the form (c.f. Tennekes and Lumley, (1972))

$$\left.\begin{aligned} &\overline{u_1 u_1} \sim \overline{u_2 u_2} \sim \overline{u_3 u_3} \sim q^2/3 \quad , \quad -\overline{u_1 u_2} \sim q^2/7 \\ &\text{and} \\ &\varepsilon \sim -\overline{u_1 u_2} \frac{\partial U_1}{\partial x_2} \end{aligned}\right\} \qquad (23a)$$

---

†We will show that the assumption of the temporally local character of $\overline{u_i u_j u_k}$ is consistent with this model. This self-consistency provides *a posteriori* verification that the initial assumption is probably a good one.

On the other hand, for boundary-layers (c.f. Klebanoff, (1955) the Reynolds stress tensor is somewhat more anisotropic and can be approximated by

$$\left.\begin{aligned} \frac{a_{ij}}{q^2} &\sim \begin{bmatrix} 0.24 & -0.16 & 0.0 \\ -0.16 & -0.18 & 0.0 \\ 0.0 & 0.0 & -0.06 \end{bmatrix} \\ \text{and} \quad \varepsilon &\sim -\overline{u_1 u_2}\,\frac{\partial U_1}{\partial x_2} \end{aligned}\right\} \qquad (23b)$$

With the estimates (22) and (23a) or (23b), the characteristic times and P may be evaluated. Certainly, there are many flows (or regions of flows) for which (23) is not satisfied. For instance, in channel flows $|\overline{u_1 u_2}|$ is maximum at the walls and goes to zero somewhere in the core of the flow. However, the two cases (23a) and (23b) do represent a nearly-isotropic and a highly anisotropic flow, respectively, and in this sense are likely to yield representative results for a reasonably broad cross-section of flows.

For the x_2-component of turbulence energy flux (i.e. $\overline{u_1 u_1 u_2} + \overline{u_2 u_2 u_2} + \overline{u_3 u_3 u_2}$), (23a) gives

$$P \sim 0.28$$

and (23b) gives

$$P \sim 0.22$$

Thus, the rate of production of $\overline{u_i u_j u_k}$ by turbulence-turbulence inter-

action is about four times greater than the rate of mean flow-turbulence production. This conclusion is consistent with Hanjalic and Launder's (1972b) assumption that the mean flow-turbulence production terms in equation (20) may be neglected as a first approximation. Since the turbulence-turbulence production term dominates equation (20), $\tau_{p.t.}$ will be adopted as the time scale which characterizes $\overline{u_i u_j u_k}$.

To justify the assumption that $\overline{u_i u_j u_k}$ depends only on instantaneous values of $\overline{u_i u_j}$ and ε, it is now necessary to compare its dominant time scale, $\tau_{p.t.}$, with similar time scales which characterize the evolution of $\overline{u_i u_j}$ and ε. If the latter are long compared with $\tau_{p.t.}$, the expansion in the ratio of time scales is justified for the triple correlation. Changes in $\overline{u_i u_j}$ for a shear flow can occur no faster than its rate of production. Hence,

$$\tau_{\overline{u_i u_j}} \sim \frac{q^2}{-2\,\overline{u_1 u_2}\,\frac{\partial U_1}{\partial x_2}} \sim 3.5\left(\frac{\partial U_1}{\partial x_2}\right)^{-1}$$

The dissipation rate, on the other hand, is governed by the turbulence-turbulence interaction. Hence,

$$\tau_\varepsilon \sim q^2/(\varepsilon\, B_{11})$$

where B_{11} will be shown later to be approximately equal to 4. With the previous estimate for ε, τ_ε becomes

$$\tau_\varepsilon \sim \frac{7}{B_{11}}\left(\frac{\partial U_1}{\partial x_2}\right)^{-1}$$

Thus, $\overline{u_i u_j}$ and ε have approximately the same characteristic evolution times. τ_c and $\tau_{p.t.}$ may also be evaluated on the basis of the estimates (22) and (23). For the x_2-component of turbulent energy flux, (23a) gives

$$\tau_{p.t.} \sim 0.52 \left(\frac{\partial U_1}{\partial x_2}\right)^{-1}$$

while (23b) gives, for the boundary-layer,

$$\tau_{p.t.} \sim 0.15 \left(\frac{\partial U_1}{\partial x_2}\right)^{-1}$$

For both (23a) and (23b)

$$\tau_c \sim \frac{q^4}{\varepsilon} \frac{\partial q^2}{\partial x_2} \Big/ U_j \frac{\partial}{\partial x_j} \left(\frac{q^4}{\varepsilon} \frac{\partial q^2}{\partial x_2}\right)$$

With these estimates, the ratio of characteristic times for the evolution of $\overline{u_i u_j u_k}$ and $\overline{u_i u_j}$ (or ε) may be compared. For (23a), the result is

$$\frac{\tau_{p.t.}}{\tau_{\overline{u_i u_j}}} \sim 0.15 \qquad (24a)$$

while, for (23b) we find

$$\frac{\tau_{p.t.}}{\tau_{\overline{u_i u_j}}} \sim 0.04 \qquad (24b)$$

These estimates indicate that, for the class of flows characterized by (23a) (i.e. mixing-layers, wakes, etc.), the triple-velocity correlation adjusts to changes in the turbulence field between five

and ten times faster than $\overline{u_i u_j}$ (or ε) can change; for the boundary-layer class of flows $\overline{u_i u_j u_k}$ adjusts about 20 times faster than the turbulence characteristics can change. Hence, an approximation for $\overline{u_i u_j u_k}$ based on expansion about instantaneous values for $\overline{u_i u_j}$ and ε is clearly justified. Indeed, at least for flows of the boundary-type, we may expect to be able to truncate the expansion without inclusion of any dependence on time derivatives of $\overline{u_i u_j}$ or ε.

A comparison of the characteristic production time for $\overline{u_i u_j u_k}$ with the convection scale, τ_c, gives

$$\frac{\tau_{p.t.}}{\tau_c} \sim \frac{0.07\ U_j \frac{\partial}{\partial x_j}\left(\frac{q^4}{\varepsilon}\frac{\partial q^2}{\partial x_2}\right)}{q^2 \frac{\partial q^2}{\partial x_2}} \tag{24c}$$

for (23a), and

$$\frac{\tau_{p.t.}}{\tau_c} \sim \frac{0.02\ U_j \frac{\partial}{\partial x_j}\left(\frac{q^4}{\varepsilon}\frac{\partial q^2}{\partial x_2}\right)}{q^2 \frac{\partial q^2}{\partial x_2}} \tag{24d}$$

for (23b). Thus, the convective time scale will be much larger than the characteristic time for $\overline{u_i u_j u_k}$, even for substantial streamwise gradients. In particular, if as in (24a), 0.15 is assumed to be small, then the condition $\tau_c >> \tau_{p.t.}$ requires that streamwise variations in the turbulence occur on a length scale, L, such that

$$L \gtrsim 3.5\ U_1 \left(\frac{\partial U_1}{\partial x_2}\right) \tag{25}$$

For boundary-layer-like flows, an even smaller value of L can be accommodated. Thus, if the length scale for streamwise changes in the turbulence exceeds the transverse length scale of the mean velocity field by a factor of 3.5, convective terms in the evolution equation (20) for $\overline{u_i u_j u_k}$ may be neglected as a first approximation, compared to the production terms. Clearly, subject to the approximations in (23), the Reynolds stress has a length scale for streamwise change which is bounded from below by

$$L_{\overline{u_i u_j}} \gtrsim U_1 \, \tau_{\overline{u_i u_j}} = 3.5 \, U_1 \left(\frac{\partial U_1}{\partial x_2}\right)^{-1}$$

Thus, in a Lagrangian framework, the examination of characteristic time scales also provides some evidence to support the assumption that $\overline{u_i u_j u_k}$ may be expressed as a function of *spatially local variables*. A more thorough analysis of the spatial dependence would entail a comparison of the turbulent diffusion term,

$$\frac{\partial \overline{u_i u_j u_k u_\ell}}{\partial x_j} ,$$

and the pressure velocity correlation term,

$$\overline{\frac{\partial p}{\partial x_i} u_k u_\ell} ,$$

to the production terms. However, since estimates of these quantities are not available, such a comparison cannot be made.

It would be desirable to examine the validity of the instantaneous and local assumption for the unknown correlations in the

dissipation equation also. However, due to the complexity of the equations which govern these terms, such an analysis is *extremely* complex and has not been undertaken at this time.

C. The Concept of Invariant Modeling

In the previous section, we have discussed the hypotheses of instantaneity and limited awareness, which allow the unknown third-order moments at a space-time point, ($\underline{x}$, b), to be expressed as functions only of $\overline{u_i u_j}$, ε and their lowest order spatial derivatives at the same point. To implement this approximation, it is necessary to adopt a systematic scheme for generating the most general form for these functions at each level of approximation. To achieve this, each unknown moment is expressed as a power series expansion about the homogeneous, isotropic state, with the expansion ordered in terms of increasing degrees of inhomogeneity and anisotropy, as proposed by Lumley and Khajeh-Nouri (1973).

To obtain the power series representation, it is essential that orders of magnitude be systematically assigned to terms so that each may be included at the appropriate order. To this end, $\overline{u_i u_j}$ is decomposed into its isotropic and anisotropic components, a_{ij} and $q^2/3\ \delta_{ij}$, respectively where

$$a_{ij} = \overline{u_i u_j} - q^2/3\ \delta_{ij}$$

is the deviatoric component of the Reynolds stress tensor. This decomposition is useful since, now, for isotropic turbulence, $a_{ij} = 0$,

$\varepsilon \neq 0$ and $q^2 \neq 0$. Thus one can assign an *'order of anisotropy'* to each term, i.e.

zero order terms: ε, q^2, $\frac{\partial^n \varepsilon}{\partial x_k{}^n}$, etc.

first order terms: a_{ij}, $\frac{\partial^n a_{ij}}{\partial x_k{}^n}$, etc.

second order terms: $a_{ik}a_{kj}$, $a_{ik}\frac{\partial^n a_{kj}}{\partial x_\ell{}^n}$, etc.

Higher degrees of inhomogeneity are characterized by higher order spatial derivatives of q^2, ε and a_{ij}. For example, the term $\frac{\partial^2 a_{ij}}{\partial x_k{}^2}$ is first order in anisotropy and second order in inhomogeneity. To simplify the following discussion, the notation '0(n,m)' will be used to designate a term of order n in anisotropy and order m in inhomogeneity.

Finally, to establish the most general way in which each term (for example q^2, ε, a_{ij}, $\frac{\partial^2 a_{ij}}{\partial x_k{}^2}$, etc.) can enter the expansion in inhomogeneity and anisotropy, the method of invariant modeling is employed. This approach has been used extensively to develop the theory of homogeneous, isotropic turbulence (c.f. Robertson (1940), Batchelor (1953) and Hinze (1959)) and in the derivation of constitutive relations for non-Newtonian fluids (Coleman and Noll (1961)). Lumley (1970), Donaldson (1972), Daly and Harlow (1970) and Hanjalic and Launder (1972b) have also used this technique to some extent in the development of their turbulence transport models. However, none

of the above authors has pursued this technique to the extent proposed by Lumley et al. (1973). It is the latter work which forms the basis of our own analysis.

The basic requirement for a satisfactory invariant model is that the tensor rank, symmetry properties and dimensionality of the model be identical with those of the higher order moments that the model represents. In the present case for which the model takes the form of an infinite series, each term in the series must satisfy these requirements. In addition, the scalar coefficients which enter the series must be invariant under general transformations of the coordinate system. Lumley (1970) presented a straightforward method of generating terms which satisfy these requirements. For convenience, a short discussion of invariant modeling and the relevant symbols to be used in what follows, has been included in Appendix B.

D. Closure of Reynolds Stress Tensor Equation

Since the method of invariant modeling considers only the tensor order, symmetry properties and dimensionality of a term, it is convenient (with no loss of generality) to lump together moments which have the same tensor character, and to model them as a single moment. Hence, it is convenient to rewrite equation (12) in the form

$$\frac{D\overline{u_i u_j}}{Dt} = -\overline{u_i u_k}\frac{\partial U_j}{\partial x_k} - \overline{u_j u_k}\frac{\partial U_i}{\partial x_k} - \frac{\partial}{\partial x_k}\left(\overline{u_i u_j u_k} + \frac{2}{3}\frac{1}{\rho}\overline{u_k p}\delta_{ij}\right) -$$

Term (1)

$$\overline{(u_j \frac{\partial p}{\partial x_i}} + \overline{u_i \frac{\partial p}{\partial x_j}} - \frac{2}{3} \frac{\overline{\partial u_k p}}{\partial x_k} \delta_{ij})/\rho \quad - \frac{2}{3} \varepsilon \delta_{ij} \tag{26}$$

Term (2)

With this regrouping, each term is amenable to direct physical interpretation. Term (1) represents the turbulent diffusion of $\overline{u_i u_j}$ due to both velocity and pressure fluctuations. Term (2) (henceforth to be denoted A_{ij}) expresses the rate of intercomponent transfer of turbulence energy. Champagne, Harris and Corrsin (1970) interpret the off-diagonal elements of Term (2) as diffusion and production (or dissipation) of turbulent shear stress, by the interaction of pressure and velocity fluctuations. It has often been noted (c.f. Tennekes and Lumley (1972)) that this term always tends to drive the turbulence toward the isotropic state. Hence, it is generally referred to as either the 'tendency-toward-isotropy' term or the 'intercomponent energy transfer term.'

The tendency-toward-isotropy term is a second order, symmetric tensor, with vanishing trace. To second order in anisotropy, its homogeneous representation may be deduced from the discussion in Appendix B to be

$$A_{ij} = g_1 \delta_{ij} + g_2 a_{ij} + g_3 a_{ik} a_{kj} \tag{27}$$

where the coefficient functions, g_i, must be chosen to achieve dimensional consistency and to ensure $A_{ij} = 0$. These conditions are satisfied by the choice

$$A_{ij} = \frac{\varepsilon}{cq^2}\left\{ f_2\left(\frac{II}{q^4},\frac{III}{q^6}\right) a_{ij} + f_3\left(\frac{II}{q^4},\frac{III}{q^6}\right)\left(a_{ik}a_{kj} - \frac{II}{3}\delta_{ij}\right)/q^2 \right\}$$

where II and III are respectively the second and third invariants of a_{ij} and $T = cq^2/\varepsilon$ is the time scale which characterizes the return to isotropy of mildly anisotropic turbulence. In general, the functionality of f_2 and f_3 may be very complex. However, even for strongly anisotropic turbulence, such as that which characterizes turbulent boundary-layers, II/q^4 and III/q^6 are very small. For example, in a turbulent boundary-layer (c.f. Klebanoff, (1955)) approximation (23b) is appropriate so that, by direct calculation, we find $II/q^4 \sim 0.15$ and $III/q^6 \sim 0.01$. Hence, it should be possible to expand the functions f_2 and f_3 as Taylor series about the isotropic state, $II/q^4 = III/q^6 = 0$ and thereby achieve a reasonable approximation to the true functionality, even for significant anisotropy.

Once the functions f_2 and f_3 have been expanded, it follows directly from the discussion in Appendix B (c.f. equation B-8) that equation (27) is, in fact, correct to 0(3,0)

$$A_{ij} = -\frac{\varepsilon}{cq^2}\left\{(1.0 + B_1\frac{II}{q^4})\, a_{ij} + \frac{B_2}{q^2}\left(a_{ik}a_{kj} - \frac{II}{3}\delta_{ij}\right)\right\} \quad (28)$$

where, in the context of the Taylor series expansion,

$$f_2(0,0) = 1.0 \ ,$$

$$\left.\frac{\partial f_2}{\partial (II/q^4)}\right|_{0,0} = B_1$$

and

$$f_3(0,0) = B_2$$

Rotta (1951) originally suggested the 0(1,0) form of equation (28) with $c \sim 1/5$. Lumley et al. (1973) propose $c \sim 1/8$. Virtually all models which include equations for each of the Reynolds stress components have included the 0(1,0) term.

Equation (28) provides only the *homogeneous* form of the intercomponent transfer model. For inhomogeneous flows, the expansion strategy requires that derivatives of q^2, a_{ij} and ε be included in the functionality. It can easily be shown that, in the absence of buoyancy, one cannot construct terms of first order in inhomogeneity which are tensorially appropriate for the intercomponent transfer. However, at second order in inhomogeneity, and correct to first order in anisotropy there are 24 possible contributions. The terms which must be added to equation (28) to make it correct to 0(1,2)[†] are:

[†]Although only 0(0,2) and 0(1,2) *inhomogeneous* terms will be examined, all of the terms, to 0(3,0), in equation (28) will be included in the comparisons which follow in sections 3 and 4.C.

$$\gamma_1 \frac{q^4}{\varepsilon}\left\{\frac{\partial^2 q^2}{\partial x_i \partial x_j} - \frac{\delta_{ij}}{3}\frac{\partial^2 q^2}{\partial x_k \partial x_k}\right\} + \gamma_2 \frac{q^6}{\varepsilon^2}\left\{\frac{\partial^2 \varepsilon}{\partial x_i \partial x_j} - \frac{\delta_{ij}}{3}\frac{\partial^2 \varepsilon}{\partial x_k \partial x_k}\right\} +$$

$$\gamma_3 \frac{q^4}{\varepsilon^2}\left(\frac{\partial \varepsilon}{\partial x_i}\frac{\partial q^2}{\partial x_j} + \frac{\partial \varepsilon}{\partial x_j}\frac{\partial q^2}{\partial x_i} - \frac{2}{3}\delta_{ij}\frac{\partial \varepsilon}{\partial x_k}\frac{\partial q^2}{\partial x_k}\right) + \gamma_4 \frac{q^2}{\varepsilon}\left(\frac{\partial q^2}{\partial x_i}\frac{\partial q^2}{\partial x_j} -\right.$$

$$\left.\frac{\delta_{ij}}{3}\frac{\partial q^2}{\partial x_k}\frac{\partial q^2}{\partial x_k}\right) + \gamma_5 \frac{q^6}{\varepsilon^3}\left(\frac{\partial \varepsilon}{\partial x_i}\frac{\partial \varepsilon}{\partial x_j} - \frac{\delta_{ij}}{3}\frac{\partial \varepsilon}{\partial x_k}\frac{\partial \varepsilon}{\partial x_k}\right) + \left(\gamma_6 \frac{q^2}{\varepsilon}\frac{\partial^2 q^2}{\partial x_k \partial x_k} +\right.$$

$$\left.\gamma_7 \frac{q^4}{\varepsilon^2}\frac{\partial^2 \varepsilon}{\partial x_k \partial x_k} + \gamma_8 \frac{1}{\varepsilon}\frac{\partial q^2}{\partial x_k}\frac{\partial q^2}{\partial x_k} + \gamma_9 \frac{q^2}{\varepsilon^2}\frac{\partial q^2}{\partial x_k}\frac{\partial \varepsilon}{\partial x_k} + \gamma_{10}\frac{q^4}{\varepsilon^3}\frac{\partial \varepsilon}{\partial x_k}\frac{\partial \varepsilon}{\partial x_k}\right) a_{ij}$$

$$+ \gamma_{11}\frac{q^2}{\varepsilon}\left(a_{ik}\frac{\partial^2 q^2}{\partial x_k \partial x_j} + a_{jk}\frac{\partial^2 q^2}{\partial x_k \partial x_i} - \frac{2}{3}\delta_{ij}\, a_{\ell k}\frac{\partial^2 q^2}{\partial x_\ell \partial x_k}\right) +$$

$$\gamma_{12}\frac{q4}{\varepsilon^2}\left(a_{ik}\frac{\partial^2 \varepsilon}{\partial x_k \partial x_j} + a_{jk}\frac{\partial^2 \varepsilon}{\partial x_k \partial x_i} - \frac{2}{3}\delta_{ij}\, a_{\ell k}\frac{\partial^2 \varepsilon}{\partial x_k \partial x_\ell}\right) + \gamma_{13}\frac{q^2}{\varepsilon^2}$$

$$\left(a_{ik}\frac{\partial \varepsilon}{\partial x_k}\frac{\partial q^2}{\partial x_j} + a_{jk}\frac{\partial \varepsilon}{\partial x_k}\frac{\partial q^2}{\partial x_j} - \frac{2}{3}\delta_{ij}\, a_{\ell k}\frac{\partial \varepsilon}{\partial x_k}\frac{\partial q^2}{\partial x_\ell}\right) + \gamma_{14}\frac{1}{\varepsilon}$$

$$\left(a_{ik}\frac{\partial q^2}{\partial x_k}\frac{\partial q^2}{\partial x_j} + a_{jk}\frac{\partial q^2}{\partial x_k}\frac{\partial q^2}{\partial x_i} - \frac{2}{3}\delta_{ij}\, a_{\ell k}\frac{\partial q^2}{\partial x_k}\frac{\partial q^2}{\partial x_\ell}\right) + \gamma_{15}\frac{q^4}{\varepsilon^3}\left(a_{ik}\right.$$

$$\left.\frac{\partial \varepsilon}{\partial x_k}\frac{\partial \varepsilon}{\partial x_j} + a_{jk}\frac{\partial \varepsilon}{\partial x_k}\frac{\partial \varepsilon}{\partial x_i} - \frac{2}{3}\delta_{ij}\, a_{\ell k}\frac{\partial \varepsilon}{\partial x_\ell}\frac{\partial \varepsilon}{\partial x_k}\right) + \gamma_{16}\frac{q^4}{\varepsilon}\frac{\partial^2 a_{ij}}{\partial x_k \partial x_k} +$$

$$\gamma_{17}\frac{q^4}{\varepsilon}\left(\frac{\partial^2 a_{i\ell}}{\partial x_\ell \partial x_j} + \frac{\partial^2 a_{k\ell}}{\partial x_\ell \partial x_i} - \frac{2}{3}\delta_{ij}\frac{\partial^2 a_{k\ell}}{\partial x_\ell \partial x_k}\right) + \gamma_{18}\frac{q^2}{\varepsilon}\frac{\partial a_{ij}}{\partial x_k}\frac{\partial q^2}{\partial x_k} +$$

$$\gamma_{19} \frac{q^2}{\varepsilon} \left(\frac{\partial a_{ik}}{\partial x_j} \frac{\partial q^2}{\partial x_k} + \frac{\partial a_{jk}}{\partial x_i} \frac{\partial q^2}{\partial x_k} - \frac{2}{3} \delta_{ij} \frac{\partial a_{\ell k}}{\partial x_\ell} \frac{\partial q^2}{\partial x_k} \right) + \gamma_{20} \frac{q^2}{\varepsilon}$$

$$\left(\frac{\partial a_{ik}}{\partial x_k} \frac{\partial q^2}{\partial x_j} + \frac{\partial a_{jk}}{\partial x_k} \frac{\partial q^2}{\partial x_i} - \frac{2}{3} \delta_{ij} \frac{\partial a_{\ell k}}{\partial x_k} \frac{\partial q^2}{\partial x_\ell} \right) + \gamma_{21} \frac{q^4}{\varepsilon^2} \frac{\partial a_{ij}}{\partial x_k} \frac{\partial \varepsilon}{\partial x_k} +$$

$$\gamma_{22} \frac{q^4}{\varepsilon^2} \left(\frac{\partial a_{ik}}{\partial x_j} \frac{\partial \varepsilon}{\partial x_k} + \frac{\partial a_{jk}}{\partial x_i} \frac{\partial \varepsilon}{\partial x_k} - \frac{2}{3} \delta_{ij} \frac{\partial a_{\ell k}}{\partial x_\ell} \frac{\partial \varepsilon}{\partial x_k} \right) + \gamma_{23} \frac{q^4}{\varepsilon^2}$$

$$\left(\frac{\partial a_{ik}}{\partial x_k} \frac{\partial \varepsilon}{\partial x_j} + \frac{\partial a_{jk}}{\partial x_i} \frac{\partial \varepsilon}{\partial x_k} - \frac{2}{3} \delta_{ij} \frac{\partial a_{\ell k}}{\partial x_\ell} \frac{\partial \varepsilon}{\partial x_k} \right) + \gamma_{24} \frac{q^2}{\varepsilon^2} \left(a_{ik} \frac{\partial q^2}{\partial x_k} \frac{\partial \varepsilon}{\partial x_j} + \right.$$

$$\left. a_{ik} \frac{\partial q^2}{\partial x_k} \frac{\partial \varepsilon}{\partial x_i} - \frac{2}{3} \delta_{ij} a_{\ell k} \frac{\partial q^2}{\partial x_k} \frac{\partial \varepsilon}{\partial x_\ell} \right) \qquad (29)$$

In addition to the terms given in (29) there are 53 possible terms at O(2,2). Combined with the terms already given in (29), this leads to a completely unmanageable number of unknown parameters. However, we found it unnecessary to include these O(2,2) terms, since, as will be demonstrated in section 3.C, the terms in (29) seem to account adequately for the inhomogeneous contributions.

To facilitate the quantitative comparisons to be presented at various stages of the present work, it is useful to examine the models of intercomponent transfer which have been proposed by other authors. Wyngaard, Coté and Rao (1973) use the model

$$A_{\alpha\beta} = - a_{\alpha\beta} c_{\alpha\beta} \varepsilon / q^{2*} \qquad (30)$$

*Throughout the thesis, repeated Greek symbols are not summed.

where $c_{11} = c_{22} = c_{33} = 6.7$ and $c_{12} = c_{21} = 13.2$. This form for the intercomponent transfer model was motivated by the idea that the rate of intercomponent transfer should be proportional to the deviation from anisotropy, coupled with the requirement that the model should correctly predict the Reynolds stress distribution in the hypothetical, constant stress layer. To achieve this, Wyngaard et al. found it necessary to use coefficients of proportionality which were different for diagonal and off-diagonal elements. Clearly, this model is *not* invariant under a rotation of the coordinate system. Hence, this model cannot be universal.

Daly (1974) presented a more recent version of the model proposed by Daly and Harlow (1970). The high Reynolds number form is

$$A_{ij} = -\frac{\varepsilon}{q^2}\left(3-2\,\frac{\overline{u_k u_\ell}}{\varepsilon}\frac{\partial U_k}{\partial x_\ell}\right) a_{ij} - 0.2\left(\overline{u_i u_k}\frac{\partial U_k}{\partial x_j} + \overline{u_j u_k}\frac{\partial U_k}{\partial x_i} - \overline{u_i u_k}\frac{\partial U_j}{\partial x_k} - \overline{u_j u_k}\frac{\partial U_i}{\partial x_k}\right) + 0.035\,\frac{q^4}{\varepsilon}\left(\frac{1}{3}\,\overline{u_k u_m}\,n_k n_m\,\delta_{ij} - \frac{1}{2}\,\overline{u_i u_k}\,n_k n_j - \frac{1}{2}\,\overline{u_j u_k}\,n_i n_k\right)\psi(\bar{r}) \qquad (31)$$

where $\bar{n}$ is a unit vector, normal to the solid surface. The final term is referred to as the 'wall-effect-tensor' by the authors. It is meant to account for intercomponent transfer induced by wall-turbulence interactions of the type described by the surface integral in equation (17). In this term, $\psi(\bar{r})$ is a scalar function which depends on a position and wall geometry. It is hypothesized to be a

surface integral of the form

$$\psi(\bar{r}) = \frac{1}{\pi}\int \frac{1}{|\bar{r} - \bar{r}'|^4}\, ds$$

where $\bar{r}$ is a position vector, $\bar{r}'$ is the wall vector and ds is the unit area of wall surface at $\bar{r}'$. For a horizontal flat surface

$$\psi(\bar{r}) = \left(\frac{1}{\bar{n} \cdot \bar{r}}\right)^2$$

Our discussion concerning equation (17) suggested that the inclusion of such dependence on the boundary conditions is not required in the region away from the walls. However, in the context of our high Reynolds number expansion, with its associated 'inner' and 'outer' solutions, such effects may appear in the 'inner' (or wall) region. For the flows that will be discussed in section 4.C, the wall-effect term contributes only a negligible correction to equation (31) in the outer region.

Hanjalic and Launder (1972b) propose the model

$$A_{ij} = -5.6\,\frac{\varepsilon}{q^2}\,a_{ij} + \phi_{ij} + \phi_{ji} \qquad (32)$$

where

$$\phi_{ij} = (\alpha\,\overline{u_m u_i}\,\delta_{\ell j} + \beta\,(\overline{u_m u_\ell}\,\delta_{ij} + \overline{u_m u_j}\,\delta_{i\ell} + \overline{u_i u_\ell}\,\delta_{mj}) +$$

$$(\gamma\,\delta_{mi}\,\delta_{\ell j} + \eta(\delta_{m\ell}\,\delta_{ij} + \delta_{mj}\,\delta_{i\ell}))q^2 + \nu(\overline{u_m u_j}\,\overline{u_i u_\ell} +$$

$$\overline{u_m u_\ell}\,\overline{u_i u_j})/q^2 + c_2\,\overline{u_m u_i}\,\overline{u_\ell u_j}/q^2)\,\frac{\partial U_\ell}{\partial x_m},$$

$$c_2 = -\nu = 0.90,\ \alpha = 0.0582,\ \beta = -0.07,\ \gamma = -1.27 \times 10^{-3}$$

and $\eta = -1.91 \times 10^{-3}$. The form of this model resulted from an approximate closure of the first integral in equation (17). The two free coefficients which resulted were chosen to match the downstream Reynolds stress distribution in Champagne, Harris and Corrsin's (1970) homogeneous shear flow (c.f. section 3.A). The remaining model coefficients are related to these two by the tensor character of equation (17).

Finally, Shir (1973) adopted various components of his turbulence model from Donaldson (1972), Reynolds (1970), and Daly and Harlow (1970). The final form proposed for the intercomponent transfer term is

$$A_{ij} = -7.0 \frac{\varepsilon}{q^2} a_{ij} + 0.5 \left(\overline{u_i u_k} \frac{\partial U_j}{\partial x_k} + \overline{u_j u_k} \frac{\partial U_i}{\partial x_k} - \frac{2}{3} \delta_{ij} \right.$$

$$\left. \overline{u_\ell u_m} \frac{\partial U_\ell}{\partial x_m}\right) + 0.035 \frac{q^4}{\varepsilon} \left(\frac{1}{3} \overline{u_k u_m} n_k n_m \delta_{ij} - \frac{1}{2} \overline{u_i u_k} \right.$$

$$\left. n_k n_j - \frac{1}{2} \overline{u_j u_k} n_i n_k \right) \psi (\bar{r}) \qquad (33)$$

The wall effect term is identical to that proposed by Daly and Harlow. It should be noted here that Daly and Harlow, and Shir include in their models an *anisotropic dissipation rate*, with the anisotropy being of O(1) with respect to Reynolds number, of the form

$$D_{ij} = \frac{\varepsilon}{3} \delta_{ij} + c_3 \varepsilon \frac{a_{ij}}{q^2}$$

Such a term is clearly not compatible with the high Reynolds number

form of the dissipation tensor discussed in section 2.A.[†] However, since the anisotropic component of D_{ij} can easily be retained in the return to isotropy term (as a return to isotropy contribution), it has been included in equations (31) and (33) as a contribution to intercomponent transfer.

The most obvious difference between the above models and that of equations (28) and (29) is that all of the former models include explicit dependence on the mean velocity field. Such dependence was not included in the present model, and we have argued that it is not required providing a given Reynolds stress distribution defines a unique mean velocity field. In that case, any dependence on the mean velocity field is included implicitly through dependence on $\overline{u_i u_j}$ and ε. All of the models have used basically the same 'first order in anisotropy' term, which is formed as the product of the reciprocal characteristic time for return to isotropy and the tensor a_{ij}, which describes the deviation from anisotropy. Whereas Wyngaard et al., Shir, and Hanjalic and Launder proposed a reciprocal time which is proportional to ε/q^2, Daly and Harlow adopted a slightly different reciprocal time which is meant to account, to some extent, for the effect of non-equilibrium (i.e. $\overline{u_i u_k} \frac{\partial U_i}{\partial x_k} \neq -\varepsilon$) on the rate of return to isotropy. They use

$$\left\{ 3. - 2 \frac{\overline{u_k u_\ell}}{\varepsilon} \frac{\partial U_k}{\partial x_\ell} \right\} \varepsilon/q^2$$

[†]This incompatability was previously noted by Corrsin (1973).

This can be compared with equation (28) which includes the same effect in the term

$$\left(1 + B_1 \frac{II}{q^4} \right) \varepsilon/cq^2$$

A more quantitative comparison of models (30) - (33) with the present model (28) and (29) will be presented in sections 3.C and 4.C.

The other term which must be modeled in equation (26) is the diffusion term

$$F_{ijk} = \left(\overline{u_i u_j u_k} + \frac{2}{3} \frac{1}{\rho} \delta_{ij} \overline{p u_k} \right)$$

Lumley et al. (1973) have proposed that the closure model be applied directly for F_{ijk}, which is symmetric in i and j but not in k. However, a closer examination of this term indicates that the two parts exhibit different symmetry properties. The first term $(\overline{u_i u_j u_k})$ is symmetric in all three subscripts, while the second, $(\frac{2}{3} \frac{1}{\rho} \delta_{ij} \overline{p u_k})$ is symmetric only in i and j. Hence, we suggest that each part of the diffusion term should be modeled separately. This is particularly desirable since $\overline{u_i u_j u_k}$ can be measured directly to allow the determination of its model parameters by direct comparison with experimental data.

For the triple-velocity correlation, there are no homogeneous contributions. To zero order in anisotropy, it can be a function only of $\partial q^2/\partial x_\ell$, $\partial \varepsilon/\partial x_\ell$, q^2 and ε. Hence, at O(0,1) it takes the form

$$\overline{u_i u_j u_k} = \alpha_1 \frac{q^4}{\varepsilon} M_{ijk\ell} \frac{\partial q^2}{\partial x_\ell} + \alpha_3 \frac{q^6}{\varepsilon^2} M_{ijk\ell} \frac{\partial \varepsilon}{\partial x_\ell}$$

where $M_{ijk\ell}$ is the most general fourth order tensor that can be constructed from δ_{ij} and that is symmetric in i, j and k,

$$M_{ijk\ell} = (\delta_{ij} \delta_{k\ell} + \delta_{ik} \delta_{j\ell} + \delta_{kj} \delta_{i\ell})$$

The next corrections enter at 0 (1,1) and must be constructed from a_{ij}, $\frac{\partial a_{ij}}{\partial x_k}$, $\frac{\partial q^2}{\partial x_k}$ and $\frac{\partial \varepsilon}{\partial x_k}$. The most general form, correct to 0 (2,1) is

$$\overline{u_i u_j u_k} = \frac{q^4}{\varepsilon} (\alpha_1 + \alpha_2 \frac{II}{q^4}) M_{ijk\ell} \frac{\partial q^2}{\partial x_\ell} + \frac{q^6}{\varepsilon^2} (\alpha_3 + \alpha_4 \frac{II}{q^4}) M_{ijk\ell} \frac{\partial \varepsilon}{\partial x_\ell}$$

$$+ \frac{q^4}{\varepsilon} (\alpha_5 (\frac{\partial a_{ik}}{\partial x_j} + \frac{\partial a_{ij}}{\partial x_k} + \frac{\partial a_{kj}}{\partial x_i}) + \alpha_6 (\delta_{ik} \frac{\partial a_{jp}}{\partial x_p} + \delta_{ij} \frac{\partial a_{kp}}{\partial x_p} +$$

$$\delta_{jk} \frac{\partial a_{ip}}{\partial x_p})) + \frac{q^2}{\varepsilon} (\alpha_7 (\delta_{ik} a_{j\ell} + \delta_{ij} a_{k\ell} + \delta_{jk} a_{i\ell}) + \alpha_8$$

$$(a_{ik} \delta_{j\ell} + a_{ij} \delta_{k\ell} + a_{jk} \delta_{i\ell})) \frac{\partial q^2}{\partial x_\ell} + \frac{q^4}{\varepsilon^2} (\alpha_9 (\delta_{ik} a_{j\ell} +$$

$$\delta_{ij} a_{k\ell} + \delta_{jk} a_{i\ell}) + \alpha_{10} (a_{ik} \delta_{j\ell} + a_{ij} \delta_{k\ell} + a_{jk} \delta_{i\ell})) \frac{\partial \varepsilon}{\partial x_\ell}$$

$$+ \alpha_{11} \frac{q^2}{\varepsilon} (a_{i\ell} \frac{\partial a_{\ell k}}{\partial x_j} + a_{k\ell} \frac{\partial a_{\ell i}}{\partial x_j} + a_{j\ell} \frac{\partial a_{\ell k}}{\partial x_i} + a_{j\ell} \frac{\partial a_{\ell i}}{\partial x_k} + a_{k\ell}$$

$$\frac{\partial a_{\ell j}}{\partial x_i} + a_{i\ell} \frac{\partial a_{\ell j}}{\partial x_k}) + \alpha_{12} \frac{q^2}{\varepsilon} (a_{ik} \frac{\partial a_{j\ell}}{\partial x_\ell} + a_{ij} \frac{\partial a_{k\ell}}{\partial x_\ell} + a_{kj} \frac{\partial a_{i\ell}}{\partial x_\ell})$$

$$+ \alpha_{13} \frac{q^2}{\varepsilon} (a_{\ell j} \frac{\partial a_{ik}}{\partial x_\ell} + a_{\ell i} \frac{\partial a_{jk}}{\partial x_\ell} + a_{\ell k} \frac{\partial a_{ij}}{\partial x_\ell}) + (a_{ik} a_{j\ell} +$$

$$a_{ij} a_{k\ell} + a_{jk} a_{i\ell}) (\frac{\alpha_{14}}{\varepsilon} \frac{\partial q^2}{\partial x_\ell} + \frac{\alpha_{15}}{\varepsilon^2} q^2 \frac{\partial \varepsilon}{\partial x_\ell}) + (\delta_{ik} a_{jm} a_{m\ell} +$$

$$\delta_{ij}\, a_{km}a_{m\ell} + \delta_{jk}\, a_{im}a_{m\ell})\left(\frac{\alpha_{16}}{\varepsilon}\,\frac{\partial q^2}{\partial x_\ell} + \frac{\alpha_{17}}{\varepsilon^2}\, q^2\,\frac{\partial \varepsilon}{\partial x_\ell}\right) + (a_{im}a_{mk}$$

$$\delta_{j\ell} + a_{im}a_{mj}\,\delta_{k\ell} + a_{jm}a_{mk}\,\delta_{i\ell})\left(\frac{\alpha_{18}}{\varepsilon}\,\frac{\partial q^2}{\partial x_\ell} + \frac{\alpha_{19}}{\varepsilon^2}\, q^2\,\frac{\partial \varepsilon}{\partial x_\ell}\right) \quad (34)$$

Terms in equation (34) have only been included to O(2,1). However, since the next contributions enter at third order in inhomogeneity (in the absence of buoyancy), this expression is, in fact, correct to O(2,2). Furthermore, since only the divergence of $\overline{u_i u_j u_k}$ enters the Reynolds stress equations, the representation is actually accurate to *third* order in inhomogeneity (i.e. to O(2,3)) once substituted into equation (26).

Once again, for the pressure velocity correlation, $\overline{pu_j}$, there are no homogeneous contributions in the absence of buoyancy. To O(2,2) the model is

$$\overline{pu_j} = (\beta_1 + \beta_2\,\frac{II}{q^4})\,\frac{q^4}{\varepsilon}\,\frac{\partial q^2}{\partial x_j} + (\beta_3 + \beta_4\,\frac{II}{q^4})\,\frac{q^6}{\varepsilon^2}\,\frac{\partial \varepsilon}{\partial x_j} + \beta_5\,\frac{q^4}{\varepsilon}$$

$$\frac{\partial a_{j\ell}}{\partial x_\ell} + \beta_6\,\frac{q^2}{\varepsilon}\,a_{j\ell}\,\frac{\partial q^2}{\partial x_\ell} + \beta_7\,\frac{q^4}{\varepsilon^2}\,a_{j\ell}\,\frac{\partial \varepsilon}{\partial x_\ell} + \beta_8\,\frac{1}{\varepsilon}\,a_{jk}\,a_{k\ell}$$

$$\frac{\partial q^2}{\partial x_\ell} + \beta_9\,\frac{q^2}{\varepsilon^2}\,a_{jk}\,a_{k\ell}\,\frac{\partial \varepsilon}{\partial x_\ell} + \beta_{10}\,\frac{q^4}{\varepsilon}\,a_{j\ell}\,\frac{\partial a_{\ell p}}{\partial x_p} + \beta_{11}$$

$$\frac{q^4}{\varepsilon}\,a_{\ell m}\,\frac{\partial a_{\ell m}}{\partial x_j} \quad (35)$$

It is true that this pressure-velocity correlation contributes to the spatial transport of Reynolds stress. However, the available experimental data shows that the magnitude of the contribution is often small.† In particular, of the four inhomogeneous flows that will be examined in section 4, only the data of Wygnanski and Fiedler (1970) exhibit a non-negligible contribution from this term. Certainly, the many coefficients in equation (35) cannot be evaluated on the basis of a single flow. Hence, it will be assumed that these coefficients are zero until further data, which exhibit a substantial pressure-diffusion contribution, are available for a more reliable parameter estimate.

At this point, it is interesting to compare the formulations for the diffusion term used in other models, with that of equation (34). Shir (1973) modeled this term by

$$\overline{u_i u_j u_k} = - 0.01 \frac{q^4}{\varepsilon} \frac{\partial \overline{u_i u_j}}{\partial x_k} ; \tag{36}$$

Wyngaard, Coté and Rao (1973) used the model

$$(\overline{u_i u_j u_k} + \frac{2}{3} \frac{1}{\rho} \delta_{ij} \overline{p u_k}) = -0.15 \frac{q^2}{\varepsilon} \overline{u_\ell u_k} \frac{\partial \overline{u_i u_j}}{\partial x_\ell} ; \tag{37}$$

Daly and Harlow (1970) adopted the form

---

†As was noted previously, pressure-velocity correlations are extremely difficult to measure experimentally. Hence, profiles of $\overline{pu_j}$ are not generally established by direct measurement. Instead, for flows in which *all* other correlations and mean quantities in equation (26) have been measured, $\partial \overline{pu_j}/\partial x_j$ may be estimated as the closing term of this equation.

$$\overline{u_i u_j u_k} = -1.0 \frac{q^2}{\varepsilon} \overline{u_k u_\ell} \frac{\partial \overline{u_i u_j}}{\partial x_\ell} ; \tag{38}$$

and, finally, Hanjalic and Launder (1972b) used the model

$$\overline{u_i u_j u_k} = -0.04 \frac{q^2}{\varepsilon} (\overline{u_\ell u_j} \frac{\partial \overline{u_i u_k}}{\partial x_\ell} + \overline{u_\ell u_k} \frac{\partial \overline{u_j u_k}}{\partial x_\ell}$$

$$+ \overline{u_\ell u_k} \frac{\partial \overline{u_i u_j}}{\partial x_\ell}) \tag{39}$$

Shir's formulation was motivated by the notion that, since the triple-velocity correlation can be interpreted as a turbulent flux of Reynolds stress, it should be possible to express it as the product of an eddy viscosity (q^4/ε) and the gradient of the Reynolds stress. The models of Wyngaard, Coté and Rao and Daly and Harlow can be viewed as a slight generalization of Shir's closure assumption, since they have simply replaced the scalar eddy viscosity by the tensor eddy viscosity ($\overline{u_k u_\ell}\, q^2/\varepsilon$) so that the flux in the k-direction depends on Reynolds stress gradients in all three directions. These three models have the common difficulty that they do not predict the correct symmetry for $\overline{u_i u_j u_k}$. (In the case of Wyngaard et al. this, of course, is subject to the observation that $\overline{u_k p}$ is often negligible.) Our previous discussion emphasized that $\overline{u_i u_j u_k}$ is symmetric in all three indices, whereas models (36) - (38) are symmetric only in i and j. Hanjalic and Launder obviously recognized this symmetry and derived model (39) by the approximate closure of equation (20). In this derivation they neglected the mean velocity-turbulence production term,

which seems to be a good first approximation on the basis of the analysis presented in section 2.B. However, the final form of their model rests squarely upon the validity of an *ad hoc* assumption which was made for the quadruple correlation term in equation (20).

Clearly, the model proposed in equation (34) is a generalization of the above models, since it can be reduced to the triply symmetric form of any of these models, by a suitable selection of coefficients. Also included in this formulation are other terms which have not been considered by the other authors. In section 4.B, it will be shown that only four coefficients in equation (34) appear to be important (i.e. non-zero) and that the resulting four parameter model better predicts the experimental distributions of $\overline{u_i u_j u_k}$ than do the existing models, (36) - (39).

E. Closure of the Energy Dissipation Equation

It is convenient to model the terms in equation (13) as two groups:

i) production and dissipation of ε by vortex stretching and viscosity

$$P = -2\nu\left[\overline{\frac{\partial u_j}{\partial x_\ell}\frac{\partial u_k}{\partial x_\ell}\frac{\partial u_j}{x_k}} + \nu\left[\overline{\left(\frac{\partial^2 u_j}{\partial x_k \partial x_k} \right)^2} \right] \right],$$

and ii) turbulent flux of ε due to velocity and pressure fluctuations

$$D_k = \nu\left[\overline{u_k \left(\frac{\partial u_j}{\partial x_\ell}\right)^2} + \frac{2}{\rho}\overline{\frac{\partial u_k}{\partial x_\ell}\frac{\partial p}{\partial x_\ell}} \right]$$

Subject to the series of assumptions outlined in section 2.B, the most general form for the scalar function P, correct to 0(3,1), is P_H

$$P_H = \frac{\varepsilon^2}{q^2}\left(B_{11} + B_{12}\frac{II}{q^4} + B_{13}\frac{III}{q^6}\right) \tag{40a}$$

Although the general strategy is to retain terms only to 0(2,2) we found it necessary to include terms in P_H to third order in anisotropy since, for homogeneous flows, the 0(3,0) term was found to be significant.

Once again, in the absence of buoyancy, there can be no terms of first order in inhomogeneity. However, at second order in inhomogeneity and correct to second order in anisotropy, there are 34 possible scalar invariants that can enter the functionality. Expanded in their Taylor series form, the inhomogeneous contribution to P, P_I, correct to 0(2,2) is

$$\begin{aligned} P_I = {} & \left(b_1 + b_{25}\frac{II}{q^4}\right)\frac{\partial q^2}{\partial x_k}\frac{\partial q^2}{\partial x_k} + \left(b_2 + b_{26}\frac{II}{q^4}\right)\frac{q^4}{\varepsilon^2}\frac{\partial \varepsilon}{\partial x_k}\frac{\partial \varepsilon}{\partial x_k} \\ & + \left(b_3 + b_{14}\frac{II}{q^4}\right) q^2 \frac{\partial^2 q^2}{\partial x_k \partial x_k} + \left(b_4 + b_{15}\frac{II}{q^4}\right)\frac{q^4}{\varepsilon}\frac{\partial^2 \varepsilon}{\partial x_k \partial x_k} \\ & + \left(b_5 + b_{16}\frac{II}{q^4}\right)\frac{q^2}{\varepsilon}\frac{\partial \varepsilon}{\partial x_k}\frac{\partial q^2}{\partial x_k} + b_6\frac{a_{ij}}{q^2}\frac{\partial q^2}{\partial x_i}\frac{\partial q^2}{\partial x_j} \\ & + b_7\, a_{ij}\frac{q^2}{\varepsilon^2}\frac{\partial \varepsilon}{\partial x_i}\frac{\partial \varepsilon}{\partial x_j} + b_8\, a_{ij}\frac{\partial^2 q^2}{\partial x_i \partial x_j} + b_9\frac{q^2}{\varepsilon}\, a_{ij}\frac{\partial^2 \varepsilon}{\partial x_i \partial x_j} \end{aligned}$$

$$b_{10} \frac{\partial a_{ip}}{\partial x_p} \frac{\partial q^2}{\partial x_i} + b_{11} \frac{q^2}{\varepsilon} \frac{\partial a_{ip}}{\partial x_p} \frac{\partial \varepsilon}{\partial x_i} + b_{12} q^2 \frac{\partial a_{jp}}{\partial x_j \partial x_p} + b_{13}$$

$$\frac{1}{\varepsilon} a_{ij} \frac{\partial \varepsilon}{\partial x_i} \frac{\partial q^2}{\partial x_j} + b_{17} \frac{a_{ik}a_{kj}}{q^4} \frac{\partial q^2}{\partial x_i} \frac{\partial q^2}{\partial x_j} + b_{18} \frac{a_{ik}a_{kj}}{q^2} \frac{\partial^2 q^2}{\partial x_i \partial x_j}$$

$$+ b_{19} \frac{a_{ik}a_{kj}}{\varepsilon} \frac{\partial^2 \varepsilon}{\partial x_i \partial x_j} + b_{20} \frac{\partial a_{ip}}{\partial x_p} \frac{\partial a_i}{\partial x_\ell} + b_{21} \frac{a_{ij}}{q^2} \frac{\partial q^2}{\partial x_k} \frac{\partial a_{ij}}{\partial x_k}$$

$$+ b_{22} \frac{a_{ij}}{\varepsilon} \frac{\partial \varepsilon}{\partial x_k} \frac{\partial a_{ij}}{\partial x_k} + b_{23} a_{ij} \frac{\partial^2 a_{ij}}{\partial x_k \partial x_k} + b_{24} a_{ij} \frac{\partial^2 a_{ip}}{\partial x_j \partial x_p}$$

$$+ b_{27} \frac{a_{ik}a_{kj}}{\varepsilon^2} \frac{\partial \varepsilon}{\partial x_i} \frac{\partial \varepsilon}{\partial x_j} + b_{28} \frac{a_{mk}a_{k\ell}}{\varepsilon q^2} \frac{\partial q^2}{\partial x_m} \frac{\partial \varepsilon}{\partial x_\ell} + b_{29} \frac{a_{pm}}{q^2}$$

$$\frac{\partial a_{mk}}{\partial x_p} \frac{\partial q^2}{\partial x_k} + b_{30} \frac{a_{k\ell}}{q^2} \frac{\partial a_{pk}}{\partial x_p} \frac{\partial q^2}{\partial x_\ell} + b_{31} \frac{\partial a_{kp}}{\partial x_\ell} \frac{\partial a_{kp}}{\partial x_\ell} + b_{32} \frac{\partial a_{kn}}{\partial x_\ell}$$

$$\frac{\partial a_{n\ell}}{\partial x_k} + b_{33} \frac{a_{k\ell}}{\varepsilon} \frac{\partial a_{pk}}{\partial x_p} \frac{\partial \varepsilon}{\partial x_\ell} + b_{34} \frac{a_{pm}}{\varepsilon} \frac{\partial a_{mk}}{\partial x_p} \frac{\partial \varepsilon}{\partial x_k} \qquad (40b)$$

In the absence of buoyancy, the diffusion term, D_k, contains no homogeneous terms. To 0(2,2), the most general representation is:

$$D_k = (d_1 + d_2 \frac{II}{q^4}) q^2 \frac{\partial q^2}{\partial x_k} + (d_3 + d_4 \frac{II}{q^4}) \frac{q^4}{\varepsilon} \frac{\partial \varepsilon}{\partial x_k} + d_5 q^2$$

$$\frac{\partial a_{k\ell}}{\partial x_\ell} + a_{k\ell} (d_6 \frac{\partial q^2}{\partial x_\ell} + d_7 \frac{q^2}{\varepsilon} \frac{\partial \varepsilon}{\partial x_\ell} + d_8 \frac{\partial a_{\ell p}}{\partial x_p}) + \frac{a_{kj}a_{j\ell}}{q^2}$$

$$(d_9 \frac{\partial q^2}{\partial x_\ell} + d_{10} \frac{q^2}{\varepsilon} \frac{\partial \varepsilon}{\partial x_\ell}) + d_{11} a_{\ell m} \frac{\partial a_{\ell m}}{\partial x_k} \qquad (41)$$

The analysis to establish the coefficients of the homogeneous term,

equation (40a), will be presented in section 3.C, and the analysis of the inhomogeneous contributions will be presented in section 4.D.

Other models which have been proposed to describe the dynamics of the dissipation are:

the model of Daly and Harlow (1970)

$$\frac{D\varepsilon}{Dt} = -\frac{\varepsilon^2}{q^2}\left(4. + 1.6\,\frac{\overline{u_i u_k}}{\varepsilon}\frac{\partial U_k}{\partial x_i}\right) + \frac{\varepsilon}{q^2}\frac{\partial}{\partial x_k}\frac{q^2}{\varepsilon}\overline{u_k u_\ell}\frac{\partial q^2}{\partial x_\ell} + \frac{\partial}{\partial x_k}\frac{q^2}{\varepsilon}\overline{u_k u_\ell}\frac{\partial \varepsilon}{\partial x_\ell}\,, \tag{42}$$

the model of Hanjalic and Launder (1972b)

$$\frac{D\varepsilon}{Dt} = -\frac{\varepsilon^2}{q^2}\left(4. + 2.9\,\frac{\overline{u_i u_k}}{\varepsilon}\frac{\partial U_k}{\partial x_i}\right) + 0.065\,\frac{\partial}{\partial x_k}\frac{q^2}{\varepsilon}\overline{u_k u_\ell}\frac{\partial \varepsilon}{\partial x_\ell}, \tag{43}$$

the model of Wyngaard, et al. (1973)

$$\frac{D\varepsilon}{Dt} = -\frac{\varepsilon^2}{q^2}\left(4. + 3\,\frac{\overline{u_i u_k}}{\varepsilon}\frac{\partial U_k}{\partial x_i}\right) + 0.083\,\frac{\partial}{\partial x_k}\frac{q^2}{\varepsilon}\overline{u_k u_\ell}\frac{\partial \varepsilon}{\partial x_\ell}\,, \tag{44}$$

and the model of Shir (1973)

$$\frac{D\varepsilon}{Dt} = -\frac{\varepsilon^2}{q^2}\left(4 - 2\,\frac{u_i u_k}{\varepsilon}\frac{\partial U_k}{\partial x_i}\right) + .0193\,q^4\,\psi\,(\bar{r}) + 0.0186\,\frac{\varepsilon}{q^2}\frac{\partial}{\partial x_k}\frac{q^4}{\varepsilon}\frac{\partial q^2}{\partial x_k} - 0.011\,\frac{\varepsilon^2}{q^3}\frac{\partial}{\partial x_k}\frac{q^4}{\varepsilon}\frac{\partial q^3/\varepsilon}{\partial x_k} \tag{45}$$

Shir's model contains terms which differ considerably from those suggested by the other authors, since it was actually derived to model

the integral length scale, $\ell \sim q^3/\varepsilon$. The awkward formulation results upon transformation to an explicit equation for ε. In this model, the coefficient of

$$\frac{\varepsilon}{q^2} \frac{\partial}{\partial x_k} \frac{q^4}{\varepsilon} \frac{\partial q^2}{\partial x_k}$$

is *not* an adjustable parameter, since it is fixed by the choice of coefficients in the Reynolds stress tensor equation.

All of the above models contain a term which is the weighted difference between the rates of production and dissipation of turbulence energy. However, there is considerable variability in the numerical values of the coefficients used. Lumley (1970) suggested that such a term might be appropriate to model the difference between the first and second terms in equation (13) which, as argued previously, must be O(1) even though each term separately is $O(Re_\ell^{1/2})$. Lumley reasoned that such a term would provide a positive contribution to $D\varepsilon/Dt$ in regions where $-\overline{u_i u_k}\, \partial U_k/\partial x_i >> \varepsilon$ and a negative contribution if $-\overline{u_i u_k}\, \partial U_k/\partial x_i << \varepsilon$. However, the turbulence energy production term was included in models (42) - (45) in an attempt to model the *first* and *second* terms in equation (8) (production of ε by mean flow stretching of turbulence vorticity), which were shown to be higher order in Re_ℓ (i.e. $O(Re_\ell^{-1/2})$). Hence, these models apparently retain a suitable term for the wrong reason.

Shir's dissipation equation also contains a 'wall-effect' term ($q^4\psi(\bar{r})$) which was included in his original model of ℓ to account for the influence of a solid wall on the distribution of ℓ. However, the

physical explanation for the appearance of such a term in the *dissipation* equation is not clear, since the discussion in section 2.A indicated that at high Reynolds numbers the production-dissipation term is dominated by the local effects of vortex stretching by turbulent fluctuations. Hence, such a term seems to be inconsistent in the high Re_ℓ limit.

The motivation for the inhomogeneous terms which enter these models is similar to the motivation for the triple-velocity correlation models discussed previously. The argument is that the turbulent flux of ε should be proportional to the product of the gradient of ε and an eddy diffusivity (a tensor in the models of Hanjalic and Launder, and Daly and Harlow, and a scalar in the model of Shir). However, the functional expansion approach suggests that this term may take a much more general form. In particular, this flux may be proportional to gradients of all turbulence quantities. From this point of view, Daly and Harlow's inclusion of an additional term (the divergence of the gradient of q^2) represents a step in the right direction, for the wrong reason. The invariant modeling approach suggests that such a term might be appropriate for either P_I or D_k. However, Daly et al. included this term to approximate the first term in equation (13) which (by itself) is $O(Re_\ell^{\frac{1}{2}})$.

Finally, with regard to the inhomogeneous terms, it should be noted that, even when comparable terms are included in different models, there is significant disagreement on the values of the coefficients used. In particular, the parameters used by Daly and Harlow are

an order of magnitude larger than those used by Hanjalic and Launder, Wyngaard et al. and Shir.

F. Homogeneous Form of Turbulence Model

In the strictest sense, homogeneous flows have uniform properties throughout (i.e. derivatives of *all* mean variables and correlations are zero). However, the *turbulence* properties of many wind tunnel flows are nearly homogeneous in the sense that gradients are confined to the streamwise direction with uniform properties on any cross-section of the flow. Homogeneous turbulence of this type can also exist in the presence of mean velocity shear (c.f. the experiment of Champagne, Harris and Corrsin (1970)). Hence, for wind tunnel flows, in which the streamwise gradients of all variables are small enough to allow the inhomogeneous terms of the invariant model to be neglected, the equations for the Reynolds stress tensor and turbulence energy dissipation rate may be simplified to the form

$$\frac{D\overline{u_i u_j}}{Dt} = -\overline{u_i u_k}\frac{\partial U_j}{\partial x_k} - \overline{u_j u_k}\frac{\partial U_i}{\partial x_k} - \left[\left(1 + B_1 \frac{II}{q^4}\right) a_{ij} + \frac{B_2}{q^2} \left(a_{ik}a_{kj} - \frac{II}{3}\delta_{ij}\right) \right] / T - \frac{2}{3}\varepsilon\,\delta_{ij} \qquad (46)$$

and

$$\frac{D\varepsilon}{Dt} = \frac{\varepsilon^2}{q^2}\left(B_{11} + B_{12}\frac{II}{q^4} + B_{13}\frac{III}{q^6}\right) \qquad (47)$$

On the basis of homogeneous data, for which equations (46) - (47) apply, one can establish the constants required for the leading (homogeneous) approximation to the turbulence model. Since these terms are dominant in their respective asymptotic expansions, their accurate specification is essential to the proper modeling of turbulence phenomena.

3. EVALUATION OF HOMOGENEOUS MODEL PARAMETERS

A. Homogeneous Flow Experimental Data

i) Decay of Isotropic Turbulence

It is found experimentally (c.f. Gad-el-Hak and Corrsin (1972)) that, for precisely isotropic wind tunnel turbulence, decay of turbulence energy is very well approximated by a power-law relation of the form

$$q^2 = \gamma \, x_1^{-\alpha} \tag{48}$$

where x_1 is the streamwise distance measured from some virtual origin of the turbulence, and α is an experimentally determined, positive number.

If equation (48) is substituted into the isotropic form of equation (46) to yield a corresponding power-law expression for ε, it may be shown that the result is consistent with equation (47) only if

$$B_{11} = -2 \left(\frac{1 + \alpha}{\alpha} \right)$$

Hence, a knowledge of α defines the first of the unknown model parameters.

The precise value of the exponent, α, has been a question of considerable interest. In a series of papers, Batchelor and Townsend (1947, 1948) found experimentally that, for large Re_ℓ,

$$\alpha \simeq 1.0$$

Although several similarity arguments (c.f. Batchelor (1948)) lead to decay laws that are not inconsistent with the experimental observations, a rigorous proof has not been derived.

Comte-Bellot and Corrsin (1966) studied the decay behind three different grids in an attempt to establish the value of α more precisely. Their experiments on one of the grids encompassed a significant range of Reynolds numbers ($1.7 \times 10^4 \leq Re_M \leq 13.5 \times 10^4$) and in this study, α ranged from a value of 1.29 at the smallest Re_M to 1.15 at the largest Re_M.

The data of Comte-Bellot and Corrsin also indicate that, for fixed Reynolds number, the value of α depends on grid type. This suggests that α may depend as much on the distribution of energy in wave number space as it does on Re_M. This is substantiated to some degree by the most recent data of Gad-el-Hak and Corrsin (1974) for the decay of nearly isotropic turbulence behind a uniform grid of jets, for which changes in the energy spectrum accompanied changes in jet flow rate. These data suggest that the broader the inertial subrange, the smaller is α, with a minimum for Gad-el-Hak's experiments of 1.0. This is best demonstrated by figure 12 of Gad-el-Hak and Corrsin (1974) and figures 63 to 65 of Gad-el-Hak (1972).

Large Re_M also implies a broad inertial subrange. Hence, the observations of Comte-Bellot et al. on the passive grid are apparently consistent with the jet grid results. However, Gad-el-Hak's experiments on a passive grid, over the somewhat smaller Reynolds number range of $4.83 \times 10^4 \leq Re_M \leq 7.34 \times 10^4$ show almost no

Re_M dependence. A value of $\alpha \sim 1.3$ was reported. That no Re_M dependence was observed in this case, may be due to the small range of Re_M examined.

Finally, we cite the results of Kistler and Vrebalovich (see Gad-el-Hak and Corrsin (1974) for these data) who reported, for a passive grid, $\alpha = 1.0$ at $Re_M = 2.42 \times 10^6$. This value of grid Reynolds number is larger than that for any of the other data reported, by a factor of about twenty.

In conclusion, the value of the decay exponent is not clearly defined. However, the evidence seems to indicate that $\alpha = 1.0$ is appropriate at large Reynolds numbers. Thus, in keeping with the high Reynolds number nature of the model $B_{11} = -4.0$ is adopted. This choice for B_{11} is the same as the parameterization of the other turbulence models, in section 2.E, and is also the same as the value suggested by Lumley (1970), and Lumley and Khajeh-Nouri (1973).

ii) Decay of Anisotropic Wind Tunnel Turbulence

The turbulence produced by a grid in a wind tunnel is, in general, nearly isotropic. That is, the turbulence energy is nearly equipartitioned between the three energy components. Hence, a different technique must be used to produce significant anisotropy. Uberoi (1956, 1957) produced homogeneous, highly anisotropic turbulence by passing grid turbulence through a sudden 4:1 contraction in wind tunnel cross-section. The anisotropic decay data were recorded in a section, with uniform mean velocity, downstream of the contraction. The data reported include the three energy components for grid Reynolds numbers of 3,710, 6,150, 10,000 and 12,300.

The relevant model equations for the energy components and dissipation rate, normalized with respect to the mean velocity, U_1, are:

$$\frac{\partial \overline{u_i u_j}}{\partial x_1} = - \left[\{ 1 + B_1 \frac{II}{q^4} \} a_{ij} + \frac{B_2}{q^2} \{ a_{jk} a_{kj} - \frac{II}{3} \delta_{ij} \} \right] / T - \frac{2}{3} \varepsilon \delta_{ij} \qquad (49)$$

and

$$\frac{\partial \varepsilon}{\partial x_1} = \frac{\varepsilon^2}{q^2} \left(B_{11} + B_{12} \frac{II}{q^4} + B_{13} \frac{III}{q^6} \right) \qquad (50)$$

iii) Distortion of Turbulence by Irrotational Plane Strain

Tucker and Reynolds (1968) considered the irrotational plane strain of a laterally homogeneous turbulent flow as it passed

through a laterally distorting wind tunnel of constant cross-sectional area. The resulting non-zero rates of strain were

$$\frac{\partial U_3}{\partial x_3} = - SU_2 \ , \quad \frac{\partial U_1}{\partial x_1} = SU_2$$

where U_2 is the constant streamwise velocity. The magnitudes of the three energy conponents were recorded as a function of downstream position.

If the dependent variables are scaled with respect to the mean streamwise velocity as in ii), the governing ordinary differential equations are:

$$\frac{\partial \overline{u_1 u_1}}{\partial x_2} = -2\overline{u_1 u_1}\, S - \frac{1}{T}\left[\{ 1 + B_1 \frac{II}{q^4} \} a_{11} + \frac{B_2}{q^2}\{a_{1j}a_{j1} - \frac{II}{3}\}\right] - \frac{2\varepsilon}{3} \tag{51a}$$

$$\frac{\partial \overline{u_2 u_2}}{\partial x_2} = - \frac{1}{T}\left[\{ 1 + B_1 \frac{II}{q^4} \} a_{22} + \frac{B_2}{q^2}\{ a_{2j}a_{j2} - \frac{II}{3} \}\right] - \frac{2\varepsilon}{3} \tag{51b}$$

$$\frac{\partial \overline{u_3 u_3}}{\partial x_2} = + 2\overline{u_3 u_3}\, S - \frac{1}{T}\left[\{ 1 + B_1 \frac{II}{q^4}\} a_{33} + \frac{B_2}{q^2}\{ a_{3j}a_{j3} - \frac{II}{3} \}\right] - \frac{2\varepsilon}{3} \tag{51c}$$

$$\overline{u_1 u_2} \equiv 0$$

$$\frac{\partial \varepsilon}{\partial x_2} = \frac{\varepsilon^2}{q^2} \left(B_{11} + B_{12} \frac{II}{q^4} + B_{13} \frac{III}{q^6}\right) \tag{52}$$

where

$$S = 0.2225 \text{ ft}^{-1} \quad \text{for } 0.0 \leq x_2 \leq 97.0$$

$$S = 0.0 \quad \text{for } x_2 > 97.0$$

iv) Homogeneous Turbulent Shear

The final simple flow, for which fully documented experimental data exist, is the homogeneous shear flow of Champagne, Harris and Corrsin (1970). The flow was unidirectional and became homogeneous in the cross-stream direction within a few feet of the turbulence generating grid. A uniform mean velocity gradient

$$\frac{\partial U_1}{\partial x_2} = SU_o$$

where U_1 is the streamwise mean velocity, was achieved by careful adjustment of internal flow resistances (screens) at the upstream end of the channel.

In addition to measurements which verify the homogeneity of the flow to within a few percent, the three energy components and the turbulent shear stress were recorded as the flow evolved from its initial, almost isotropic condition, toward a final steady state at the downstream end of the channel, where the rate of turbulence energy production was approximately balanced by the rate of turbulence energy dissipation.

The governing equations, with dependent variables scaled with respect to the center-line velocity, U_o, as in ii) are

$$\frac{\partial \overline{u_1 u_1}}{\partial x_1} = -2\overline{u_1 u_2}\, S - \frac{1}{T}\left[\{1 + B_1 \frac{II}{q^4}\}a_{11} + \frac{B_2}{q^2}\{a_{1j}a_{j1} - \frac{II}{3}\}\right] - \frac{2}{3}\varepsilon \tag{53a}$$

$$\frac{\partial \overline{u_\alpha u_\alpha}}{\partial x_1} = -\frac{1}{T}\left[\{1 + B_1 \frac{II}{q^4}\}a_{\alpha\alpha} + \frac{B_2}{q^2}\{a_{\alpha j}a_{j\alpha} - \frac{II}{3}\}\right] - \frac{2}{3}\varepsilon, \quad \alpha = 2,3 \tag{53b}$$

$$\frac{\partial \overline{u_1 u_2}}{\partial x_1} = -\overline{u_2 u_2}\, S - \frac{1}{T}\left[\{1 + B_1 \frac{II}{q^4}\}a_{12} + \frac{B_2}{q^2} a_{1j}a_{j2}\right] \tag{53c}$$

$$\frac{\partial \varepsilon}{\partial x_1} = \frac{\varepsilon^2}{q^2}\left(B_{11} + B_{12}\frac{II}{q^4} + B_{13}\frac{III}{q^6}\right) \tag{54}$$

where $S = 0.318\ ft^{-1}$.

B. Tendency-Toward-Isotropy Constants

Of the four types of well documented flows, only that of Champagne et al. can potentially attain a steady-state, non-isotropic, Reynolds stress distribution. However, Lumley (1970) argued, on the basis of a more or less *ad hoc* assumption, that such a steady state cannot exist in a homogeneous flow. The experimental evidence of Champagne et al. does not clearly refute or verify this speculation.

The uncertainty arises because the Reynolds stress components appear to approach a steady state distribution at the downstream end of the test section (characterized by zero streamwise derivatives), but the integral length scale (as measured experimentally) continues to grow, indicating a non-steady condition. This question of an equilibrium stress distribution will be examined further in section 3.C.

Regardless of whether the conditions at the downstream of the test section are steady, or slowly varying (pseudo-steady), the experimental data indicate that the rate of turbulence energy production almost identically balances the rate of dissipation. Furthermore, the rate of change of the Reynolds stress components is much smaller than the characteristic rate of interchange of turbulence energy between the three components (ε/q^2). Hence, the downstream distribution of $\overline{u_i u_j}$ can be used to evaluate the homogeneous constants in the tendency-toward-isotropy term.

With the assumptions

$$-\overline{u_1 u_2}\,\frac{\partial U_1}{\partial x_2} = \varepsilon \quad \text{and} \quad \frac{\overline{Du_i u_j}}{Dt} \equiv 0$$

the differential equations (53) can be reduced to the algebraic relationships:

$$\left.\begin{aligned} \left(1 + B_1 \frac{II}{q^4}\right) \frac{a_{11}}{cq^2} + \frac{B_2}{cq^4}\left(a_{1j}a_{j1} - \frac{II}{3}\right) &= \frac{4}{3} \\ \left(1 + B_1 \frac{II}{q^4}\right) \frac{a_{\alpha\alpha}}{cq^2} + \frac{B_2}{cq^4}\left(a_{\alpha j}a_{j\alpha} - \frac{II}{3}\right) &= -\frac{2}{3}\,, \quad \alpha = 2,3 \end{aligned}\right\} \tag{55}$$

$$\left(1 + B_1 \frac{II}{q^4}\right) \frac{a_{12}}{cq^2} + \frac{B_2}{cq^4} a_{1j} a_{j2} = \frac{(a_{22} + 1/3)}{a_{12}}$$

Clearly, for specified values of c, B_1 and B_2, the equations (55) can be solved only for the variables a_{ij}/q^4. They cannot yield any information concerning the magnitude of q^2 since, being homogeneous, the flow lacks a relevant characteristic velocity scale. Further examination of equations (55) indicates that the three universal parameters enter only as *two* independent parameters. $(1 + B_1\ II/q^4)/c$ and B_2/c. These parameters should be chosen so that the Reynolds stress components, as calculated from equation (55) best match the experimental values. Unfortunately, since equations (55) are nonlinear, they cannot be solved for a_{ij}/q^2 as an explicit function of the unspecified parameters. This eliminates the possibility of determining the optimal parameters analytically. Instead, a Rosenbrock hillclimbing procedure (Rosenbrock (1960)) was used to determine numerically the parameter values which minimize the root mean square deviation of a_{ij}/q^2 from the experimental values. At each step in the search, the equations (55) were solved by Newton iteration. With numerous initial guesses of the two independent parameters, the search procedure always converged to the same optimal values. Rearranged to give explicit expressions for B_1 and B_2 in terms of c, the optimal parameters are

$$B_1 = 82.7\ c - 10.9$$

and

$$B_2 = 11.22\ c$$

Table 1: Numerical and Experimental Reynolds Stress Components for Homogeneous Shear Flow

	a_{11}/q^2	a_{22}/q^2	a_{33}/q^2	a_{12}/q^2
Numerical	0.146	-0.101	-0.0461	-0.170
Experimental	0.146	-0.101	-0.0455	-0.173

A comparison between the values of a_{ij}/q^2, calculated with these parameters, and the experimental values is given in table 1. Clearly, the agreement is excellent.

Finally, it should be noted from equation (54), that if the level of turbulence intensity is to reach the controversial 'steady state',

$$\frac{\partial \varepsilon}{\partial x_2} = 0$$

This, in turn, requires the model constants B_{12} and B_{13}, which are yet to be determined, to satisfy the constraint

$$B_{11} + B_{12}\left(\frac{II}{q^4}\right)_s + B_{13}\left(\frac{III}{q^6}\right)_s \equiv 0 \qquad (56)$$

(c.f. equation (54)). Here, $(II/q^4)_s$ and $(III/q^6)_s$ are the 'steady-state' values which correspond to the numerically determined a_{ij}/q^2 in table 1. It will be shown in section 3.C that the values of B_{12} and B_{13} which give the best model fit to the dynamic data from the studies of Uberoi (1956, 1957) and Champagne et al. (1970), are *not* consistent with the constraint (56), and the estimate $B_{11} = -4$ from section 3.A.i. Thus, we provide some evidence that the 'steady-state' turbulence energy level cannot be achieved in a homogeneous shear flow.

C. Determination of Best Values for c, B_{12} and B_{13}

There remain three constants, c, B_{12} and B_{13}, whose specification completes the turbulence model. Since the predicted 'steady-state'

configuration of the homogeneous shear flow does not depend upon the values of these constants, they must be evaluated on the basis of the available *dynamic* data. To obtain the dynamic response of the model, equations (46) - (47) were numerically integrated in the streamwise direction with a fourth order Runga-Kutta procedure. The initial streamwise point was chosen to ensure satisfactory cross-stream homogeneity. The values of the Reynolds stress components (presented in table 2) were taken directly from the experimental data, and the initial values of ε were determined from the slope of the experimental turbulence energy curve. (Any local energy production was also included.) This gives the most reliable estimate of the dissipation rate in any homogeneous, decaying flow.

For the initial calculations of the homogeneous flows, B_{13} was fixed at various values, and the values of B_{12} and c, that gave the optimal (least-squares) fit to the dynamic experimental data, were determined by means of the numerical hillclimbing procedure. These calculations showed that for each flow and any (fixed) B_{13}, values of c and B_{12} could be obtained, which gave a uniform best-fit to the experimental data, in the sense that the error between the experimental data and the numerical model was independent of B_{13}. Furthermore, the value of c which gave this minimum was independent of B_{12} and B_{13}. For the data of Champagne et al. and Uberoi, c = 0.162. This value is somewhat larger than the value 0.125 suggested by Lumley et al. (1973), but smaller than the value of 0.2 originally suggested by Rotta (1951).

Table 2: Initial Conditions and Integration Step-Size for the Homogeneous Flows

Flow	$\overline{u_1^2}$	$\overline{u_2^2}$	$\overline{u_3^2}$	$\overline{u_1 u_2}$	ε	ΔX	x_o
Champagne, Harris and Corrsin (1970)	$.33X10^{-3}$	$.26X10^{-3}$	$.244X10^{-3}$	$-.108X10^{-3}$	$.75X10^{-4}ft^{-1}$	0.1ft	5.0ft
Tucker and Reynolds (1968)	$.185X10^{-3}$	$.37X10^{-3}$	$.361X10^{-3}$	0	$.104X10^{-4}in^{-1}$	1.0in	40.0in
Uberoi Re_M = 12,300	$.23X10^{-3}$	$.178X10^{-2}$	$.178X10^{-2}$	0	$.236X10^{-4}in^{-1}$	0.1in	55.0in
Re_M = 10,000	$.5X10^{-4}$	$1.74X10^{-4}$	$1.74X10^{-4}$	0	$.275X10^{-5}$	1.0in	4.0in
Re_M = 6,150	$.1066X10^{-3}$	$.692X10^{-3}$	$.692X10^{-3}$	0	$.912X10^{-5}in^{-1}$	.1in	57.0in
Re_M = 3,170	$.174X10^{-3}$	$.1245X10^{-2}$	$.1245X10^{-2}$	0	$.131X10^{-4}in^{-1}$	.1in	66.5in

A somewhat smaller value of c resulted from the data of Tucker and Reynolds. However, there are a number of uncertainties associated with Tucker and Reynolds' experiments. The apparatus was designed to deliver a constant rate of strain. However, a check to verify the cross-stream uniformity of the mean velocity field was not reported. Thus, the actual strain rate could have been significantly different from the design value which was reported, and could also have varied with horizontal position in the straining section. Another source of experimental uncertainty results from the close proximity of the walls to the point where the turbulence measurements were taken. Whereas Uberoi and Champagne et al. used a 12 in. X 12 in. cross-section test channel, Tucker and Reynolds used a test section with walls only 7 in. apart. Townsend (1954) performed a similar strain experiment, at approximately the same Re_ℓ, in a 6 in. duct. His careful measurements indicated that the walls produced significant turbulence energy. In fact, at the downstream end of the channel, Townsend found that wall generation could account for as much as 25% of the turbulence intensity. Even in the absence of these experimental uncertainties, a straining flow of this type is extremely difficult to model, since even small errors in the predicted dissipation rate and rate of energy redistribution are amplified, by the mechanism of turbulence-meanflow interaction, as the flow is strained. Hence, due to the large experimental uncertainties and to the inherent difficulties associated with the numerical simulation of rapidly straining flows, the data of Tucker and Reynolds were not included in choosing the values for c, B_{12} and

B_{13}.

The above calculations indicate that the values of B_{12} and B_{13} which provide a best fit to the dynamic data, for any one laboratory flow, are *not* unique. Instead, for each flow there exists a locus of such points in B_{12}-B_{13} space. These loci are shown in figure 1 to be straight lines, which divide the parameter domain into two segments. Parameter values which lie above the division produce a model response which is more dissipative than the experimental data for that flow, and parameters which lie below the division produce responses which are less dissipative than the data.

If the numerical model were exact, and if the experimental data contained no error, the parameter curves would have one point in common. In fact, the loci of Uberoi and Champagne et al. do cross in the vicinity of the point

$(B_{12}, B_{13}) = (23., 200.)$ (parameter values A)

An obvious exception to this point of intersection (in addition to Tucker and Reynolds' flow) is the Uberoi flow for $Re_M = 6{,}150$. However, we believe that this is of minor consequence since the data record for this flow is very short. Consequently, the 'minimum' represented by the line on figure 1 is extremely shallow (i.e. the relative change in model fit with a change in the parameters B_{13}, B_{12} is small). Thus, this flow carries considerably less significance than do the other data .

It is unfortunate that the data for most of Uberoi's experiments fall on essentially the same line of positive slope in figure 1 since,

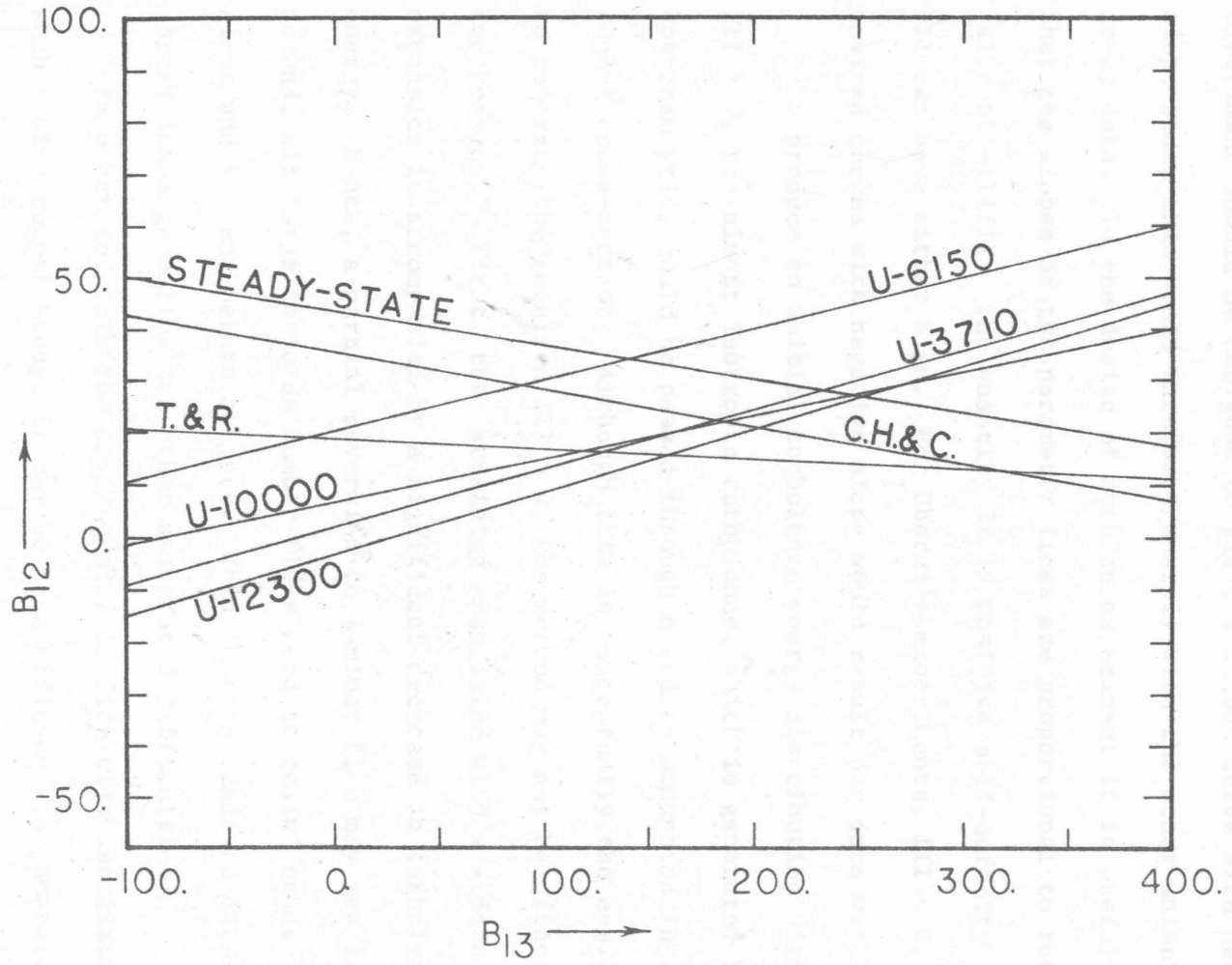

FIGURE 1: B_{12}-B_{13} PARAMETER DOMAIN SHOWING LOCI OF BEST FIT.

otherwise, with four sets of independent, anisotropic decay data, one could specify B_{12} and B_{13} with more confidence. Ideally, a future experiment should be designed to yield a second curve with negative slope since this would intersect sharply with the other anisotropic decay data. In the design of such an experiment it is useful to note that the slopes of the parameter lines are proportional to the initial value of -III/II. The quantity II is positive semi-definite whereas III can have either sign. For Uberoi's experiments, III < 0. The desired curves with negative slope would result for data with III > 0.

To produce an initial turbulence energy distribution with III > 0, the almost isotropic turbulence, which is generated by an upstream grid, could be passed through a sudden *expansion* in wind tunnel cross-section. Although this is conceptually the easiest way to generate the required III > 0, the method may not be effective for two reasons. First, the straining associated with a sudden expansion is accompanied by a significant decrease in turbulence energy. Hence, a partial reversion to laminar flow may result. Second, all large Reynolds number flows tend to resist sudden expansions and instead behave as jets. This in turn leads to cross-stream inhomogeneities and other associated difficulties.

In order to avoid the *experimental* difficulties associated with such a wind tunnel study, it may be more efficient to generate the desired data by means of a direct solution technique such as that of Orszag (1969, 1971, 1972). In this case one may simply initialize the computation with turbulence having the desired properties.

In figures 2 - 4, the model response for parameters A is compared to the experimental data. Although the overall agreement is quite good, a close examination indicates that the model gives a return to isotropy for Uberoi's flows which is slightly too rapid in the early stages. This is best demonstrated by the experiments that are taken entirely from the early transition period (Re_M = 12,300, 6,150, and 3,710). The data record for Uberoi's fourth experiment (Re_M = 10,000) is considerably longer and includes the final stages of transition. From this flow it is apparent that although the initial return to isotropy is a little too rapid, the overall agreement of the model and experiment is within the bounds of the experimental uncertainties.

The reason for the minor discrepancy between the experimental and model responses in the early transition period is not known at this time. Originally, it had been thought that the neglect of higher order terms in Re_ℓ, such as the anisotropic contribution to the dissipation tensor, might be responsible. However, an error of this origin must show a Reynolds number dependence. Table 3 provides a classification of flows according to Re_ℓ. Of particular relevance are Uberoi's flows which vary in Re_ℓ over the range

$$2{,}240 > Re_\ell > 1{,}000$$

For all of these flows the model error is reasonably consistent and clearly independent of the Reynolds number.

The values of B_{12} and B_{13}, chosen from the intersection of the

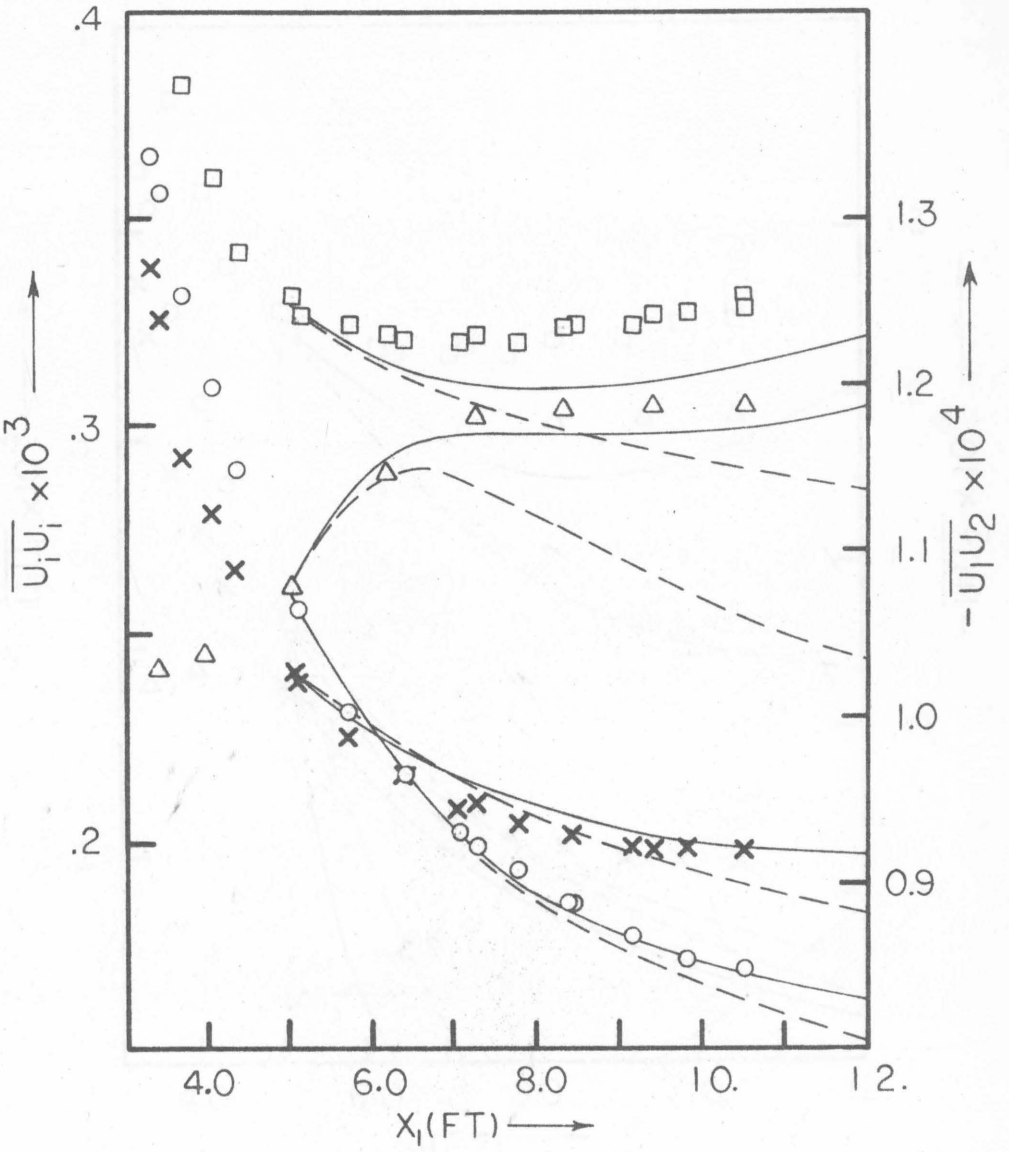

FIGURE 2A: HOMOGENEOUS SHEAR FLOW; DATA OF CHAMPAGNE, HARRIS, AND CORRSIN(1970): □- $\overline{U_1U_1}$, ○ - $\overline{U_2U_2}$, × - $\overline{U_3U_3}$, △- $\overline{U_1U_2}$; ——— PARAMETERS A, — — — — PARAMETERS B.

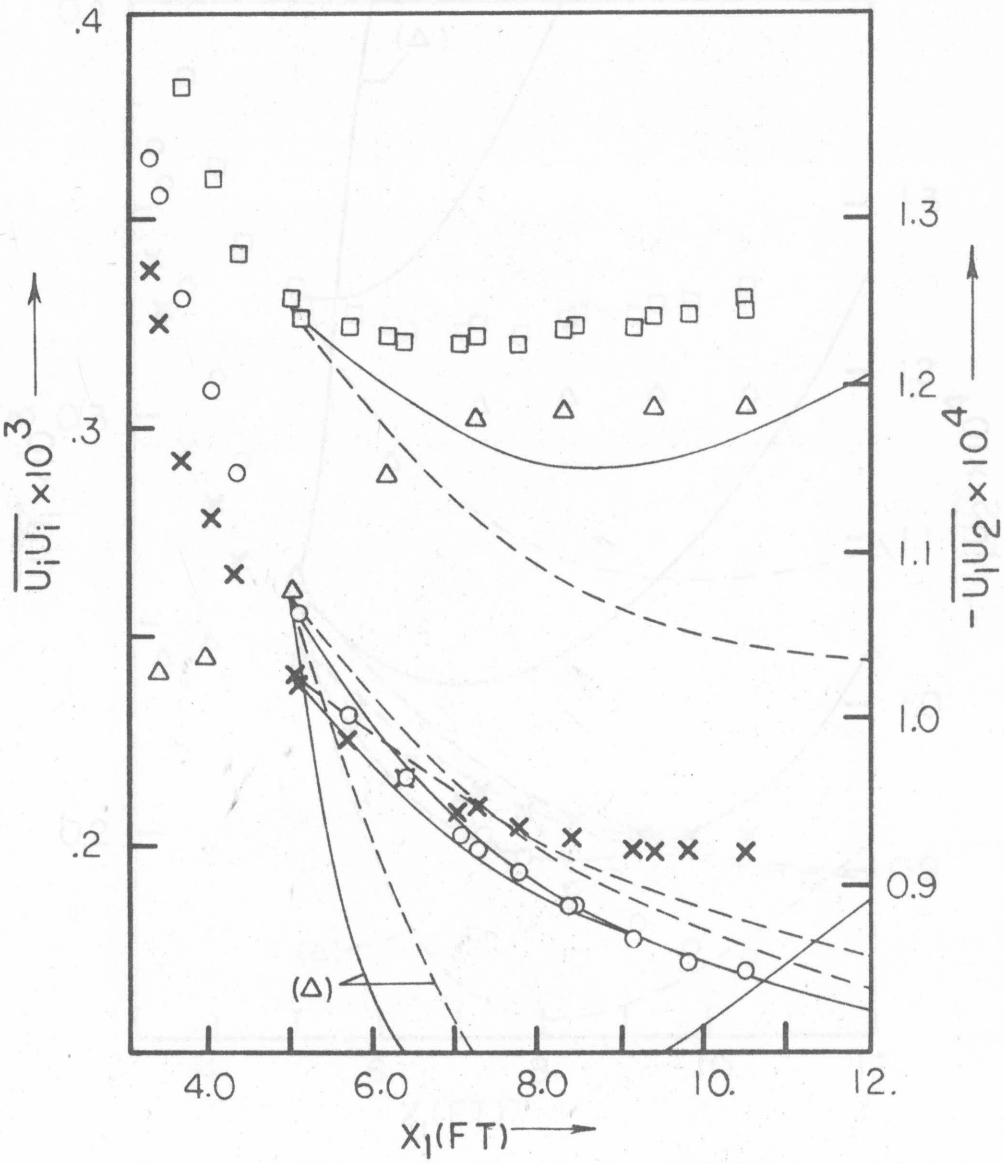

FIGURE 2B: HOMOGENEOUS SHEAR FLOW; DATA AS IN FIGURE 2A;
——— MODEL OF WYNGAARD ET AL.(1973);
— — —MODEL OF HANJALIC AND LAUNDER(1972B).

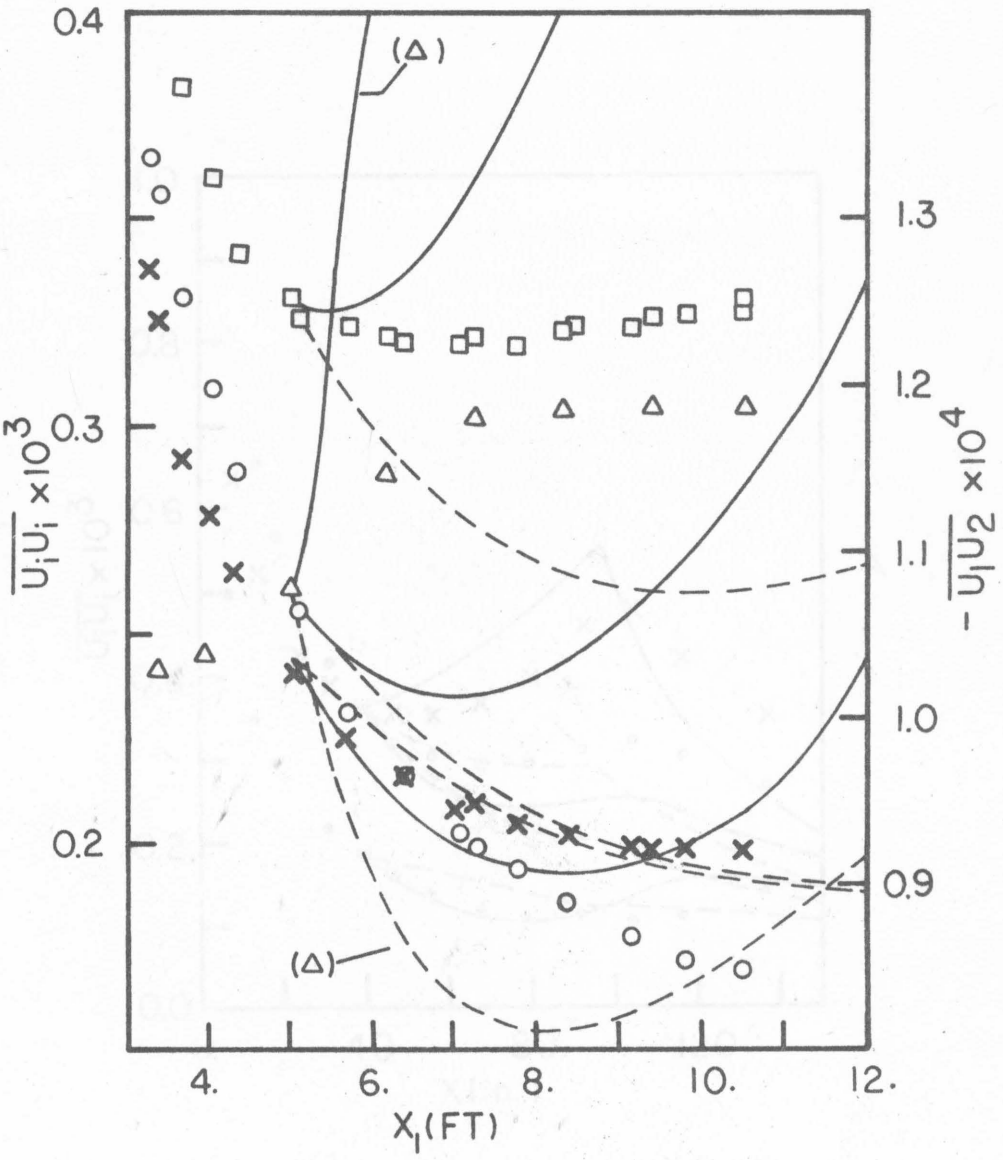

FIGURE 2c: HOMOGENEOUS SHEAR FLOW; DATA AS IN FIGURE 2A;
——— MODEL OF DALY AND HARLOW (1970);
— — — MODEL OF SHIR (1973).

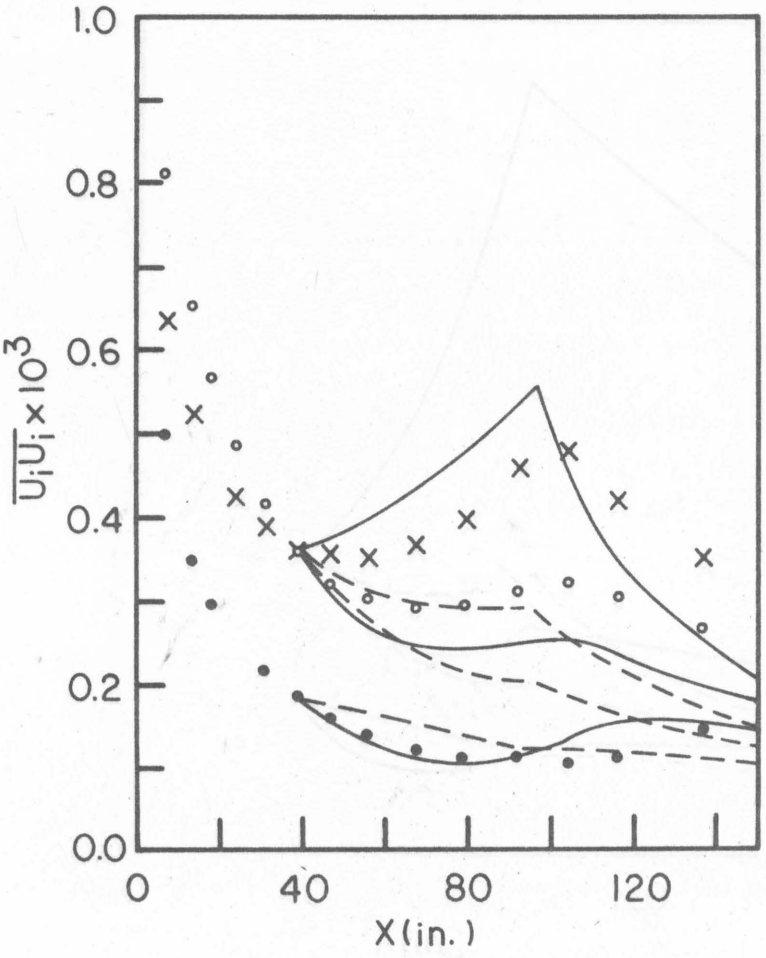

FIGURE 3A: PURE STRAIN FLOW OF TUCKER AND REYNOLDS (1968); • $-\overline{U_1U_1}$, ∘ $-\overline{U_2U_2}$, X $-\overline{U_3U_3}$; —— PRESENT MODEL ; — — MODEL OF HANJALIC AND LAUNDER (1972B).

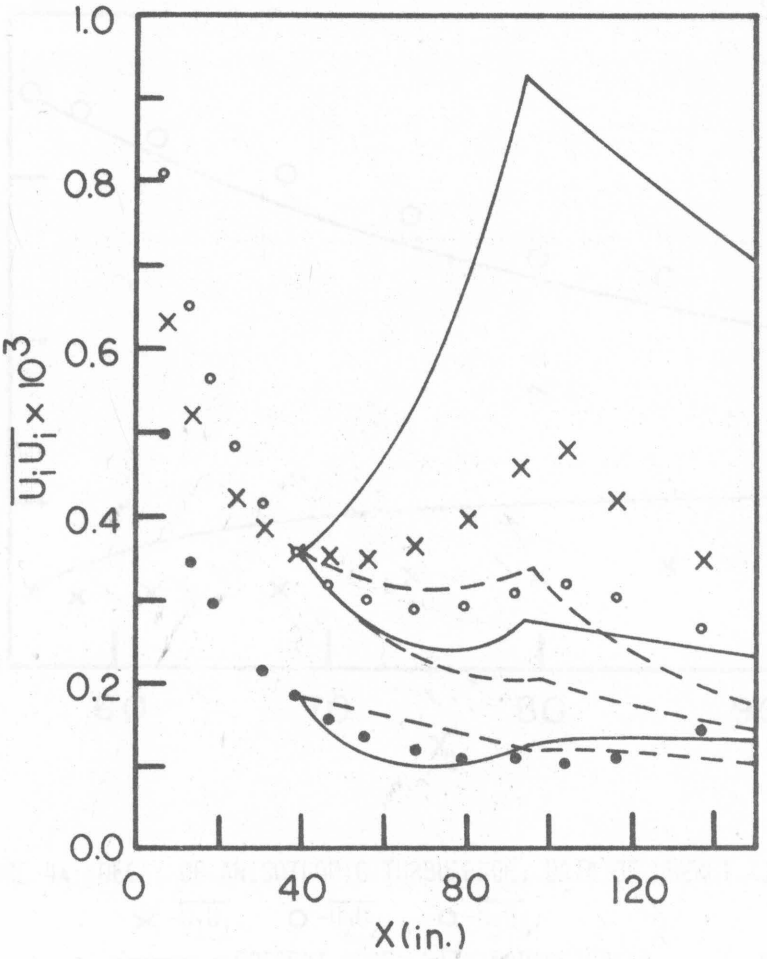

FIGURE 3B: PURE STRAIN FLOW OF TUCKER AND REYNOLDS(1968); DATA AS IN FIGURE 3A; ——— MODEL OF DALY AND HARLOW (1970); — — MODEL OF SHIR (1973).

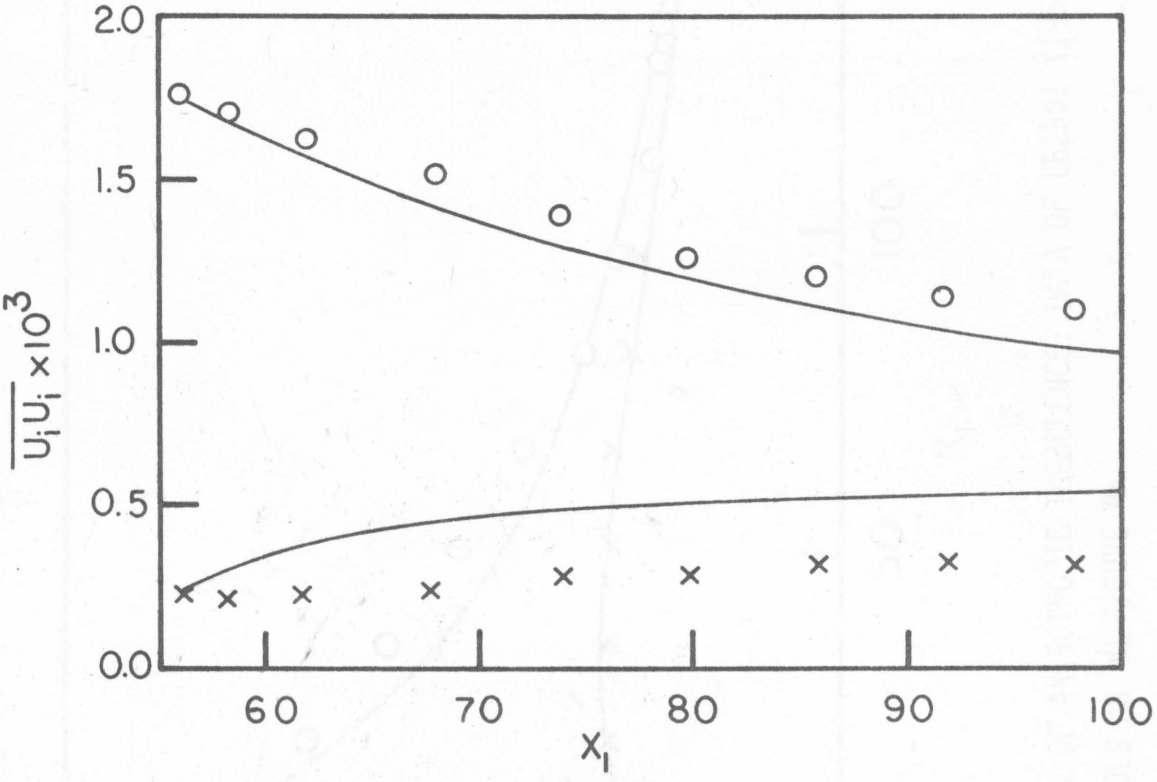

FIGURE 4A: DECAY OF ANISOTROPIC TURBULENCE; DATA OF UBEROI (1956); R_{E_M}=12300;
× -$\overline{U_1U_1}$, o -$\overline{U_2U_2}$, o -$\overline{U_3U_3}$;
——— PRESENT MODEL WITH PARAMETERS A.

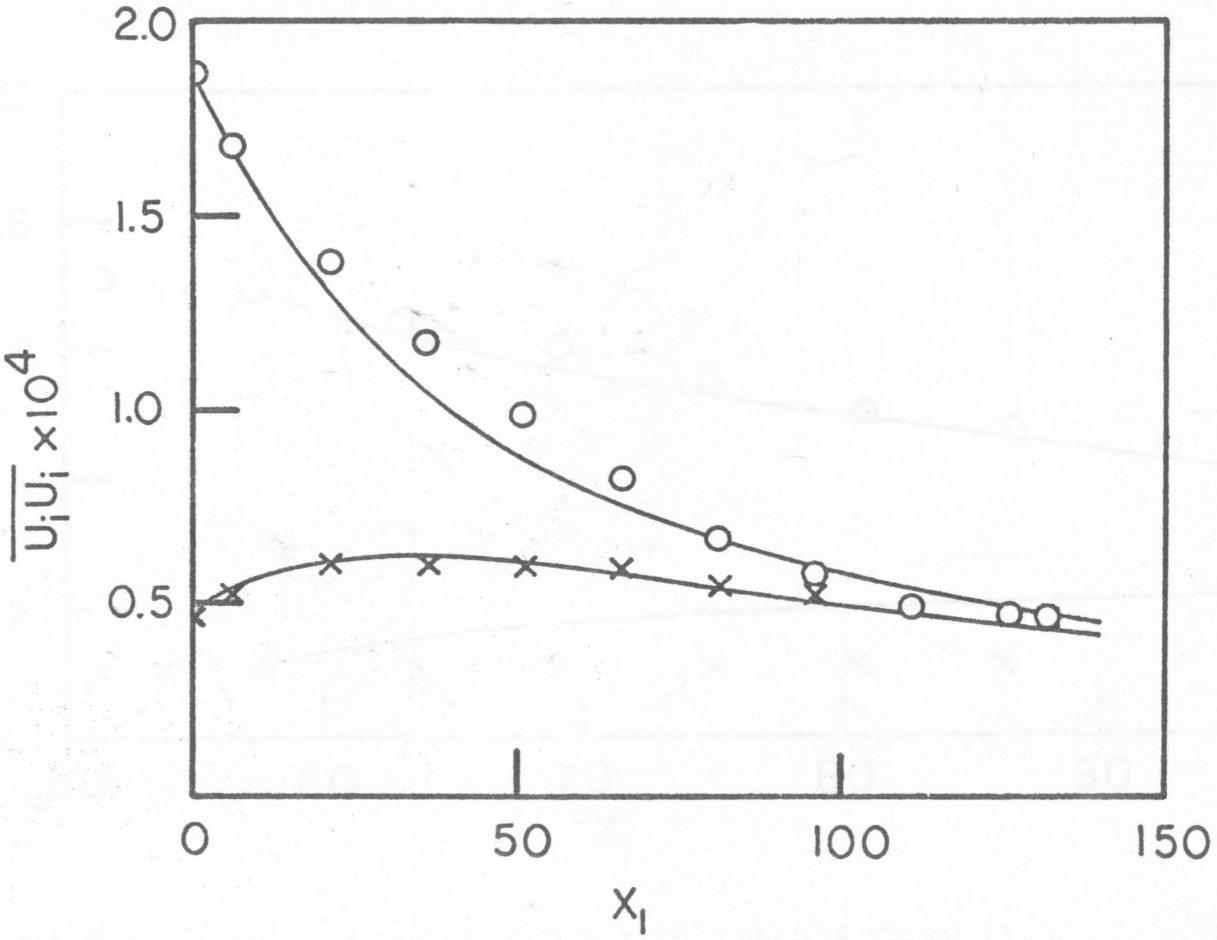

FIGURE 4B: DECAY OF ANISOTROPIC TURBULENCE; DATA OF UBEROI (1957); R_{E_M}=10000; SYMBOLS AS IN FIGURE 4A.

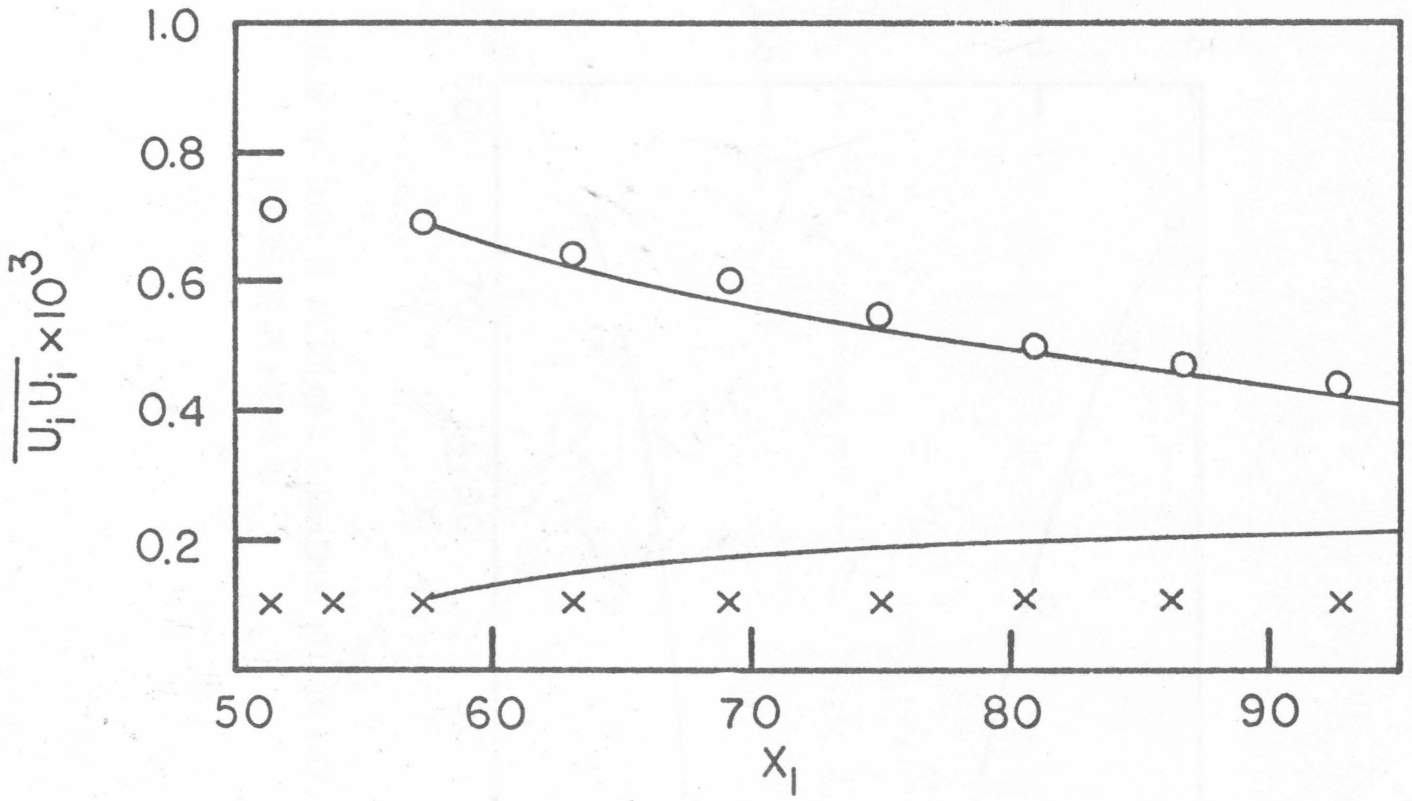

FIGURE 4c: DECAY OF ANISOTROPIC TURBULENCE; DATA OF UBEROI (1956); R_{E_M}=6150; SYMBOLS AS IN FIGURE 4A.

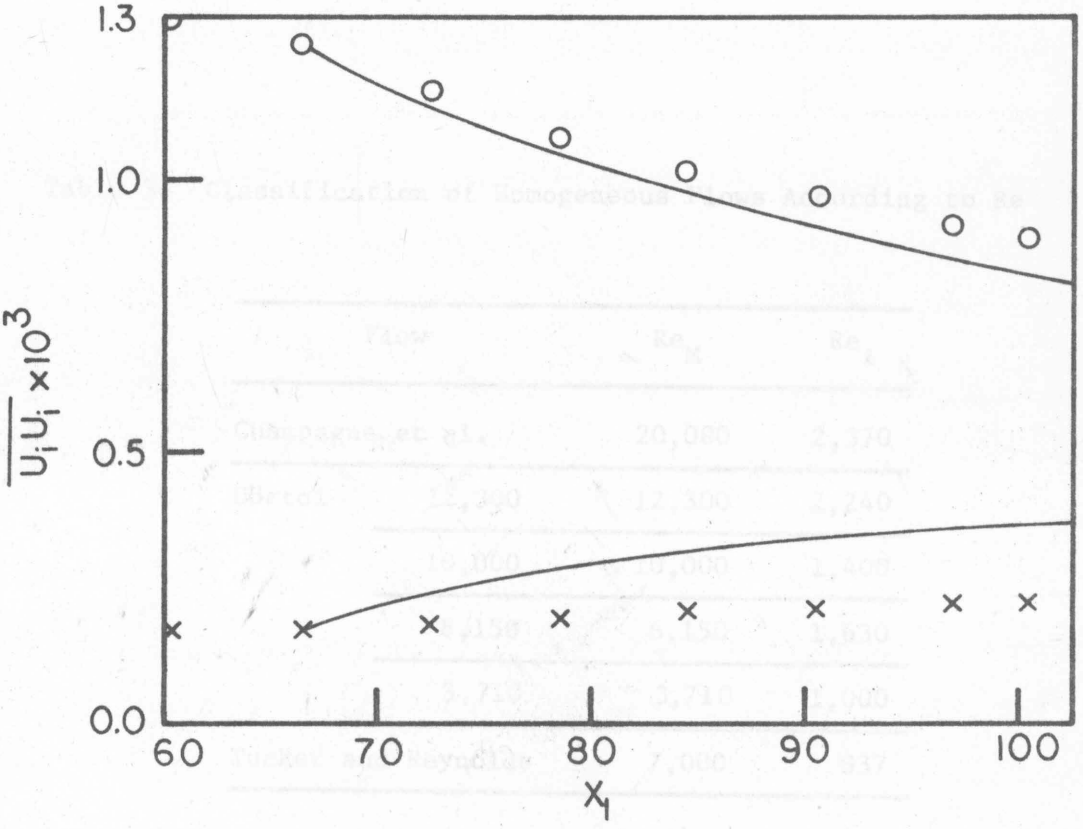

FIGURE 4D: DECAY OF ANISOTROPIC TURBULENCE; DATA OF UBEROI (1956); Re_M=3710; SYMBOLS AS IN FIGURE 4A.

Table 3. Classification of Homogeneous Flows According to Re

Flow		Re_M	Re_ℓ
Champagne et al.		20,000	2,370
Uberoi	12,300	12,300	2,240
	10,000	10,000	1,400
	6,150	6,150	1,630
	3,710	3,710	1,000
Tucker and Reynolds		7,000	837

loci of best-fit pairs for Uberoi's flow at Re_M = 12,300, 10,000 and 3,710, and for Champagne et al.'s (1970) homogeneous shear flow, appear to support Lumley's (1970) hypothesis that a homogeneous shear flow cannot attain a steady-state turbulence energy level. To demonstrate this more clearly, equation (56) has been plotted in figure 1. Clearly, the optimal choice for B_{12} and B_{13} does not satisfy equation (56). Hence, with parameters A, the dissipation rate can *never* reach a finite equilibrium value. In particular, when B_{12} and B_{13} are chosen to lie below equation (56), ε continues to decrease, even though a_{ij}/q^2 may approach an equilibrium configuration. On the other hand, the rate of turbulence energy production does not decrease, with the result that the turbulence energy level must steadily *increase*. This general increase in energy level can be detected in figure 20 as a gradual tailing up of the curves for $\overline{u_1^2}$ and $\overline{u_1 u_2}$ for $x \gtrsim 10$. This behavior is consistent with the experimental observation that the integral length scale continues to increase, since $\ell \sim q^3/\varepsilon$.

By choosing B_{12} and B_{13} to satisfy equation (56), one can force the model to approach a steady-state energy level. For example, the model response with

$$(B_{12}, B_{13}) = (27., 246.) \quad \text{(parameter values B)}$$

is represented by the broken lines in figure 2a. Since this point in the B_{12} - B_{13} plane still lies on the 'best fit' parameter curve for Uberoi's data, the model response for these flows is the same as that discussed previously. On the other hand, for parameters B, the model

response for the homogeneous shear flow is changed considerably. In particular, the model response is too dissipative and is not a satisfactory representation of the experimentally observed Reynolds stress response.

Thus, the numerical model which best matches the experimental data for the homogeneous shear flow, appears to support the physical picture of a continuously increasing turbulence energy level as a function of streamwise position. Even when combined with the experimental observation of an increasing length scale, however, this is not definitive proof that an equilibrium turbulence level cannot exist. The Reynolds stresses measured experimentally by Champagne et al. did level off suspiciously near the downstream end of the test section, and it is possible that the integral length scale simply approaches its equilibrium value more slowly, with respect to streamwise position, than the Reynolds stress tensor. A clear resolution of this question requires data for homogeneous shear flow, either taken in a longer test section, or alternatively at a higher shear Reynolds number (i.e. larger rate of shear).†

To allow a quantitative evaluation of the relative performance of the turbulence models which were discussed briefly in sections 2.D and 2.E, figures 2 and 3 compare the model responses for the homogeneous shear flow, and for the homogeneous straining flow of Tucker and

---

†During the final stages of preparation of this thesis, we have learned by private communication with S. Corrsin that such data will be reported shortly, which supports the conclusion that no equilibrium state is possible.

Reynolds (1968). It is significant that none of the models proposed by other investigators can adequately describe the homogeneous shear flow. In particular, the models of Wyngaard, Hanjalic and Launder, and Shir predict a sharp decrease in the shear stress component at the initial time (the experimental profile increases) while Daly and Harlow's model predicts an increase in $|\overline{u_1 u_2}|$ that is far too rapid. This inability to accurately predict the dynamics of the shear stress results in a model response which is much too dissipative in the first three cases, and too productive in the other case. Figures 2b, c also demonstrate the inability of the models of Wyngaard and Shir to predict the inequality of $\overline{u_2 u_2}$ and $\overline{u_3 u_3}$.

The sharp contrast between the excellent performance of the present model and the poor performance of all other models for this flow is not simply a consequence of choosing model parameters to match the downstream Reynolds stress configuration in the present model but not in the other models. In fact, Hanjalic and Launder also chose their tendency-toward-isotropy parameters to match the downstream configuration of this flow. Clearly, their model provides, at best, a poor approximation to the actual dynamic response.

Figures 3a, b provide the necessary comparison of model responses for the straining flow. None of the models provides an exact representation of the data. However, this is not surprising in view of the uncertainties already discussed. The best approximation is obtained from the present model, while the poorest approximation results from Daly and Harlow's formulation. It is significant that the data of

Tucker and Reynolds (1968) were *not* used in the determination of the parameters for the present model.

Finally, it is of interest to note that B_{12} and B_{13} are identically zero in all of the existing turbulence models other than the present one. However, all of these models give a comparable approximation to Uberoi's anisotropic decay flows. The reason for the perhaps surprising consistency of all models is evident in figure 1. By chance, the origin of the $B_{12} - B_{13}$ plane lies reasonably close to all loci representing Uberoi's experiments. Hence, in the absence of Champagne, Harris and Corrsin's data, $B_{12} = B_{13} = 0$ would appear to be an adequate choice. Anisotropic decay data with $III > 0$ should provide yet another example of a simple turbulent flow for which the existing models are inadequate, since the present investigation indicates that the loci for these flows will not pass through the origin but instead, will bisect the Uberoi experiments in the vicinity of point A.

4. ESTIMATION OF INHOMOGENEOUS MODEL PARAMETERS

A. Inhomogeneous Flows for Model Development

i) Description of the Flows

In order to evaluate constants which enter through inhomogeneous terms and higher order inhomogeneous corrections, it is necessary to examine inhomogeneous flows. Ideally, these flows should exhibit significant inhomogeneities and be well documented, but at the same time the governing equations should be simple, preferably ordinary differential equations. Four experimental flows which satisfy these requirements are the asymmetric channel flow of Hanjalic and Launder (1972a), the pipe flow of Lawn (1971), the two-dimensional mixing-layer of Wygnanski and Fiedler (1970) and the self-preserving wall-jet of Irwin (1973). Another potential source of data for parameter evaluation and model validation is the direct numerical simulation technique of Orszag, as indicated in section 1.A and 3.C. In this regard, it should be noted that Wyngaard and Coté (1974) and Wyngaard, Coté and Rao (1973) have also made extensive use of numerical results from Deardorff's three-dimensional simulation technique in evaluating the performance of their model. However, as the previous discussion has indicated, this method employs the eddy-viscosity type of closure assumption at the smallest scales of motion. This assumption has not been adequately validated. In fact, in the only direct comparison that has been published (Deardorff, 1970a), the numerical results from Deardorff's model deviate substantially from the experimental measurements of Laufer's channel flow. Thus, unlike the direct numerical simulation

technique of Orszag, which is limited only by the range of wave numbers that can be economically handled by the computer, the computational model of Deardorff does not appear appropriate, without further validation, for the generation of turbulence data which is to be used for parameter evaluation in phenomenological models of the type considered here.

The flow examined by Hanjalic and Launder was a close approximation, at the channel centerline, to unidirectional, isothermal flow between two infinite horizontal plane boundaries. Asymmetry was introduced by roughening one wall, while the opposite was left smooth. The flow near each wall was essentially an equilibrium layer, with the velocity profile in each case obeying the law of the wall. However, in the center of the channel there was a strong interaction between the two wall layers with the result that the plane of zero shear stress did not coincide with the plane of maximum velocity. The data reported include profiles of $\overline{u_i u_j}$, $\overline{u_i u_j u_2}$ and ε. In our analysis of the data, all lengths are nondimensionalized by the width of the channel, and all velocities are nondimensionalized by the slip velocity, u_*, at the rough wall. The variable x_2 will denote the dimensionless distance from the smooth wall.

Lawn (1971) considered the classical problem of turbulent flow in a circular pipe. Profiles of all Reynolds stresses were reported and, with the exception of $\overline{u_3 u_3 u_2}$, all relevant triple-velocity correlations may be calculated from the data. In our analysis of the data, the length and velocity scales are taken as the radius of the pipe and the

slip velocity, respectively, and the radial variable is denoted by x_2.

Irwin reported measurements of a plane wall-jet as it advanced into an adverse pressure gradient, which was suitably adjusted to yield a self-preserving velocity field. Among the measurements are mean velocity profiles, all Reynolds stresses, dissipation rate and all non-zero single-point triple-velocity correlations. Like Hanjalic and Launder's flow, this wall jet exhibits a non-correspondence of the points of zero shear stress and velocity maximum. Streamwise mean velocity gradients are about 4% of cross stream derivatives.

Wygnanski and Fiedler's two-dimensional mixing-layer was also self-preserving. Their data include all of the measurements reported by Irwin, as well as measurements of the intermittency factor, and turbulent-zone-averages of turbulence quantities. Streamwise velocity gradients in this case are about 15% of the cross stream derivatives.

The flows of Hanjalic and Launder, and Lawn are simplified by the parallel character of the mean flow. Hence, all variables are functions only of the coordinate normal to the solid wall, x_2, and so may be completely described by ordinary differential equations. On the other hand, the wall jet and mixing-layer are not parallel but are simplified by their self-preserving nature. In particular, if the similarity variable is

$$\eta = \frac{x_2}{bx_1} ,$$

where x_1 and x_2 are the streamwise- and cross-stream coordinates,

then the mean flow and turbulence structure can be completely described in terms of the functions

$$U_1 = U_e(x_1) + U_o(x_1)\ f\ (\eta)$$

$$\overline{u_i u_j} = U_o^2(x_1)\ g_{ij}\ (\eta)$$

$$\varepsilon = \frac{U_o^3(x_1)}{bx_1}\ e\ (\eta)$$

and

$$\overline{u_i u_j u_k} = U_o^3(x_1)\ h_{ijk}\ (\eta)$$

The function $U_e(x_1)$ is the velocity of the irrotational flow for the wall-jet and zero for the mixing-layer, and $U_o(x_1)$ is a velocity scale. For Irwin's flow b = 0.0436, $U_e = x_1^{-0.448}$ and $U_o/U_e = 1.65$, while for Wygnanski and Fiedler's flow b = 1.0, $U_e = 0.0$ and $U_o = U_m$ where U_m is the free-stream velocity on the high velocity side ($\eta = -\infty$) of the mixing-layer. Thus, all four flows can be described in terms of ordinary differential equations. However, the numerical solution of these equations is complicated by the fact that the boundary conditions are specified at two points in space, to yield a 'two-point-boundary-value' problem.

The four flows which we have selected provide a particularly diverse base for parameter estimation and model validation since they include both parallel and non-parallel flows; three flows which are dominated by shear, and one which has a significant straining component; and finally, two flows which experience intermittency (the

wall jet exhibits intermittency in the outer region, while the mixing-layer is intermittently laminar on both boundaries).

ii) Treatment of the Data

The data were taken directly from the figures reported in the literature. For those flows in which a number of realizations were available (for instance, in the wall-jet and mixing-layer) data were recorded from a smooth curve, fared through a representative realization. For the other cases in which only a single realization was reported, a smooth curve was fared through that realization.

In the analysis of the data (and estimation of parameters) that is to follow, it will be necessary to take first and second derivatives of turbulence quantities. Since the data is available in discrete form, the most straightforward approach is to approximate derivatives by their finite-difference representations. However, our preliminary attempts at parameter estimation indicated that, although this leads to adequate estimates of first order derivatives, second order derivatives estimated in this manner display an unacceptable random error. Hence, an alternative approach is necessary. The approach which led to more reasonable estimates of second order derivatives was to differentiate analytically a polynomial representation of the data. The coefficients of the polynomials were calculated to minimize the standard deviation between the polynomial representation and the discrete data. For profiles which could not be adequately represented by a single polynomial, a composite representa-

tion of two or more polynomials, constructed to give continuous first and second derivatives over the complete domain, was used. With only one exception, polynomial representations were found, which approximate all of the data to within 2% and most to within less than 1%. This is certainly within the accuracy of the data, which have an uncertainty between any series of flow realizations of the order of 5% (c.f. Irwin (1973) or Wygnanski and Fiedler (1972)). The actual order of each polynomial was chosen, somewhat qualitatively, by taking into consideration the improvement in standard deviation upon including an extra term in the polynomial, a graphical comparison of the analytical and discrete representations, and finally a comparison of the central difference first derivatives with the analytical derivatives as calculated from the polynomial. The coefficients of the polynomials which were used in the analysis are presented in table 4. (Note that, for the mixing-layer of Wygnanski and Fiedler, the *inverse* of the turbulence quantities were approximated by the polynomials since this led to better agreement at large $|\eta|$).

Only for the dissipation profile of Hanjalic and Launder, near the rough wall, were we unable to achieve what we deemed an acceptable polynomial representation of the data. The primary difficulty in this case is that the second derivative of ε in this region is very large and increases very rapidly as the rough wall is approached. However, there are only a limited number of data points in this region with which to fit the polynomial. The result is that the second derivative of ε can only be poorly approximated by a polynomial representation. However, we found that in this region of the flow,

Table 4a. (continued)

Variable	Coefficients of Polynomial			
	y^4	y^5	y^6	y^7
$\overline{u_1u_1}(y\leq.855)$	$47.24985X10^0$	-7.016290X10	3.430899X10	-
$\overline{u_1u_1}(y\geq.855)$	-	-	-	-
$\overline{u_2u_2}(y\leq.835)$	$2.751780X10^2$	$-3.785176X10^2$	$2.622422X10^2$	-7.198895X10
$\overline{u_2u_2}(y\geq.835)$	-	-	-	-
$\overline{u_3u_3}(y\leq.218)$	-	-	-	-
$\overline{u_3u_3}(.218\leq y \leq.681)$	$-7.527607X10^2$	$9.921560X10^2$	$-6.429897X10^2$	$1.642636X10^2$
$\overline{u_3u_3}(y\geq.681)$	-	-	-	-
$\overline{u_1u_2}$	-	-	-	-
$\varepsilon(.42\leq y\leq.68)$	-	-	-	-
$\varepsilon(y\geq.68)$	$2.842340X10^4$	$-1.798602X10^4$	$4.692059X10^3$	-

Table 4b. Coefficients of Polynomial Representation of Pipe Flow

Flow	Variable	Coefficients of Polynomial			
		y^0	y^1	y^2	y^3
Pipe Flow $y \equiv x_2$ [for ε $y=\frac{1}{(1-x_2)}$]	$\overline{u_1u_1}(y\leq 0.3)$	9.172973×10^{-1}	-4.788776×10^{-2}	2.047739×10^{0}	2.241393X10
	$\overline{u_1u_1}(y\geq 0.3)$	1.960000×10^{-1}	3.920000×10^{0}	-	-
	$\overline{u_2u_2}$	5.958771×10^{-1}	-1.019163×10^{-1}	5.049376×10^{0}	-3.766003X10
	$\overline{u_3u_3}$	-4.341995×10^{2}	5.577307×10^{2}	-3.611550×10^{2}	9.422472X10
	$\overline{u_1u_2}(y\leq 0.6)$	-4.036000×10^{-2}	1.043600×10^{0}	-	-
	$\overline{u_1u_2}(y\geq 0.6)$	1.504105×10^{0}	-7.872304×10^{0}	1.896779X10	-1.735764X10
	$\varepsilon(x_2\leq 0.8)$	1.633072X10	-4.135510X10	4.268309X10	-2.096654X10
	$\varepsilon(x_2\geq 0.8)$	0.000000×10^{0}	2.216000×10^{0}	-	-

Table 4b. (continued)

Variable	Coefficients of Polynomial				
	y^4	y^5	y^6	y^7	y^8
$\overline{u_1u_1}(y\leq.3)$	-3.643854X10	-	-	-	-
$\overline{u_1u_1}(y\geq.3)$	-	-	-	-	-
$\overline{u_2u_2}$	$1.785351X10^2$	$-4.341995X10^2$	$5.577307X10^2$	$-3.631550X10^2$	9.422472X10
$\overline{u_3u_3}$	1.955026X10	-7.526068X10	8.160780X10	-2.806229X10	-
$\overline{u_1u_2}(y\leq0.6)$	-	-	-	-	-
$\overline{u_1u_2}(y\geq0.6)$	$5.602625X10^0$	-	-	-	-
$\varepsilon(x_2\leq0.8)$	$5.840066X10^0$	$9.643660X10^{-1}$	$9.345978X10^{-2}$	$-4.907984X10^{-3}$	$1.077000X10^{-4}$
$\varepsilon(x_2\geq0.8)$	-	-	-	-	-

Table 4c. Coefficients for Polynomial Representation of Wall-Jet and Mixing-Layer

Flow	Variable	Coefficients of Polynomial		
		y^0	y^1	y^2
Wall-Jet $y \equiv \eta$	$\overline{u_1u_1}$	3.006048×10^{-2}	-1.243471×10^{-1}	7.145900×10^{-1}
	$\overline{u_2u_2}$	4.115254×10^{-3}	2.080989×10^{-2}	1.538637×10^{-1}
	$\overline{u_3u_3}$	1.862066×10^{-2}	-5.665062×10^{-2}	3.203651×10^{-1}
	$\overline{u_1u_2}$	-5.626347×10^{-3}	3.381567×10^{-2}	6.589824×10^{-2}
	ε	2.605955×10^{-2}	-2.579015×10^{-1}	1.261837×10^{0}
Mixing-Layer $y \equiv \eta$	$(\overline{u_1u_1})^{-1}$	3.237447×10	2.911230×10	1.955159×10^{3}
	$(\overline{u_2u_2})^{-1}$	5.819788×10	3.156479×10^{2}	5.408629×10^{3}
	$(\overline{u_3u_3})^{-1}$	5.309465×10	5.435002×10^{2}	7.538680×10^{3}
	$(\overline{u_2u_2})^{-1}$	1.207018×10^{2}	7.635479×10^{2}	1.414827×10^{4}
	ε^{-1}	3.971577×10	3.912431×10	4.246117×10^{3}

Table 4c. (continued)

Flow	Variable	Coefficients of Polynomial		
		y^3	y^4	y^5
Wall-Jet	$\overline{u_1u_1}$	-1.531575×10^{0}	1.960143×10^{0}	-1.655154×10^{0}
	$\overline{u_2u_2}$	-5.549608×10^{-1}	9.259413×10^{-1}	-9.009809×10^{-1}
	$\overline{u_3u_3}$	-5.985862×10^{-1}	6.923956×10^{-1}	-5.830740×10^{-1}
	$\overline{u_1u_2}$	-2.950666×10^{-1}	5.134641×10^{-1}	-5.167986×10^{-1}
	ε	-3.094563×10^{0}	4.517398×10^{0}	-4.172103×10^{0}
Mixing-Layer	$(\overline{u_1u_1})^{-1}$	-1.520552×10^{3}	1.169577×10^{5}	-6.515994×10^{5}
	$(\overline{u_2u_2})^{-1}$	2.690483×10^{4}	8.652963×10^{4}	-4.163123×10^{6}
	$(\overline{u_3u_3})^{-1}$	-1.279335×10^{3}	5.662701×10^{5}	1.102409×10^{7}
	$(\overline{u_1u_2})^{-1}$	-4.206273×10^{4}	-3.898138×10^{5}	1.445556×10^{7}
	ε^{-1}	5.845586×10^{3}	-1.388601×10^{5}	-3.992147×10^{5}

Table 4c. (continued)

Flow	Variable	Coefficientis of Polynomial			
		y^6	y^7	y^8	y^9
Wall-Jet	$\overline{u_1u_1}$	$8.917483X10^{-1}$	$-2.886607X10^{-1}$	$5.077965X10^{-2}$	$-3.721695X10^{-3}$
	$\overline{u_2u_2}$	$5.188602X10^{-1}$	$-1.728408X10^{-1}$	$3.074390X10^{-2}$	$-2.260182X10^{-3}$
	$\overline{u_3u_3}$	$3.294072X10^{-1}$	$-1.123124X10^{-1}$	$2.060141X10^{-2}$	$-1.556864X10^{-3}$
	$\overline{u_1u_2}$	$3.053305X10^{-1}$	$-1.033107X10^{-1}$	$1.849789X10^{-2}$	$-1.358466X10^{-3}$
	ε	$2.448252X10^{0}$	$-8.819973X10^{-1}$	$1.776053X10^{-1}$	$-1.529590X10^{-2}$
Mixing-Layer	$(\overline{u_1u_1})^{-1}$	$1.989171X10^{7}$	$5.178550X10^{6}$	-	-
	$(\overline{u_2u_2})^{-1}$	$1.039410X10^{8}$	$4.315397X10^{8}$	$1.812468X10^{9}$	-
	$(\overline{u_3u_3})^{-1}$	$7.560341X10^{7}$	-	-	-
	$(\overline{u_1u_2})^{-1}$	$2.047481X10^{8}$	-	-	-
	ε^{-1}	$2.625477X10^{7}$	-	-	-

the rate of turbulence energy production balances the rate of dissipation, to within the accuracy of the data. Hence, for the analysis of the data that is to follow, the rate of dissipation for $(1 - x_2) \leq 0.42$ was calculated analytically on the basis of the polynomial representation for $\overline{u_1 u_2}$ and the logarithmic velocity distribution

$$U_1 = \frac{1}{0.42} \ln \left(\frac{1 - x_2 + 0.022}{0.056} \right) + 3.2$$

measured by Hanjalic and Launder. The resultant formula for ε is

$$\varepsilon = \frac{\overline{u_1 u_2}}{0.42 \ (1 - x_2) + 0.022}$$

B. Triple-Velocity Correlation Parameters

The most general model for $\overline{u_i u_j u_k}$, which is consistent with the sequence of assumptions in section 2.B, was presented as equation (34). Since not all of these terms will be important, a detailed examination of experimental data is required to establish which terms are significant and to evaluate the actual numerical values and unicity of the relevant parameters. In the absence of direct experimental measurements of the triple-velocity correlation, the determination of parameters would involve the repeated solution of the two-point-boundary value problems (described in section 4.A) at each step of a numerical search for optimal parameters. However, due not only to the large number of possible unknowns such a search would involve,

but also to the certain existence of many stationary points in the multidimensional parameter space, this approach to parameter estimation is computationally unrealistic. Instead, since the profiles of all independent variables which enter equation (34) (i.e. q^2, a_{ij} and ε) are known for the four flows discussed in section 4.A, and since the profiles of certain components of $\overline{u_i u_j u_k}$ are also known, the model parameters may be evaluated as the least-squares solution of a system of over-defined, linear algebraic equations.

To accomplish the least squares parameter estimate, the cross-stream coordinate in each flow was discretized into p grid intervals. At each node of the grid, the experimental data for q^2, a_{ij} and ε were substituted into equation (34) to yield, for each experimental profile of $\overline{u_i u_j u_k}$, a set of algebraic equations of the form

$$c_{\ell m}^{ijk} \alpha_m = f_\ell^{ijk} \qquad \ell = 1, 2, \ldots, p \qquad (57)$$

Here, f_ℓ^{ijk} is the experimental value of $\overline{u_i u_j u_k}$ at node ℓ, α_m are the unknown parameters to be estimated and $c_{\ell m}^{ijk}$ is the coefficient of parameter m (in equation (34)) at node ℓ. Each group of algebraic equations so obtained was normalized by multiplying each side of equation (57) by the inverse of the standard deviation (from zero) of f_ℓ^{ijk} for that experiment to ensure that the data for different experiments had comparable weighting in the least squares solution. (These weighting factors are presented in table 5.) Once normalized,

Table 5. Weighting Factors Used in Least-Squares Analyses

	Weighting Factors Used in Section:		
Flow	4.B	4.C	4.D
Channel Flow	7.131	0.5381	0.1271
Pipe Flow	2.926	0.2720	0.0210
Wall-Jet	1230.	384.5	888.6
Mixing-Layer	715.7	41.50	79.40

the n sets of equations, corresponding to the n experimental profiles of $\overline{u_i u_j u_k}$, were combined to yield the single system of (n X p) equations

$$C_{rs}\ \alpha_s = f'_r \qquad r = 1, 2, \ldots, (n \text{ X } p)$$

where C_{ij} and f'_j are a composite tensor and vector respectively. The parameters, which are optimal in a least-squares sense, were calculated as

$$\alpha_i = (C_{kj}\ C_{kj})^{-1}\ C_{mj}\ f'_m$$

where the superscript (-1) denotes the inverse of a tensor.

The least squares analysis outlined above can also provide a confidence interval for the estimated value of each parameter. For each set of p equations used to calculate the m parameters α_i, a somewhat different estimate of α_i will result. Hence, the estimated value of α_i, say $\hat{\alpha}_i$, will behave as a random variable. It can be shown (c.f. Arley and Buch (1950), pp. 192) that the new random variable

$$t = \frac{\alpha_\beta - \hat{\alpha}_\beta}{\sqrt{(\bar{C}^{-1})_{\beta\beta}}\ s}$$

with

$$s = \sqrt{\frac{(f'_r - C_{rq}\ \alpha_q)(f'_r - C_{r\ell}\ \alpha_\ell)}{(p - m)}}$$

obeys the t-distribution with F = (p - m) degrees of freedom. Here, $(\bar{C}^{-1})_{\beta\beta}$ denotes the (β,β) component of $\bar{C}^{-1}$. If $\hat{t}(P,F)$ denotes the value of t for which

$$|t| \geq \hat{t}\ (P,F)$$

with probability P, then the true value of α_β satisfies the inequality

$$|\alpha_\beta| \leq |\alpha_\beta| \pm \sqrt{(\bar{C}^{-1})_{\beta\beta}}\ s\ \hat{t}\ (P,\ F) \qquad (58)$$

with probability (1 - P). The values of $\hat{t}$ (P, f) are tabulated in most standard probability texts (c.f. Arley and Buch (1950)). It is common to take P = 0.05 so that inequality (58) gives the upper and lower bounds within which the true value of α_β falls within a confidence level of 95%.

Although it is not necessary that the number of model parameters be minimized, it is useful to eliminate systematically terms that have only a negligible effect on the calculated profiles, since this will ultimately facilitate the efficient application of the model to complex problems. In this work, the important terms were isolated in two phases. In the first phase, at the end of a parameter estimation, the standard error of the model prediction was calculated. This 'optimal' standard deviation was then compared with those which resulted when each parameter in succession was set to zero (with all others fixed at their optimal values). The parameter which, when set to zero, gave the smallest increase in standard deviation was excluded

from the model, and the parameter estimation was repeated. This process was continued until all parameters had been eliminated. The progress of the parameter elimination is shown in figure 5, where the standard deviation (denoted by the symbol '+') is plotted as a function of the number of parameters retained. The elimination sequence starts at the right in this figure and proceeds, as parameters are eliminated, toward the left. The parameter discarded at each iteration is also indicated in this figure by the number adjacent to each step. From this figure it is evident that significant increases in the standard deviation only begin with seven parameters remaining.

According to the above method of eliminating parameters, it would appear that the seven parameter formulation is the 'optimal' model. However, this proves not to be so. In fact, the above method of parameter elimination is only useful for the elimination of parameters which have a negligible effect on the standard deviation. It is not a suitable criterion for the rejection of terms which have a non-negligible effect on the standard deviation. Hence, a second phase, which adopted a somewhat more sensitive method for the elimination of parameters, was undertaken. At a typical step in this elimination process, for which m parameters remained, each parameter in succession was tentatively omitted from the model, and the *full least-squares solution* for the remaining (m - 1) parameters was repeated. This process led to m values of the standard deviation, one corresponding to each parameter. That parameter, which when

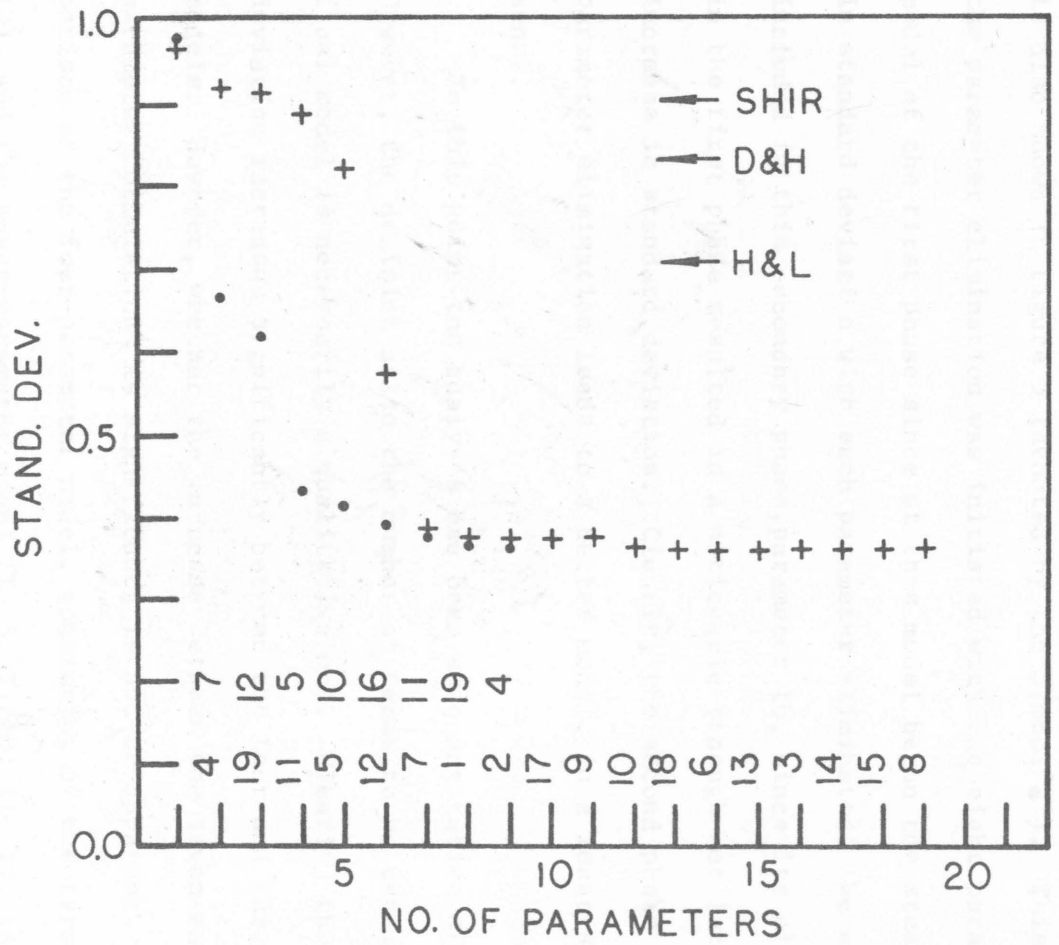

FIGURE 5: SEQUENCE OF TRIPLE-VELOCITY CORRELATION PARAMETER ELIMINATION;
+ -PRELIMINARY PHASE, • -SECONDARY PHASE.

omitted from the model, led to the smallest increase in standard deviation, was discarded from the model, and the process was repeated. As in the first phase, this process was continued until all of the parameters had been eliminated. The secondary elimination process is also shown in figure 5 (denoted by the symbol'•'). This phase of the parameter elimination was initiated with the eight parameter model of the first phase since at this model began the steady increase in standard deviation with each parameter eliminated. We also included in this secondary phase,parameter 10, since its elimination in the first phase resulted in a noticeable (though not large) increase in standard deviation. Clearly, the second phase of the parameter elimination leads to a better model, in a least-squares sense.

To this point the analysis has been as quantitative as possible. However, the decision as to the number of terms to be retained in the final model is necessarily a qualitative one. Clearly, the standard deviation increases significantly between the four-and three-parameter models. However, whether the increase between the seven-and four-parameter formulations is significant, is not as apparent. A comparison of the four-parameter model, consisting of the terms (1, 5, 7, 12), and the seven-parameter model (1, 5, 7, 10, 11, 12, 16) is presented in figures 6 - 9, where the four-parameter model is shown as the solid line, the seven parameter model is represented by the long-short broken line, and the experimental data are given by the discrete points. In general, changes of less than 5% occur in the wall-jet and mixing-layer, and although somewhat larger changes do

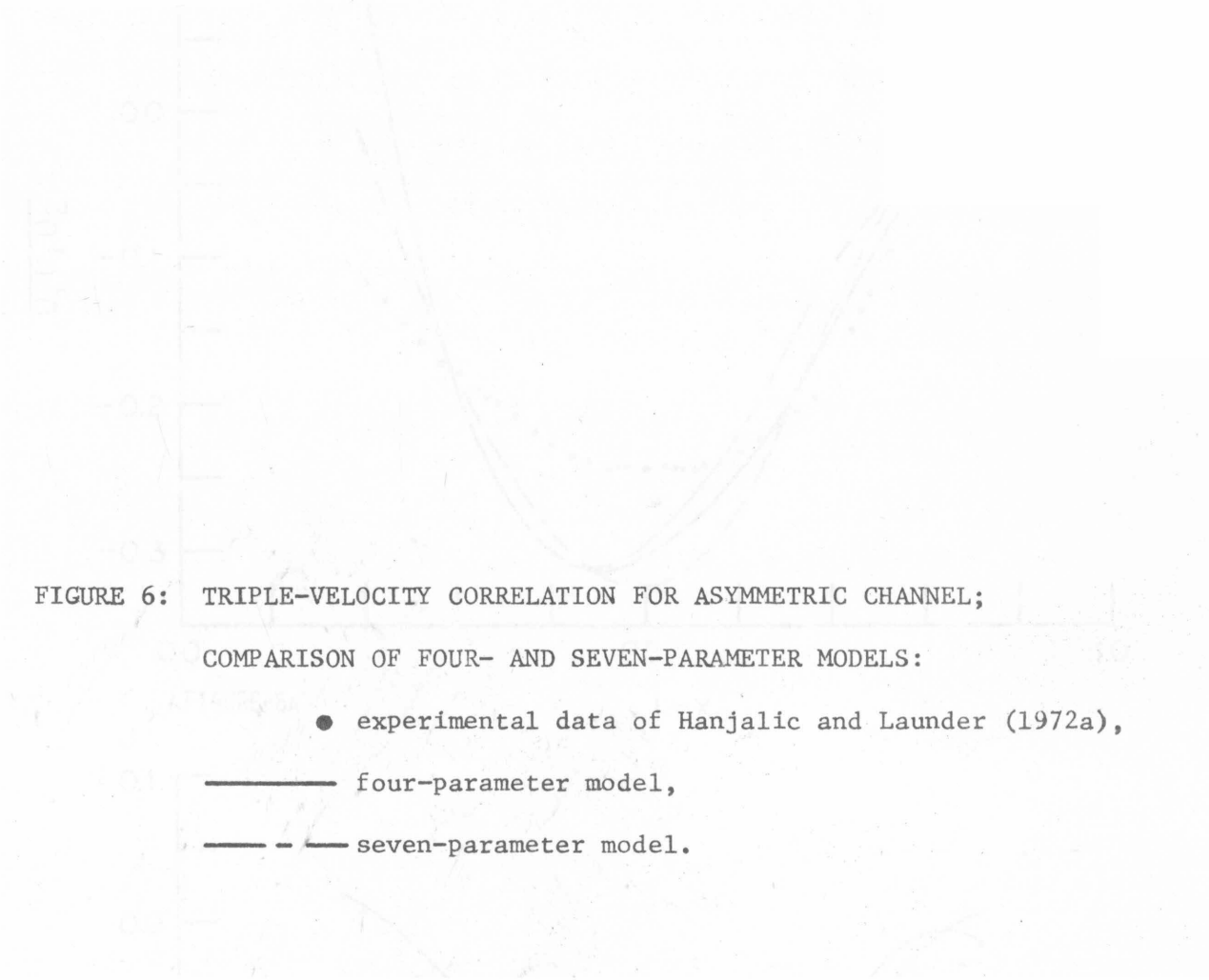

FIGURE 6: TRIPLE-VELOCITY CORRELATION FOR ASYMMETRIC CHANNEL;
COMPARISON OF FOUR- AND SEVEN-PARAMETER MODELS:

● experimental data of Hanjalic and Launder (1972a),

———— four-parameter model,

——— - ——— seven-parameter model.

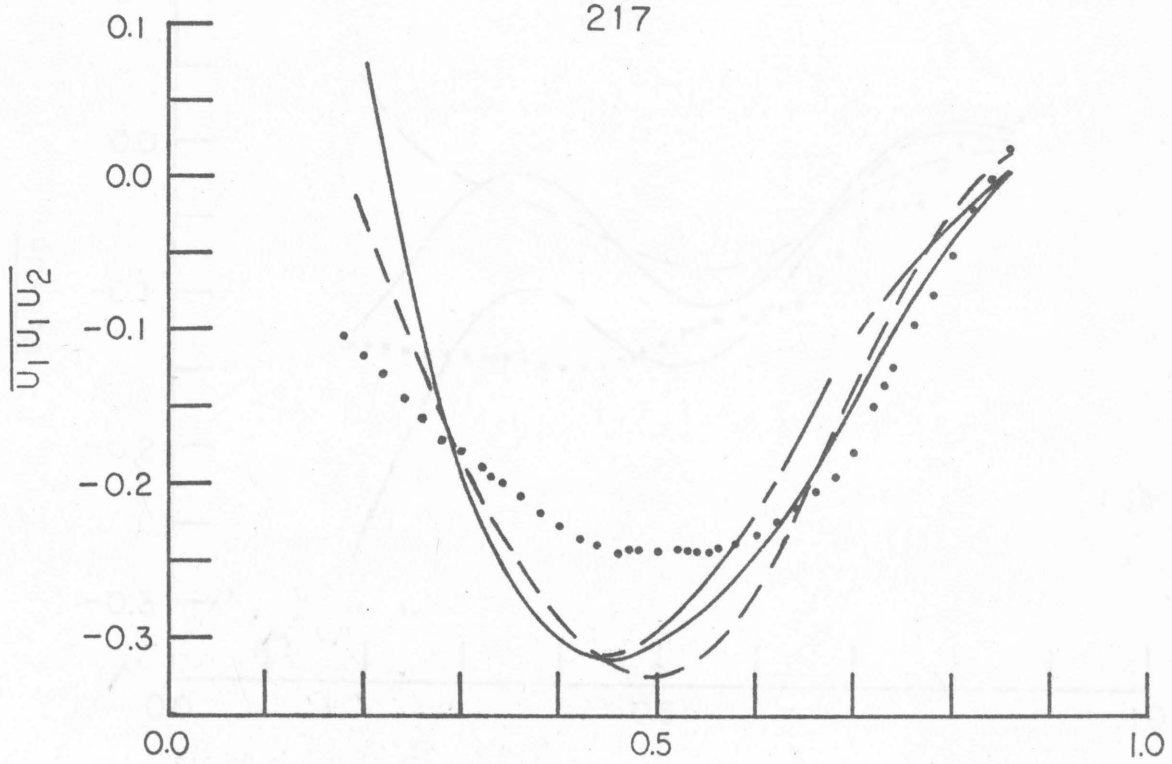

FIGURE 6A

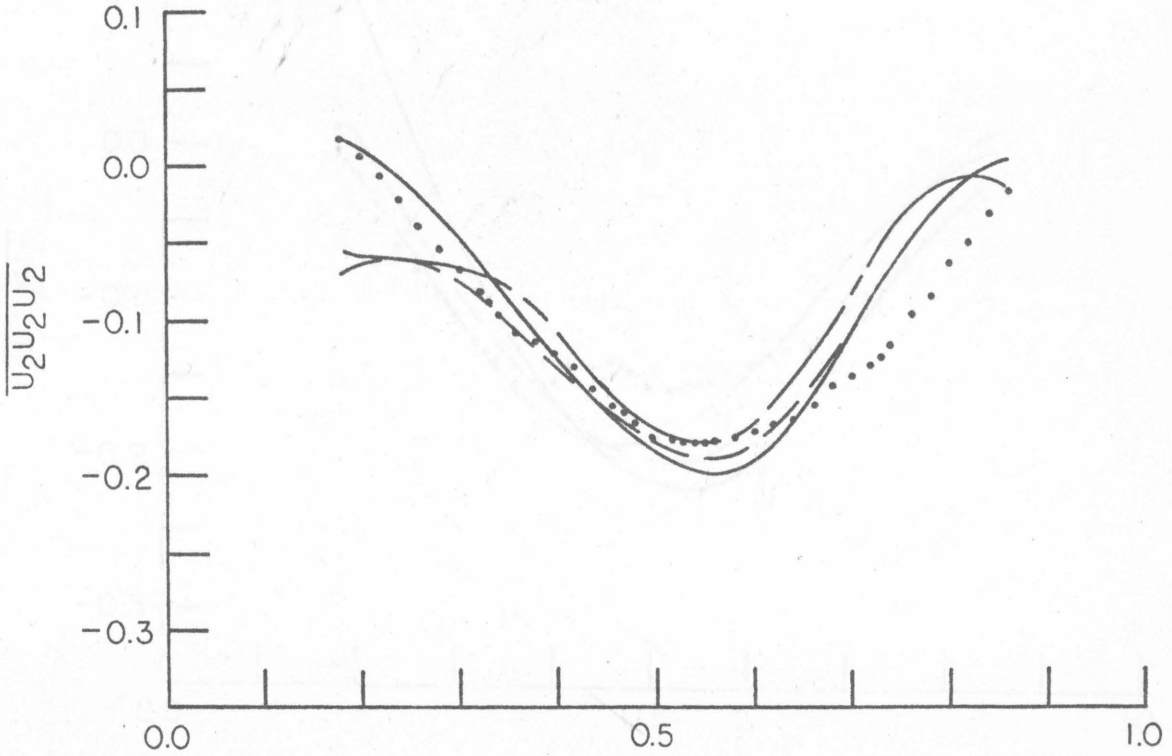

FIGURE 6B

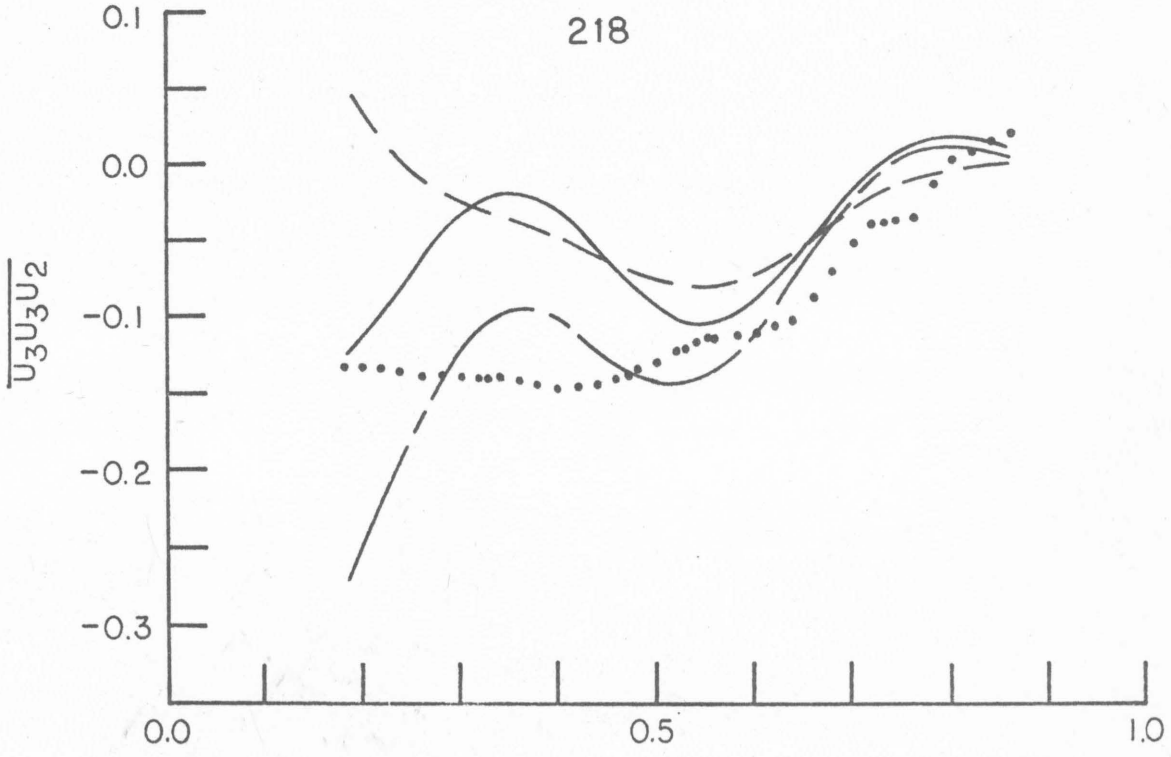

FIGURE 6c

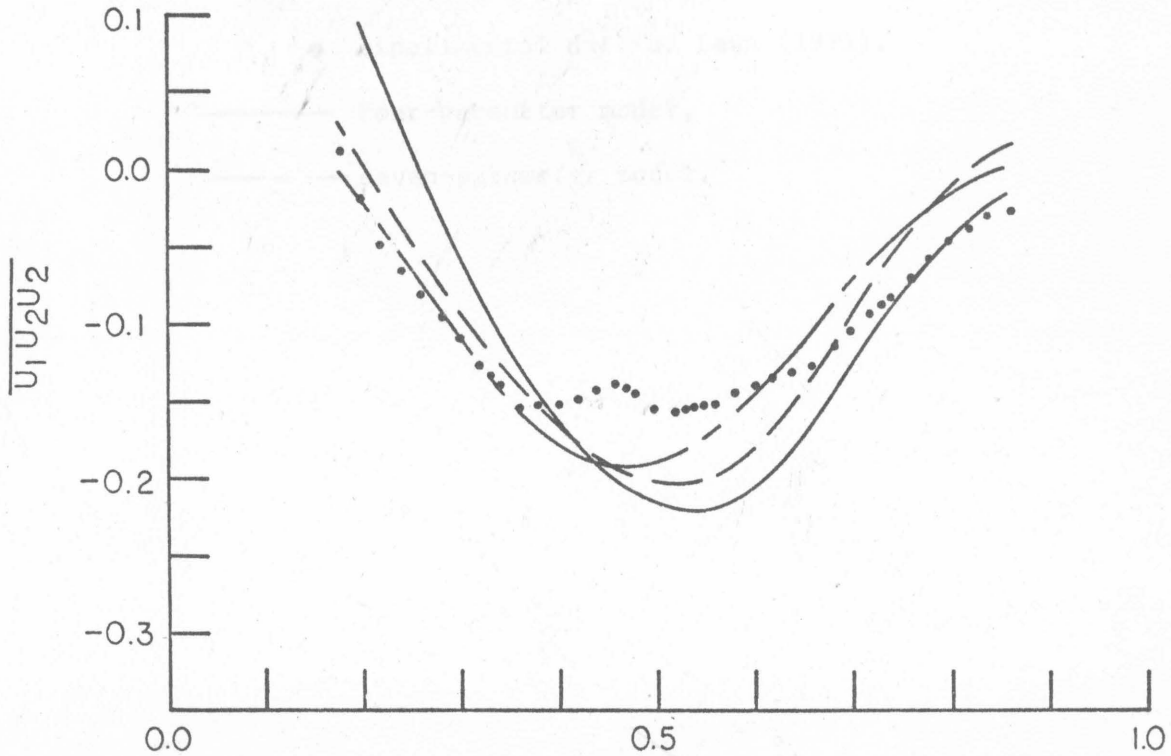

FIGURE 6D

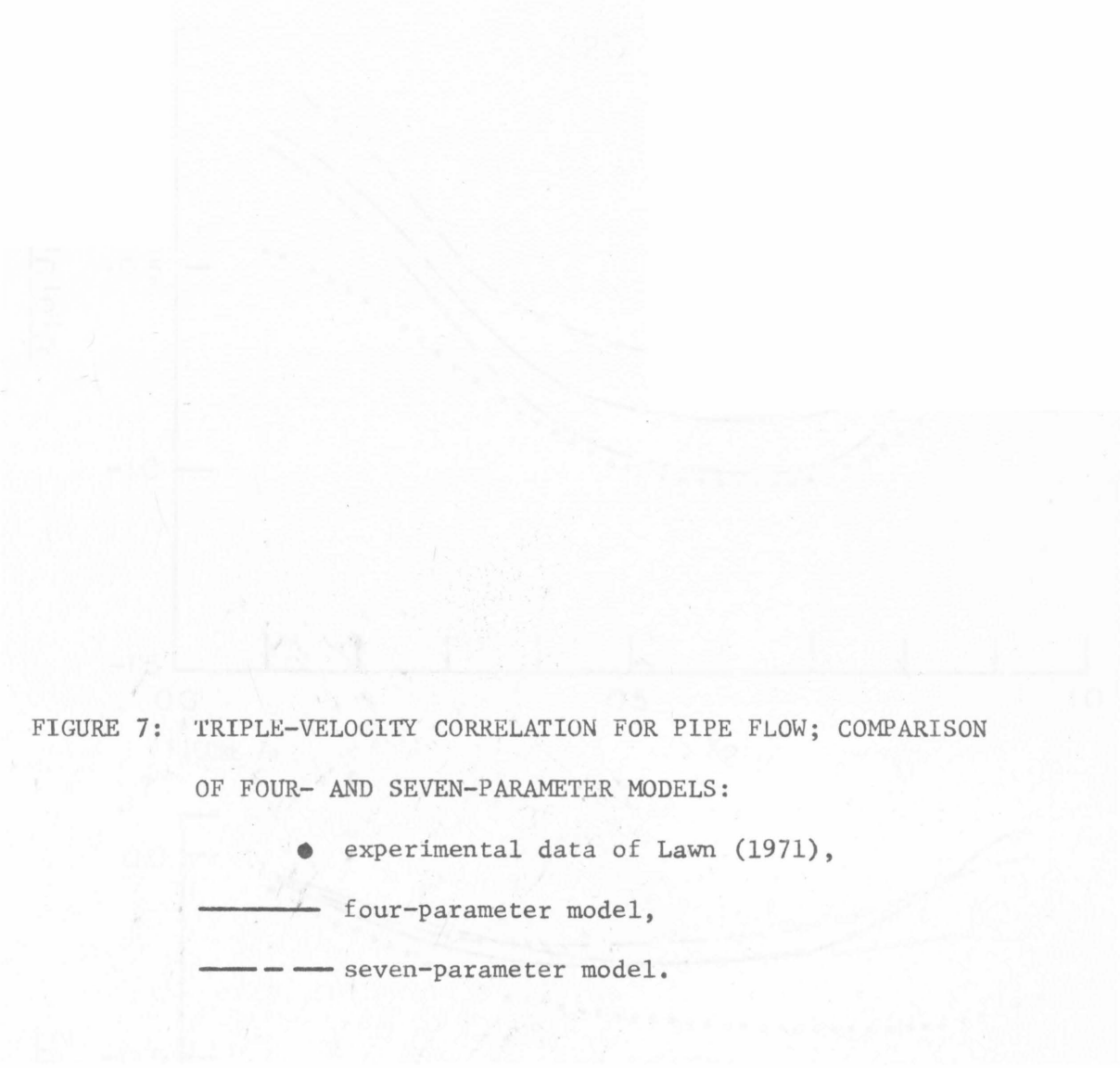

FIGURE 7: TRIPLE-VELOCITY CORRELATION FOR PIPE FLOW; COMPARISON OF FOUR- AND SEVEN-PARAMETER MODELS:

● experimental data of Lawn (1971),

———— four-parameter model,

——— — ——— seven-parameter model.

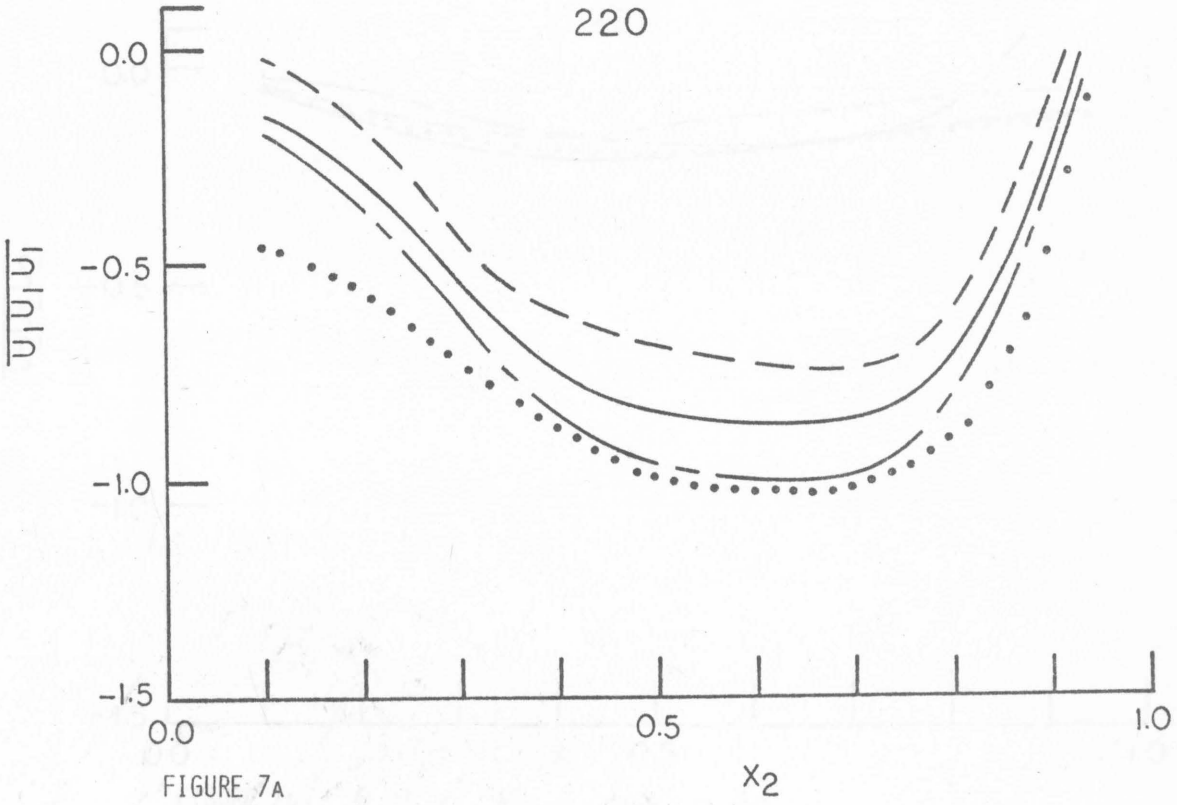

FIGURE 7A

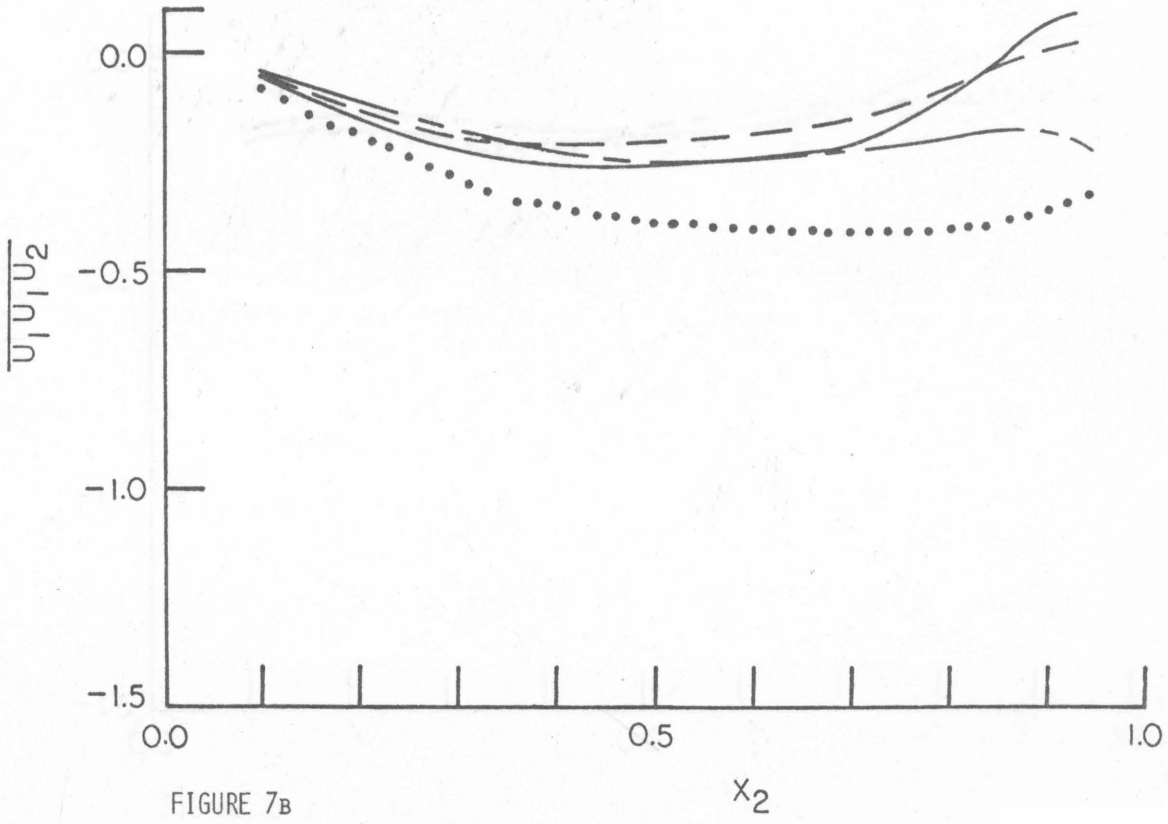

FIGURE 7B

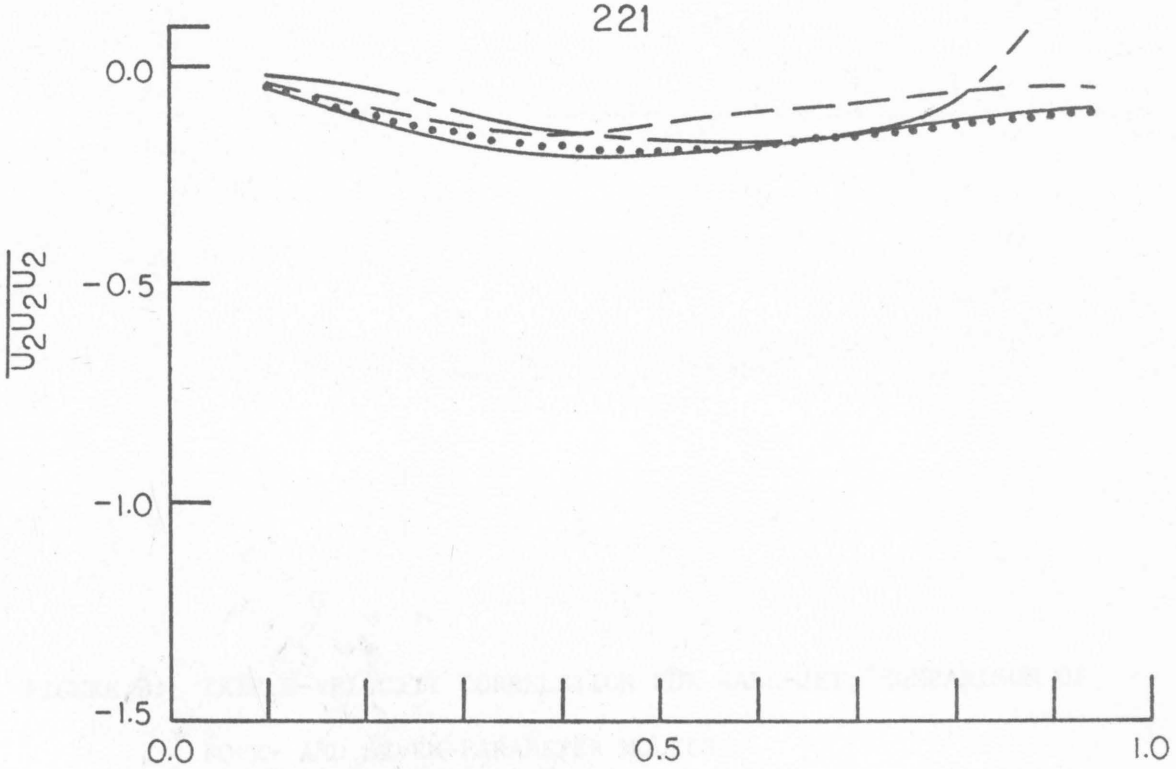

FIGURE 7C

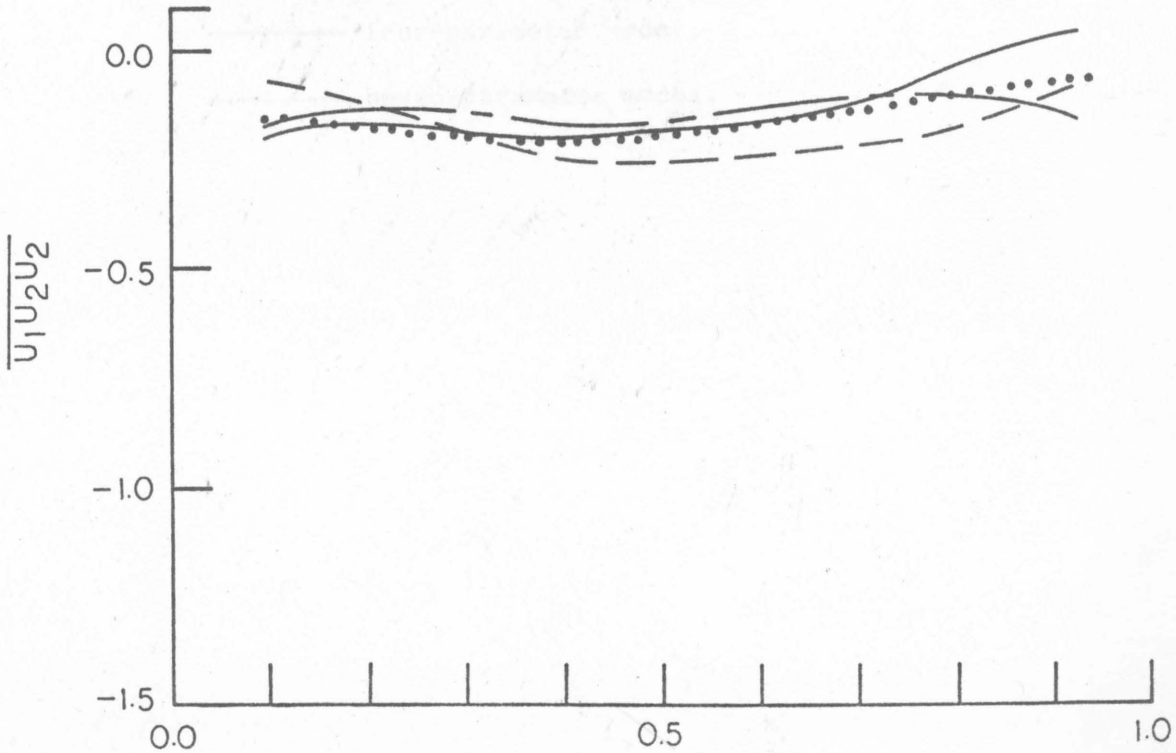

FIGURE 7D

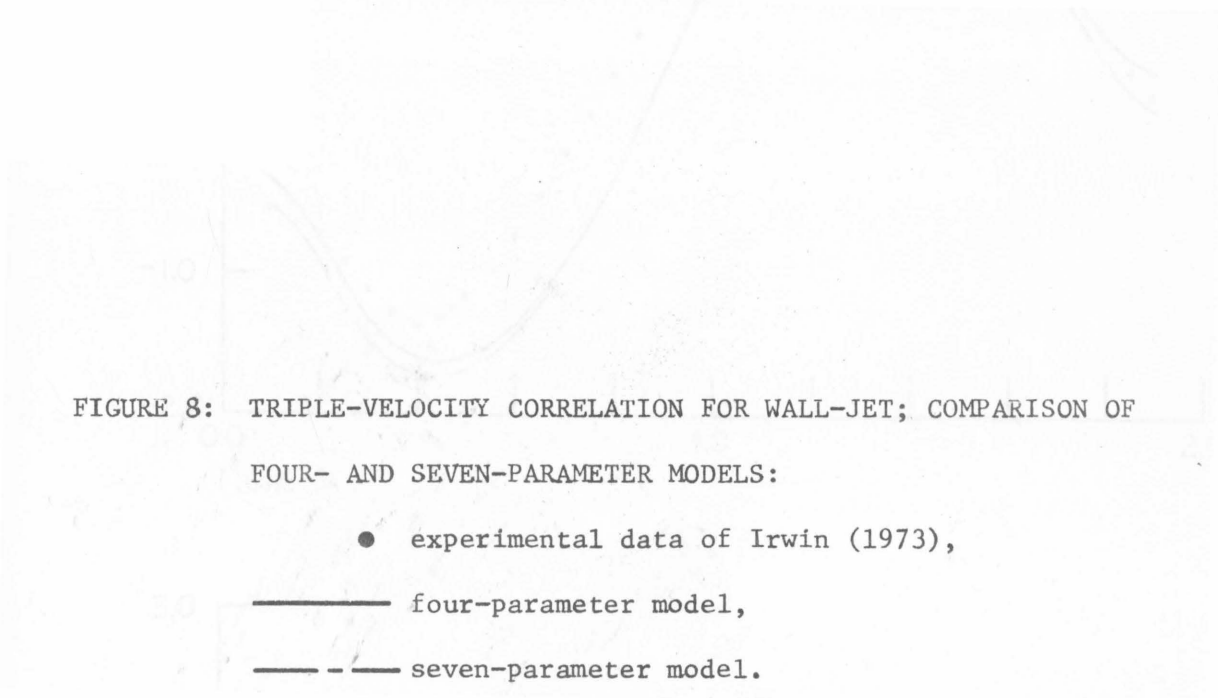

FIGURE 8: TRIPLE-VELOCITY CORRELATION FOR WALL-JET; COMPARISON OF FOUR- AND SEVEN-PARAMETER MODELS:

● experimental data of Irwin (1973),

———— four-parameter model,

——— - ——— seven-parameter model.

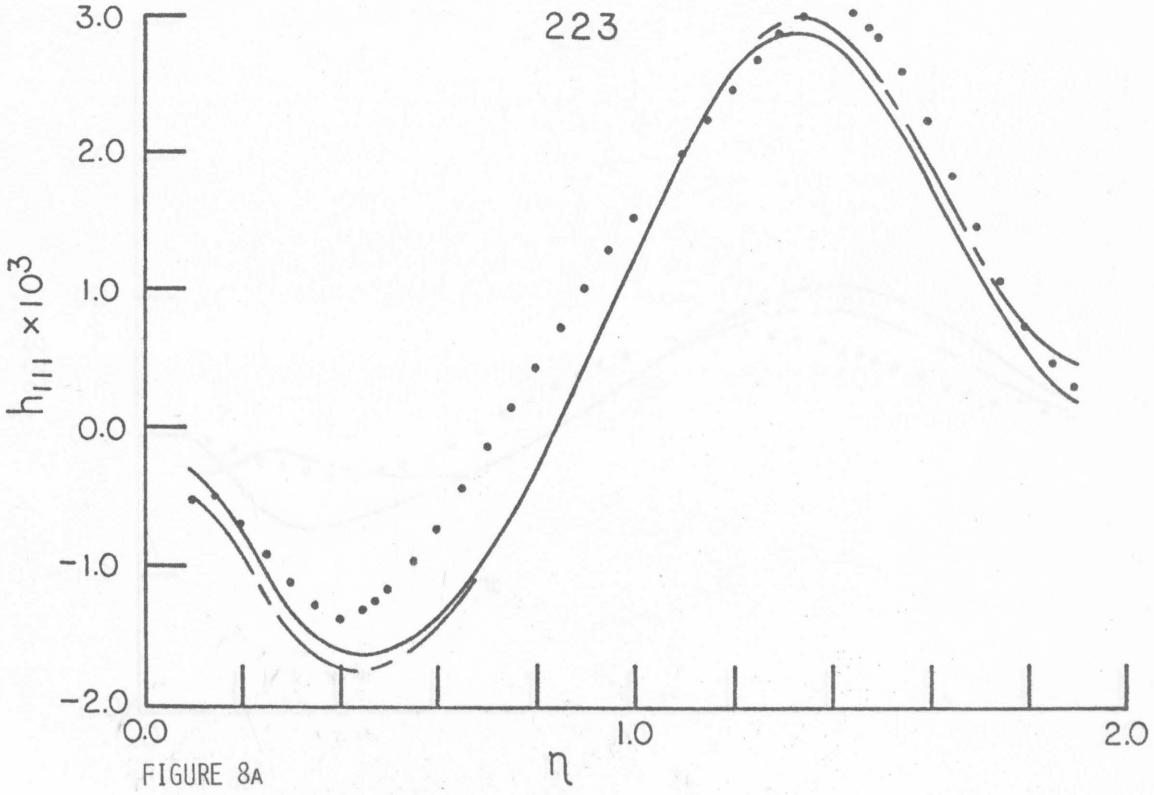

FIGURE 8A

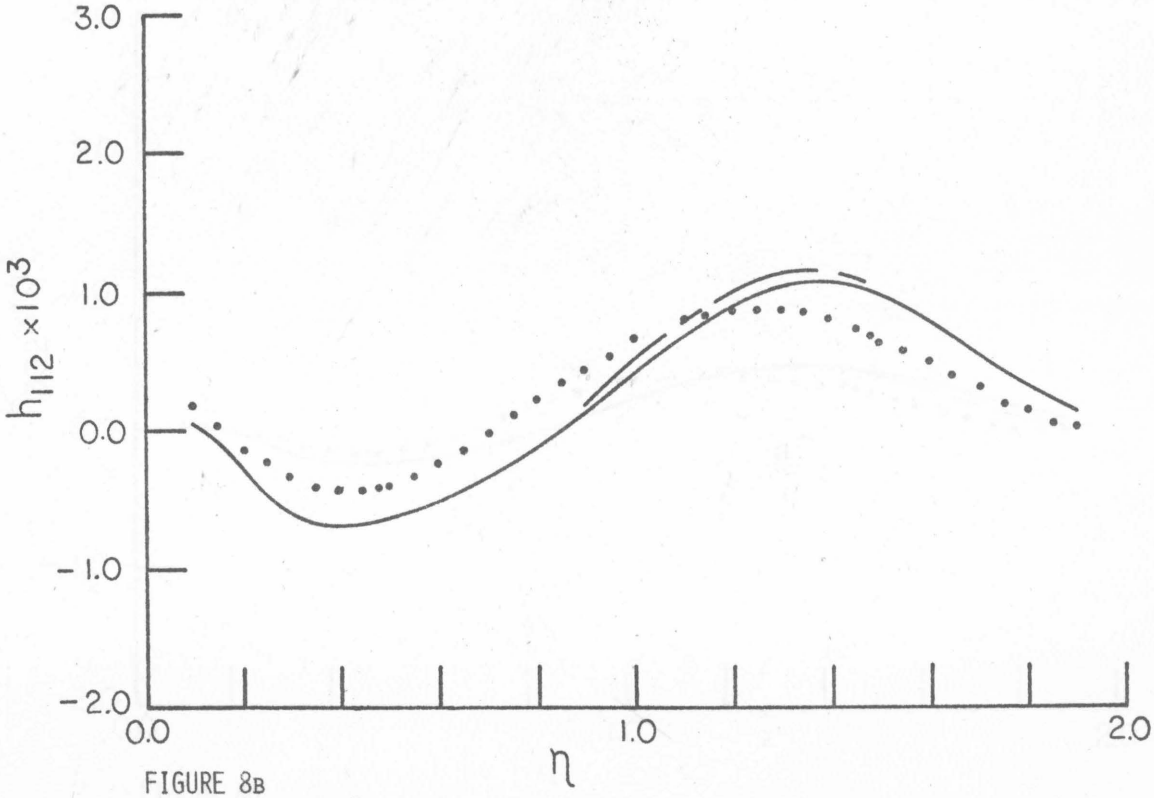

FIGURE 8B

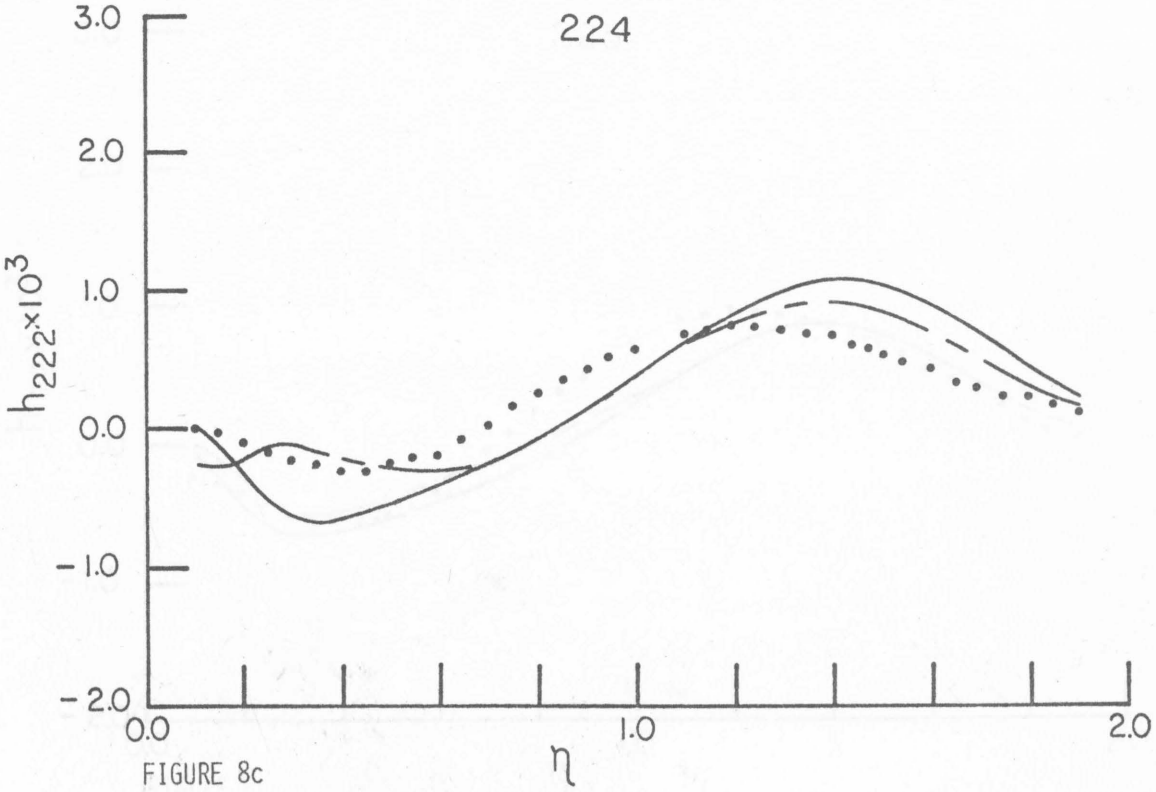

FIGURE 8c

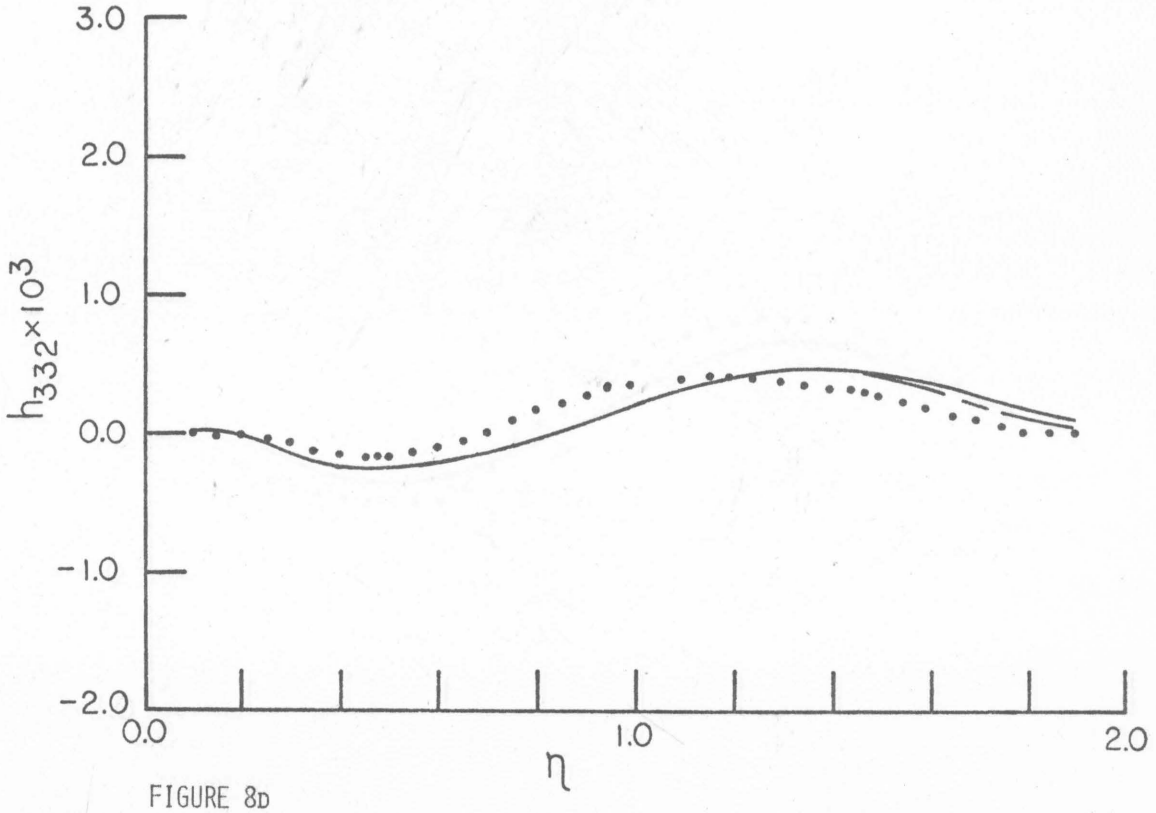

FIGURE 8D

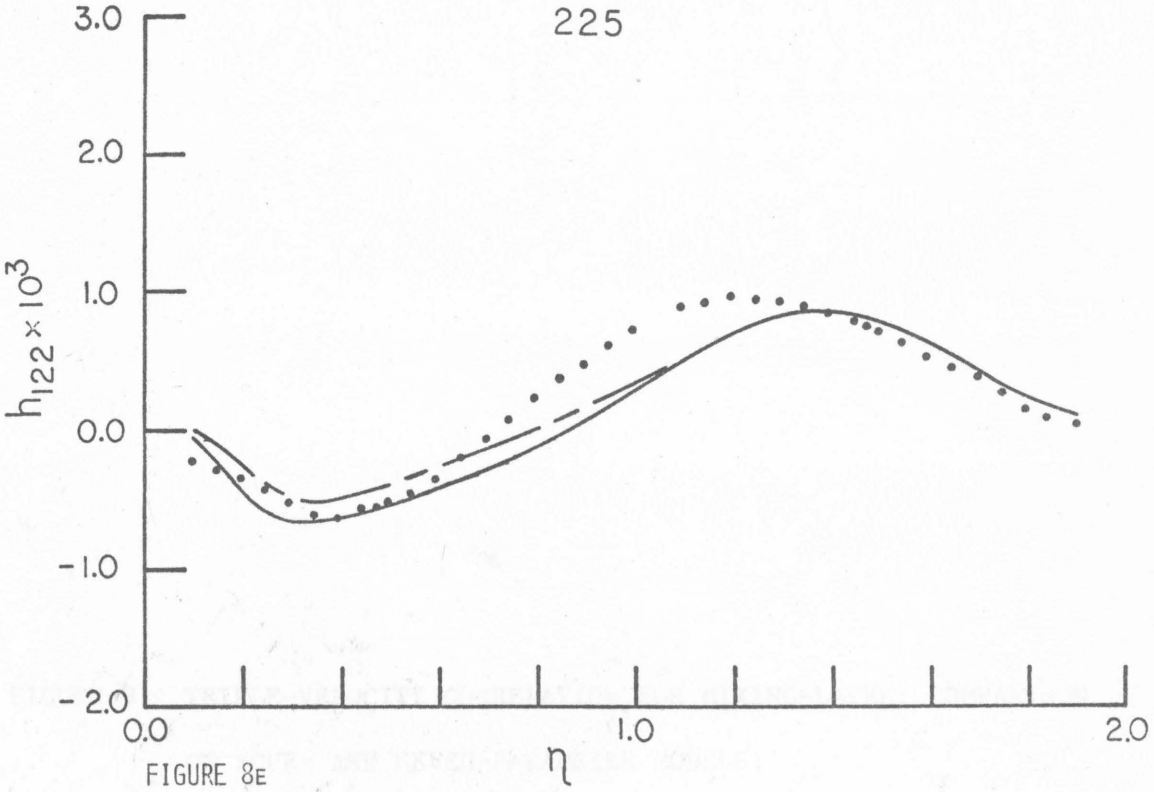

FIGURE 8E

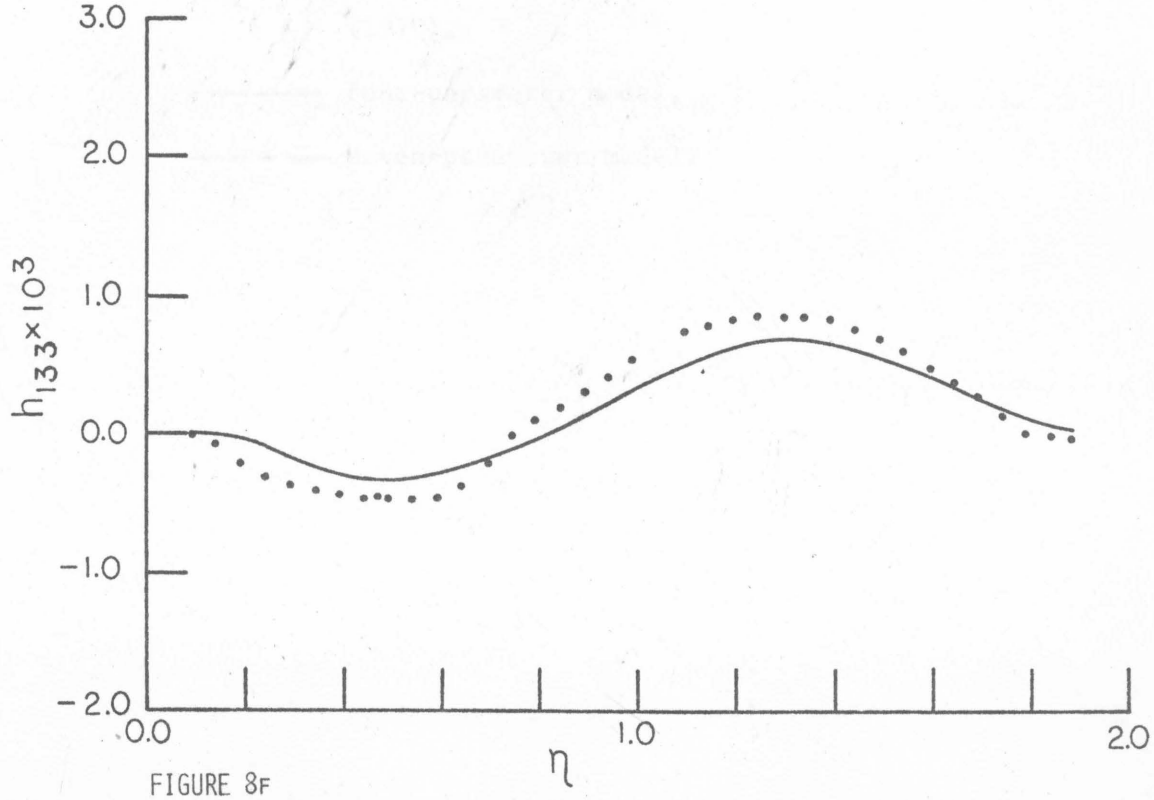

FIGURE 8F

FIGURE 9: TRIPLE-VELOCITY CORRELATION FOR MIXING-LAYER; COMPARISON OF FOUR- AND SEVEN-PARAMETER MODELS:

● experimental data of Wygnanski and Fiedler (1970),

———— four-parameter model,

——— - ——— seven-parameter model.

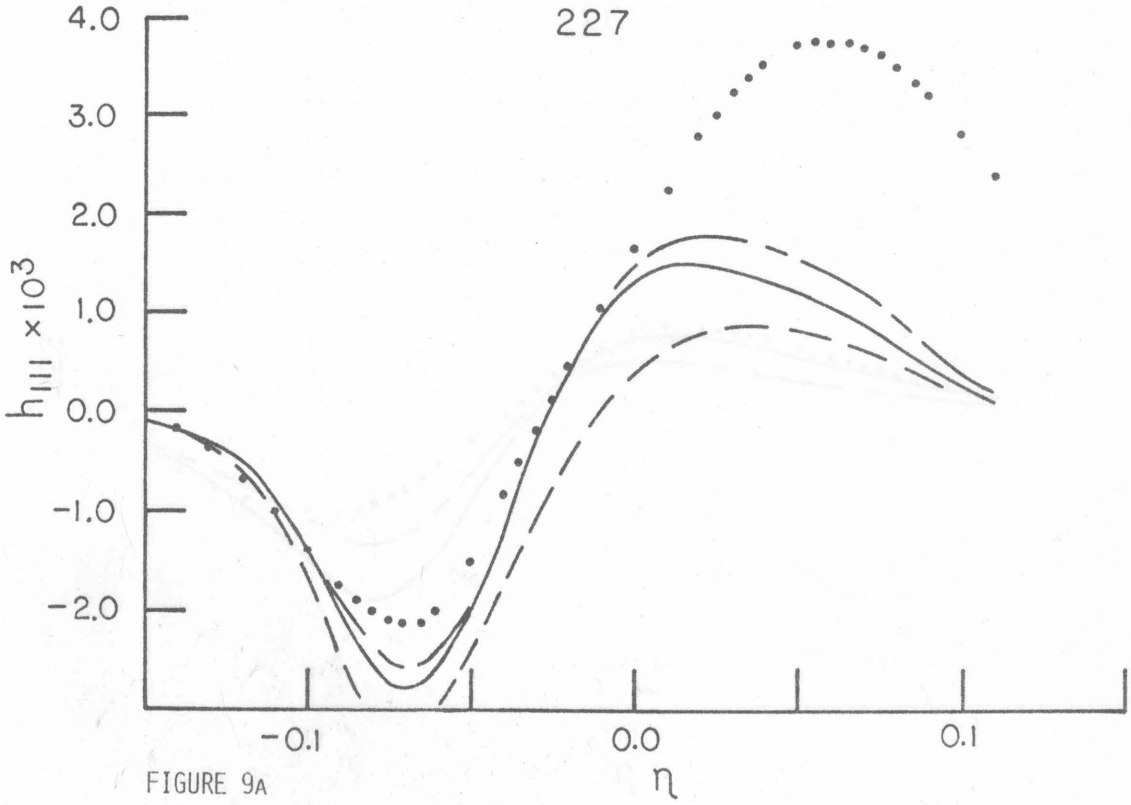

FIGURE 9A

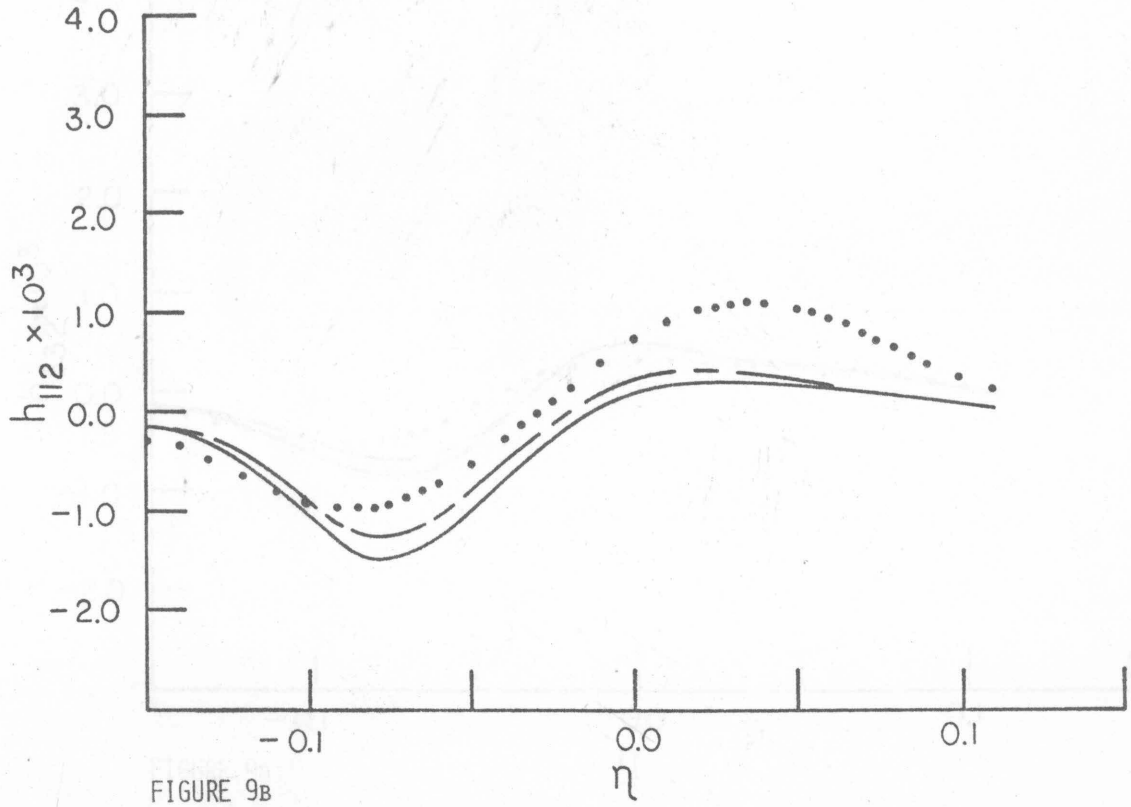

FIGURE 9B

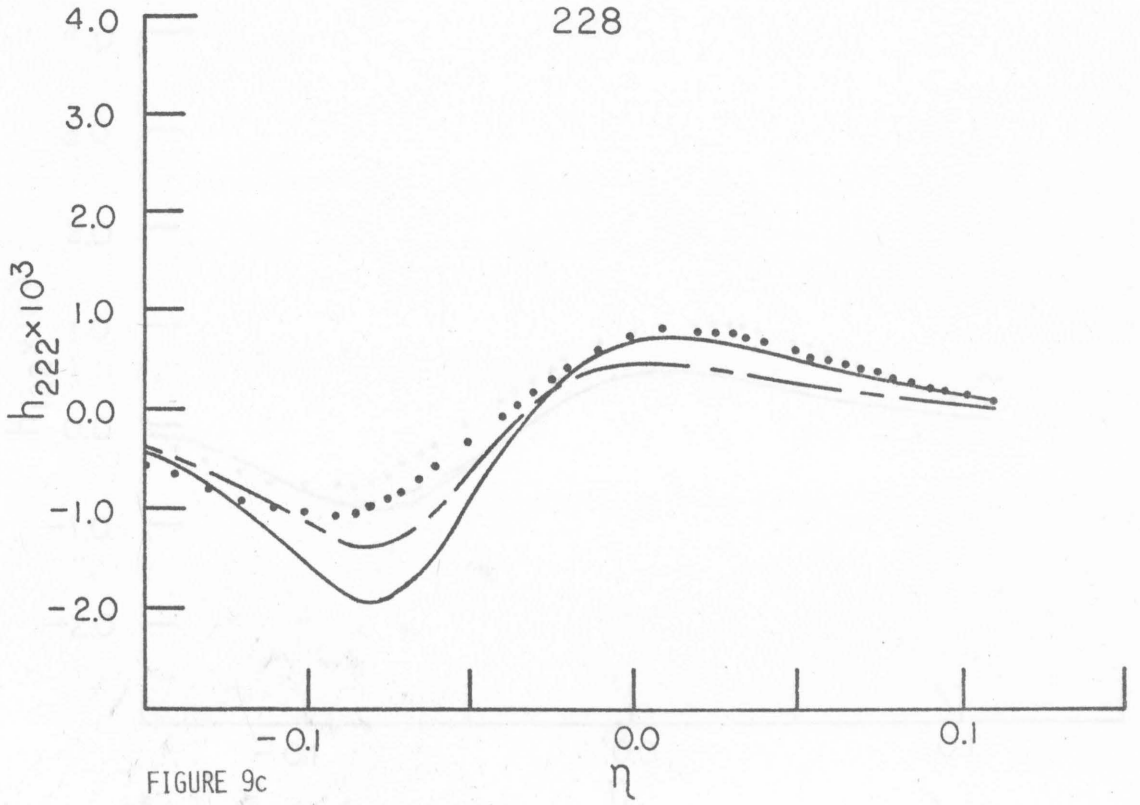

FIGURE 9C

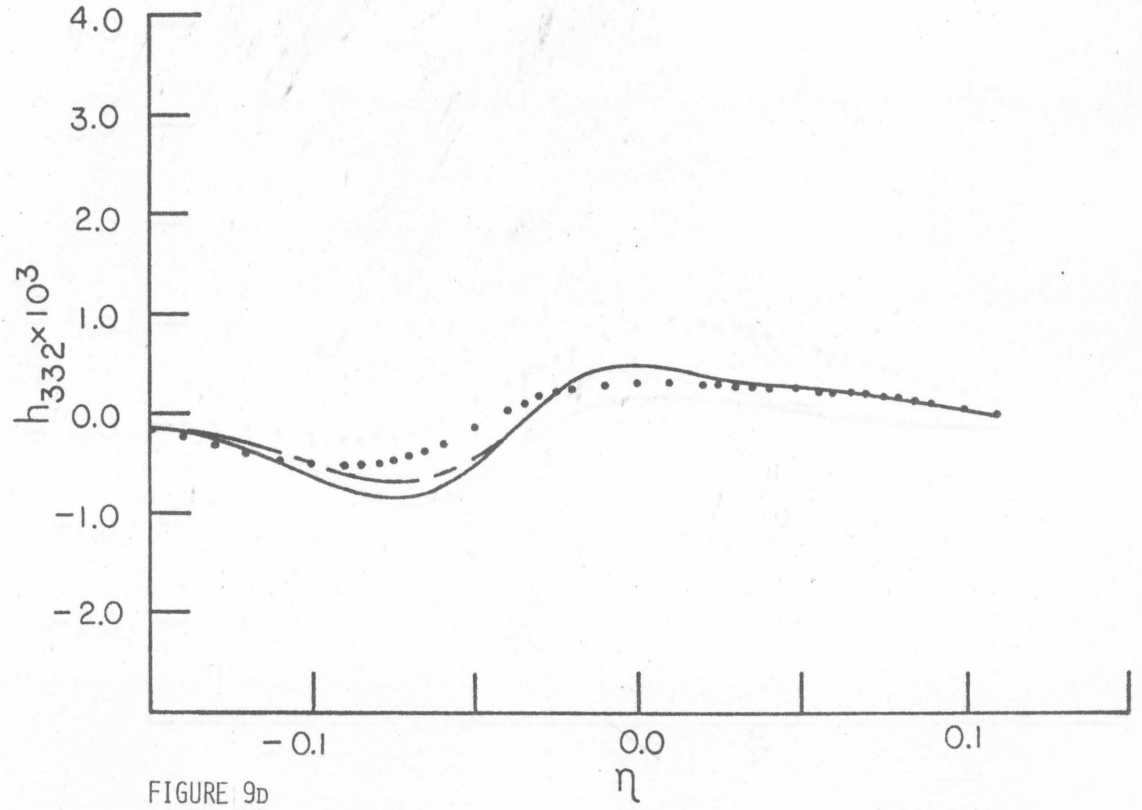

FIGURE 9D

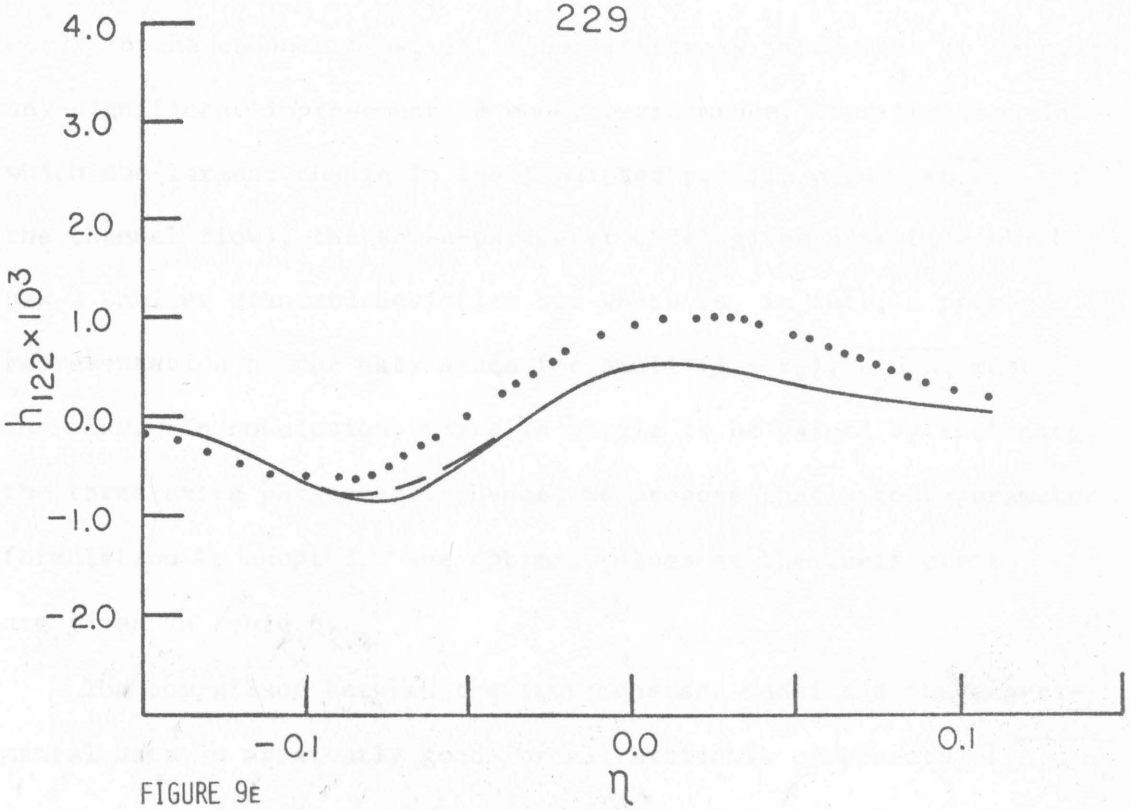

FIGURE 9E

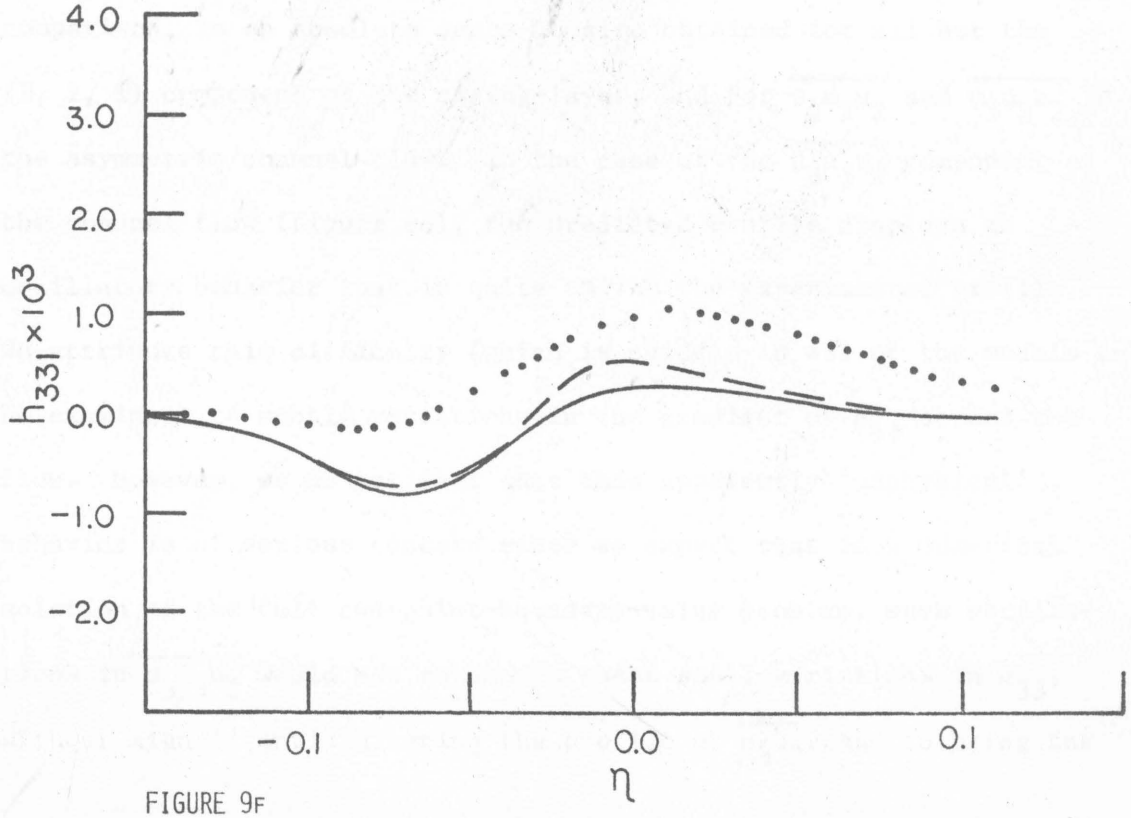

FIGURE 9F

occur in the channel flow, it is qualitatively impossible to identify any significant improvement in model performance. For the case in which the largest change in the predicted profile occurs ($\overline{u_3u_3u_2}$ of the channel flow), the seven-parameter model gives a profile which has a smaller standard deviation but which is, in fact, a poorer representation of the data since for small $(1 - x_2)$, $\overline{u_3u_3u_2}$ must *increase*. In conclusion, there is little to be gained by including the three extra parameters. Hence, we propose that a four-parameter formulation be adopted. The optimal values of the coefficients are given in table 6.

The comparison between the four-constant model and the experimental data is apparently good for all available components of $\overline{u_iu_ju_k}$ for the pipe flow of Lawn and the wall-jet of Irwin. Reasonable comparison, in an absolute sense is also obtained for all but the (1, 1, 1) component of the mixing-layer, and for $\overline{u_1u_1u_2}$ and $\overline{u_3u_3u_2}$ in the asymmetric channel flow. In the case of the $\overline{u_3u_3u_2}$ component of the channel flow (figure 6c), the predicted profile displays an oscillatory behavior that is quite unlike the experimental profile. We attribute this difficulty (which is evident in all of the models to be examined) to subtle variations in the gradient of a_{33} across the flow. However, we do not feel that this apparently 'unphysical' behavior is of serious concern since we expect that in a numerical solution of the full two-point-boundary-value problem, such oscillations in $\overline{u_3u_3u_2}$ would act to smooth these small variations in a_{33}, without significantly altering the profile of $\overline{u_3u_3}$, and to bring the

Table 6. Triple-Velocity Correlation Parameters

Parameter	Flows Included in Parameter Estimate				
	All Flows	Assymetric Channel	Pipe Flow	Wall-Jet	Mixing-Layer
$\alpha_1 X10^3$	-8.14±0.31	-5.55±0.43	-10.07±0.71	-7.27±0.42	-5.10±1.2
$\alpha_5 X10^2$	-1.72±0.12	-1.13±0.09	-3.14±0.28	-1.09±0.26	-2.58±0.85
$\alpha_7 X10^2$	-4.80±0.22	-2.41±0.36	-4.92±0.39	-5.45±0.26	-4.19±0.82
$\alpha_{12} X10$	-1.02±0.06	-0.431±0.075	-1.28±0.08	-0.553±0.14	-3.52±0.55

predicted profile into better agreement with the data.

Also relevant to the present discussion, is the comparison between the results obtained with the present four-parameter model and those obtained with the previous triple-velocity correlation models, which were discussed in section 2.D. To provide the most objective comparison of these models, we re-calculated the constants for each, using the same data and the same least-squares algorithm that were used in the development of the present model. The standard deviations that resulted for each are given in figure 5. The single constant in the model of Hanjalic and Launder (equation 39) which best fits the data, was -0.053 ± 0.003. This compares favorably with the value of -0.04 suggested by the authors. The constant obtained for Shir's model was -0.0092 ± 0.0001 which is only about 10% smaller than the value of -0.01 adopted by Shir. Finally, the optimal value for the coefficient in the model of Wyngaard et al., and Daly and Harlow was calculated to be -0.065 ± 0.006. In contrast the value used by Wyngaard et al. is larger in magnitude by a factor of about two, while Daly and Harlow's suggested value is nearly *15 times greater than the optimal value*. A graphical comparison between the profiles predicted by each of the triple-velocity correlation models, with the calculated 'optimal' parameters, is shown in figures 10 - 13.

The most important point to note with regard to these figures is the adequacy with which each model reproduces the data. Of the *one* parameter models, all are quite poor for $\overline{u_1 u_1 u_2}$ in the asymmetric channel flow, $\overline{u_1 u_1 u_1}$ for the pipe flow, $\overline{u_1 u_1 u_1}$ for the wall-jet, and,

FIGURE 10: TRIPLE-VELOCITY CORRELATION FOR ASYMMETRIC CHANNEL; COMPARISON OF MODELS:

- ● experimental data of Hanjalic and Launder (1972a),
- ——— present four-parameter model,
- — — — — model of Hanjalic and Launder (1972b),
- ——- - —— model of Shir (1973),
- ——— - —— model of Daly and Harlow (1970).

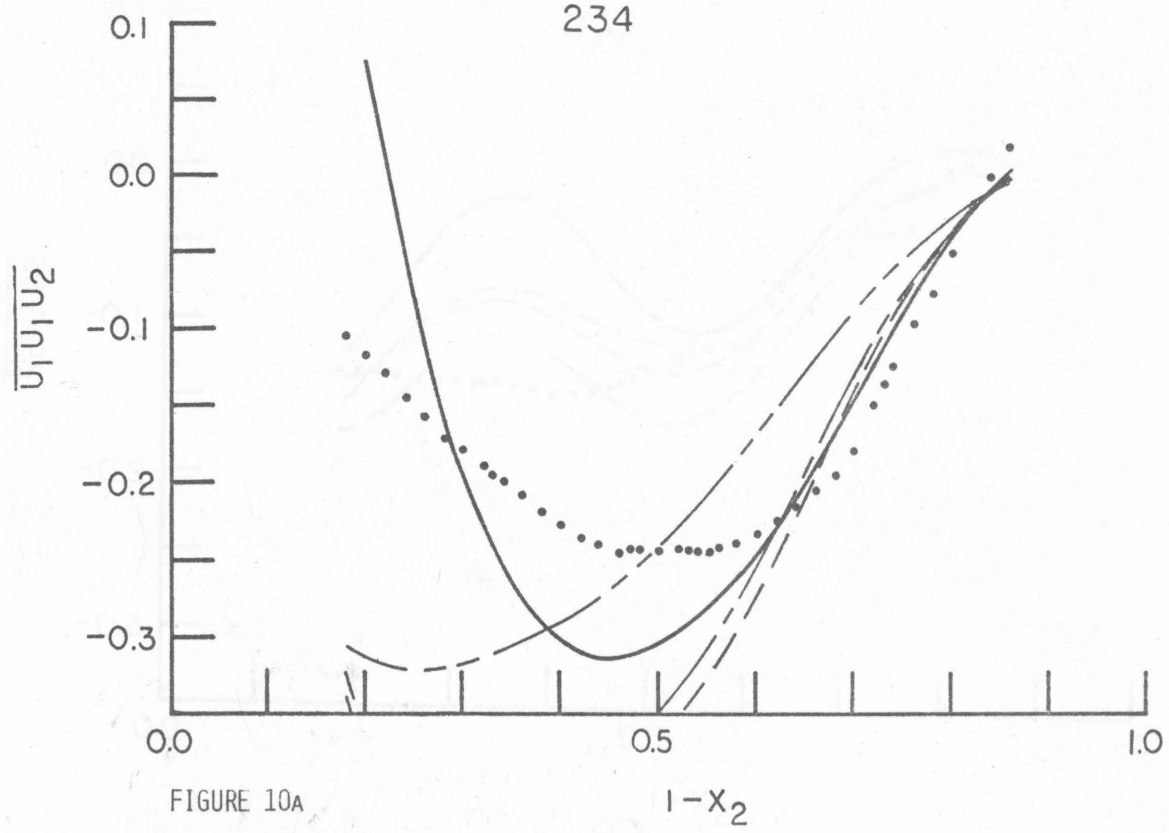

FIGURE 10A

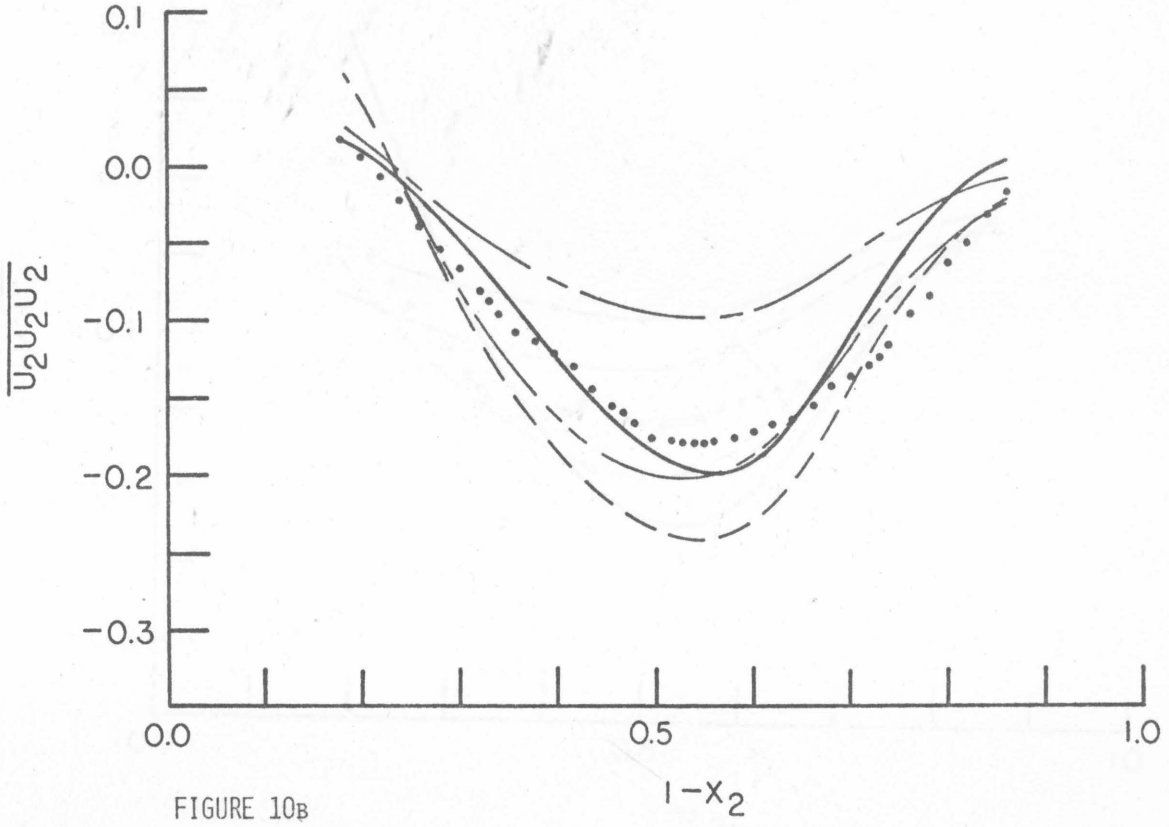

FIGURE 10B

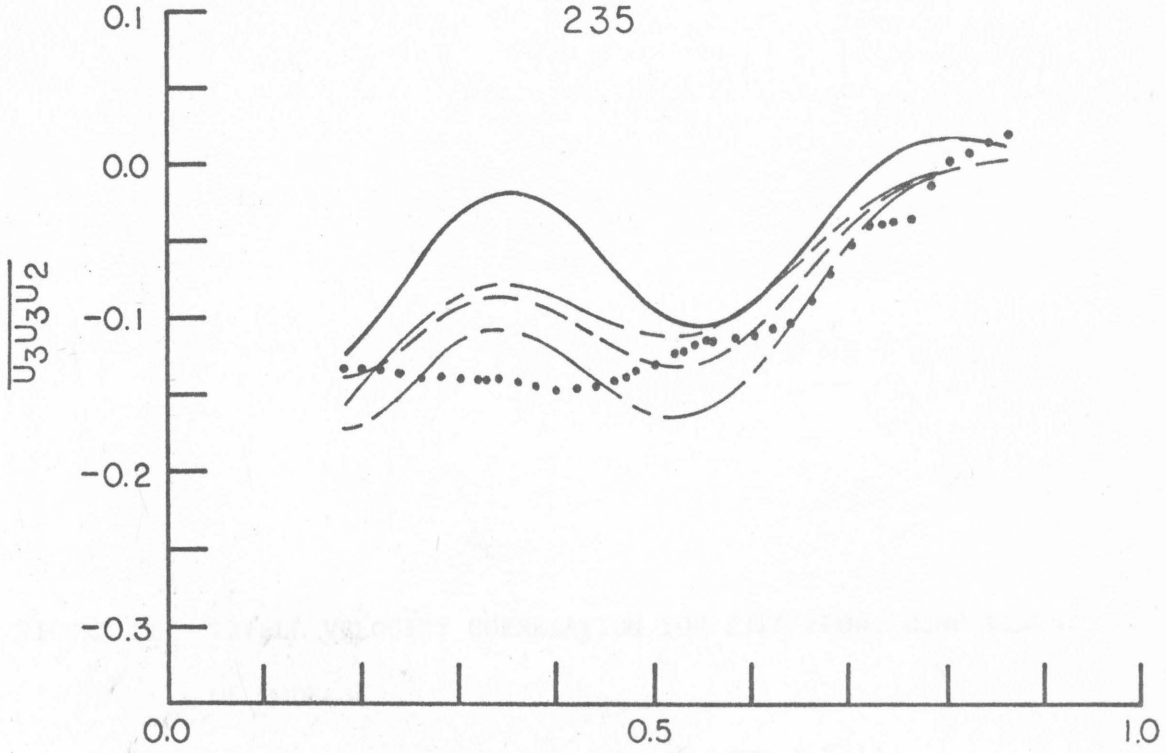

FIGURE 10c

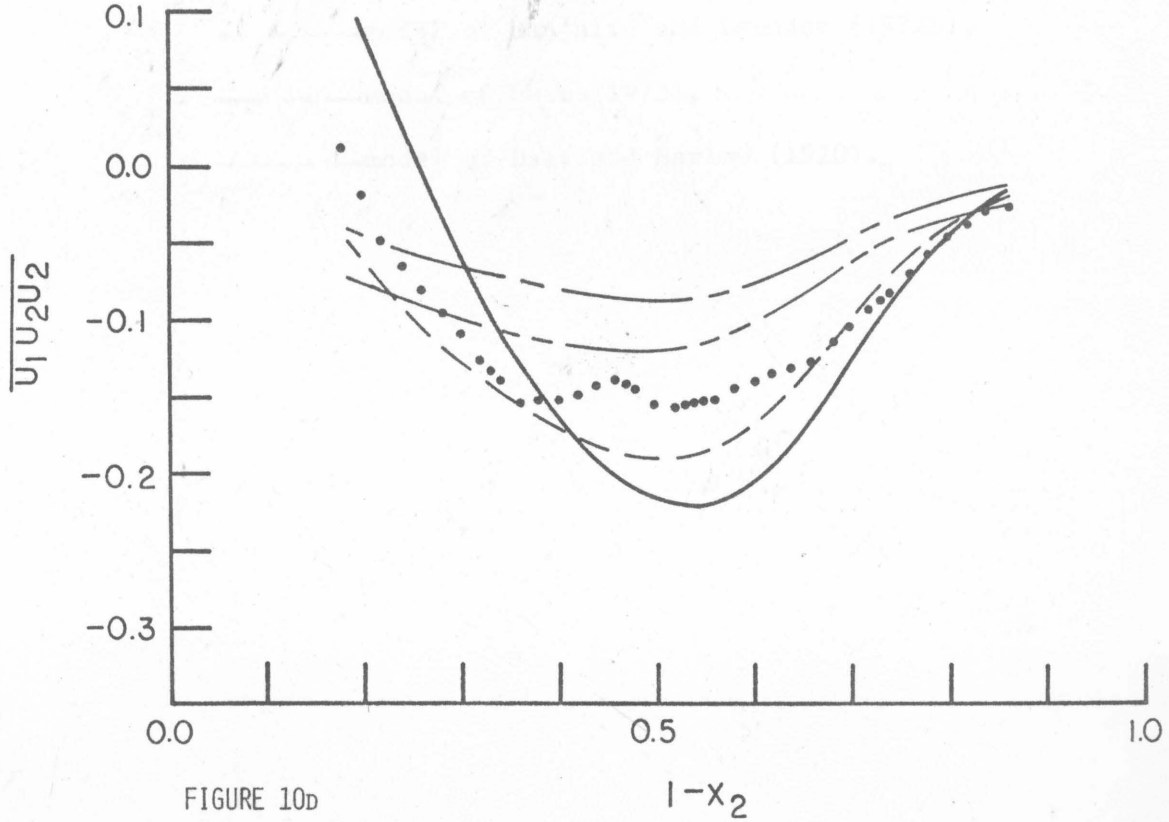

FIGURE 10D

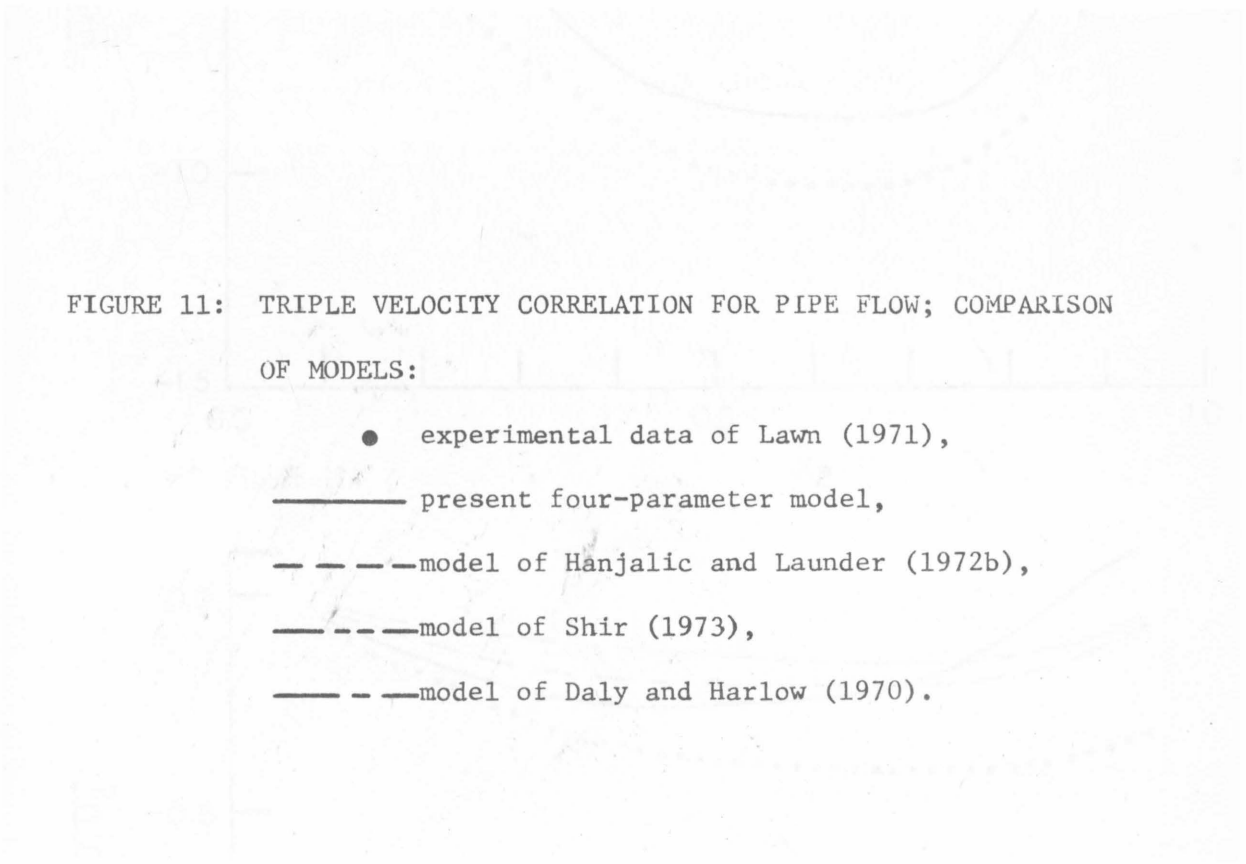

FIGURE 11: TRIPLE VELOCITY CORRELATION FOR PIPE FLOW; COMPARISON OF MODELS:

● experimental data of Lawn (1971),

———— present four-parameter model,

— — — —model of Hanjalic and Launder (1972b),

——- - - —model of Shir (1973),

—— - —model of Daly and Harlow (1970).

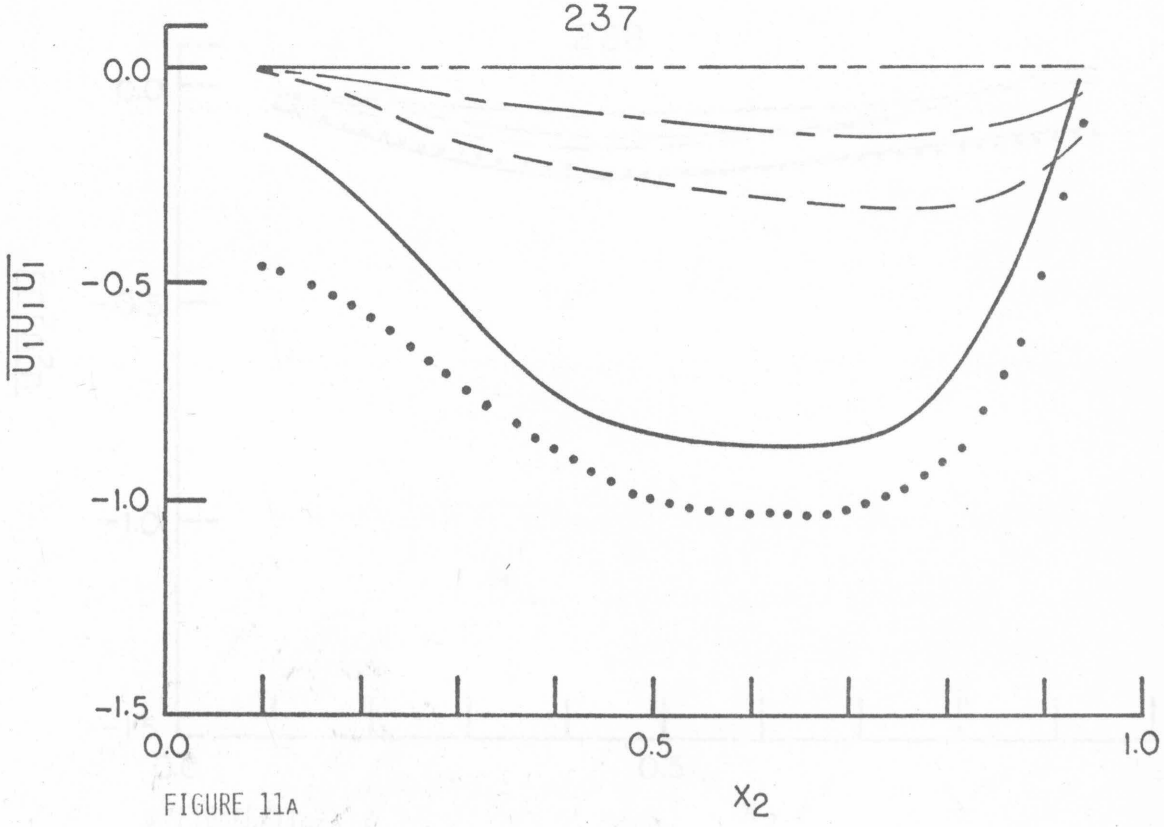

FIGURE 11A

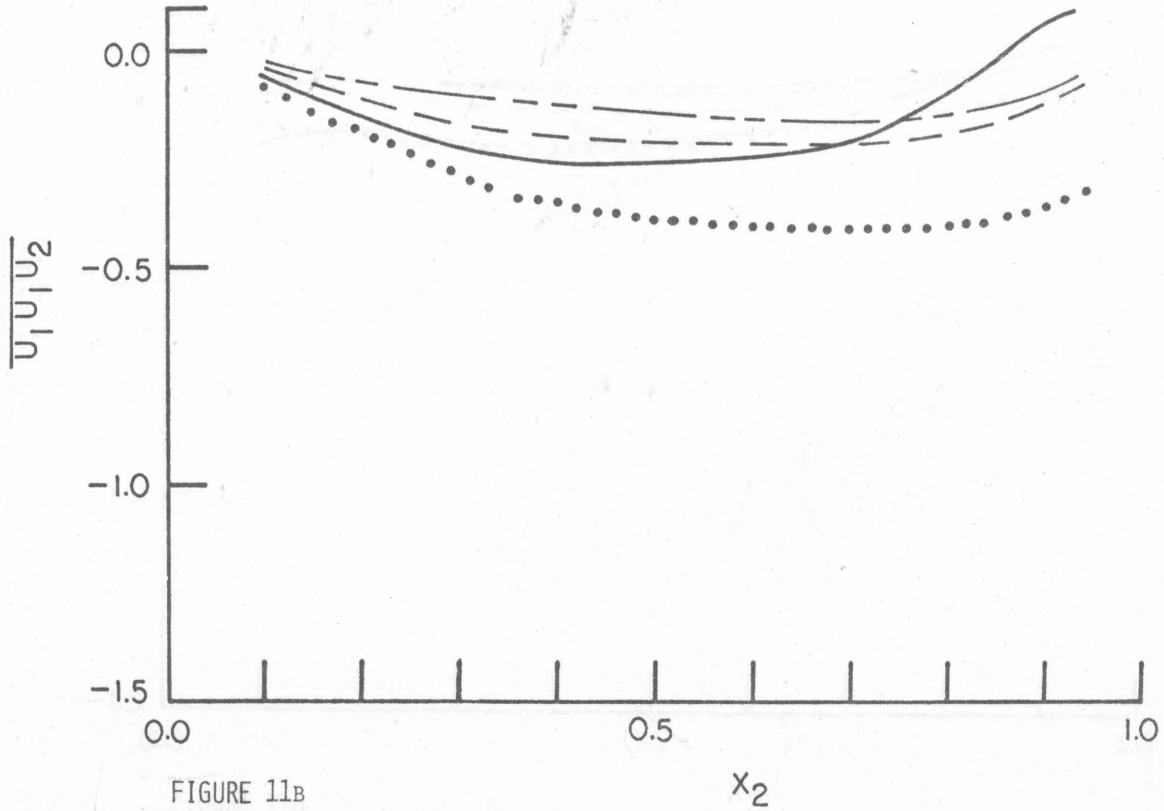

FIGURE 11B

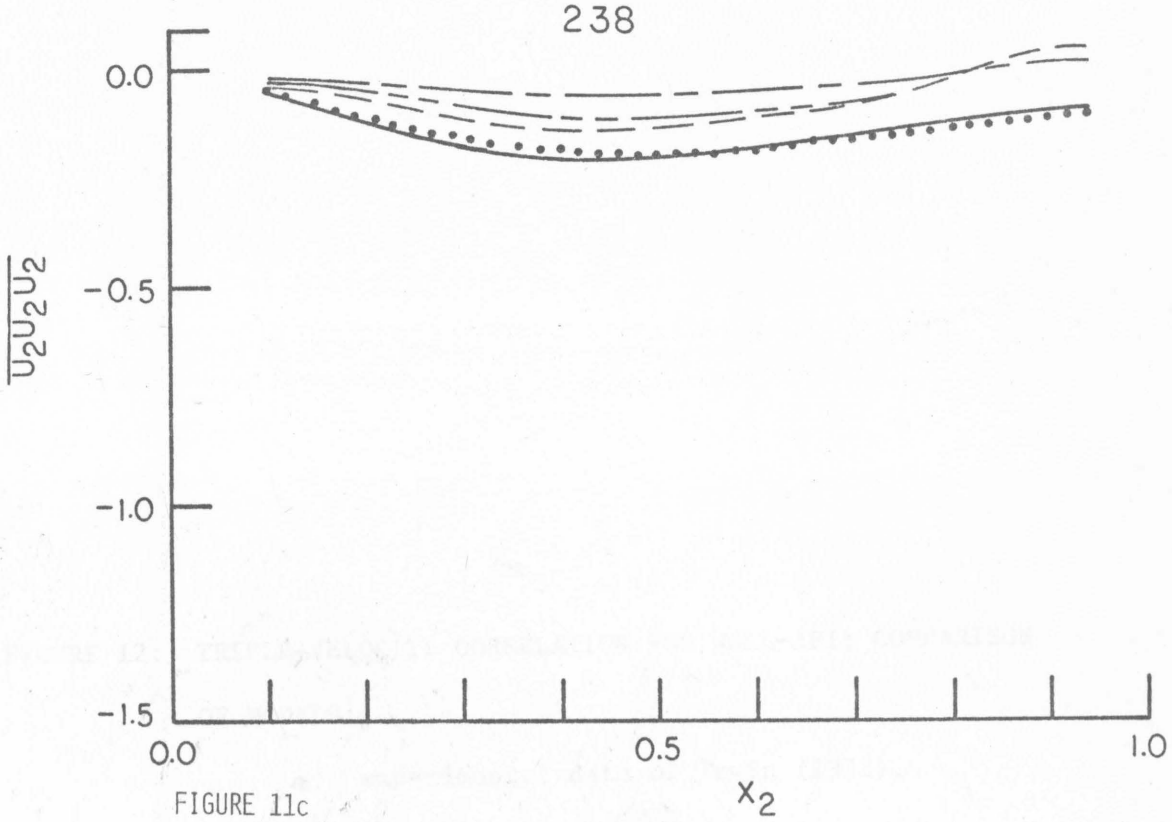

FIGURE 11c

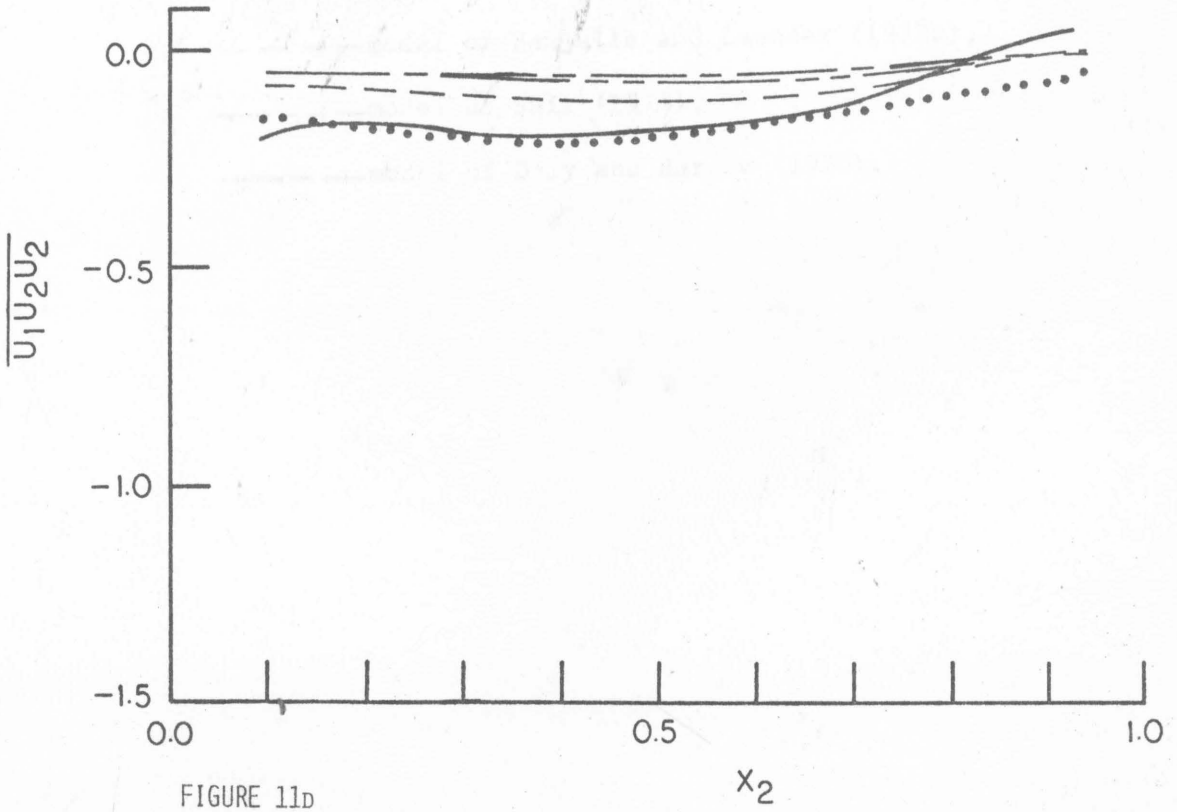

FIGURE 11D

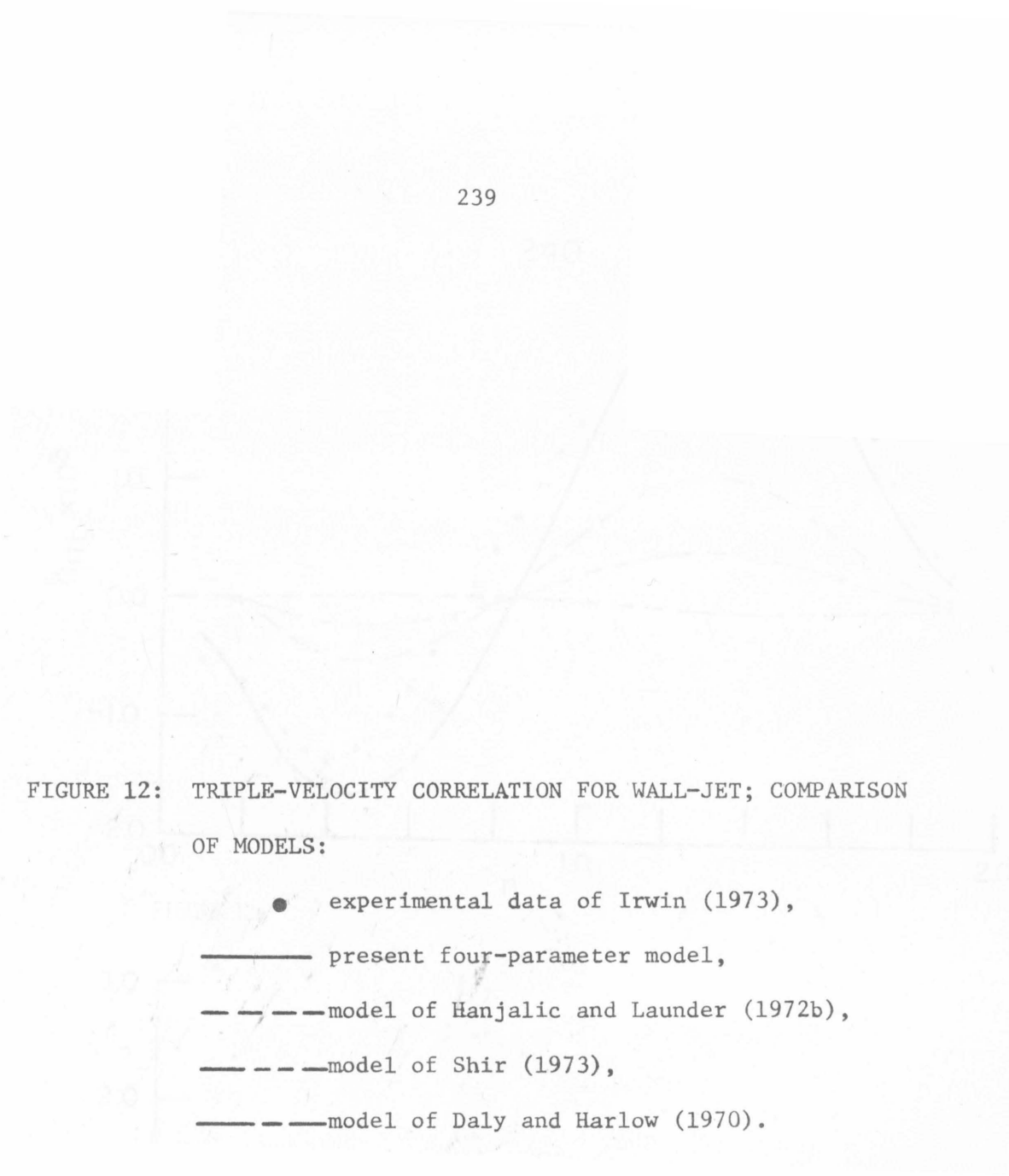

FIGURE 12: TRIPLE-VELOCITY CORRELATION FOR WALL-JET; COMPARISON OF MODELS:

● experimental data of Irwin (1973),

———— present four-parameter model,

— — — —model of Hanjalic and Launder (1972b),

——— — — —model of Shir (1973),

——— — ——model of Daly and Harlow (1970).

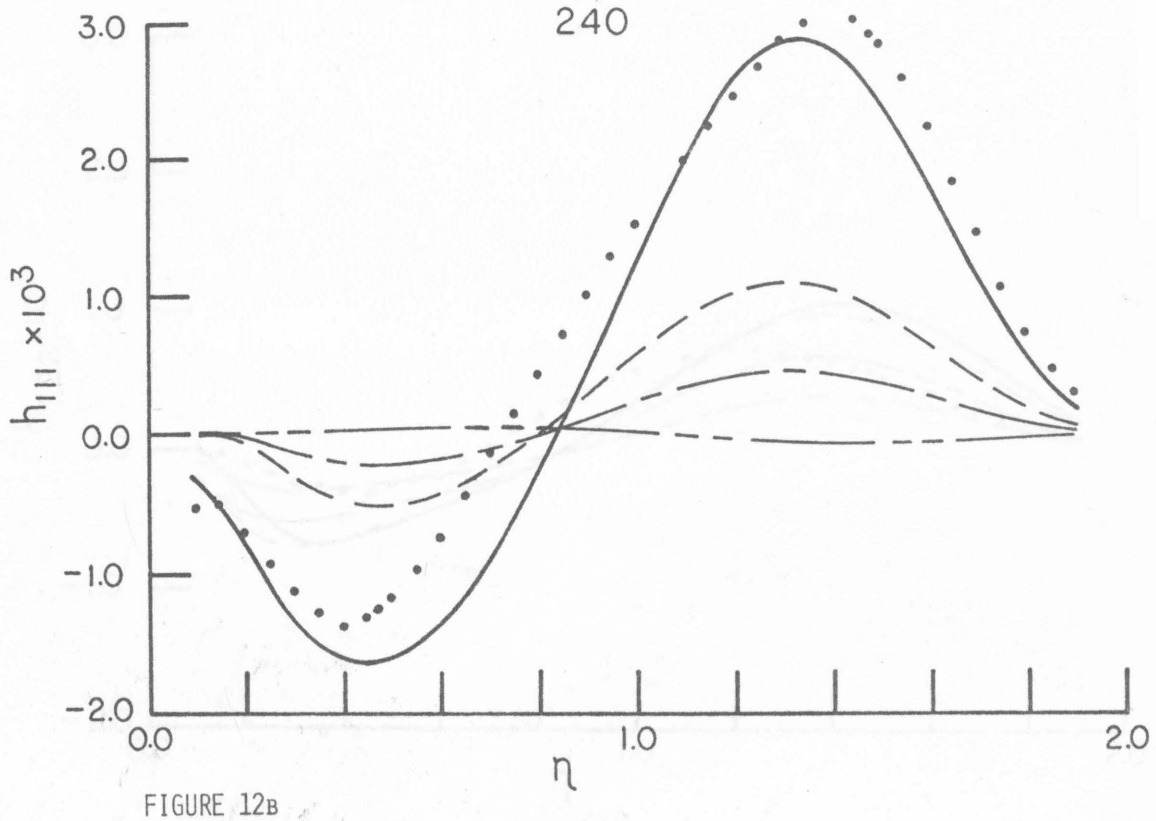

FIGURE 12B

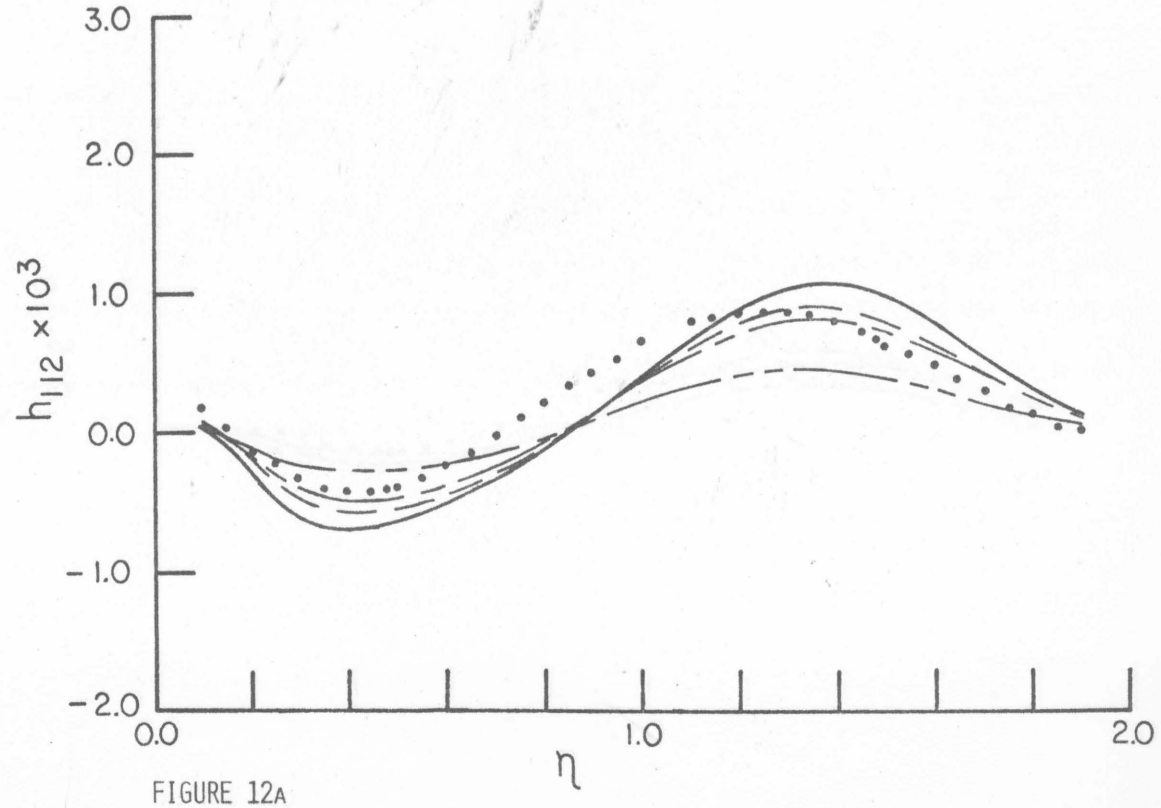

FIGURE 12A

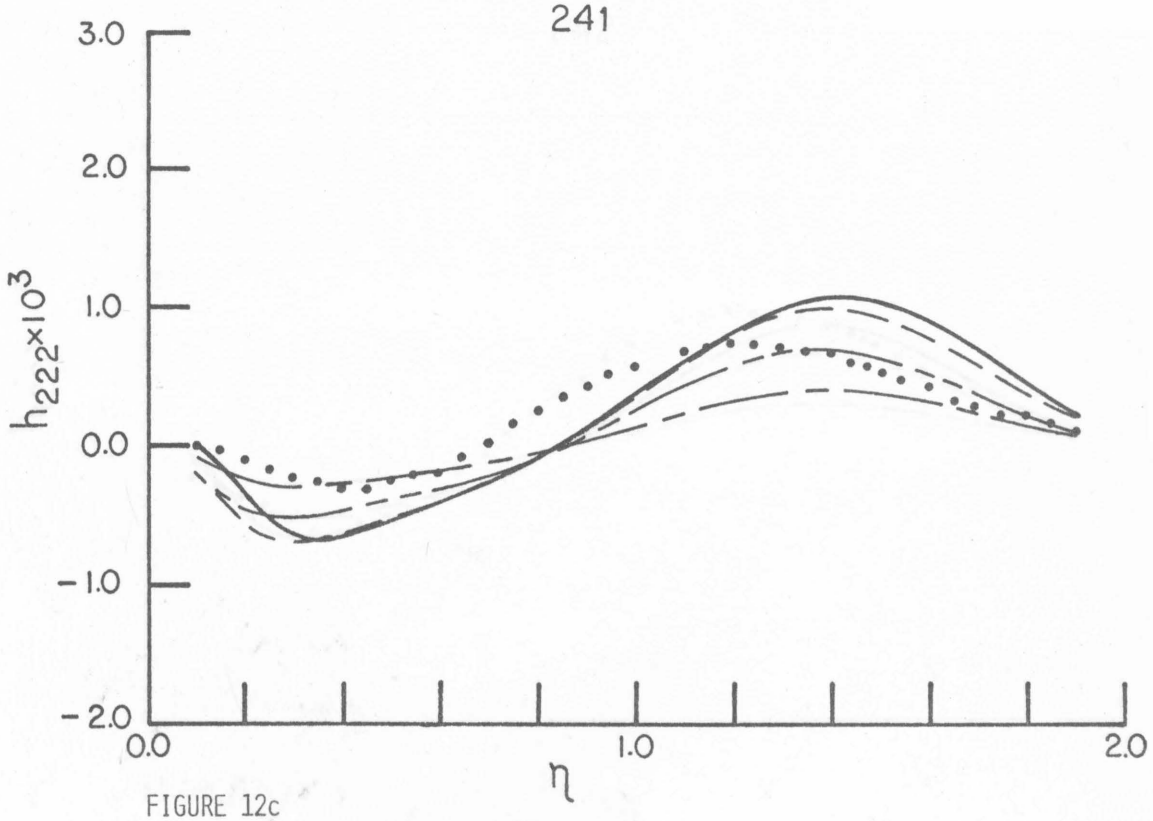

FIGURE 12c

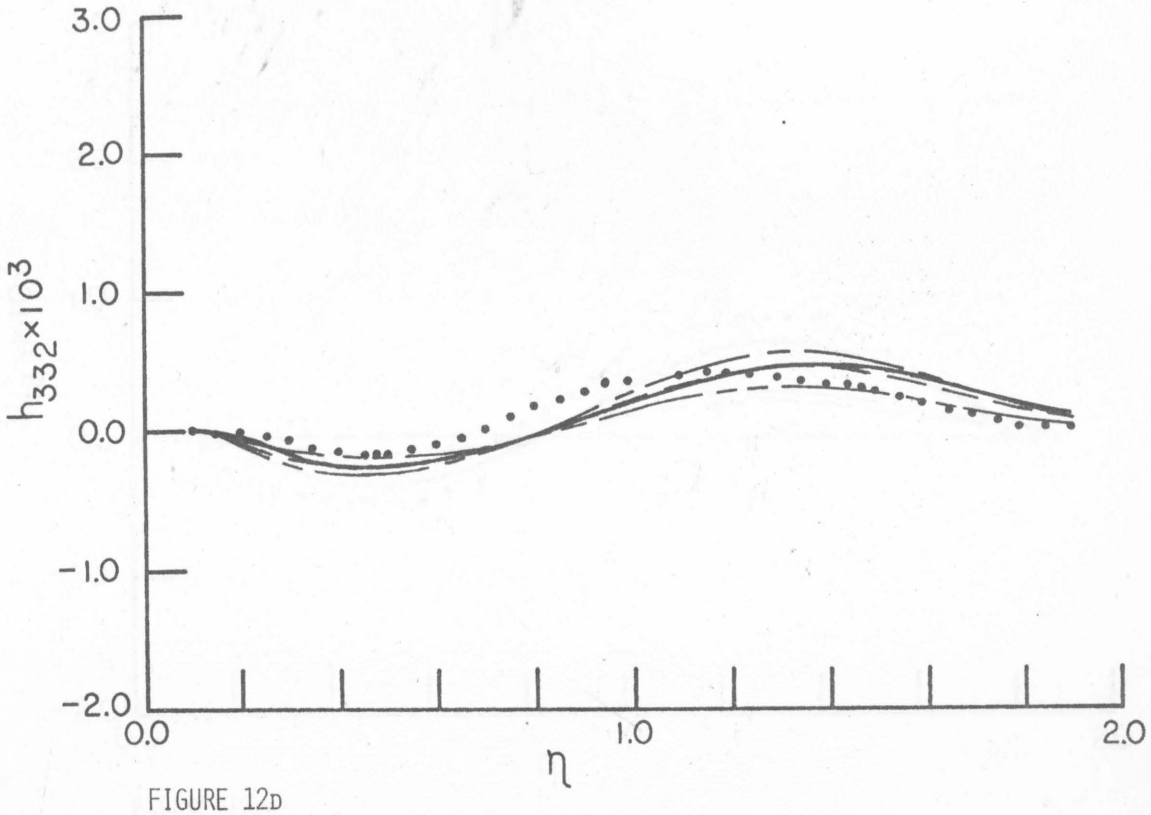

FIGURE 12D

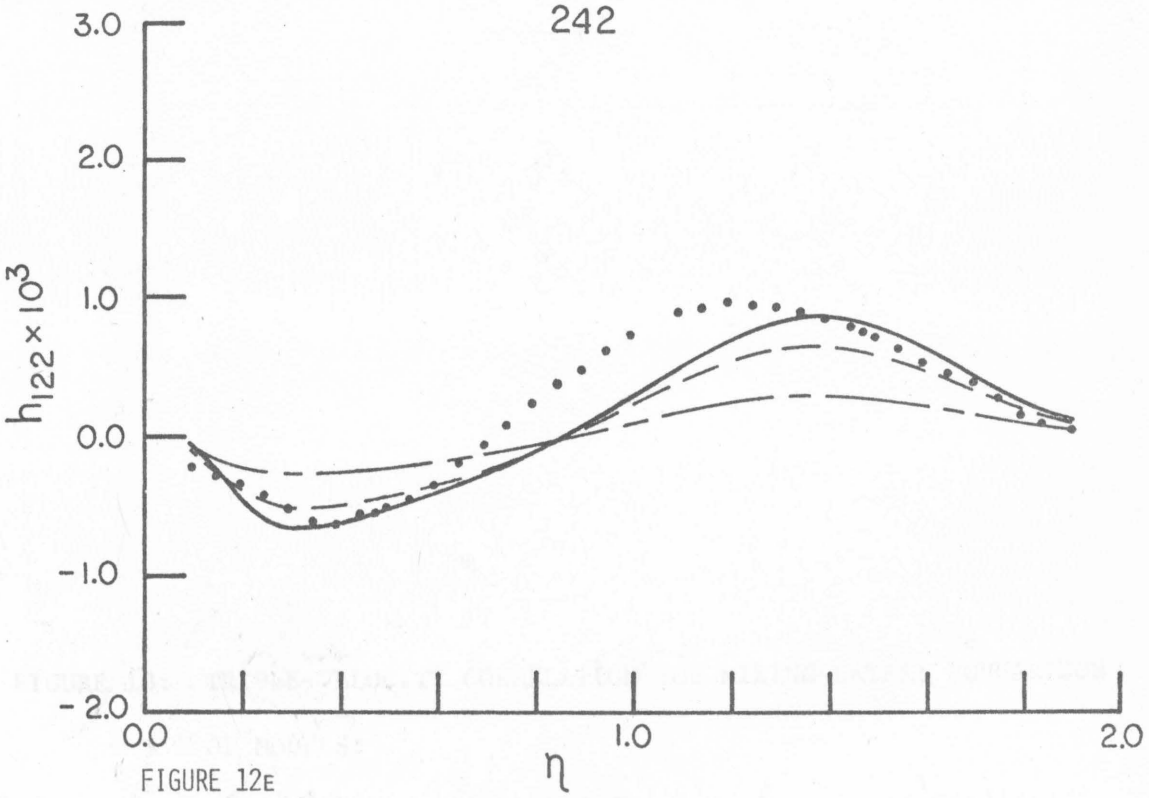

FIGURE 12E

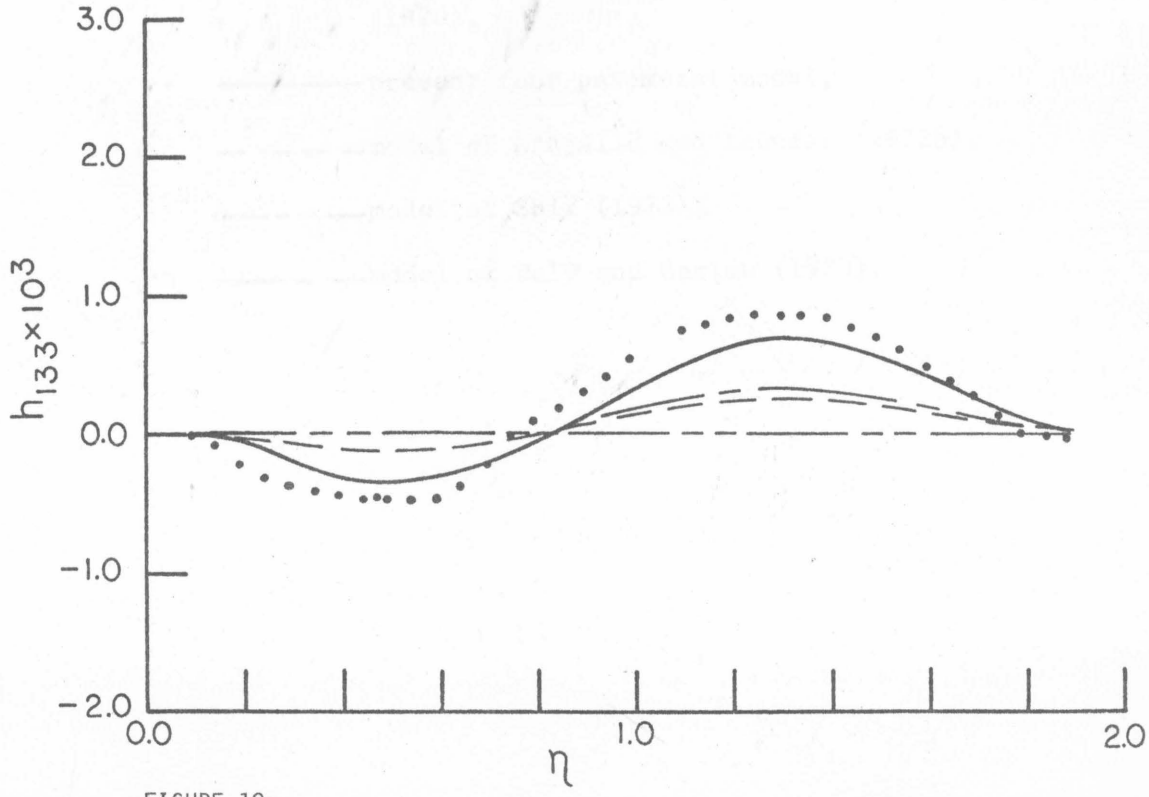

FIGURE 12F

FIGURE 13: TRIPLE-VELOCITY CORRELATION FOR MIXING-LAYER; COMPARISON OF MODELS:

● experimental data of Wygnanski and Fiedler (1970),

———— present four parameter model,

— — — — model of Hanjalic and Launder (1972b),

——— — — model of Shir (1973),

—— — — model of Daly and Harlow (1970).

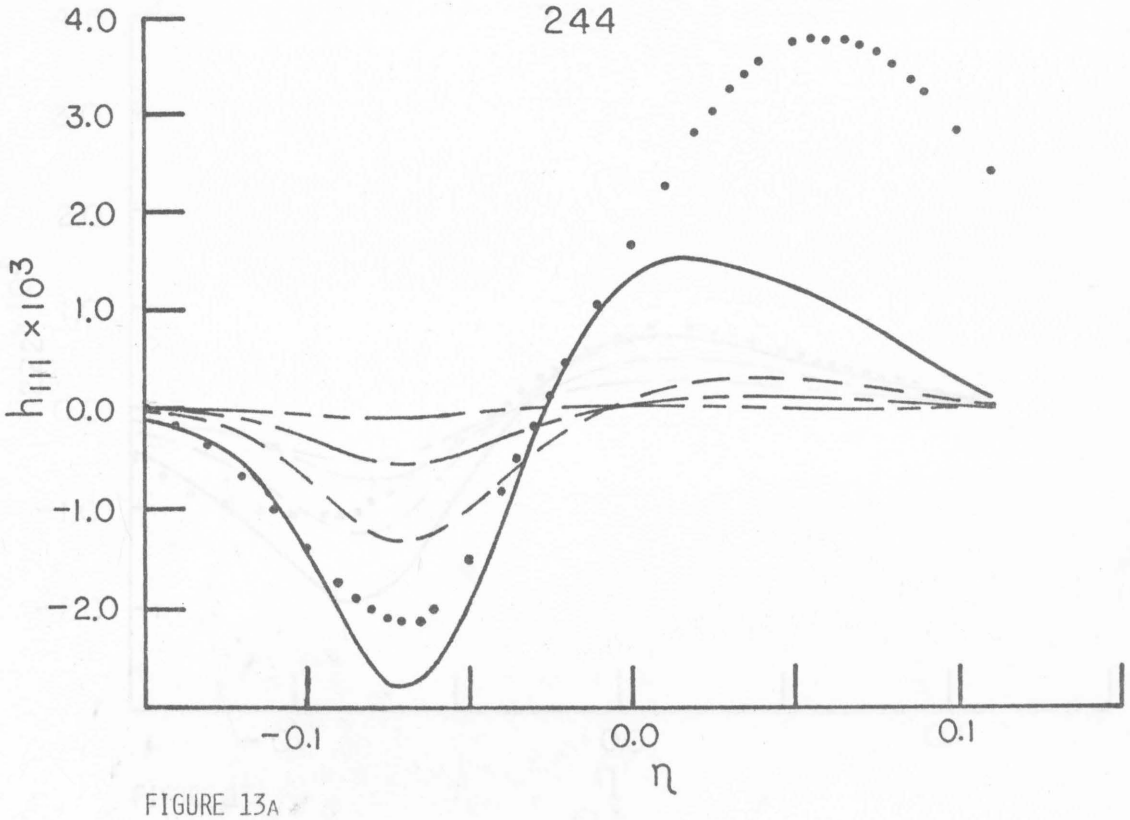

FIGURE 13A

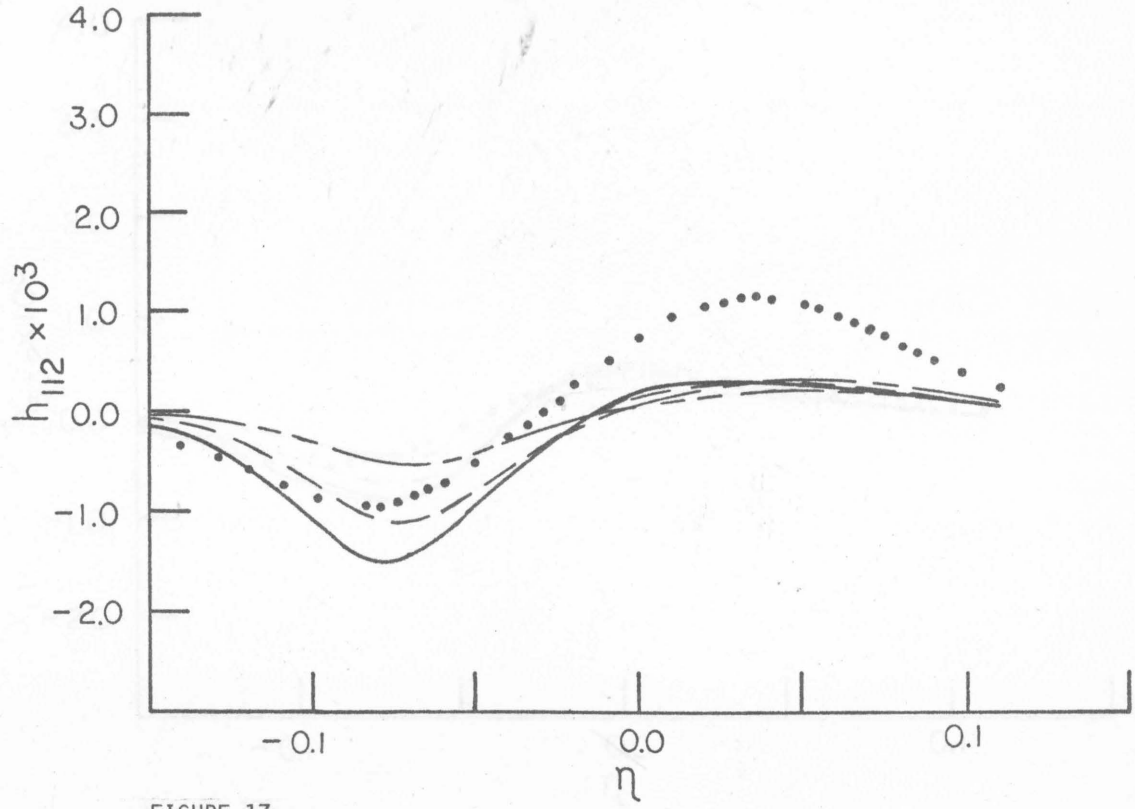

FIGURE 13B

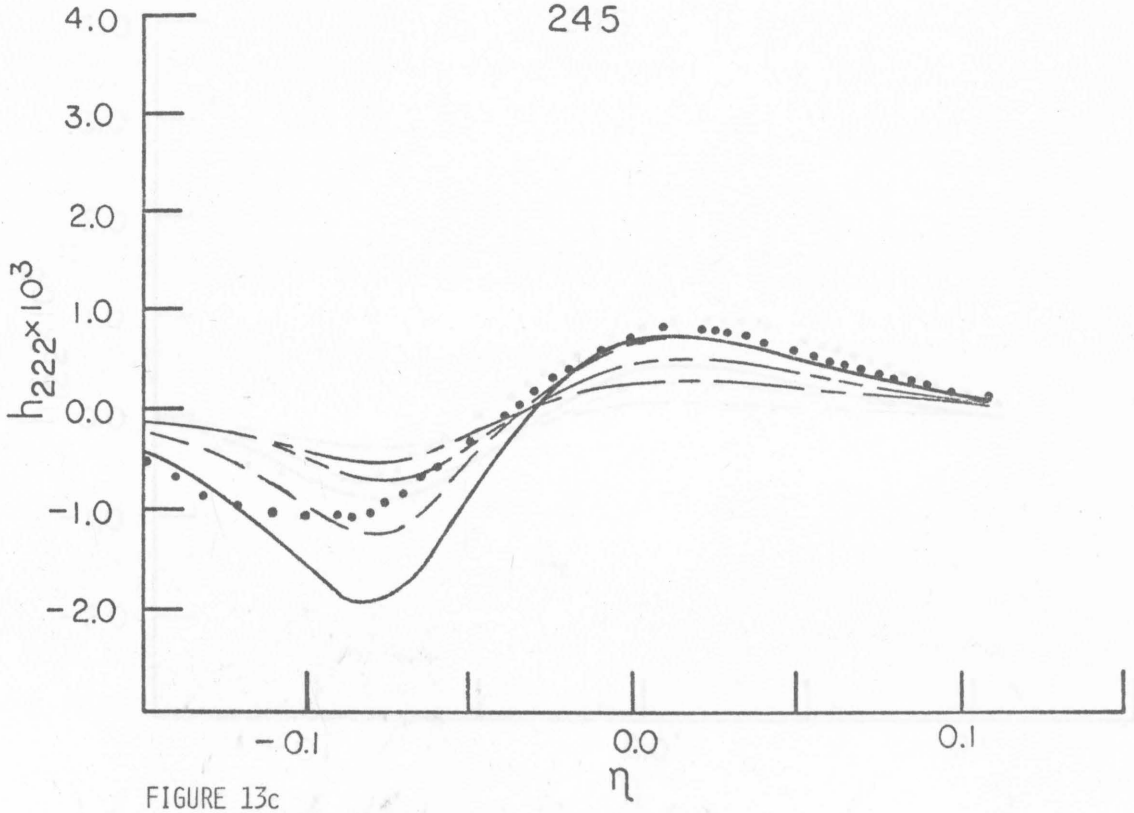

FIGURE 13c

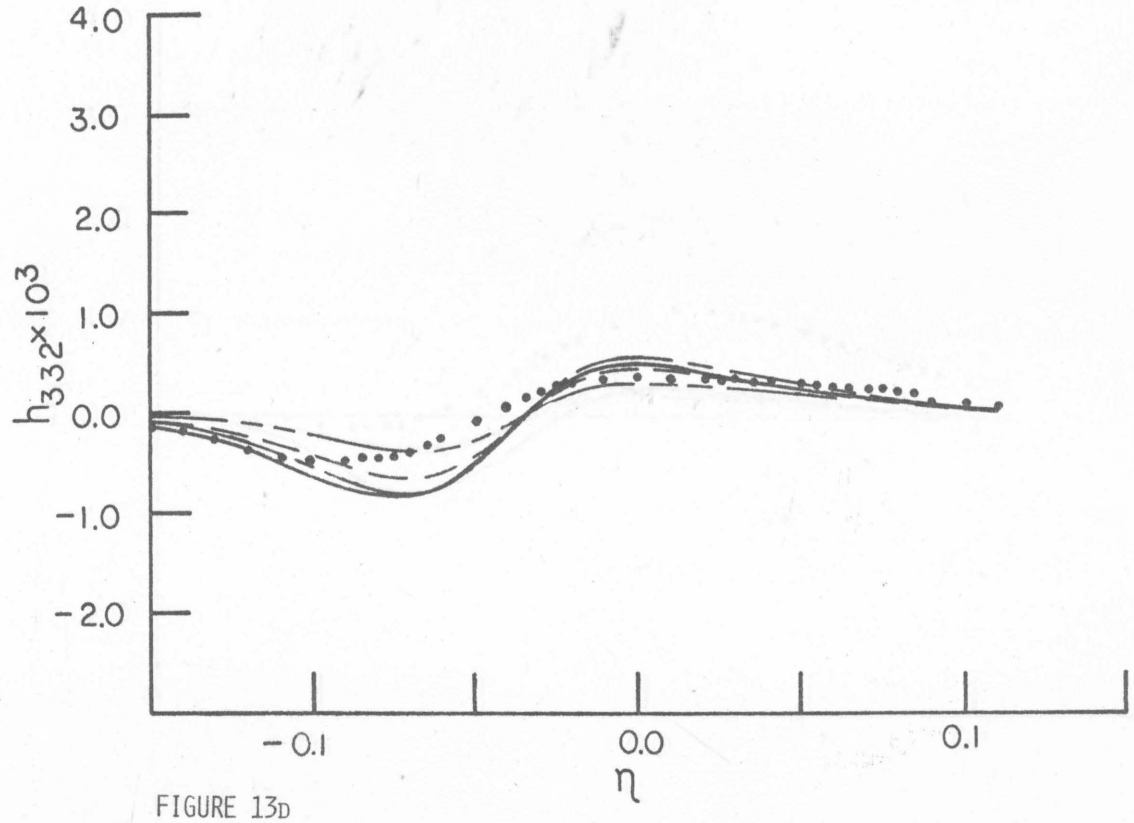

FIGURE 13D

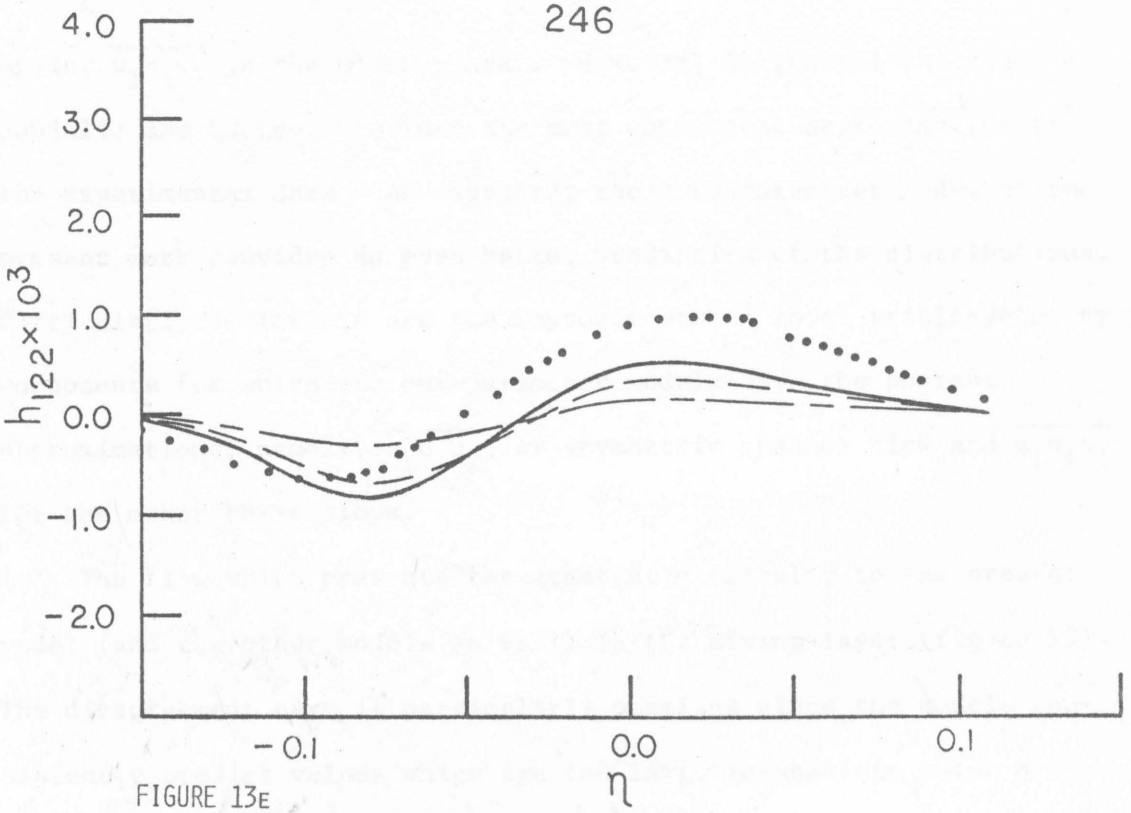

FIGURE 13E

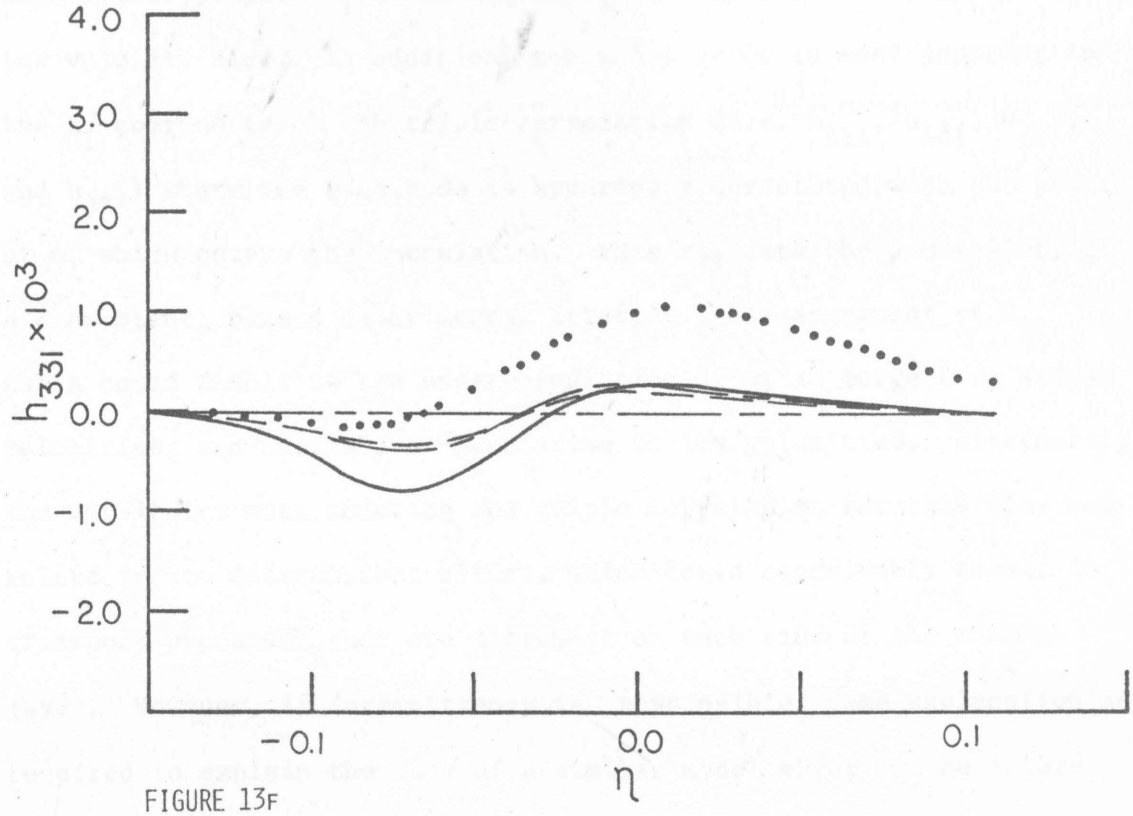

FIGURE 13F

again, $\overline{u_1 u_1 u_1}$ in the mixing-layer. However, in general the model of Hanjalic and Launder provides the most consistent approximation to the experimental data. As expected, the *four*-parameter model of the present work provides an even better prediction of the distributions. Particularly noticeable are the improvements in those triple-velocity components for which the one-parameter models give the poorest approximations; namely, $\overline{u_1 u_1 u_2}$ for asymmetric channel flow and $\overline{u_1 u_1 u_1}$ for the other three flows.

The flow which presents the greatest difficulty to the present model (and the other models as well) is the mixing-layer (figure 13). The disagreement here is particularly puzzling since the models consistently predict values which are too large in absolute value on the high velocity side of the mixing layer ($\eta < 0$) and too small on the low velocity side. In addition, the model error is most apparent in the x_1-components of the triple-correlation (i.e. h_{111}, h_{121}, h_{221}, and h_{331}) where the magnitude is apparently correlated with the power of u_1 which enters the correlation. This suggests the possibility of a consistent, biased experimental error in the measurement of u_1, which could result in the under-prediction of u_1 at large free stream velocities, and in its over-prediction at low velocities. Alternately, the difficulty with modeling the triple correlation for this flow may relate to its intermittent nature, which could conceivably result in transport processes that are different on each side of the mixing-layer. However, if intermittency is responsible, some explanation is required to explain the lack of a similar model error in the inter-

again, $\overline{u_1u_1u_1}$ in the mixing-layer. However, in general the model of Hanjalic and Launder provides the most consistent approximation to the experimental data. As expected, the *four*-parameter model of the present work provides an even better prediction of the distributions. Particularly noticeable are the improvements in those triple-velocity components for which the one-parameter models give the poorest approximations; namely, $\overline{u_1u_1u_2}$ for asymmetric channel flow and $\overline{u_1u_1u_1}$ for the other three flows.

The flow which presents the greatest difficulty to the present model (and the other models as well) is the mixing-layer (figure 13). The disagreement here is particularly puzzling since the models consistently predict values which are too large in absolute value on the high velocity side of the mixing layer ($\eta < 0$) and too small on the low velocity side. In addition, the model error is most apparent in the x_1-components of the triple-correlation (i.e. h_{111}, h_{121}, h_{221}, and h_{331}) where the magnitude is apparently correlated with the power of u_1 which enters the correlation. This suggests the possibility of a consistent, biased experimental error in the measurement of u_1, which could result in the under-prediction of u_1 at large free stream velocities, and in its over-prediction at low velocities. Alternately, the difficulty with modeling the triple correlation for this flow may relate to its intermittent nature, which could conceivably result in transport processes that are different on each side of the mixing-layer. However, if intermittency is responsible, some explanation is required to explain the lack of a similar model error in the inter-

mittent region of the wall-jet. To evaluate more thoroughly the role of intermittency, it would be interesting to repeat the experiment of Wygnanski and Fiedler with a non-zero velocity on the low-velocity side, in the presence of an upstream grid to generate substantial free-stream turbulence. This would reduce the apparent intermittency of the flow, at least at the small scale.

Finally, one must ultimately consider the important question as to whether the parameters determined in the above manner are 'universal' or simply suitable for the interpretation of a limited range of data. Some support for universality arises from the fact that the parameters are not drastically changed if they are re-evaluated on the basis of the experimental data from each flow separately. To illustrate this point, we have listed in table 6, the best-fit parameters for each flow separately. Certainly, since each set of data was compiled and reduced on different experimental equipment and instrumentation, it is not unreasonable to expect each set of data to contain a small biased error. Furthermore, we fully expect that a parameter which is important for one flow may not be important in another flow. In the latter case, not being important, the parameter cannot be estimated accurately. Hence, the variations in parameter values, evident in table 6, can be expected. Of fundamental importance is the obvious fact that the coefficients do not change sign and exhibit only reasonably small variations in magnitude from flow to flow.

C. Inhomogeneous Tendency-Toward-Isotropy Constants

It was pointed out previously that direct measurements of the pressure-velocity correlations would facilitate model development. Unfortunately, these correlations are extremely difficult to measure directly. Although several studies have reported measurements of pressure fluctuations at solid surfaces, Elliot (1972) reported the only measurements of pressure-velocity correlations away from the surface. However, even these measurements are of limited use in model development since only sparse information concerning other turbulence quantities was reported. Fortunately, even when direct measurements are not available, it is possible to estimate the tendency-toward-isotropy term from fully documented experimental data. For flows in which the profiles of all Reynolds stresses, mean velocity, dissipation rate and triple-velocity correlation are known,

$$\left(u_j \frac{\partial p}{\partial x_i} + u_i \frac{\partial p}{\partial x_j} \right) / \rho$$

may be estimated by difference from equation (12), as the closing term. This term may then be decomposed into its 'intercomponent transfer' and 'pressure-diffusion' components as in equation (26). Each of the non-homogeneous flows described in section 4.A was analyzed in this fashion.

With the experimental tendency-toward-isotropy term so estimated, we evaluated the ability of the *existing* closure models, equations (30) - (33) to describe intercomponent transfer in non-homogeneous flows, by directly substituting the experimental

distributions of U_i, $\overline{u_i u_j}$ and ε into the models, to predict A_{ij} at the nodes of the grid described in section 4.B.[†] In addition, the present *homogeneous* model was evaluated in the same manner. The resulting profiles of A_{ij} are presented in figures 14 - 17.

Although none of the models predicts *all* of the profiles exactly, some are significantly more successful than others. In particular, Daly and Harlow's model consistently gives the poorest approximation to the experimental data, with the largest error invariably occurring in the A_{12} component for all of the flows. (Note that Wyngaard's model was not included in this comparison because of its non-invariant nature.) For the asymmetric channel and pipe flows, the model of Hanjalic and Launder provides the best approximation, while the present, homogeneous formulation also produces reasonable results. For the wall-jet, Hanjalic and Launder's model once again provides the best approximation for $\eta \gtrsim 0.4$. In this range, Shir's model tends to over-predict the intercomponent transfer (this would lead to a turbulence which is too isotropic), while the present homogeneous formulation tends to underpredict this transport slightly. On the other hand, the present model provides the best prediction of this flow for $\eta \lesssim 0.4$. Hence, for Irwin's wall-jet, the profiles of A_{ij} predicted by the present homogeneous model are comparable to those of Hanjalic and Launder's non-homogeneous model. The mixing-layer

---

[†]The procedure used to calculate the wall effect contribution which appears in the models of Daly and Harlow, and Shir, is described in Appendix C.

FIGURE 14: INTERCOMPONENT TRANSFER FOR ASYMMETRIC CHANNEL; COMPARISON OF MODELS:

● experimental profile, obtained by difference from Hanjalic and Launder's (1972a) data,

———— present homogeneous model,

— — — — model of Hanjalic and Launder (1972b),

——— - - - model of Shir (1973),

——— - — model of Daly and Harlow (1970).

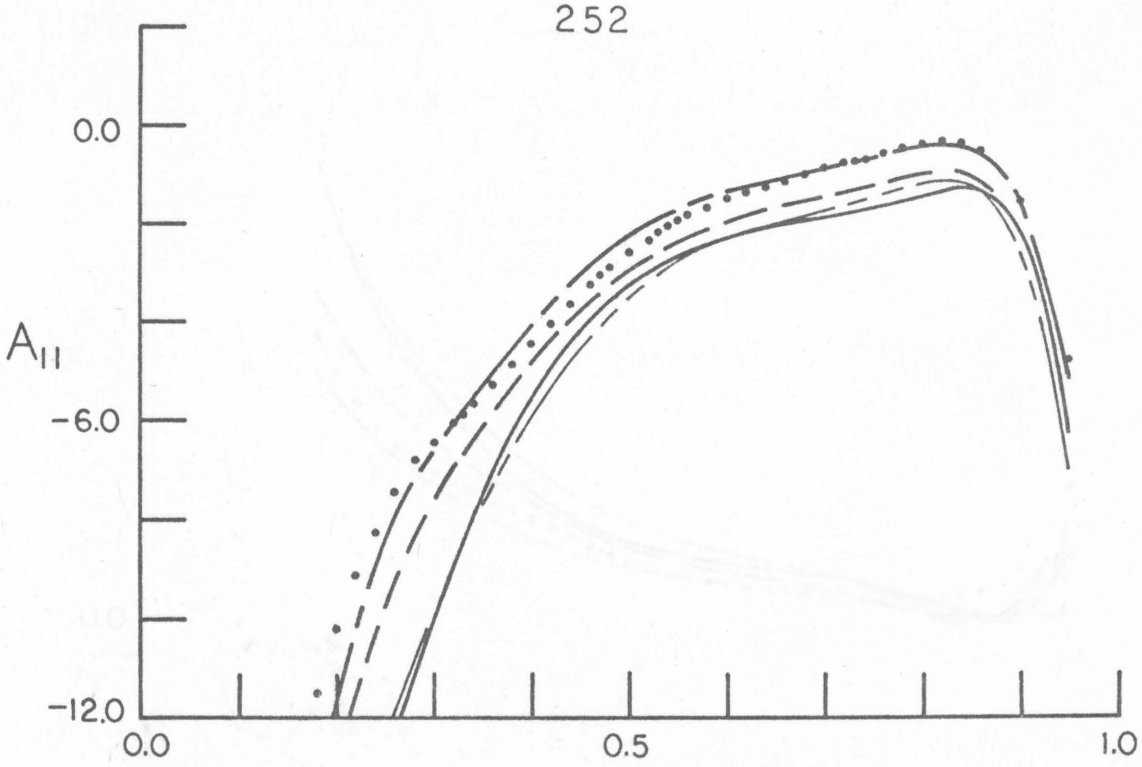

FIGURE 14A

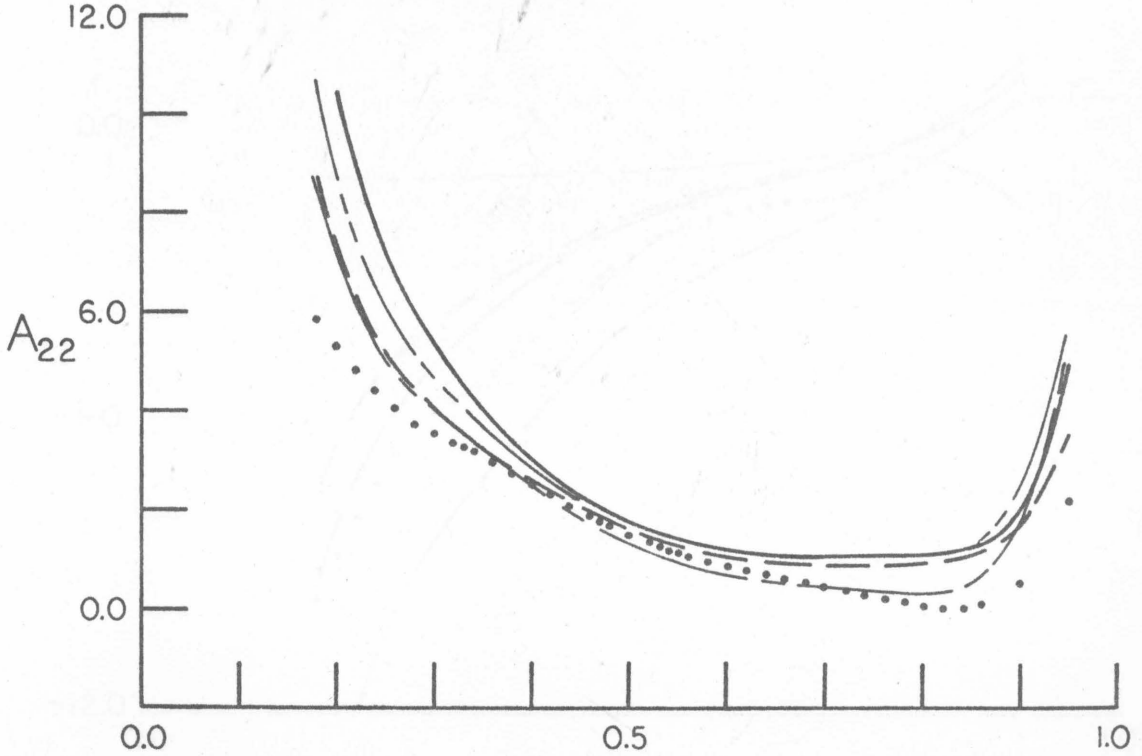

FIGURE 14B

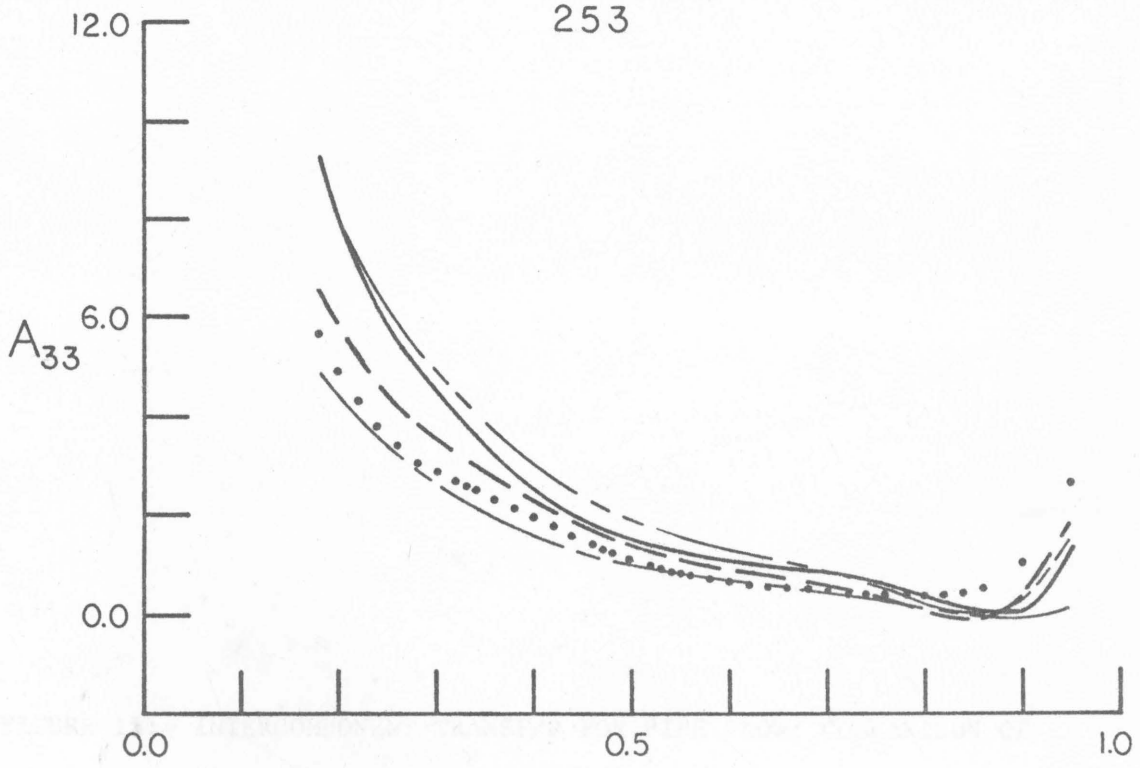

FIGURE 14c

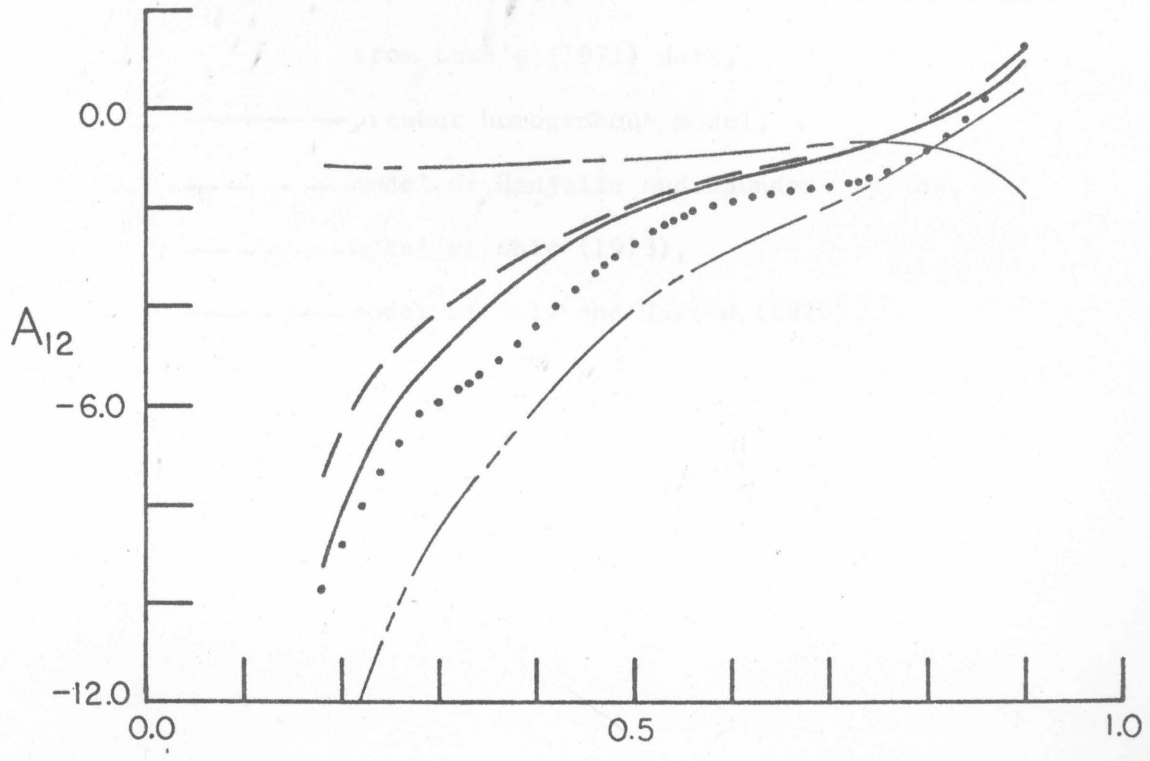

FIGURE 14D

FIGURE 15: INTERCOMPONENT TRANSFER FOR PIPE FLOW; COMPARISON OF MODELS:

● experimental profile, obtained by difference from Lawn's (1971) data,

———— present homogeneous model,

— — — — model of Hanjalic and Launder (1972b),

— - - — model of Shir (1973),

— - — model of Daly and Harlow (1970).

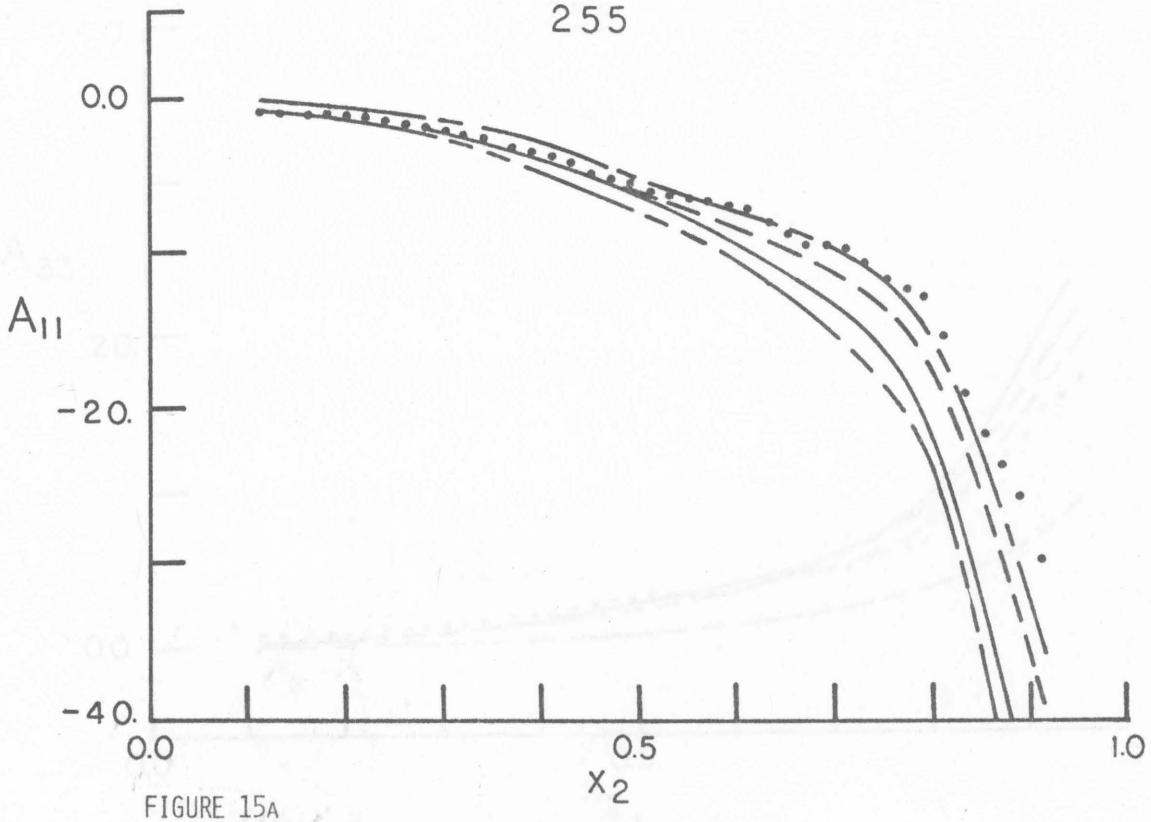

FIGURE 15A

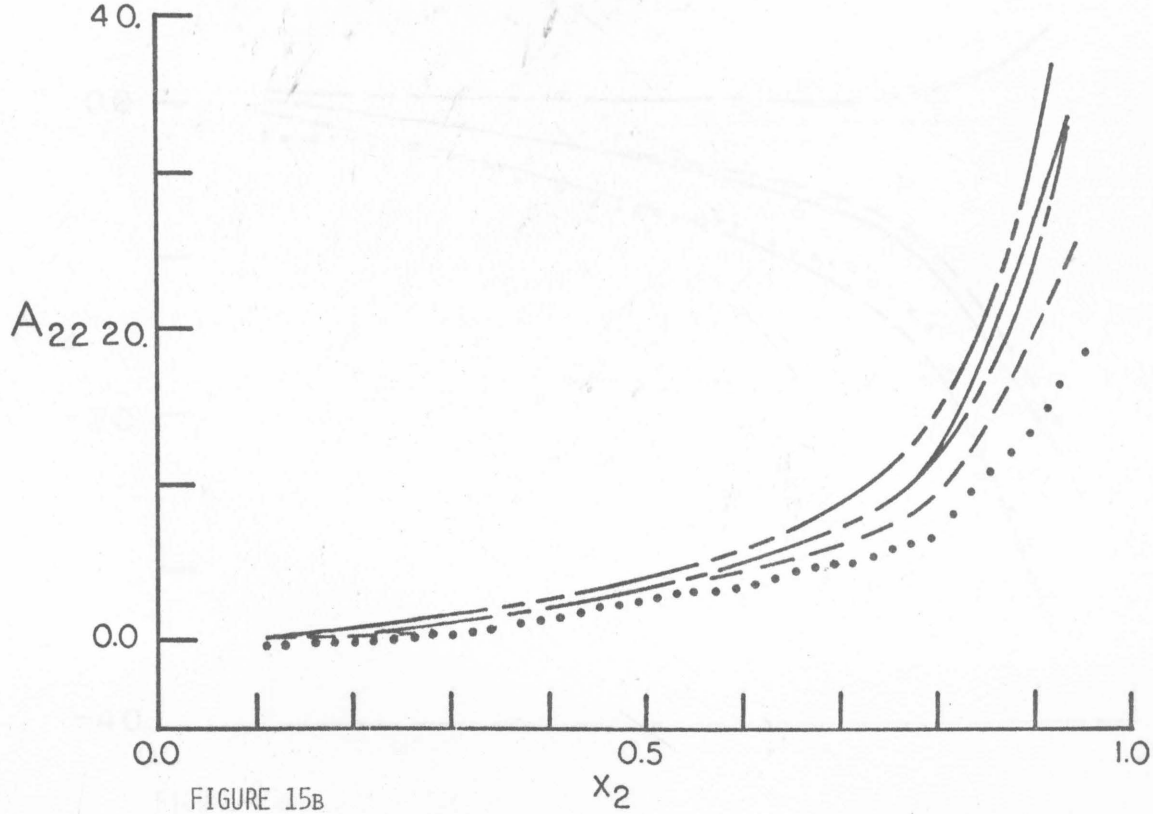

FIGURE 15B

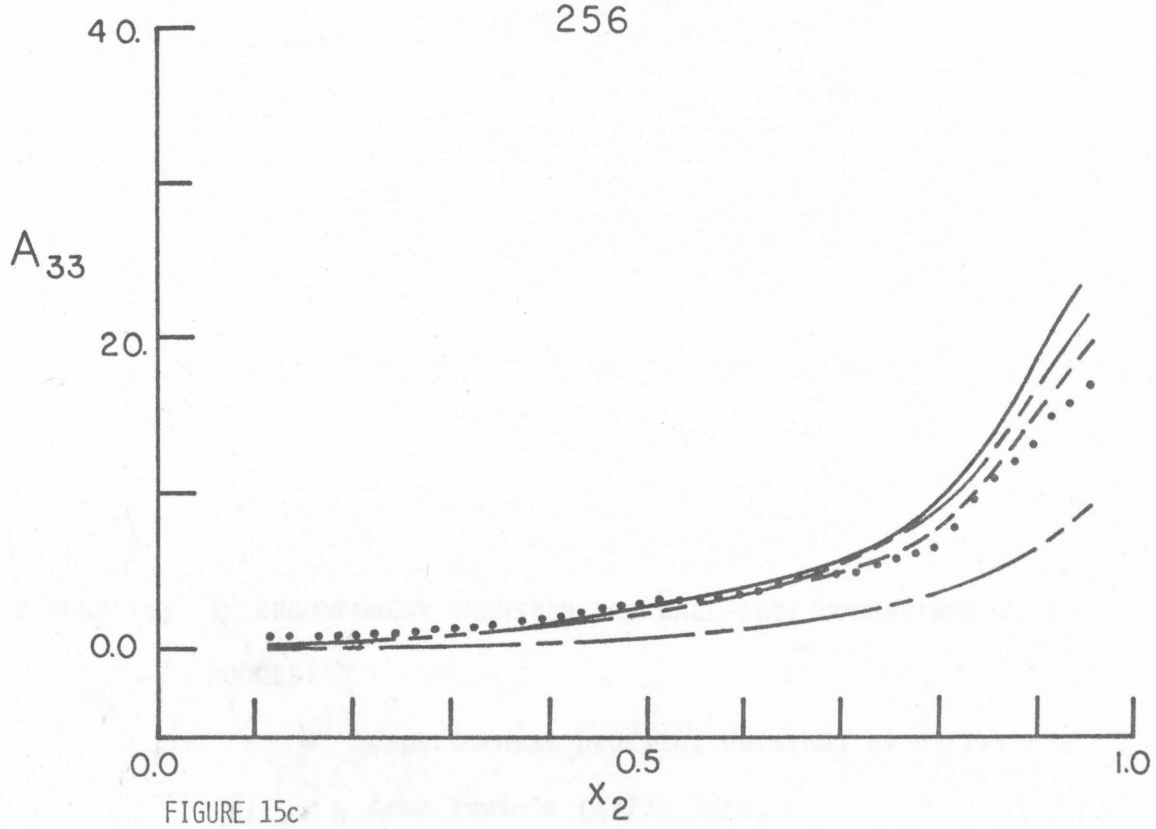

FIGURE 15c

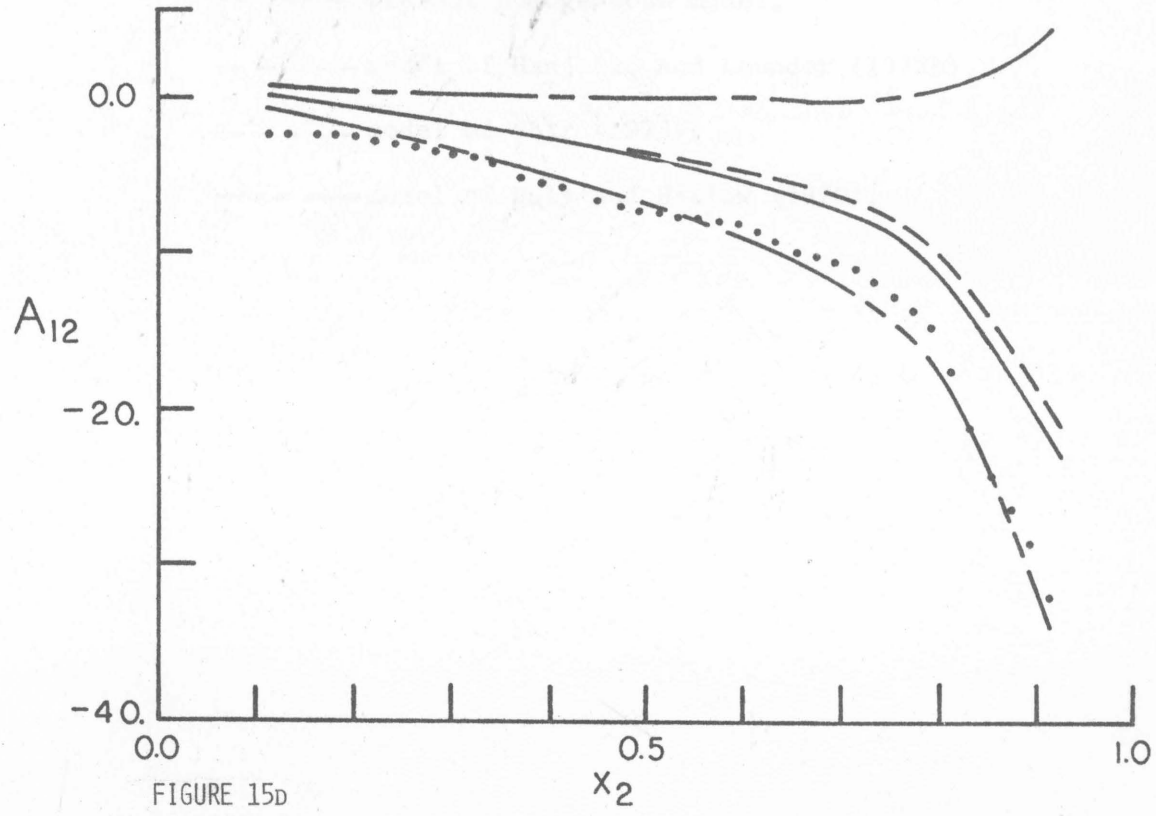

FIGURE 15D

FIGURE 16: INTERCOMPONENT TRANSFER FOR WALL-JET; COMPARISON OF MODELS:

● experimental profile, obtained by difference from Irwin's (1973) data,

——— present homogeneous model,

— — — — model of Hanjalic and Launder (1972b),

— — — — model of Shir (1973),

— — — — model of Daly and Harlow (1970).

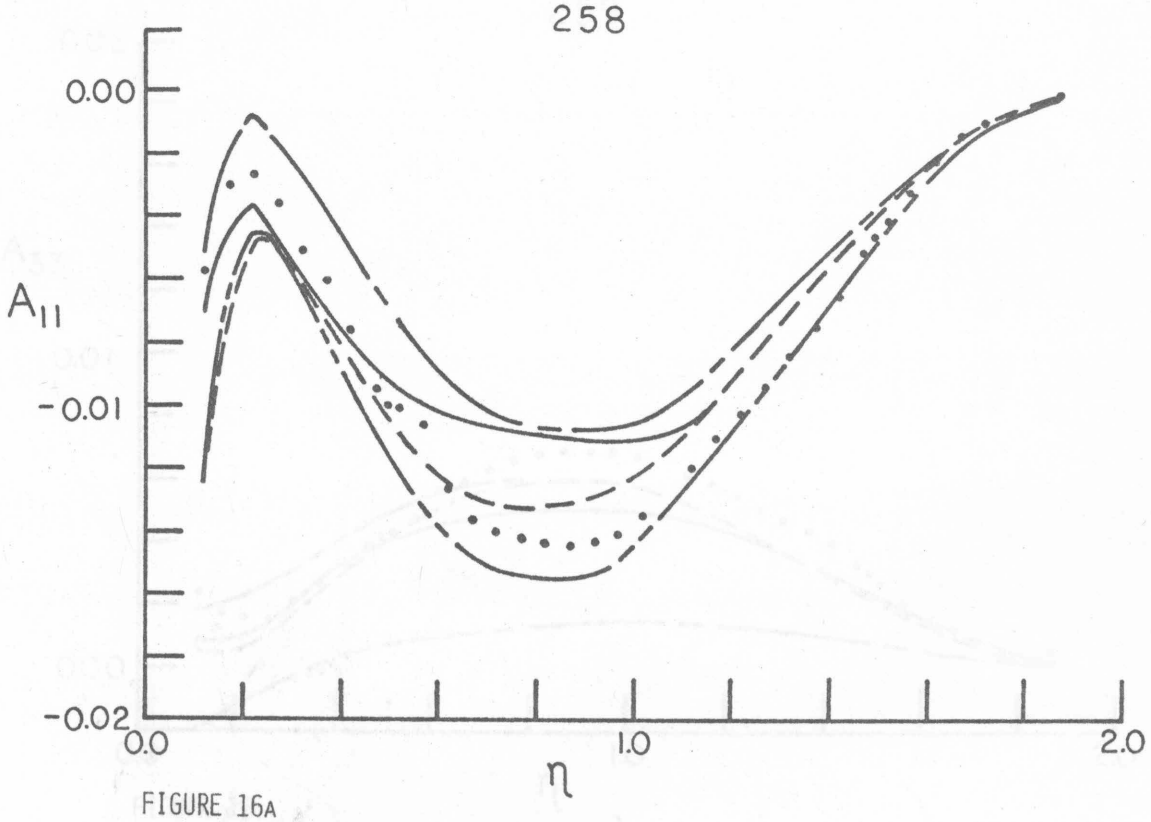

FIGURE 16A

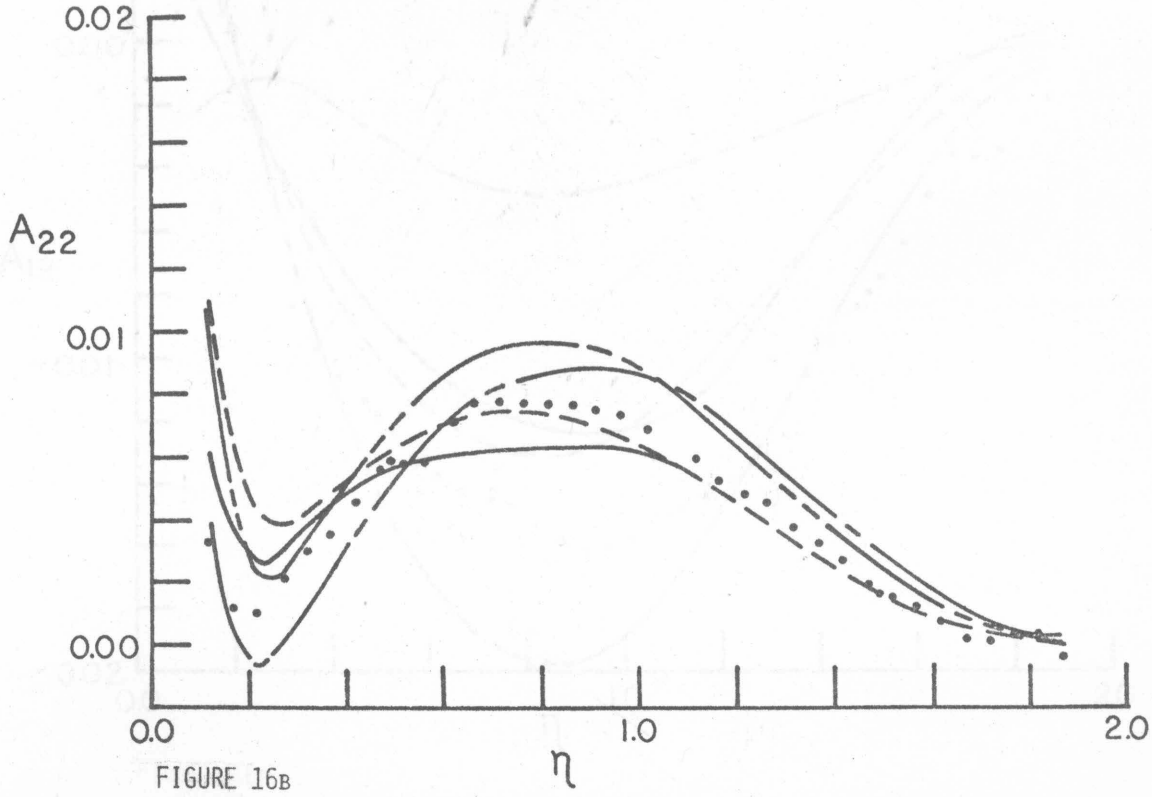

FIGURE 16B

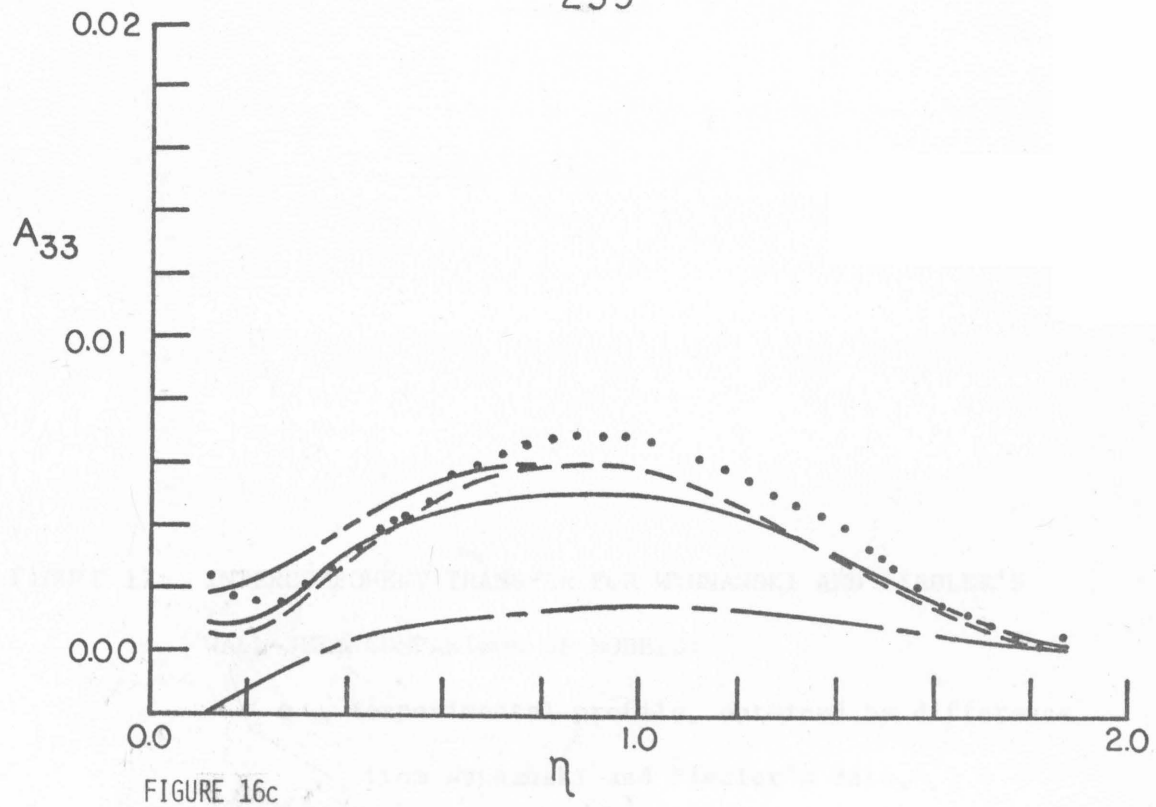

FIGURE 16c

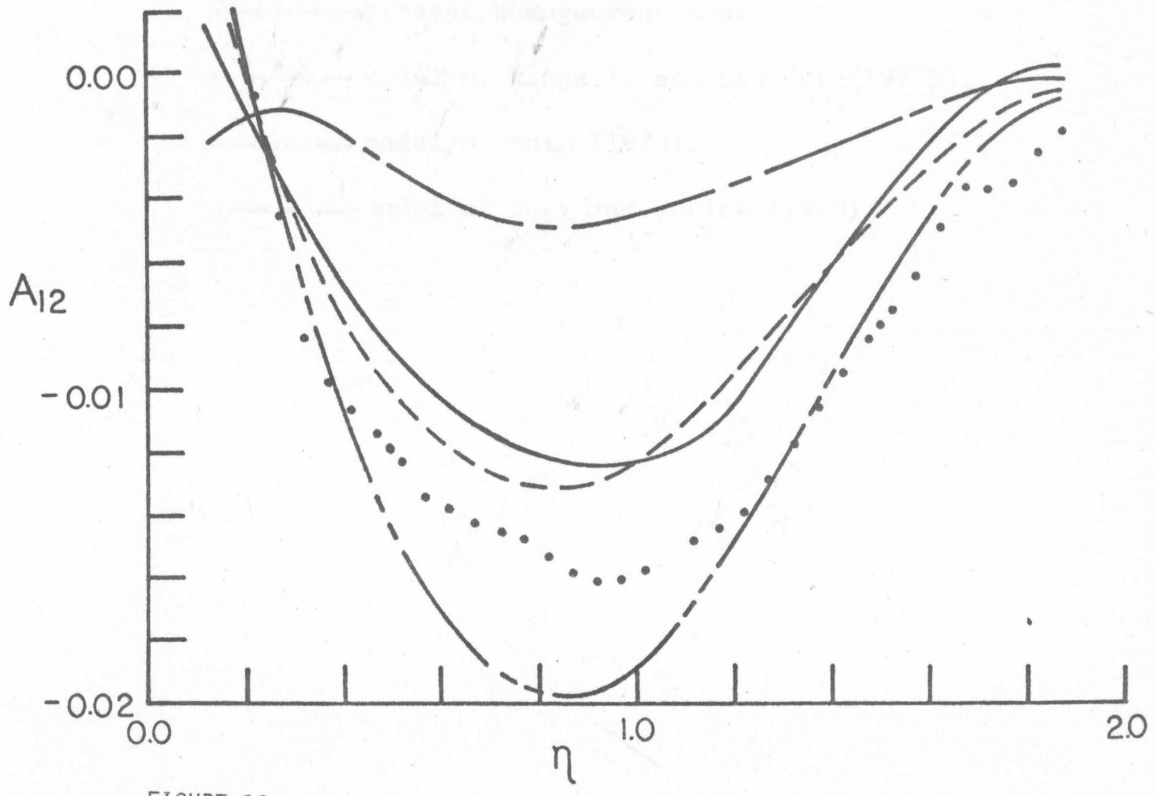

FIGURE 16D

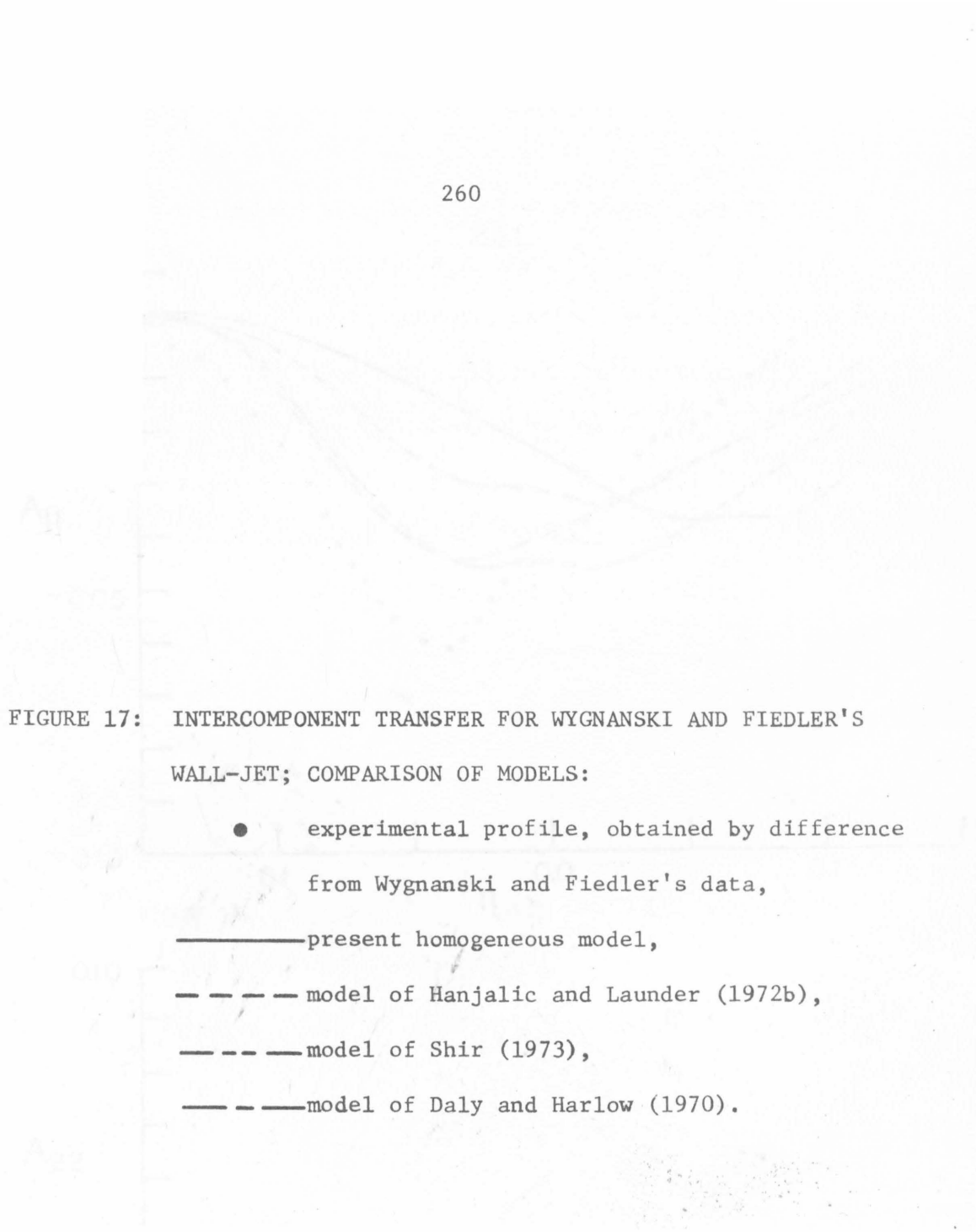

FIGURE 17: INTERCOMPONENT TRANSFER FOR WYGNANSKI AND FIEDLER'S WALL-JET; COMPARISON OF MODELS:

● experimental profile, obtained by difference from Wygnanski and Fiedler's data,

———— present homogeneous model,

— — — — model of Hanjalic and Launder (1972b),

— — — — model of Shir (1973),

— — — — model of Daly and Harlow (1970).

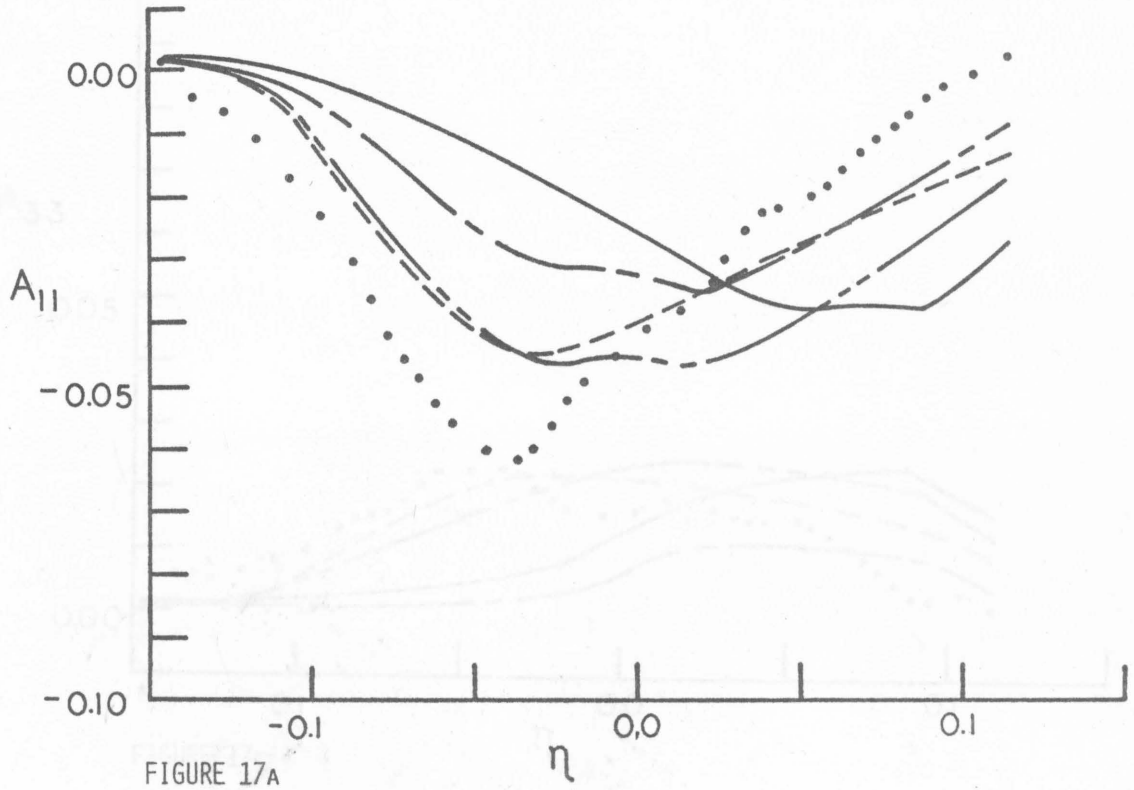

FIGURE 17A

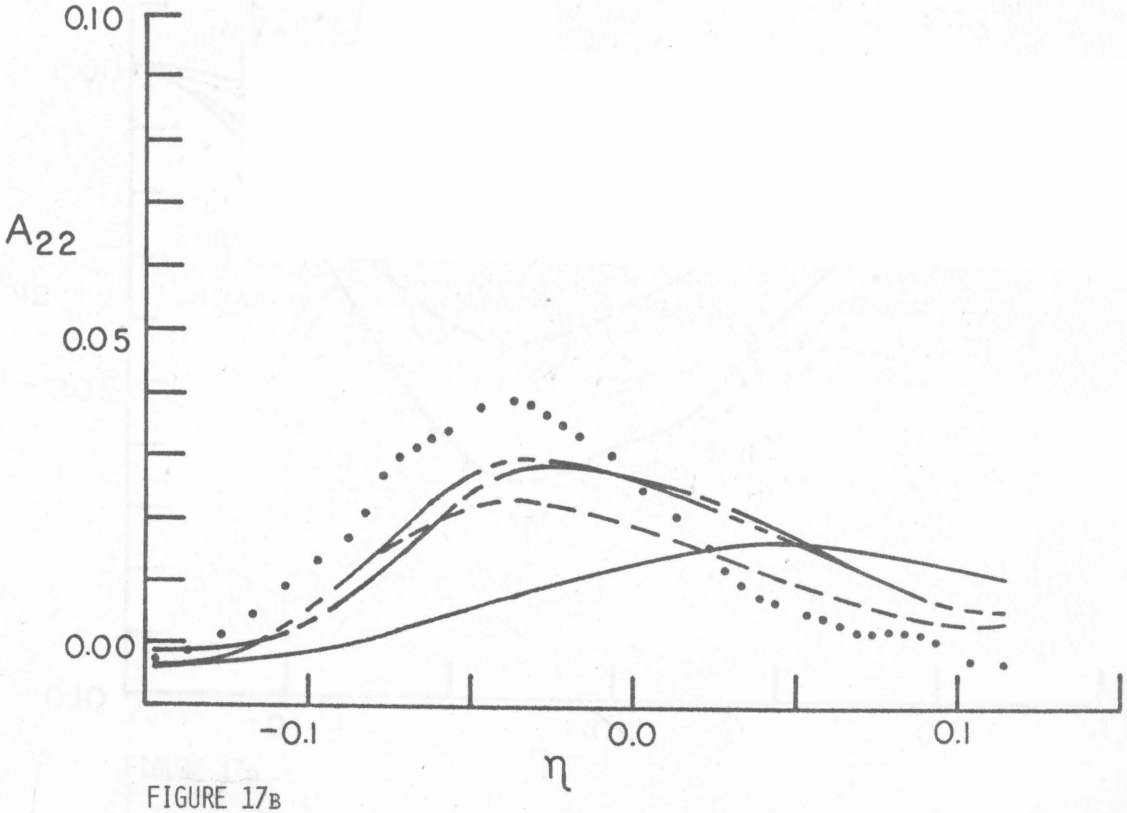

FIGURE 17B

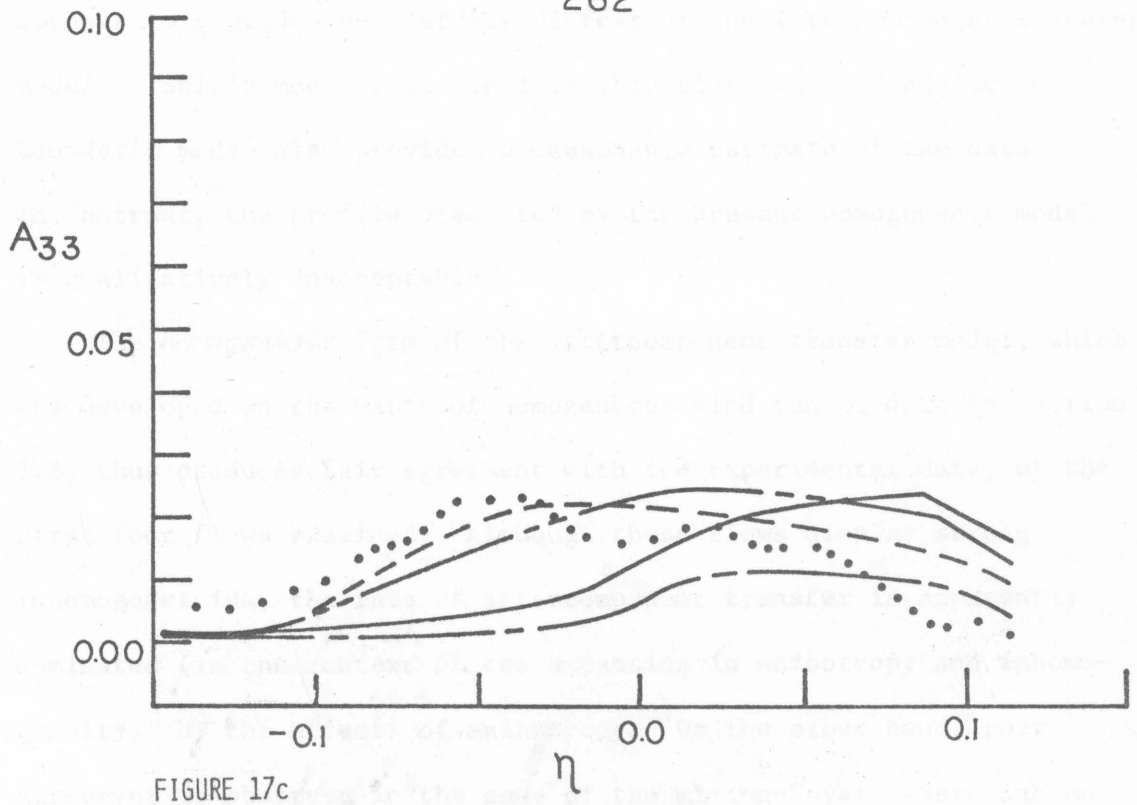

FIGURE 17c

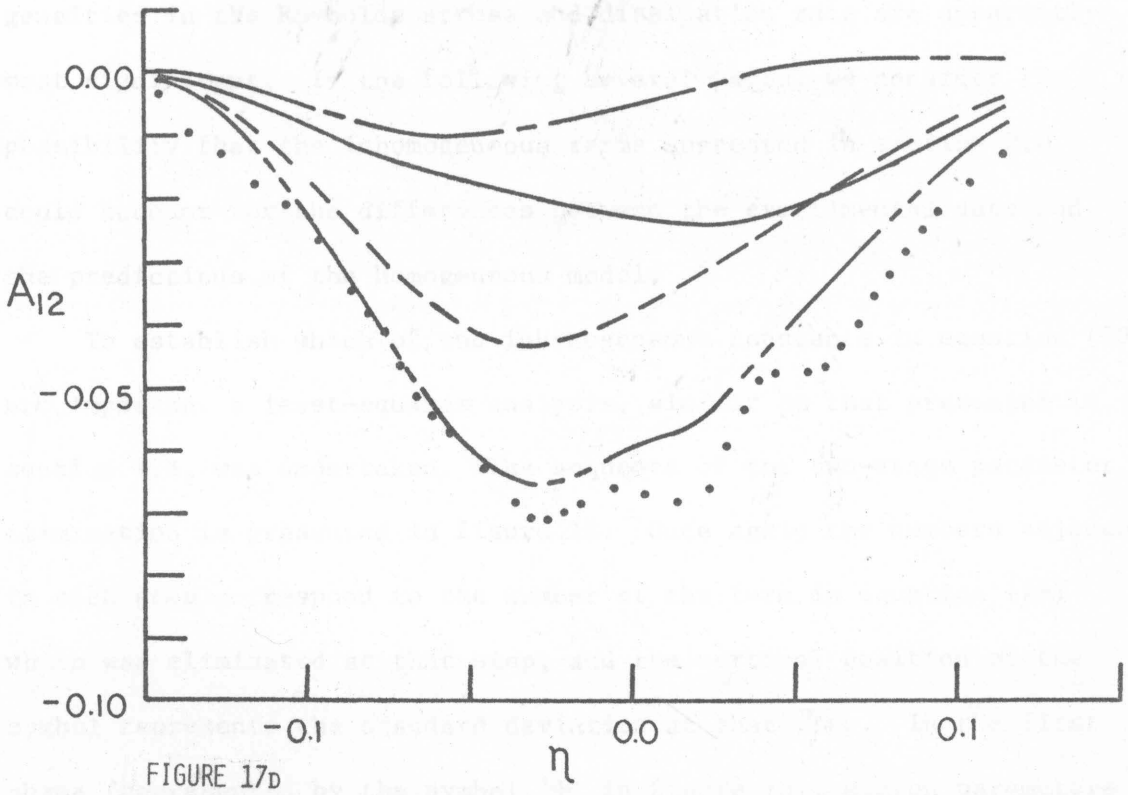

FIGURE 17D

appears to provide the most severe test of the intercomponent transfer models. Shir's model best predicts this flow, while Hanjalic and Launder's model also provides a reasonable estimate of the data. In contrast, the profile predicted by the present homogeneous model is qualitatively unacceptable.

The *homogeneous* form of the intercomponent transfer model, which was developed on the basis of homogeneous wind tunnel data in section 3.B, thus produces fair agreement with the experimental data, of the first four flows examined. Although these flows display strong inhomogeneities, the rate of intercomponent transfer is apparently dominated (in the context of the expansion in anisotropy and inhomogeneity) by the effects of anisotropy. On the other hand, poor agreement is observed in the case of the mixing-layer, where inhomogeneities in the Reynolds stress and dissipation rate are apparently most significant. In the following several pages, we consider the possibility that the inhomogeneous terms suggested in section 2.D could account for the differences between the experimental data and the predictions of the homogeneous model.

To establish which of the inhomogeneous constants in equation (29) are important a least-squares analysis, similar to that presented in section 4.B, was undertaken. The sequence of the two-stage parameter elimination is presented in figure 18. Once again the numbers adjacent to each step correspond to the number of the term in equation (29) which was eliminated at that step, and the vertical position of the symbol represents the standard deviation at that step. In the first phase (represented by the symbol '+' in figure 18), eleven parameters

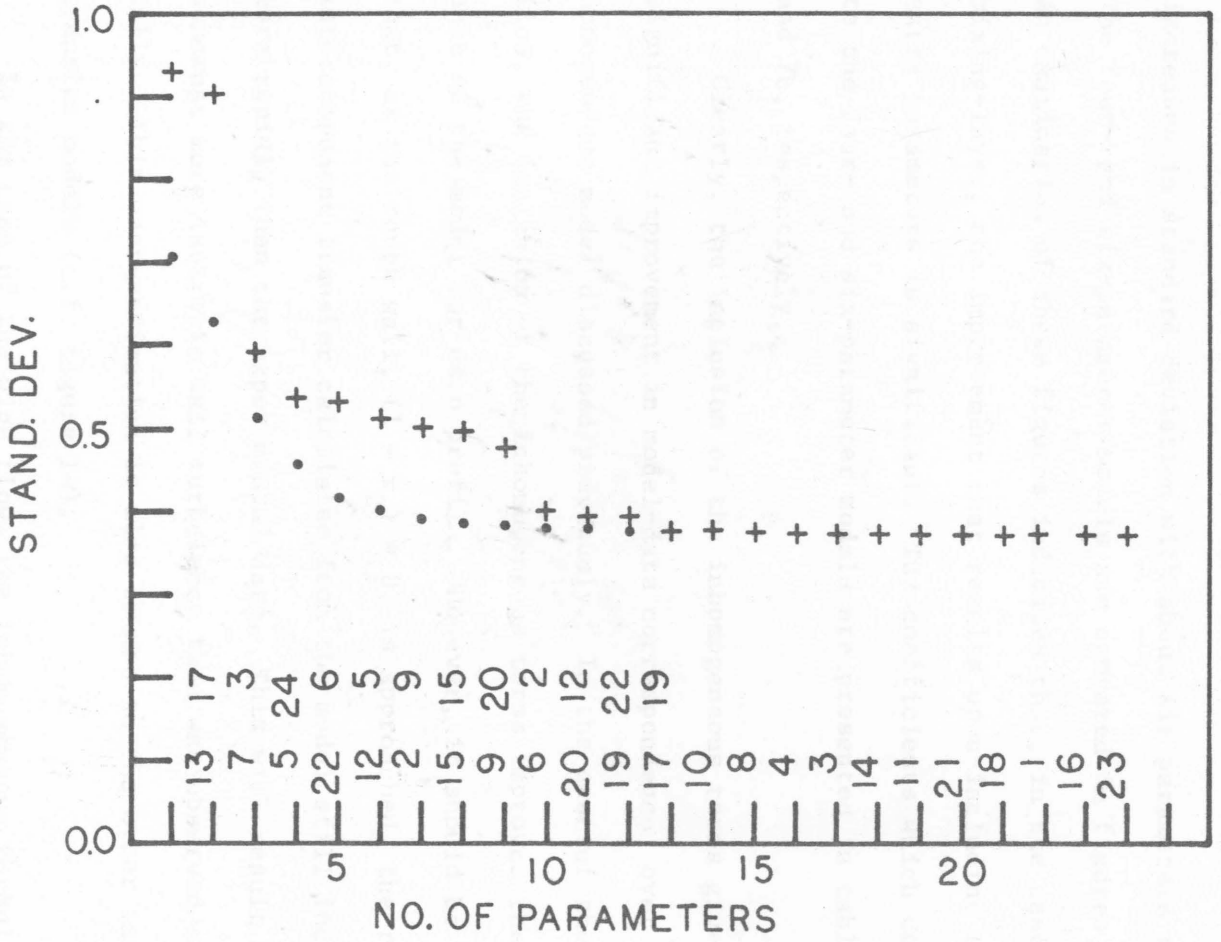

FIGURE 18: SEQUENCE OF PARAMETER ELIMINATION FOR INTERCOMPONENT TRANSFER MODEL;
+ -PRELIMINARY PHASE, • -SECONDARY PHASE.

were eliminated before a non-negligible increase in standard deviation occurred. The secondary elimination, which was initiated with the remaining thirteen-parameter model, began to show significant increases in standard deviation with about six parameters remaining. The four- and six-parameter models are compared in figures 19 - 22. An examination of these figures indicates that, in the case of the mixing-layer, the improvement that results upon including the two extra parameters is significant. The coefficients which correspond to the four- and six-parameter models are presented in tables 7a and 7b, respectively.

Clearly, the inclusion of the inhomogeneous terms gives a significant improvement in model-data correspondence over the homogeneous model discussed previously. In the case of the channel flow, the inclusion of the inhomogeneous terms improves the performance of the model for each profile. However, it should be noted that, as the rough wall, $(1 - x_2) = 0$, is approached, the rate of intercomponent transfer calculated from the model still increases more rapidly than the experimental data. This will result in a somewhat more isotropic wall turbulence than was observed experimentally. This over-estimation is also common to the other intercomponent transfer models (c.f. figure 14).

In the case of the pipe flow, the inhomogeneous formulation again gives the best overall agreement with the experimental data. However, as in the case of the channel flow, the rate of intercomponent energy transfer is over-predicted in the wall region, and the transfer is

FIGURE 19: INTERCOMPONENT TRANSFER FOR ASYMMETRIC CHANNEL;
COMPARISON OF FOUR- AND SIX-PARAMETER MODELS:
————— four-parameter model,
— — — — six-parameter model.

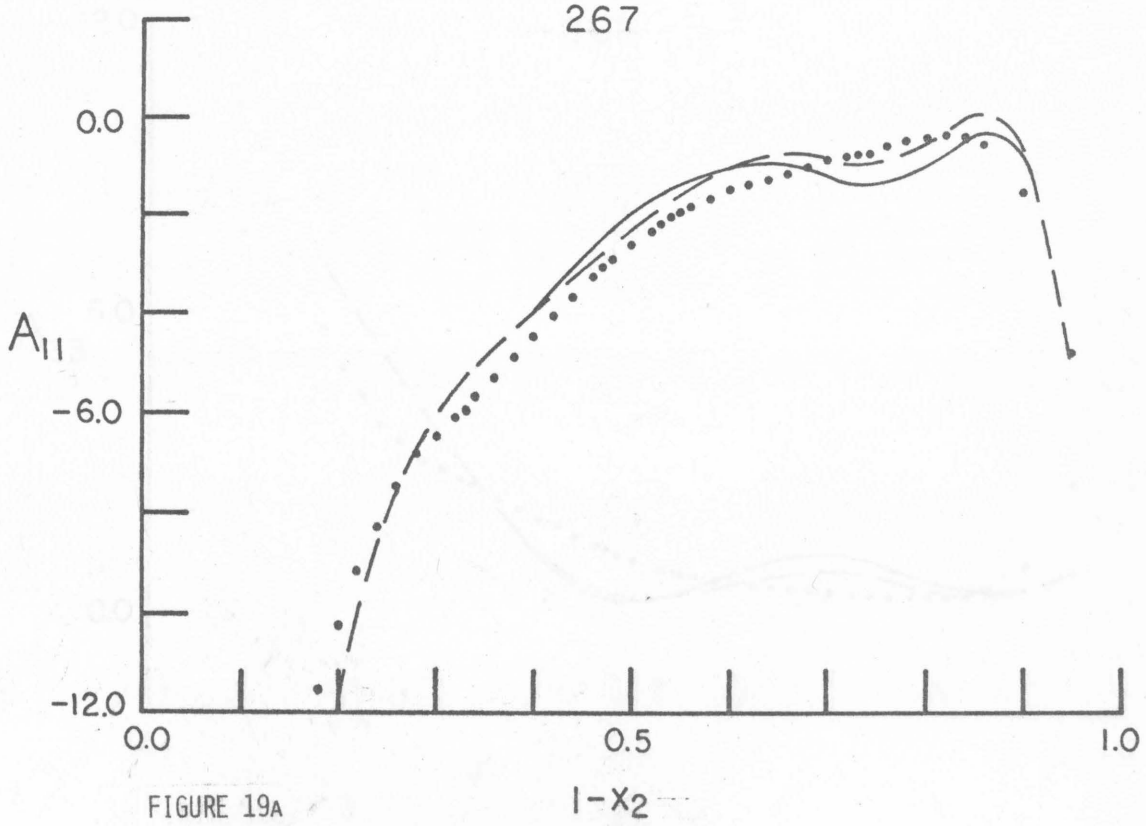

FIGURE 19A

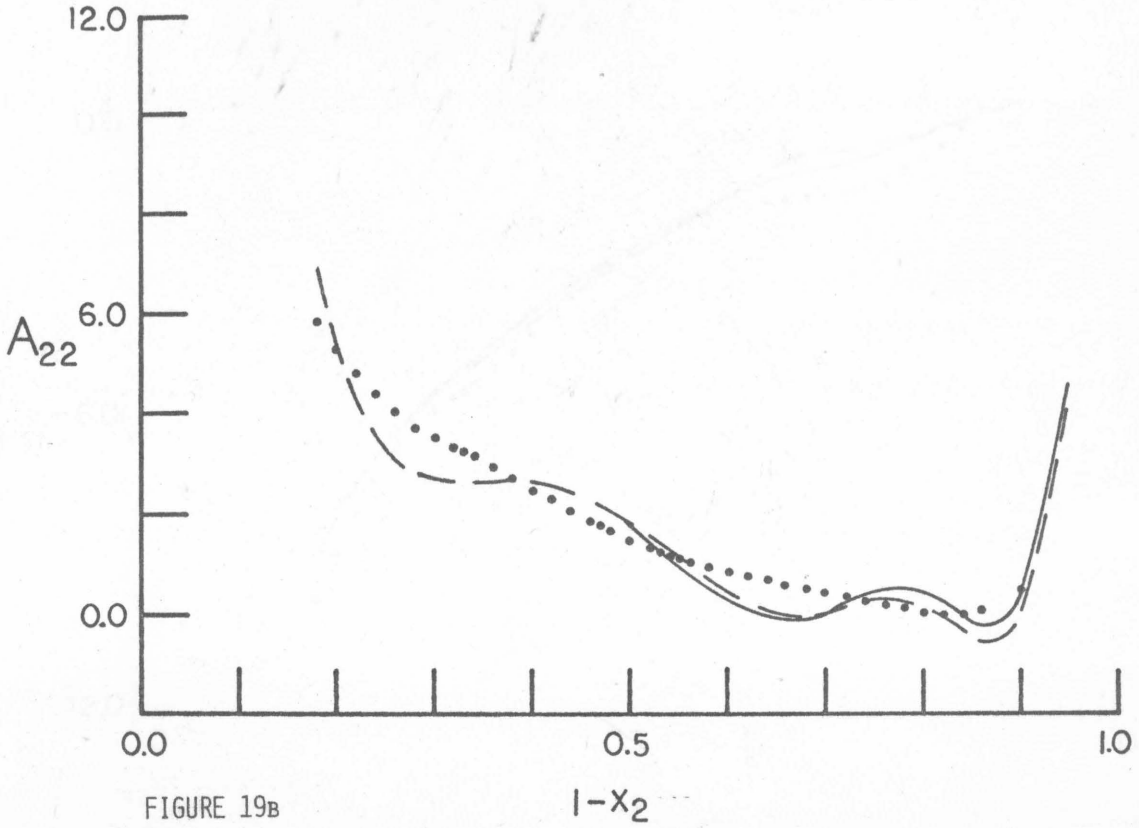

FIGURE 19B

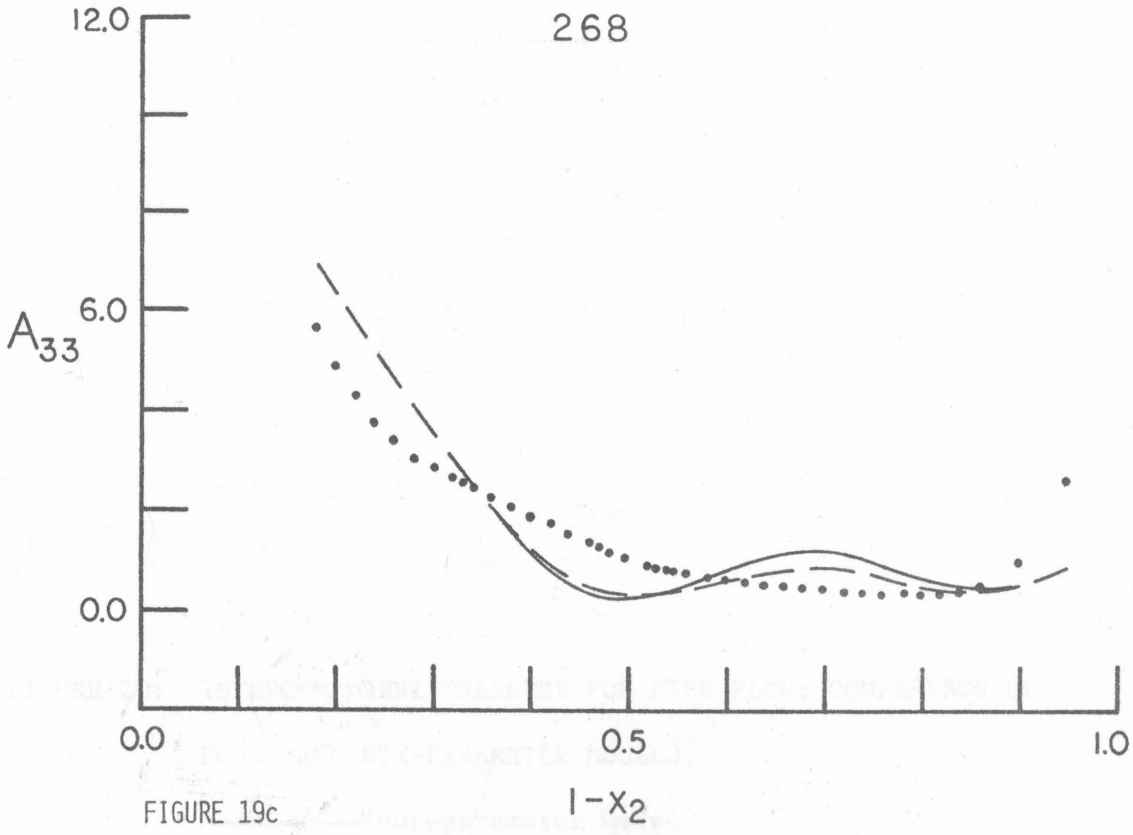

FIGURE 19c

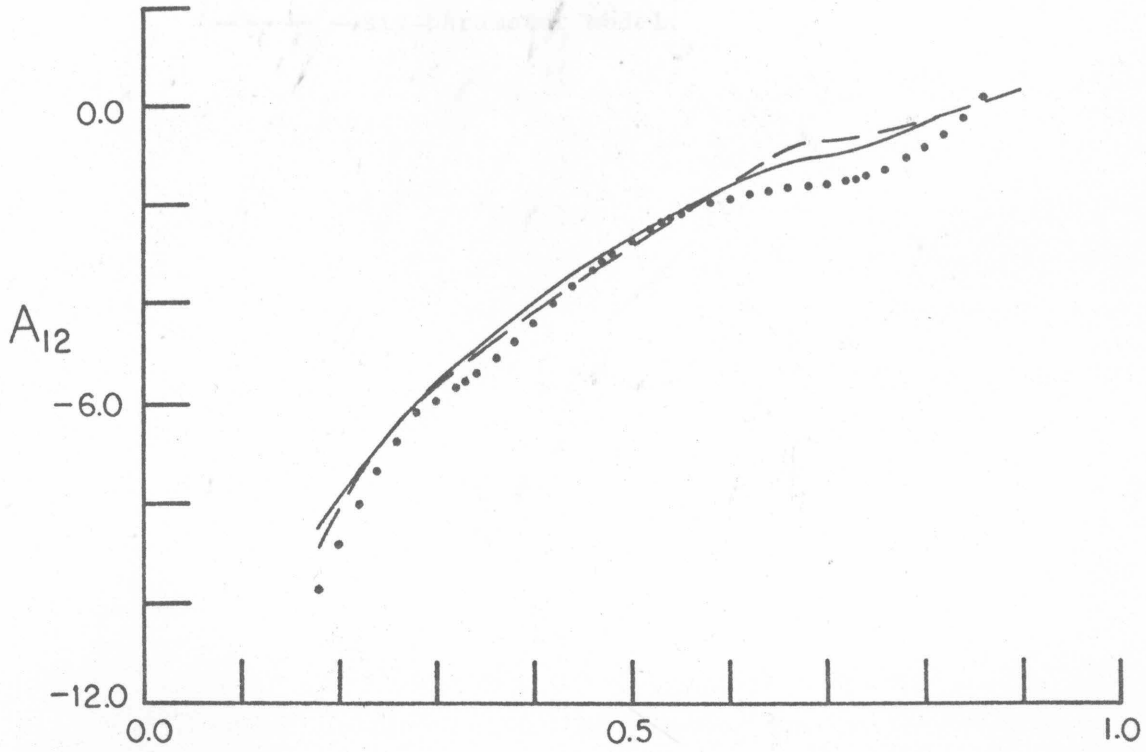

FIGURE 19D

FIGURE 20: INTERCOMPONENT TRANSFER FOR PIPE FLOW; COMPARISON OF FOUR- AND SIX-PARAMETER MODELS:

————— four-parameter model,

— — — — six-parameter model.

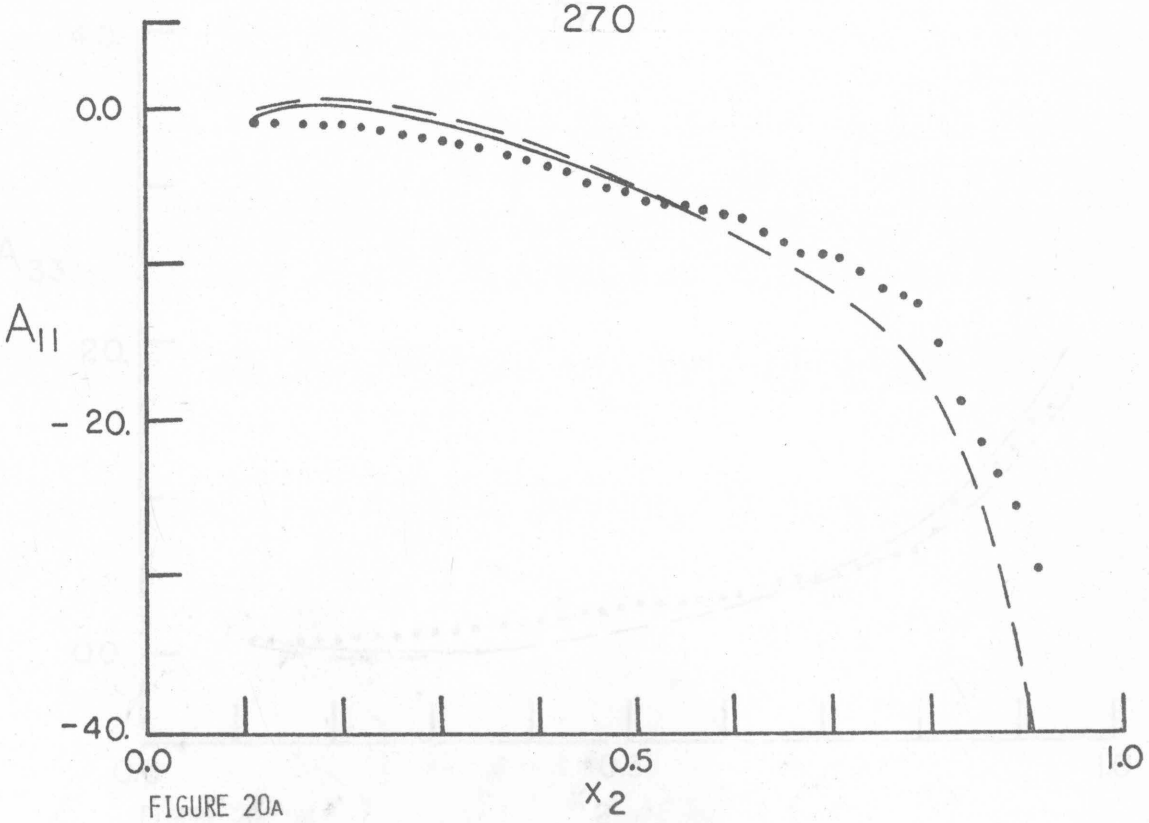

FIGURE 20A

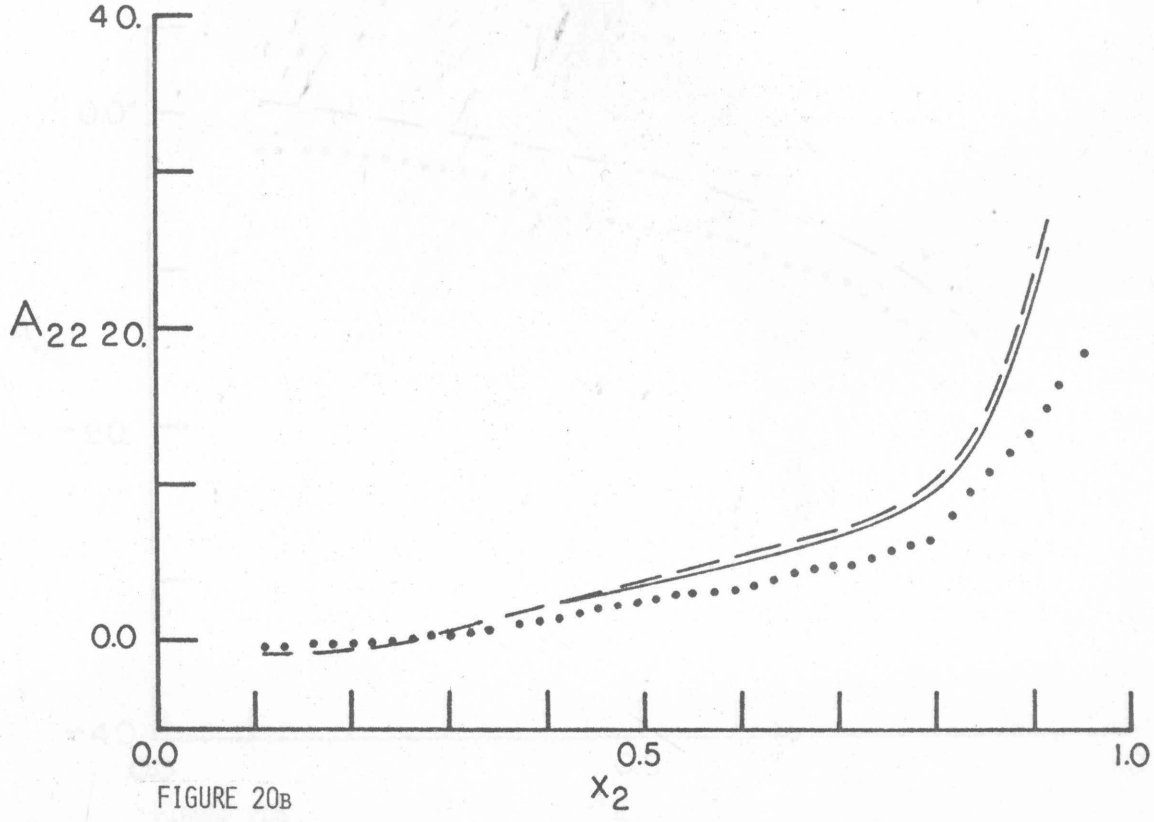

FIGURE 20B

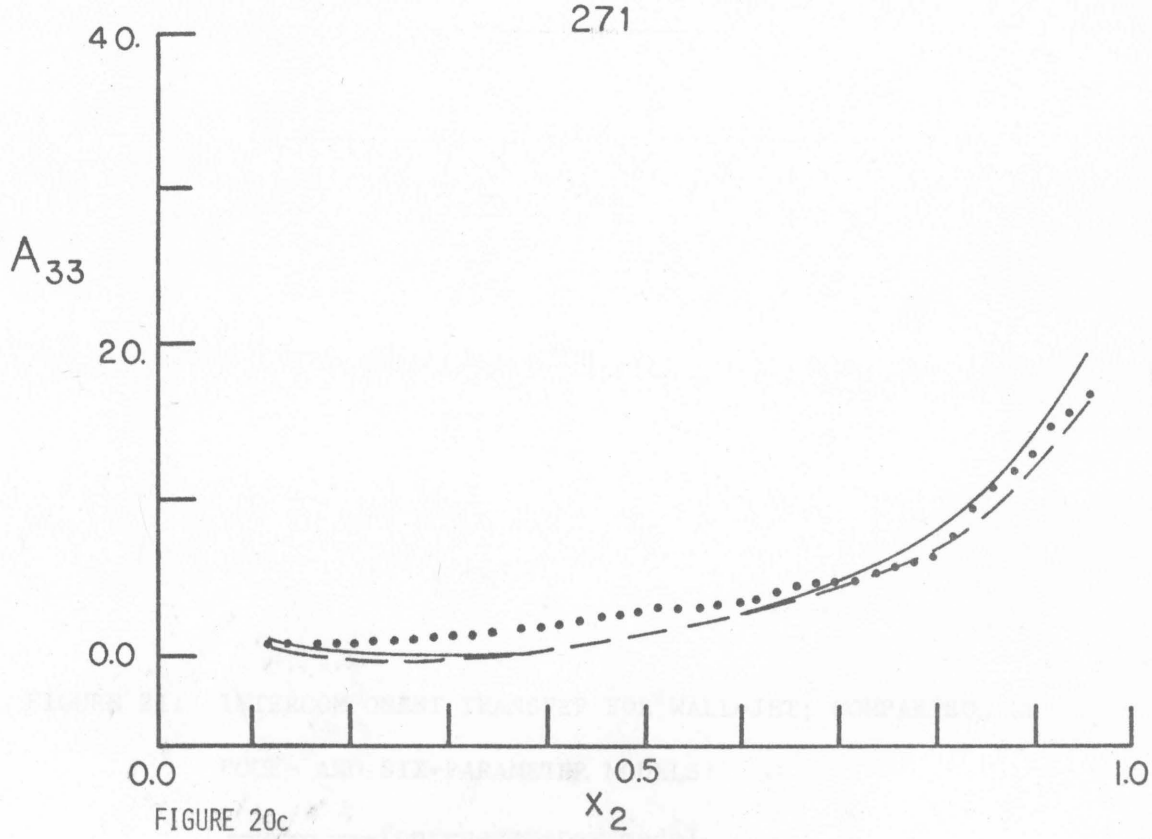

FIGURE 20c

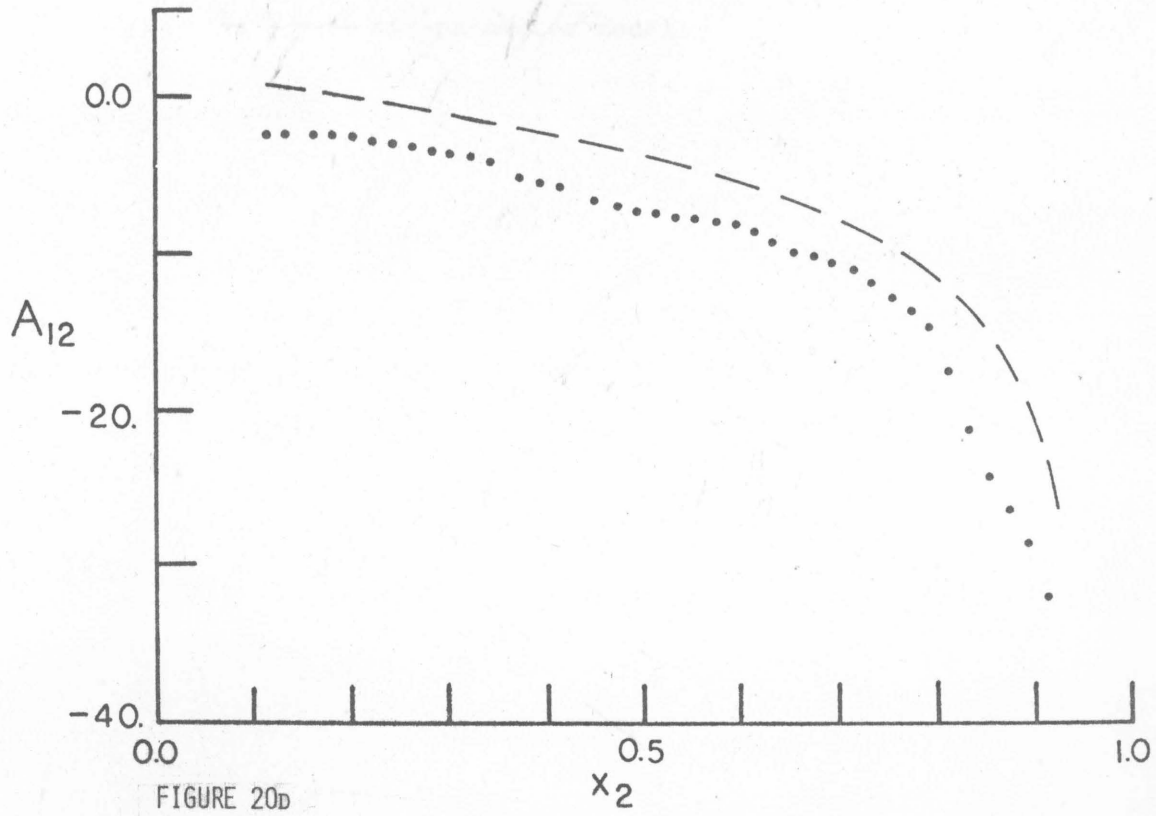

FIGURE 20D

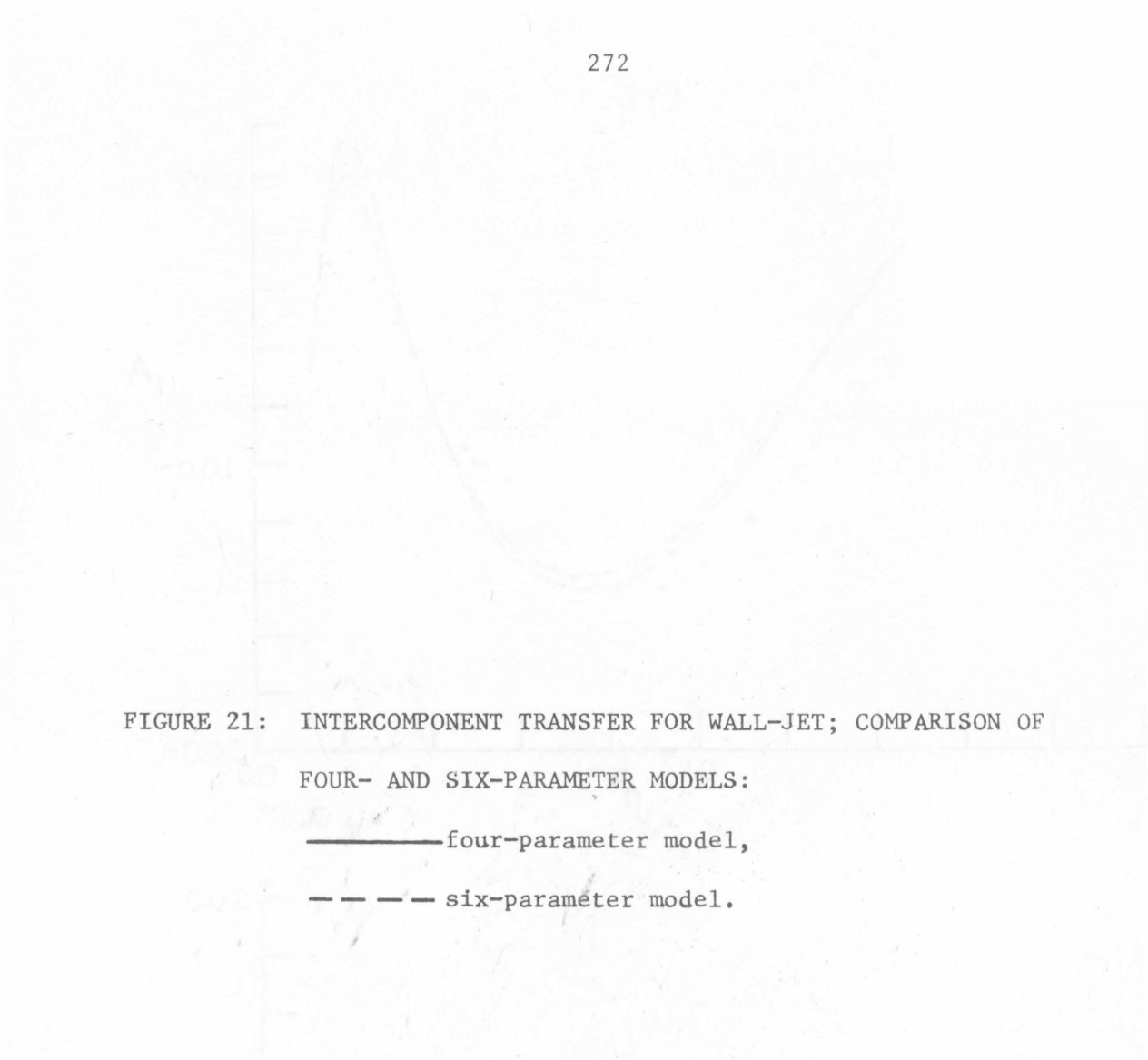

FIGURE 21: INTERCOMPONENT TRANSFER FOR WALL-JET; COMPARISON OF FOUR- AND SIX-PARAMETER MODELS:

———— four-parameter model,

— — — — six-parameter model.

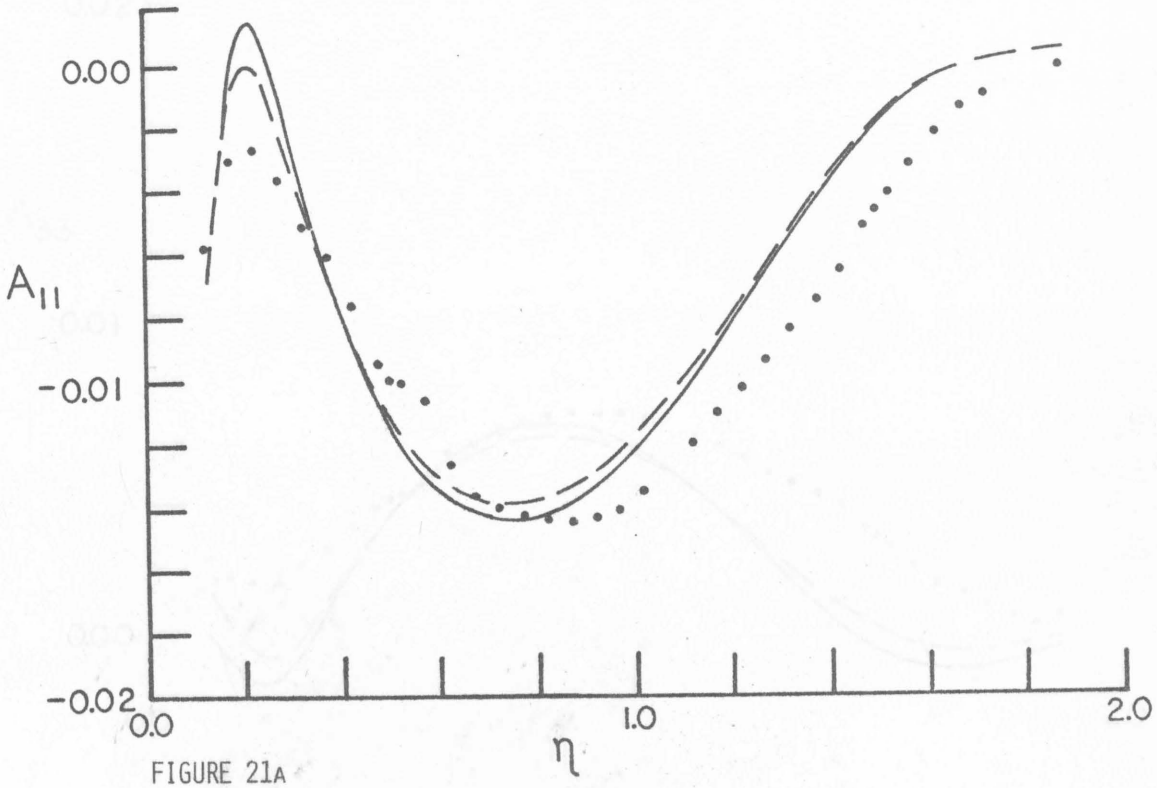

FIGURE 21A

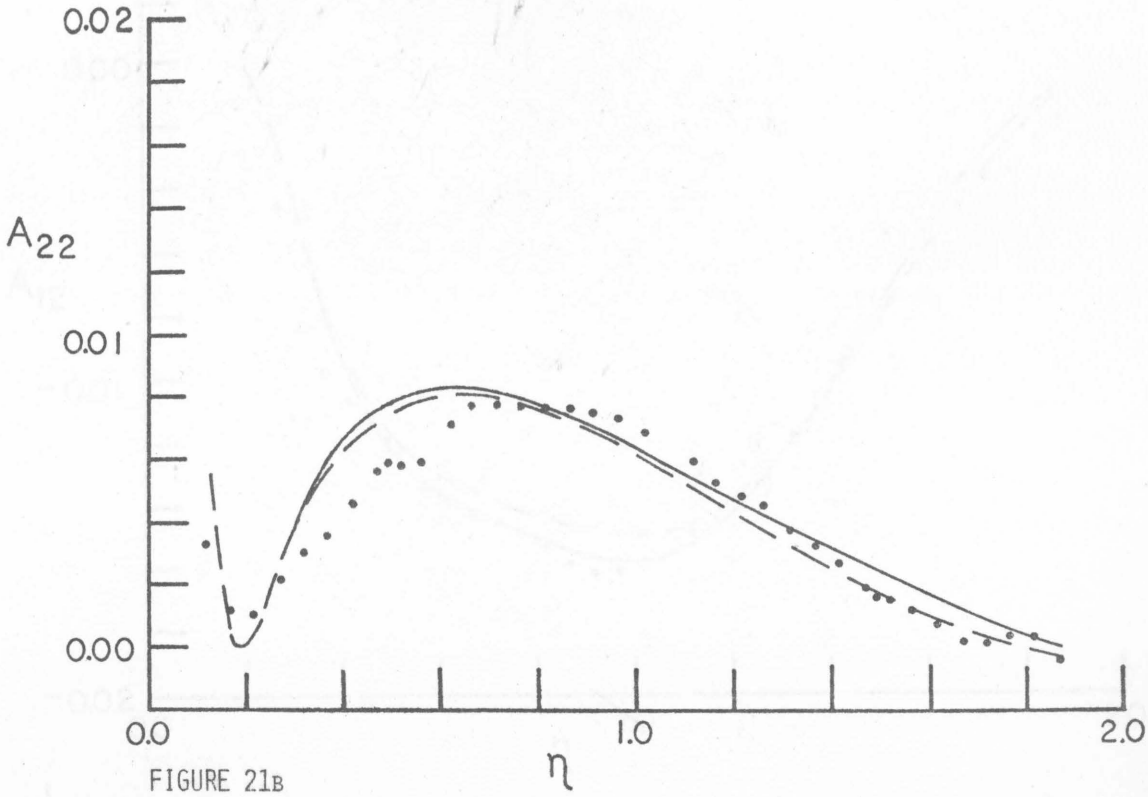

FIGURE 21B

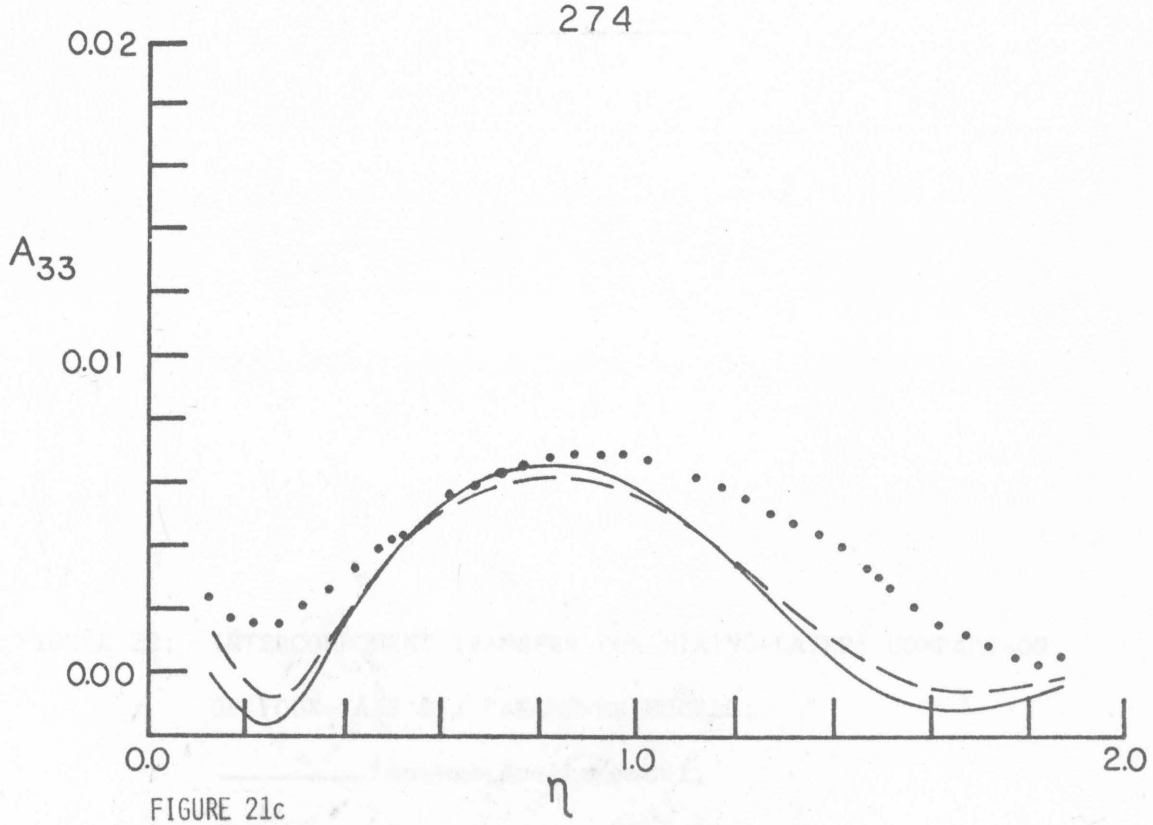

FIGURE 21c

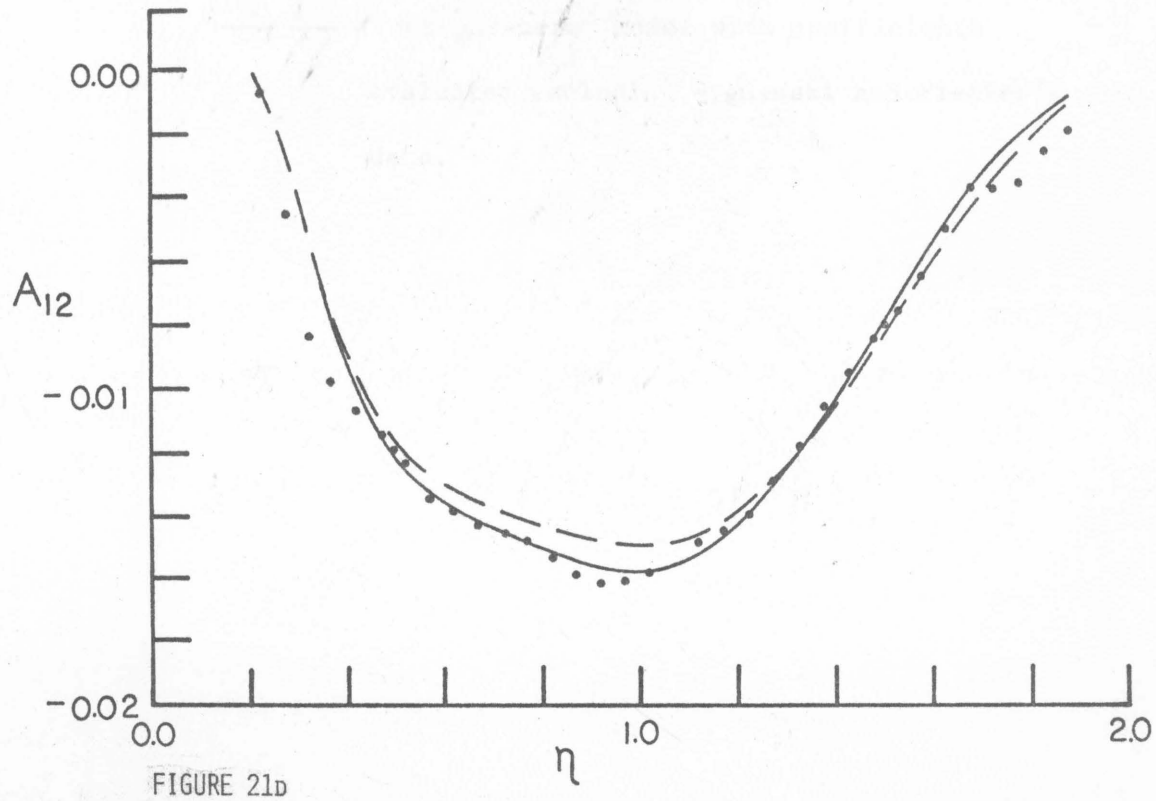

FIGURE 21D

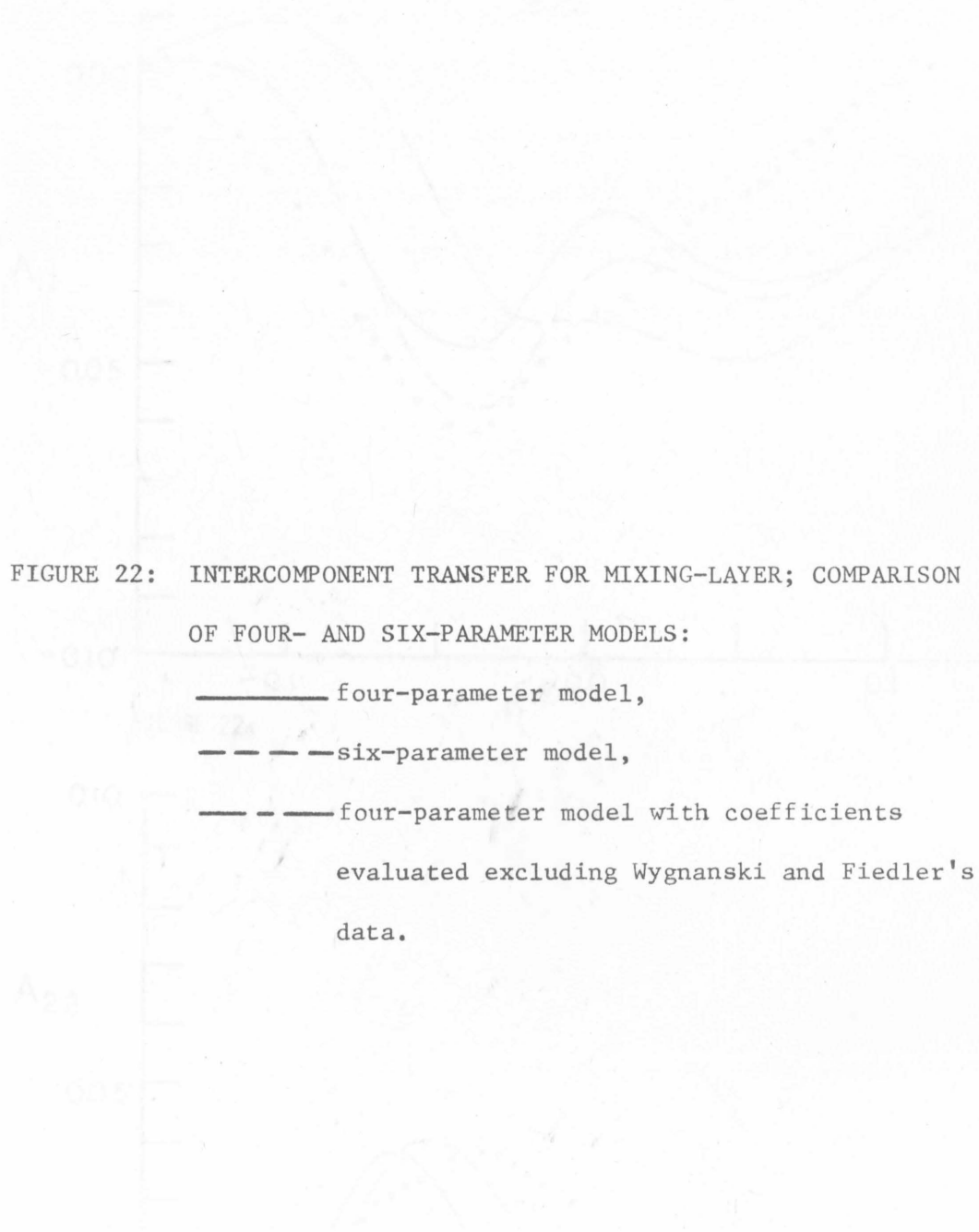

FIGURE 22: INTERCOMPONENT TRANSFER FOR MIXING-LAYER; COMPARISON OF FOUR- AND SIX-PARAMETER MODELS:

———— four-parameter model,

— — — — six-parameter model,

—— - —— four-parameter model with coefficients evaluated excluding Wygnanski and Fiedler's data.

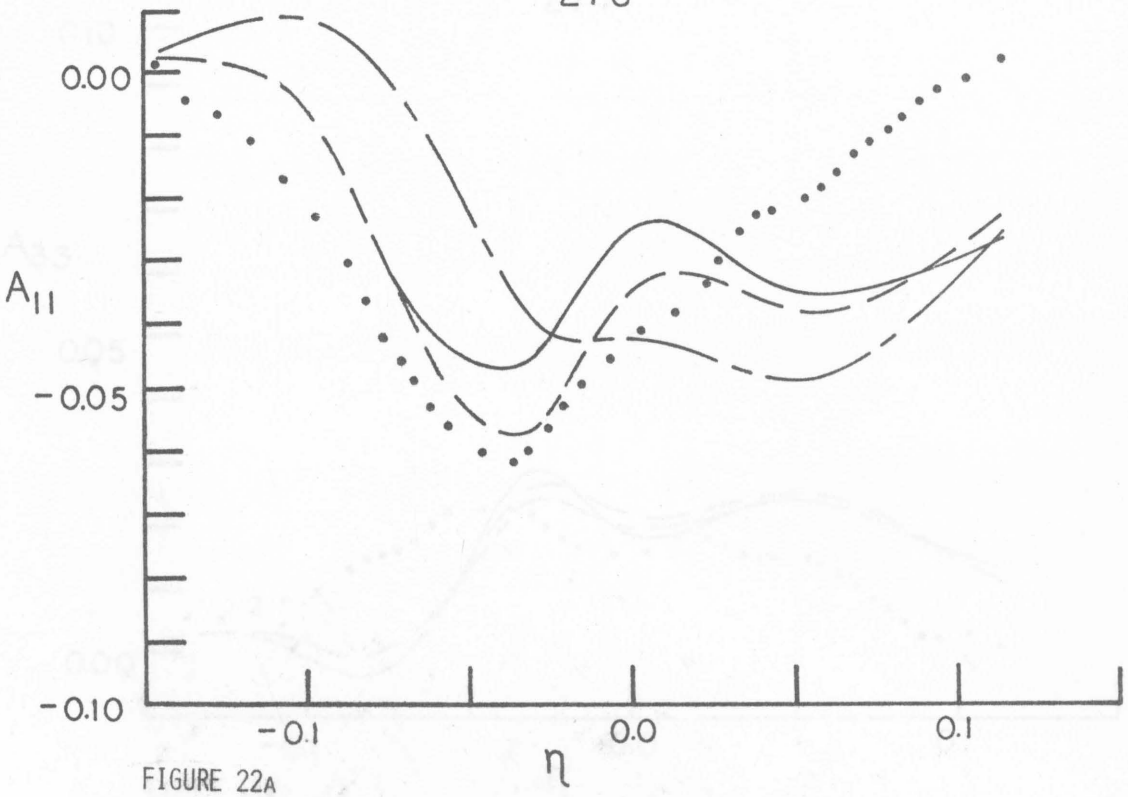

FIGURE 22A

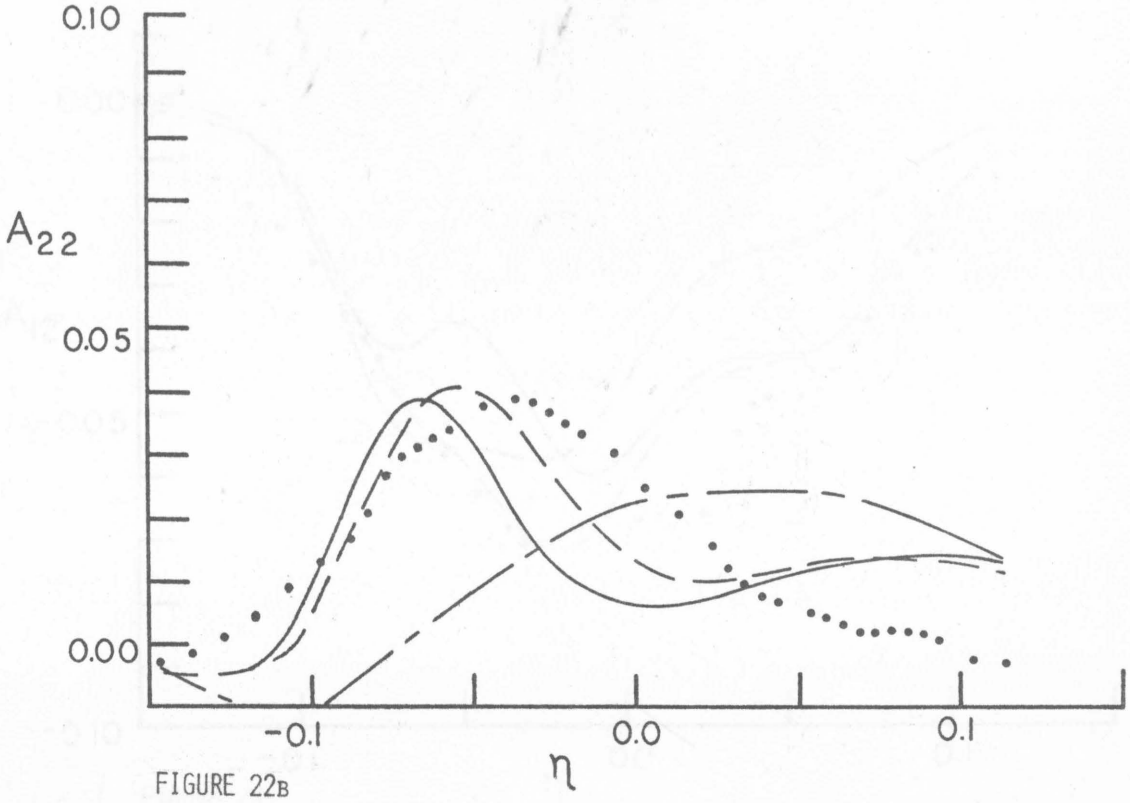

FIGURE 22B

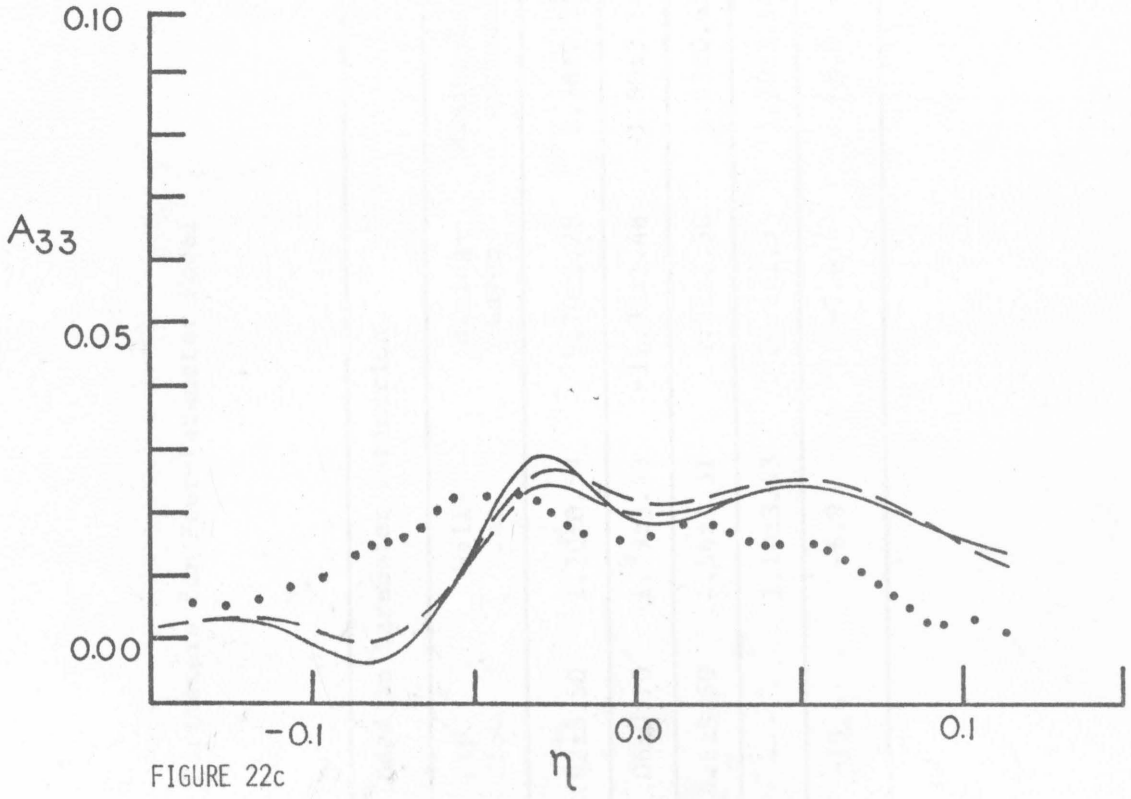

FIGURE 22c

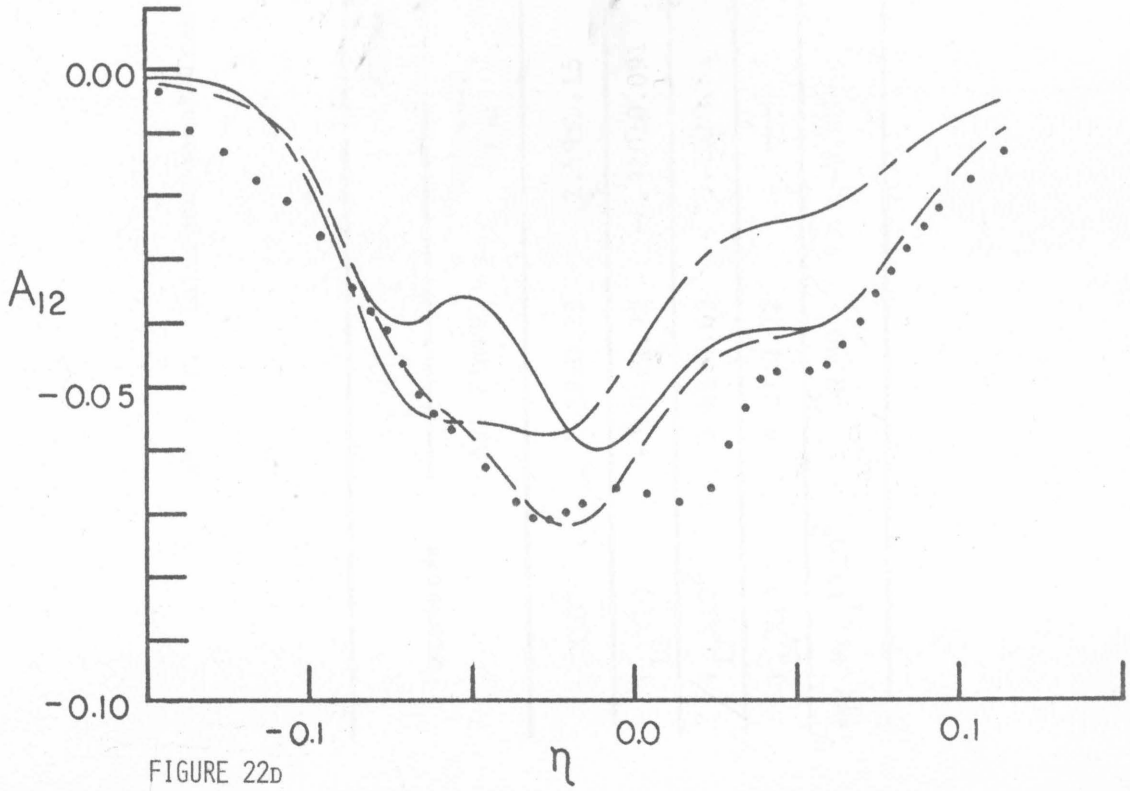

FIGURE 22D

Table 7a. Intercomponent Transfer Parameters for Four-Parameter Model

Parameter	Flows Included in Parameter Estimation					
	All Flows	Channel Flow	Pipe Flow	Wall-Jet	Mixing-Layer	Mixing-Layer excluded
$\gamma_7 X10^2$	2.39±0.23	2.68±0.15	-1.92±5.50	1.70±0.59	9.70±2.25	2.38±0.21
$\gamma_{13} X10$	-9.04±1.72	-0.920±0.091	-1.06±0.70	-1.79±3.43	-11.32±1.48	-1.80±3.14
$\gamma_{17} X10^2$	5.48±0.63	5.16±0.61	14.6±3.50	4.56±1.31	4.27±1.50	5.03±0.62
$\gamma_{24} X10$	8.21±1.72	—	—	1.10±3.43	10.6±1.5	1.20±3.14
$(\gamma_{13}+\gamma_{24}) X10^2$	-8.30	-9.20	-10.6	-6.9	-7.6	-6.0

Table 7b. Intercomponent Transfer Parameters for Six-Parameter Model

Parameter	Flows Included in Parameter Estimate					
	All Flows	Channel Flow	Pipe Flow	Wall-Jet	Mixing-Layer	Mixing-Layer excluded
$\gamma_5 X10^3$	-3.44±1.5	-9.56±2.15	-28.0±7.6	-7.36±2.50	-19.0±6.30	-4.68±1.46
$\gamma_6 X10^2$	5.76±1.65	7.02±2.55	-14.1±10.6	82.6±46.9	8.45±2.27	2.64±2.86
$\gamma_7 X10^2$	2.04±0.24	2.22±0.22	-2.55±1.24	1.44±0.52	4.54±2.47	2.21±0.26
$\gamma_{13} X10$	-8.36±1.66	-1.07±0.09	1.66±1.06	2.02±3.55	-12.5±1.38	1.81±3.25
$\gamma_{17} X10^2$	4.10±0.71	0.869±1.07	20.3±2.88	4.91±1.10	0.863±1.47	3.94±0.69
$\gamma_{24} X10$	7.45±1.66	—	—	-2.82±3.63	11.6±1.4	-2.76±3.26
$(\gamma_{13}+\gamma_{24}) X10^2$	-9.1	-10.7	16.6	-8.0	-9.0	-9.5

slightly under-estimated in the core of the pipe. The A_{12} profile, on the other hand, is under-predicted through the flow.

The profiles calculated for the mixing-layer with the inhomogeneous model show the most significant improvement over the homogeneous model. Even with this significant overall improvement, however, the predicted intercomponent energy transfer is still over-estimated for $\eta > 0$ (see also figure 17). The source of this difficulty is not clear. However, very slight errors in the profiles of $\overline{u_i u_j}$ would lead to rather large errors in a_{ij} due to the very steep gradients in the profiles in this region. It is possible that such errors are responsible for the apparent discrepancy in the model. This inconsistency between model and data could also arise from a profile of ε which is too small for $\eta > 0$, since the dissipation rate enters the intercomponent transfer expression in proportion to q^2/ε. However, the latter possibility is unlikely since over-prediction is not evident in the A_{12} profile.

Only in the near-wall region of the wall-jet (figure 21) does the inclusion of the inhomogeneous terms result in a significant reduction in model performance. In particular, $|A_{11}|$ and $|A_{33}|$ given by the model at $\eta \sim 0.2$ are smaller than the experimental values (and also smaller than the value predicted by the homogeneous model). This will result in an energy distribution which is more anisotropic than the data. Note, however, that the six-parameter model better predicts this region of the wall-jet than does the four-parameter model.

In an effort to investigate the degree of universality of the model parameters for the inhomogeneous terms in A_{ij}, the parameters were re-evaluated on the basis of only a limited portion of the data. The first test was to estimate the coefficients (as in section 4.B) on the basis of each flow individually. Before this analysis can be carried out, however, it is necessary to realize that for the pipe and channel flows, terms 13 and 24 are identical. These terms give *different* contributions to the intercomponent transfer, only for non-parallel flows. Thus, for the parallel flows, the columns in $\overline{C}$ (section 4.B) which correspond to terms 13 and 24 are linearly dependent. Hence, $\left[C_{ik}C_{jk}\right]$ cannot be inverted. To remedy this singularity, when the coefficients were evaluated on the basis of only the parallel flows, γ_{24} was assumed to be zero. Although the wall-jet is not a parallel flow, as was noted previously, its streamwise derivatives have a magnitude of only 4% of the cross-stream derivatives. Hence, in this flow also, it is primarily the sum $(\gamma_{13} + \gamma_{24})$ that is of relevance. The only flow in which the values of γ_{13} and γ_{24} have much significance individually, is the mixing-layer, since its streamwise derivatives are about 10% of the cross-stream values. The parameter values that resulted from the above analysis are presented in tables 7a, b. With the parallel-flow singularity in mind, an additional row has been included in these tables, which gives the sum $(\gamma_{13} + \gamma_{24})$ for comparison.

An examination of table 7a indicates that, for the four parameter model, the parameters chosen on the basis of each flow independently,

are remarkably consistent with the parameters chosen on the basis of all flows taken together. In fact, with the exception of γ_7 in the mixing-layer and γ_{17} in the pipe flow, the regions of uncertainty of all estimated parameters overlap. The values chosen for γ_{13} and γ_{24} on the basis of the mixing-layer differ considerably from those chosen on the basis of the wall-jet. However (as noted above), it is the sum $(\gamma_{13} + \gamma_{24})$ that is of relevance for this comparison. The agreement in this quantity is excellent.

The coefficients presented in table 7b for the six-parameter model do not show the same consistency as was observed in table 7a. In fact, there is considerable variability in both the new coefficients (γ_5 and γ_6) and the old coefficients (γ_7, γ_{13}, γ_{17} and γ_{24}). In the case of the new parameters, this is to be expected, since an examination of figures 19 to 22 shows that the two new terms are of primary significance only in the mixing-layer. Hence, these coefficients cannot be properly evaluated on the basis of the other three flows where they are of marginal significance. With all of the flow considered simultaneously, the parameter estimate is improved considerably, as substantiated by the fact that the six-parameter values fall within the uncertainty limits of the four-parameter model coefficients presented in table 7a.

A second test, which was carried out to assess the universality of the coefficients, involved the re-estimation of model parameters on the basis of only the first three flows. (i.e. The mixing-layer was excluded from the parameter estimation.) These parameters were

then used to predict the mixing-layer profiles. As one would expect, for the flows included in the parameter estimation, the correspondence between model and data was improved slightly, while for the mixing-layer the correspondence decreased. However, as indicated in figure 22, the profiles predicted by the four-parameter model for the mixing-layer (the long-short broken line) are not inconsistent with the experimental data, and, with the exception of the A_{22} component, give a significant improvement over the homogeneous model profiles. Particularly good is the profile predicted for A_{12}. The fact that parameters determined on the basis of the first three flows (for which inhomogeneities apparently account for only a small part of the total intercomponent transfer) can provide a reasonable approximation to the fourth flow, for which the inhomogeneous contribution is of primary significance, provides some additional evidence of parameter universality. The actual values of the coefficients calculated on this basis are presented in tables 7a, b. With the exception of the coefficients γ_{13} and γ_{24}, all of the predicted parameters fall within the uncertainties of the original parameter estimates. Once again we conclude that the values of γ_{13} and γ_{24}, which are very critical to the profiles of the mixing-layer, cannot be adequately estimated without a consideration of this flow.

It should be remembered that only inhomogeneous terms to first order in anisotropy (i.e. to O(1,2)) have been considered in the intercomponent transfer model to this point. Terms which are second order in anisotropy may also prove to be important, particularly in

the near-wall region of the wall-bounded flows, where anisotropy is the greatest and where the previous discussion has indicated that some systematic inconsistencies still persist. However, it is unlikely that terms which are higher order in anisotropy could significantly improve the prediction of the nearly isotropic mixing-layer. Before an effort is made to isolate possible higher order contributions in anisotropy,† the full numerical solution of the two-point-boundary-value problems which govern these four flows should be undertaken, to assess further whether such terms are indeed necessary.

D. Inhomogeneous Constants in the Dissipation Equation

For the elimination of parameters from the Reynolds stress equation (sections 4.B and 4.C), direct measurements of the turbulent diffusion term were available so that the profile of each term to be modeled could be obtained explicitly, either directly from the experimental measurements or indirectly by difference from the governing equations. Similar measurements for the turbulent diffusion of dissipation rate are not available. Hence, the contributions of the production-dissipation term and the turbulent diffusion term cannot be independently identified. Thus, it is necessary to estimate the inhomogeneous constants in both terms simultaneously. Furthermore, since the divergence of each term

†This is an extremely difficult task due to the high order of the algebraic system that must be repeatedly inverted during the parameter elimination.

suggested for D_k is simply a linear combination of the invariants proposed for P_I, only the 34 terms presented as equation (40b) must be considered in the process of parameter elimination and estimation.

To accomplish the parameter elimination and estimation for the dissipation equation, with a reasonable computational effort, a least-squares formulation was once again sought. Since the inhomogeneous constants must be consistent with the homogeneous parameters which were determined in section 3.C, they must satisfy the equation

$$\frac{\partial D_k}{\partial x_k} - P_I = P_H - \frac{D\epsilon}{Dt} \tag{59}$$

Here, P_H represents the homogeneous production-dissipation terms of equation (40a) (with parameters A) and P_I represents the inhomogeneous contributions to this term (equation (40b)), for which the parameters are as yet unknown. The parameters were estimated as the least-squares solution of equation (59) in the manner outlined in section 4.B. The weighting factors used in this analysis are given in table 5.

The elimination of dissipation parameters was carried out somewhat differently than in the previous analyses. Special consideration was required since, with all 34 terms included, $\overline{C}$ was very ill-conditioned. Although $\overline{C}$ could be adequately inverted to achieve a set of parameters with small standard deviation, *to within the accuracy of the data* it contained terms which could be constructed from one or more combinations of other terms. The consequence of

this was that, for the first 10 to 14 parameters eliminated, any one of a number of terms could be eliminated to give a comparable increase in standard deviation. It was felt that if there was an alternative as to whether a zero, first or second order (in anisotropy) term should be excluded at a particular step in the elimination (to give a comparable increase in standard deviation), the second order term should be rejected. To accomplish this, the first phase of the parameter elimination was carried out as in sections 4.B and 4.C, with the modification that in this phase *only second order terms* were discarded.

The sequence of the preliminary parameter elimination is shown in figure 23, for the final 11 second order parameters eliminated. (The parameters eliminated, but not shown in figure 23, in the order of their elimination are: 21, 32, 22, 24, 29, 30, 19, 18, 14, 23.) The standard deviation showed its first significant increase with 21 terms remaining. The second phase of the parameter elimination began with 22 parameters remaining. For this we adopted the same rejection criterion that was used in the first phase. However, no preference was given to zero and first order terms. As shown in figure 23, a significant increase in standard deviation occurred with 15 parameters remaining. The final phase of parameter elimination, which involved the inversion of the coefficient matrix $\overline{C}$ for each parameter, at each elimination step, was initiated with 16 parameters remaining. On the basis of this final sequence of parameter eliminations, three models were selected for closer examination: the four-, seven- and

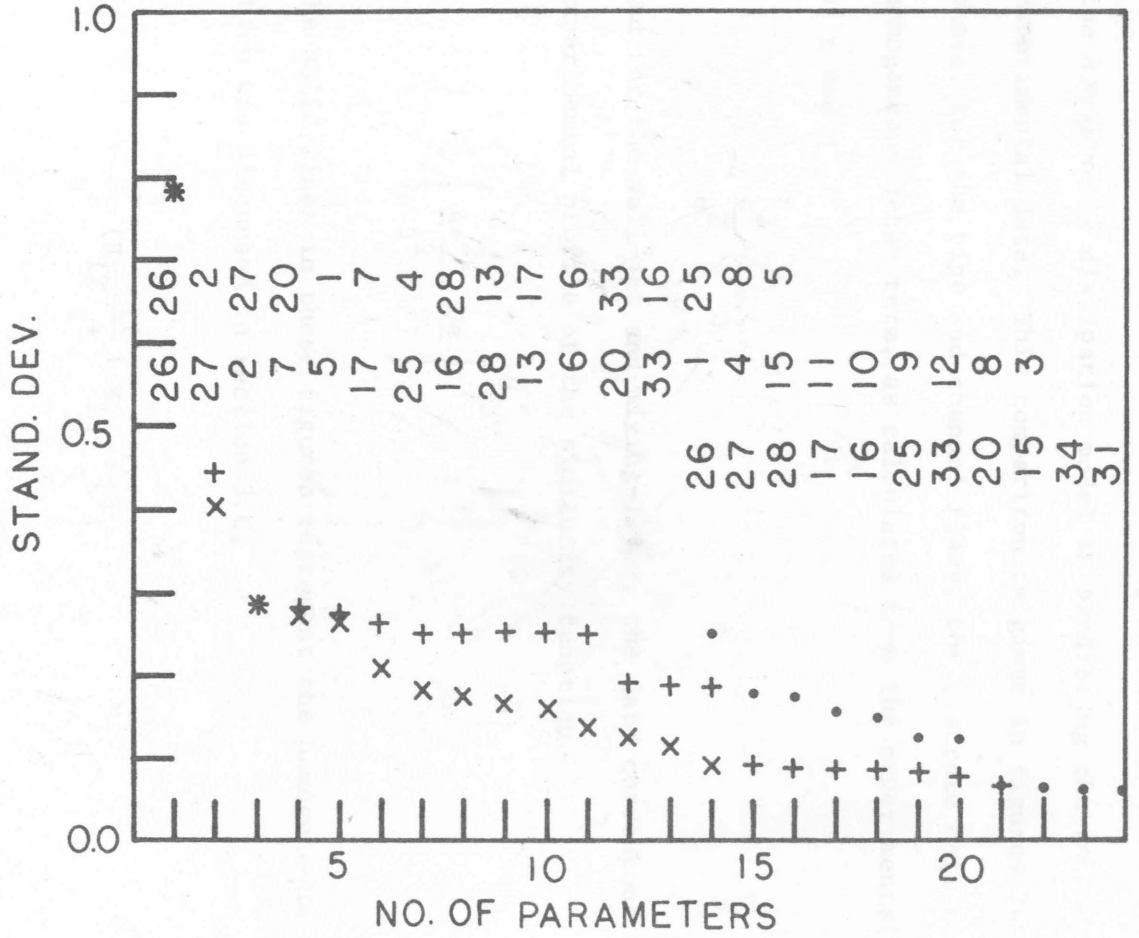

FIGURE 23: SEQUENCE OF PARAMETER ELIMINATION FOR DISSIPATION MODEL;
• -PRELIMINARY PHASE, + -SECONDARY PHASE, × -FINAL PHASE.

fourteen-parameter models. The coefficients calculated for these models are presented in tables 8a, b, c.

Before the comparison of the four-, seven- and fourteen-parameter models is presented, it is interesting to examine the performance of the *homogeneous* dissipation model in predicting the *inhomogeneous* experimental data. This comparison is given in figures 24 to 27 where, for the pipe and channel flows, the discrete data represent the homogeneous decay term, as calculated from the experimental profiles of ε and q^2,

$$-4\,\frac{\varepsilon^2}{q^2} \tag{60a}$$

and for the wall-jet and mixing-layer, the data correspond to the experimental profile of the similarity function

$$-\left(\frac{4e^2}{q^2}+\frac{De}{Dt}\right) \tag{60b}$$

The solid lines in these figures represent the homogeneous term, which was discussed in section 3.C,

$$-\frac{\varepsilon^2}{q^2}\left(B_{12}\,\frac{II}{q^4}+B_{13}\,\frac{III}{q^6}\right) \tag{61}$$

For a *homogeneous* flow (and subject to the assumption that the homogeneous model is correct) the functions (60) and (61) must be equal to satisfy equation (42). Hence, in the *inhomogeneous* flows which we are examining, one can attribute differences between these functions

Table 8a. Coefficients of the Four-Parameter Dissipation Model

Parameter	Flows Included in Parameter Estimate					
	All Flows	Channel Flow	Pipe Flow	Wall-Jet	Mixing-Layer	Mixing-Layer excluded
$b_2 X10^2$	3.05±0.87	3.63±0.47	2.77±1.64	-0.521±2.06	7.45±1.25	3.43±0.69
$b_{20} X10$	3.22±1.64	6.11±1.20	7.29±0.91	9.05±1.92	-8.03±1.97	5.71±1.28
$b_{26} X10$	-12.2±0.92	-9.42±0.70	-12.70±1.73	-4.81±3.97	-13.9±0.57	-9.82±0.89
b_{27}	2.37±0.34	1.37±0.18	2.50±0.17	1.56±0.65	2.47±0.59	1.55±0.33

Table 8b. Coefficients of Seven-Parameter Dissipation Model

	Flows Included in Parameter Estimation					
	All Flows	Channel Flow	Pipe Flow	Wall-Jet	Mixing-Layer	Mixing-Layer excluded
$b_1 X10^2$	-5.65±0.85	-7.29±0.57	-8.34±1.77	-15.8±1.9	-2.48±0.67	-5.10±1.72
$b_2 X10^2$	5.79±0.74	6.69±0.80	1.48±1.99	4.36±1.53	8.40±0.66	5.43±0.90
$b_4 X10^3$	-4.75±1.14	-7.97±2.36	-1.86±0.71	-11.7±1.06	-7.41±0.64	-3.99±1.32
$b_7 X10$	2.73±0.50	4.26±4.53	-9.93±3.67	6.05±0.87	1.99±0.32	2.50±0.99
b_{20}	1.26±0.18	2.08±0.12	1.10±0.09	2.99±0.22	-0.104±0.231	1.22±0.22
$b_{26} X10$	-9.57 ±0.77	-8.96 ±0.77	-10.1±2.0	-0.354±7.82	-11.0±0.52	-9.57±0.87
b_{27}	2.09±0.30	2.19±1.29	-1.71±1.48	1.74±1.49	1.61±0.30	2.06±0.43

Table 8c. Coefficients of the Fourteen-parameter Model

Parameter	Flows Included in Parameter Estimate	
	All Flows	Mixing-Layer Excluded
b_1 X 10	-1.18±0.15	-1.69±0.28
b_2 X 10^2	8.21±0.57	9.10±0.84
b_4 X 10^3	-7.72±0.71	-7.23±1.05
b_6 X 10^2	71.5±14.6	-2.87±0.68
b_7 X 10	9.58±1.31	12.0±2.12
b_{13}	-1.26±0.20	-1.29±0.26
b_{16}	4.10±0.82	4.56±1.56
b_{17}	12.50±1.85	14.00±4.73
b_{20}	2.22±0.15	1.98±0.37
b_{25}	-2.37±0.53	-3.05±2.05
b_{26}	-1.78±0.20	-1.82±0.24
b_{27}	7.40±0.82	8.17±1.14
b_{29}	-17.30±2.73	-19.9±4.66
b_{33}	-2.02±0.367	-1.26±0.678

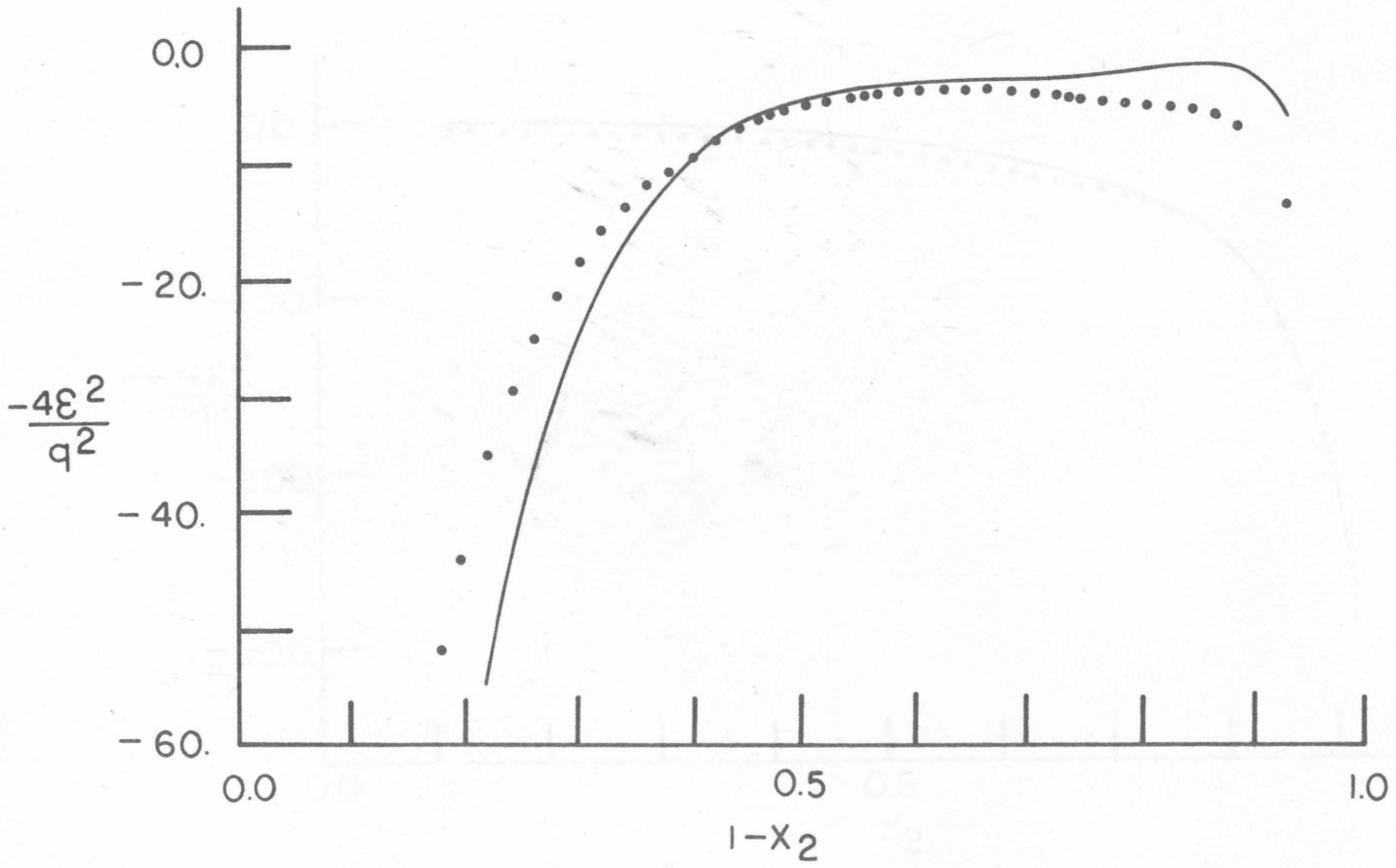

FIGURE 24: DISSIPATION BALANCE FOR CHANNEL FLOW; HOMOGENEOUS MODEL;
• -EXPERIMENTAL DATA OF HANJALIC AND LAUNDER (1972A),
——— HOMOGENEOUS MODEL WITH PARAMETERS A.

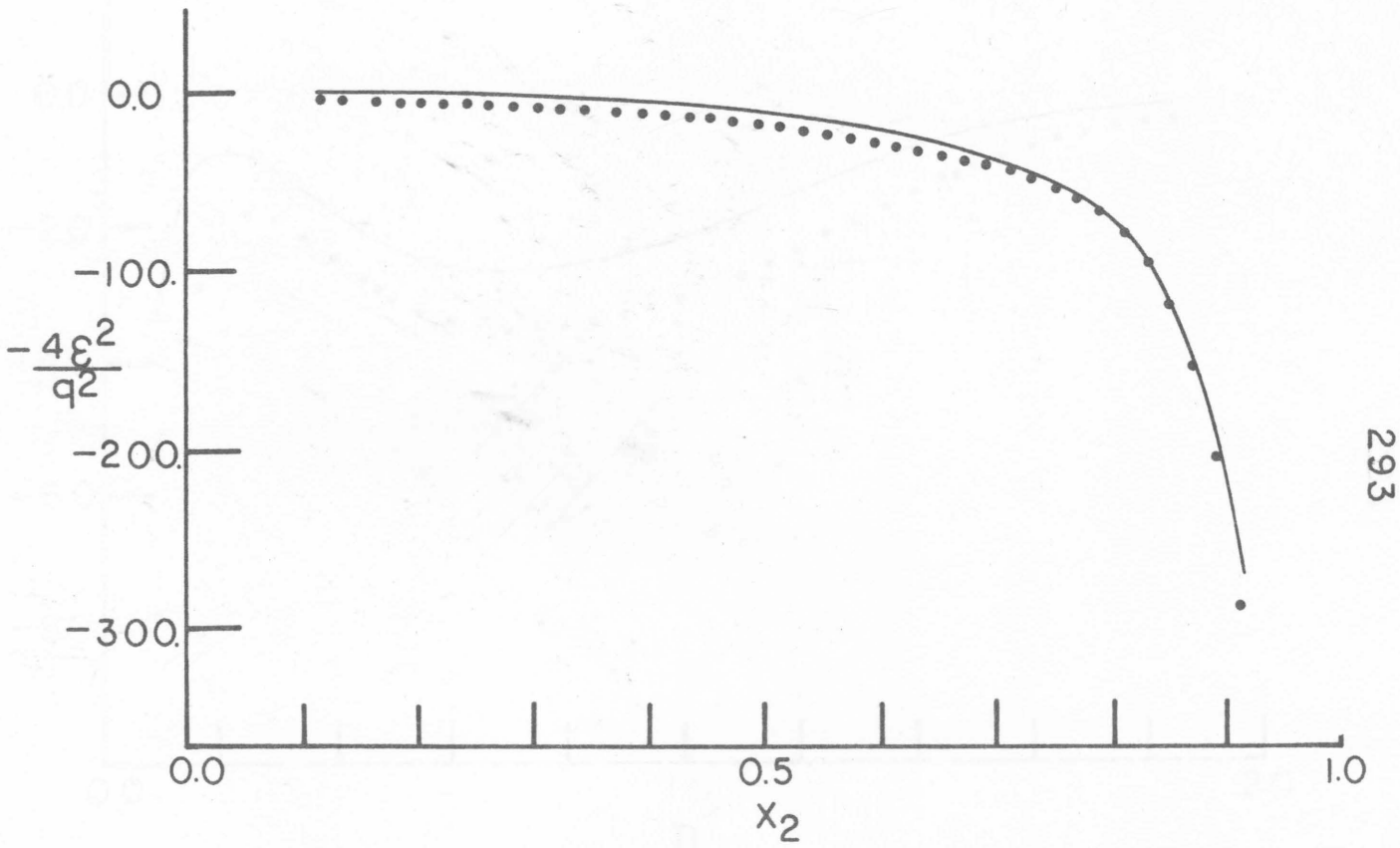

FIGURE 25: DISSIPATION BALANCE FOR PIPE FLOW; HOMOGENEOUS MODEL;
• -EXPERIMENTAL DATA OF LAWN (1971),
——HOMOGENEOUS MODEL WITH PARAMETERS A.

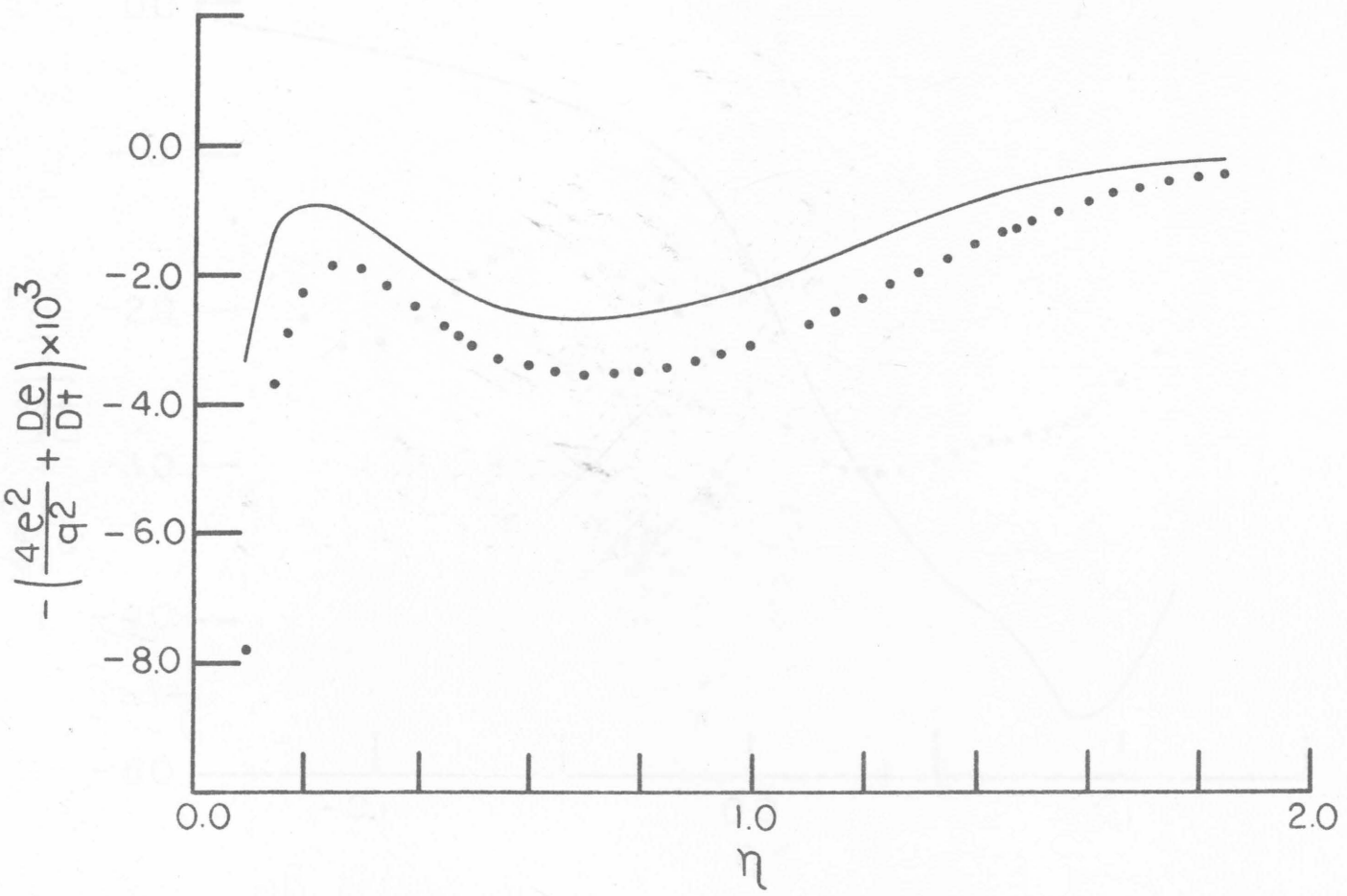

FIGURE 26: DISSIPATION BALANCE FOR WALL-JET; HOMOGENEOUS MODEL;
• -EXPERIMENTAL DATA OF IRWIN (1973),
——HOMOGENEOUS MODEL WITH PARAMETERS A.

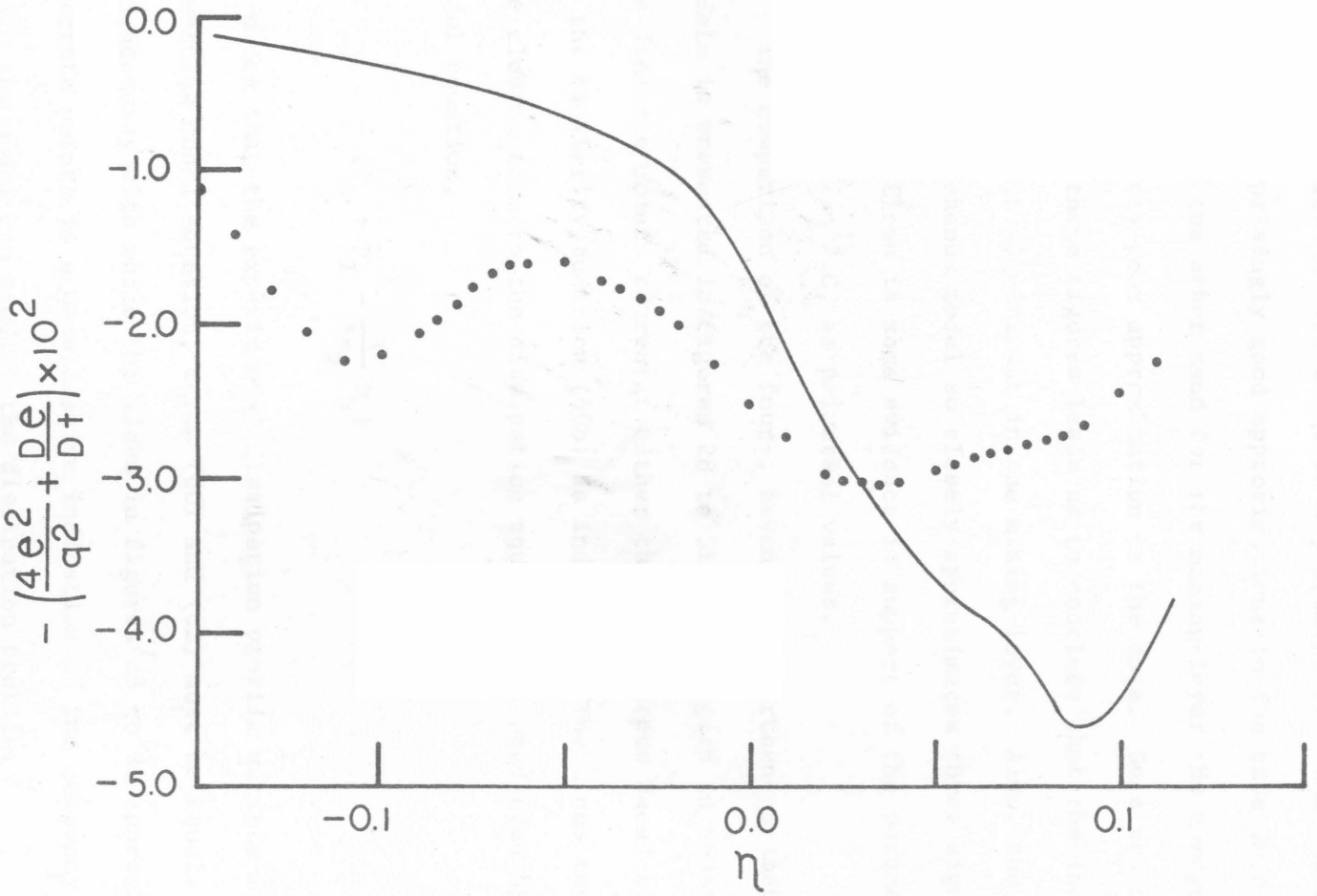

FIGURE 27: DISSIPATION BALANCE FOR MIXING-LAYER; HOMOGENEOUS MODEL;
• - EXPERIMENTAL DATA OF WYGNANSKI AND FIEDLER (1970),
——HOMOGENEOUS MODEL WITH PARAMETERS A.

to inhomogeneous effects, that must be accounted for by P_I and D_k.

The profiles in figures 24 to 26, predicted by the homogeneous model, are surprisingly good approximations to the experimental profiles. On the other hand for the mixing-layer the homogeneous profile is a very poor approximation to the data. Once again, the comparison in these figures leads us to conclude that the inhomogeneous effects are most significant in the mixing-layer. Also, the fact that the homogeneous model so closely approximates three significantly inhomogeneous flows is some evidence in support of the parameters, chosen in section 3.C, as universal values.

The comparison of the four-, seven- and fourteen-parameter models is presented in figures 28 to 31. Once again in these figures, the discrete points represent either the homogeneous decay term (60a) or the similarity function (60b) as indicated. The lines represent the closing term to the dissipation equation, as predicted by the model equation,

$$- (P_H + P_I - \frac{\partial}{\partial x_k} D_k) \qquad (62)$$

In order that the experimental dissipation profile satisfy its governing model equation, terms (60) and (62) must be equal. Hence, the adequacy with which the lines in figures 28 to 31 approximate the discrete points is a quantitative indication of the adequacy with which the model can predict the dissipation profile.

An examination of figures 28 to 31 indicates that the largest deviations between the model and the experimental data occur for the

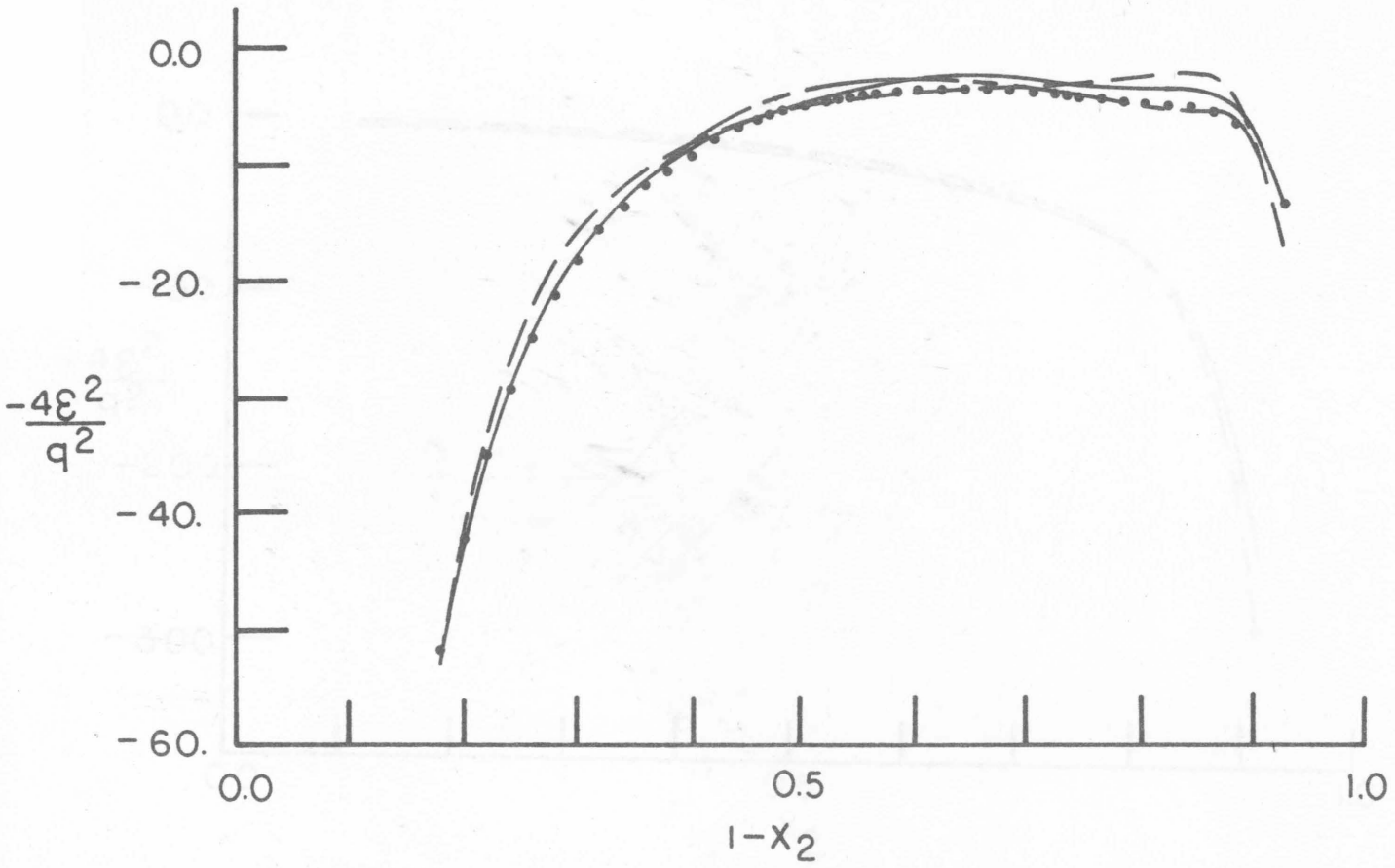

FIGURE 28: DISSIPATION BALANCE FOR CHANNEL FLOW; COMPARISON OF THE FOUR, SEVEN AND FOURTEEN PARAMETER MODELS; — — — FOUR-PARAMETERS, ——— SEVEN PARAMETERS, ——- -—FOURTEEN PARAMETERS.

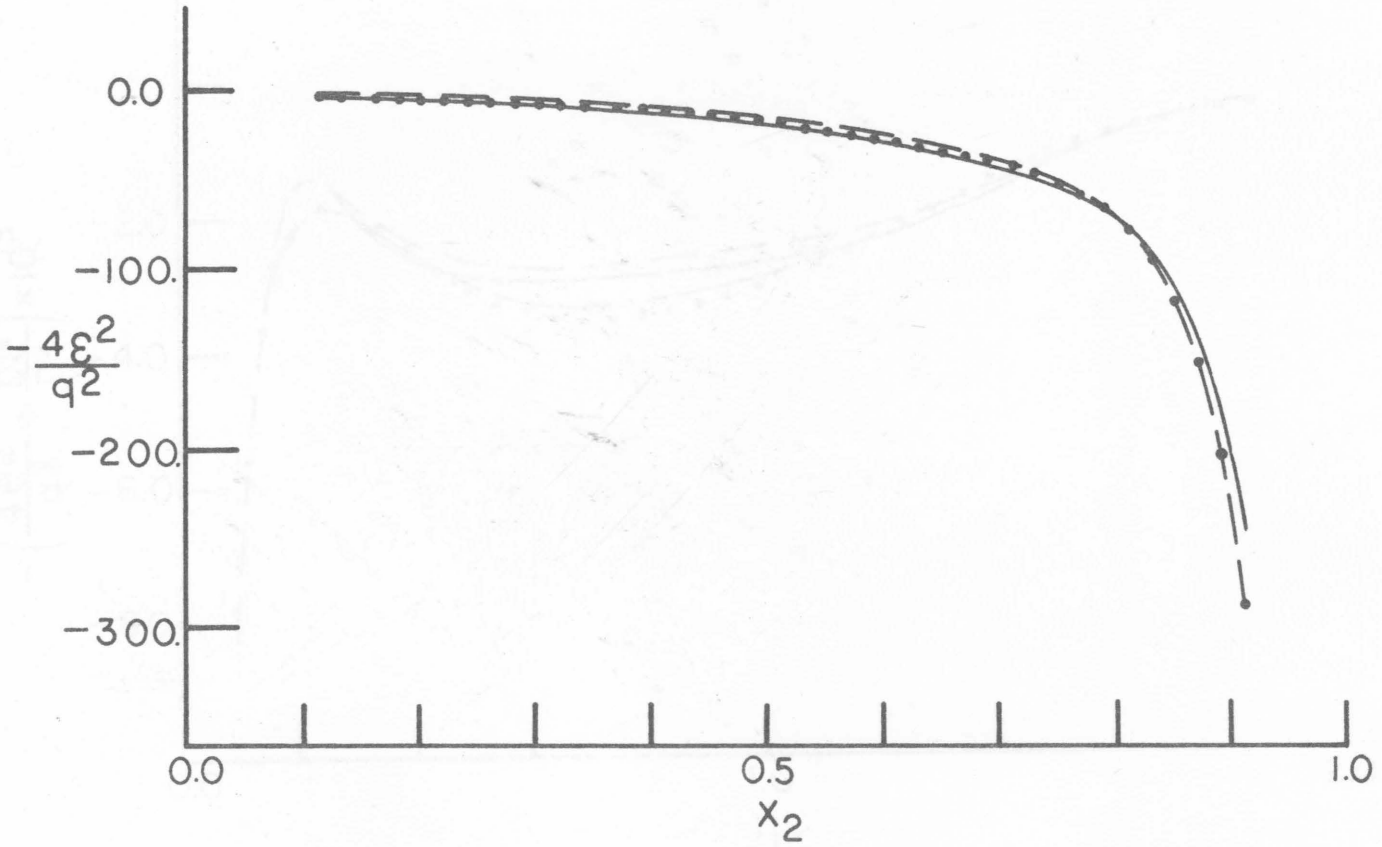

FIGURE 29: DISSIPATION BALANCE FOR PIPE FLOW; COMPARISON OF THE FOUR, SEVEN AND FOURTEEN PARAMETER MODELS;— — — FOUR PARAMETERS, ——— SEVEN PARAMETERS,— - —FOURTEEN PARAMETERS.

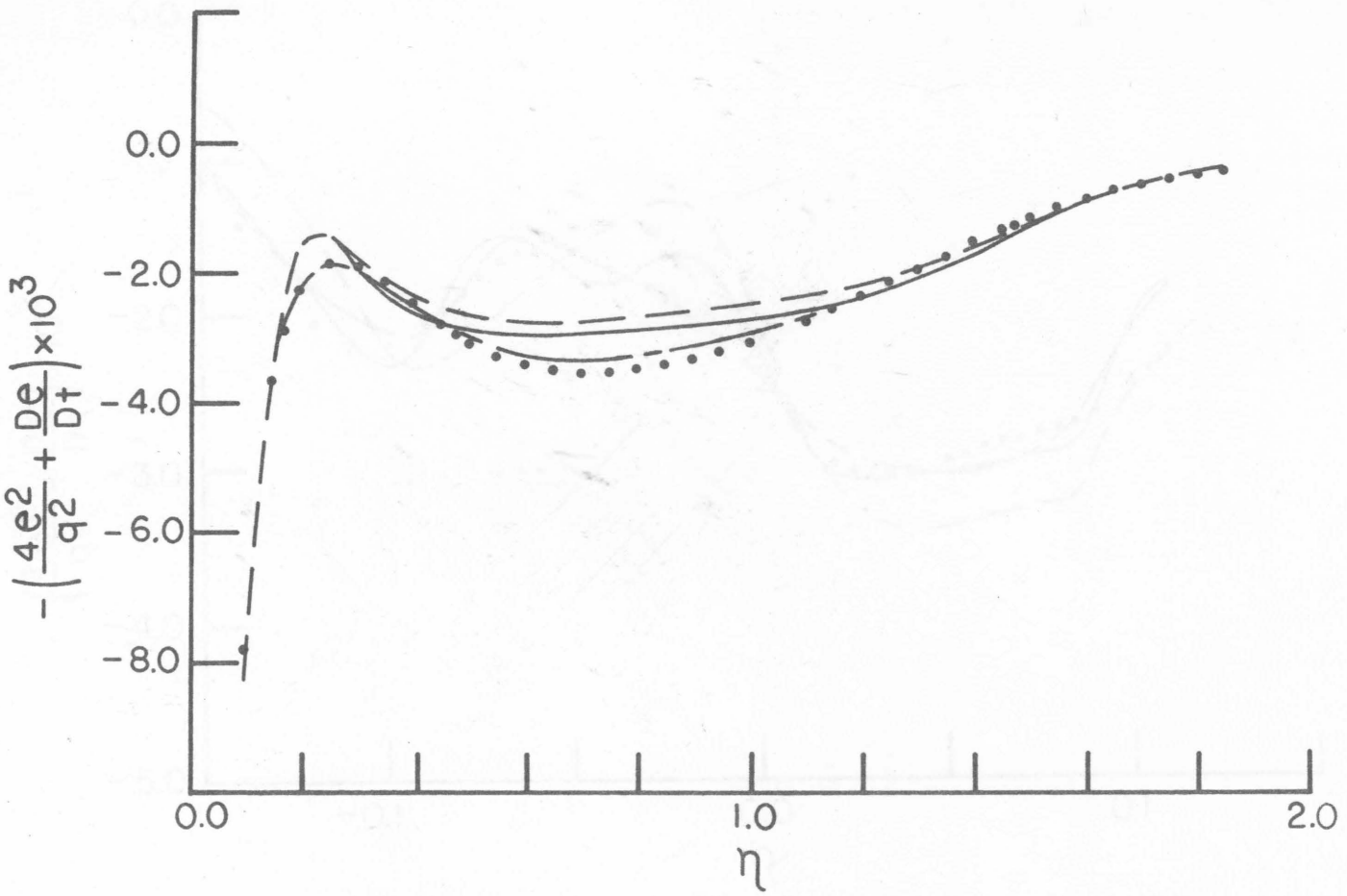

FIGURE 30: DISSIPATION BALANCE FOR WALL-JET; COMPARISON OF THE FOUR, SEVEN AND FOURTEEN PARAMETER MODELS;— — — FOUR PARAMETERS, ———— SEVEN PARAMETERS;— - —FOURTEEN PARAMETERS.

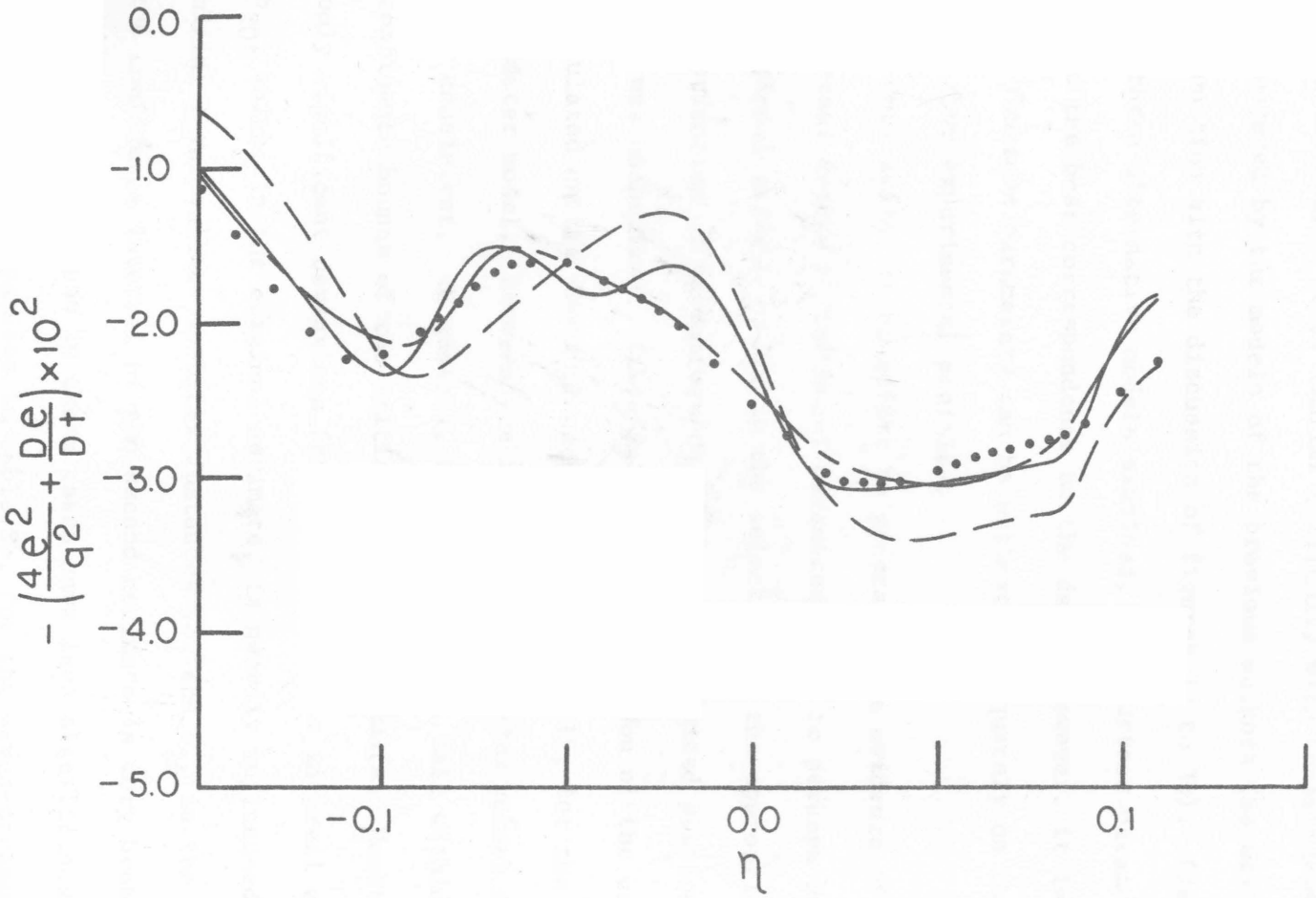

FIGURE 31: DISSIPATION BALANCE FOR MIXING-LAYER; COMPARISON OF THE FOUR, SEVEN AND FOURTEEN PARAMETER MODELS; — — —FOUR PARAMETERS, ————SEVEN PARAMETERS,—·—·—FOURTEEN PARAMETERS.

wall-jet in the range $0.3 \lesssim \eta \lesssim 1.1$, and for the mixing-layer over the entire range of ε. Similar difficulty with these flows is also encountered by the models of the previous authors (as will be seen in conjunction with the discussion of figures 33 to 36). Clearly, of the three alternative models examined, the fourteen-parameter model gives the best correspondence to the data. However, it is uncertain that *fourteen* parameters can be estimated adequately on the basis of only *four* experimental profiles.

Once again, in an effort to generate some evidence of the universal nature of the model parameters, and to perhaps provide additional insight to aid in the selection of the appropriate model, an estimation of parameters on the basis of limited portions of the data was undertaken. Table 8a gives a comparison of the coefficients calculated on the basis of each flow individually, for the four-parameter model. Between the flows, the parameter values are reasonably consistent. In general, the values do not fall within the confidence bounds of the initial parameter estimate. However, the only significant deviations from this confidence interval occur in b_{20}, which, in the original estimate, is heavily influenced by the mixing-layer value. In other instances (b_2 and b_{26} in the wall-jet), the confidence interval of the second estimate is very broad. Hence, the deviations in these cases have less significance.

A similar comparison in table 8b, for the seven-parameter model, indicates a somewhat greater variability in the values of the coefficients. However, even in this case the coefficients generally

maintain at least the same sign and magnitude for all flows. Exceptions to this behavior are b_7 for the pipe flow and b_{20} for the wall-jet. This variability in parameter values is not surprising in view of the relatively large number of parameters estimated from the very restricted amount of data which is used for each estimate. It is for this very reason that the necessity to include *diverse data* for parameter estimation was emphasized previously.

An attempt to provide a similar comparison for the fourteen-parameter model encountered considerable difficulty due to the singularity of the coefficient matrix, $\overline{C}$, when each flow was considered individually. Hence, the comparison of parameters for the fourteen-parameter model has not been presented.

As a final comparison of the four-, seven- and fourteen-parameter models, the coefficients were re-evaluated on the basis of only the first three flows. The coefficients calculated from these flows were then used to predict the mixing-layer profile as shown in figure 32. This figure gives perhaps the best demonstration of the manner in which the uncertainty of the parameter estimate (as a universal representation) increases as the number of parameters, which are retained, increases. In this comparison, the four-parameter model gives the best correspondence to the data, although it does under-predict the values for $\eta \lesssim 0.0$. As additional parameters are included, the correspondence decreases. However, it is significant that the predicted profile moves in the correct direction upon advancing from the four- to the seven-parameter model (even though it moves too far).

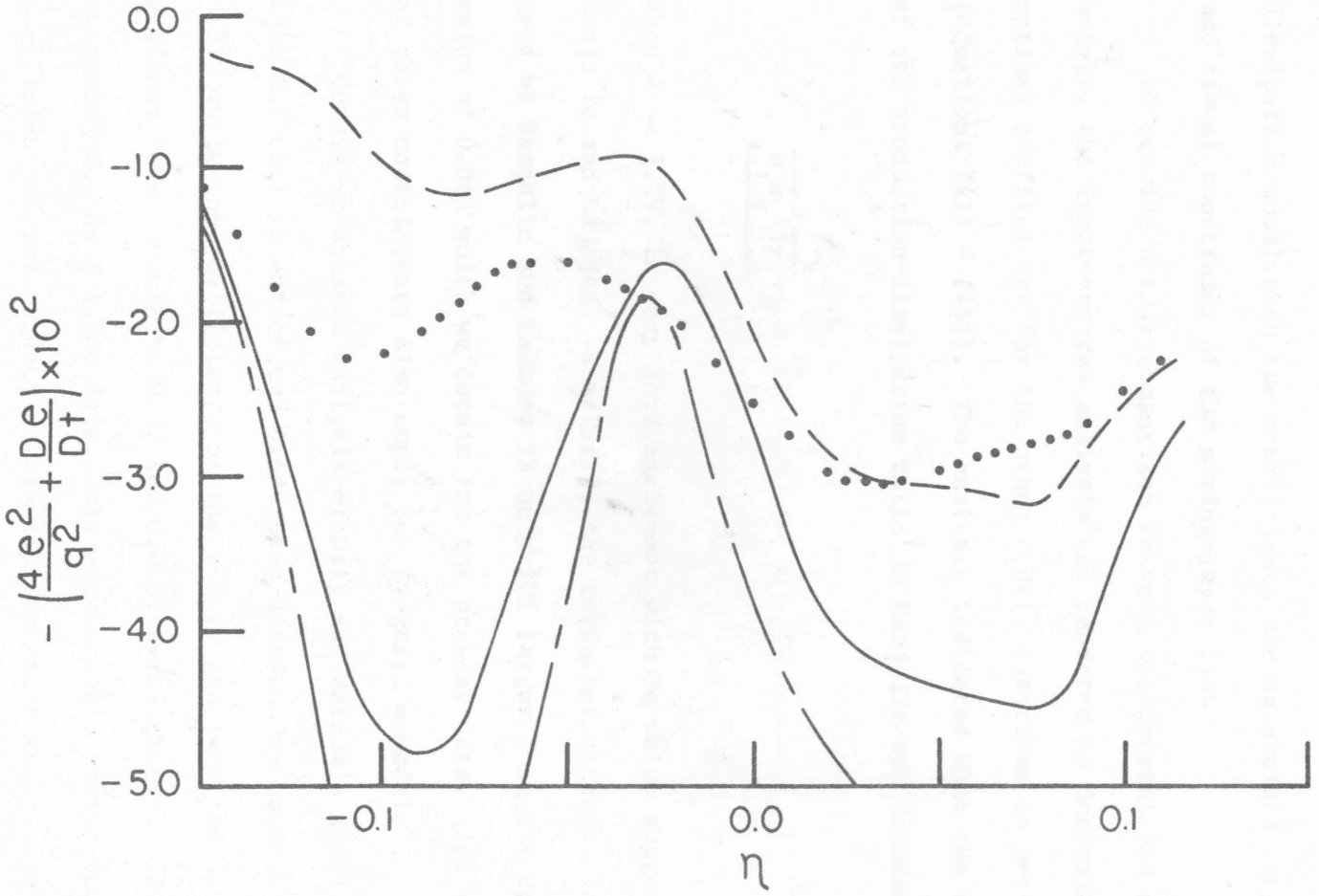

FIGURE 32: DISSIPATION BALANCE FOR MIXING-LAYER; COMPARISON OF FOUR, SEVEN AND FOURTEEN PARAMETER MODELS WITH PARAMETERS ESTIMATED WITHOUT CONSIDERATION OF MIXING-LAYER DATA; — — — FOUR PARAMETERS, ——— SEVEN PARAMETERS, —·— FOURTEEN PARAMETERS.

In conjunction with the results in tables 8a, b, this suggests that the seven-parameter system may provide a generally applicable dissipation model when the coefficients are determined subject to the additional constraint of the mixing-layer flow.

To provide a fair comparison between the present and previous models, the least-squares analysis was repeated to determine the optimal coefficients for the other models described in section 2.E (equations (42) - (45)). The analysis indicated that the coefficient of the production-dissipation ratio in Hanjalic and Launder's model,

$$\frac{\overline{u_i u_k}}{\varepsilon} \frac{\partial U_k}{\partial x_i},$$

should be 3.29, in very good agreement with the value suggested by Hanjalic and Launder. Similarly, the turbulent diffusion coefficient used by Hanjalic and Launder is only 20% larger than the optimal value of 0.041 which we obtain for the present data. The same values of these coefficients also apply for Wyngaard's model.

Our least-squares analysis of Daly and Harlow's model indicated that the coefficient of the production-dissipation ratio should be 3.51, while the coefficients of the energy gradient and dissipation gradient terms should be 0.05 and 0.063, respectively. Thus, according to the present data, Daly and Harlow's choice for the coefficient of the production-dissipation ratio is in error by a factor of two, while their tacit assumption that the other coefficients are unity, is in error by almost *two orders of magnitude*.

Shir's model contains only three parameters which may be adjusted since the fourth parameter, which corresponds to

$$\frac{\varepsilon}{q^2}\frac{\partial}{\partial x_k}\frac{q^4}{\varepsilon}\frac{\partial q^2}{\partial x_k},$$

is fixed by the choice of the coefficient for the turbulent diffusion of turbulence energy term (section 4.B). The present data suggest that Shir's choice of the production-dissipation ratio is nearly the optimal value of 2.95. However, the coefficient of the length-scale-diffusion term is larger than the value of -0.0043, which we obtain with the present data. Finally, for the coefficient of the wall-effect term, our analysis suggests a value of 0.014, which is only 20% smaller than the value used by Shir.

The necessary comparison of the dissipation models of Hanjalic and Launder, Daly and Harlow and Shir is given in figures 33 to 36. All of the models exhibit the greatest difficulty in predicting the mixing-layer profile. Although each displays the double minimum in the profile which is observed experimentally, these minima are too sharp and, in contrast to the data, are almost symmetric. Very significant deviations from the experimental data are also evident in the near-wall region of the wall-jet for the models of Hanjalic and Launder, and Daly and Harlow. Less severe deviations in this flow, for $\eta \gtrsim 0.3$, are observed with Shir's model. Most important, however, is the fact that a comparison of figures 28 to 31 with figures 33 to 36 indicates that both the four-and seven-parameter models of the

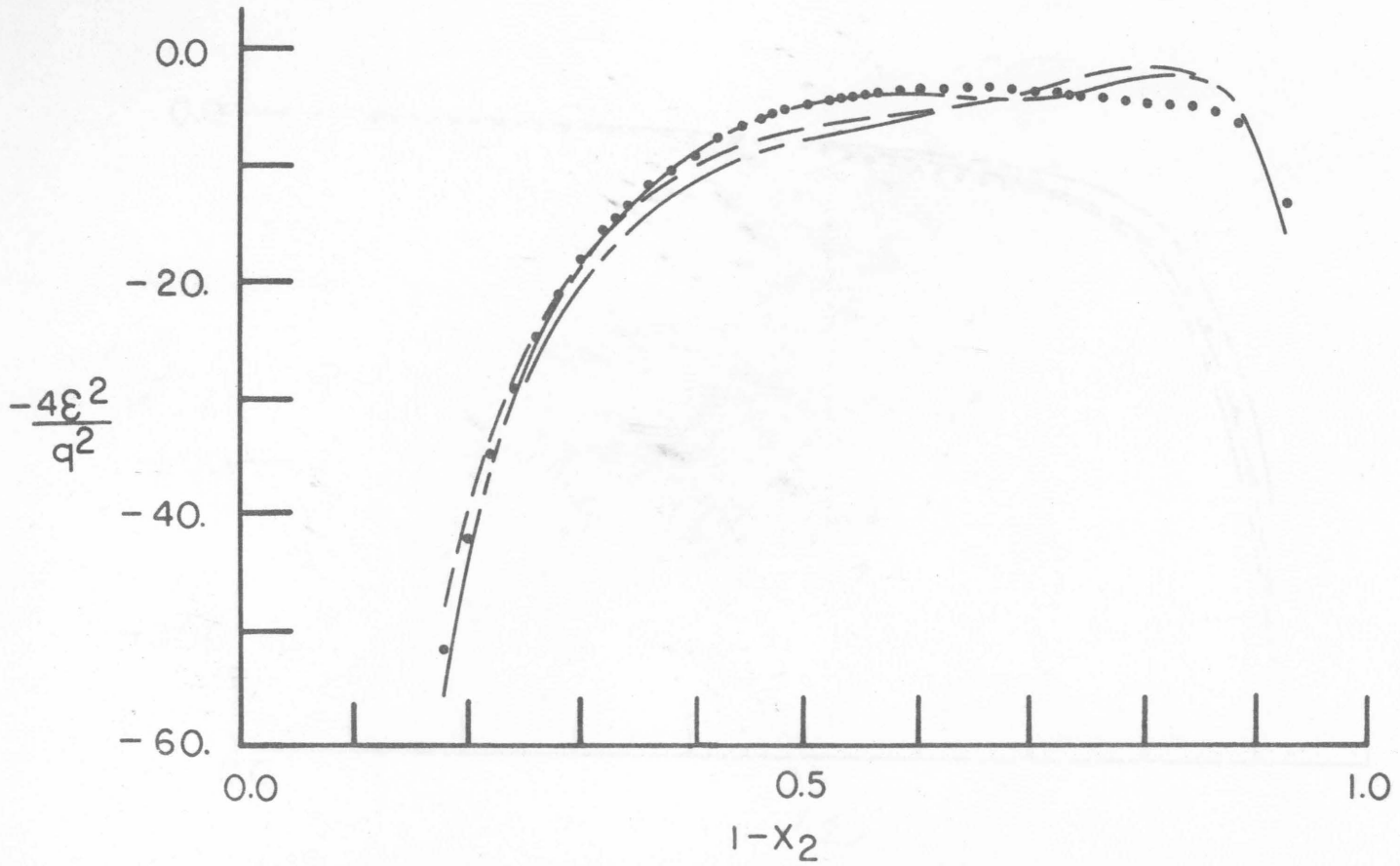

FIGURE 33: DISSIPATION BALANCE FOR CHANNEL FLOW; COMPARISON OF OTHER MODELS;
— — — MODEL OF HANJALIC AND LAUNDER (1972B),
—— - - —— MODEL OF SHIR (1973),
—— - —— MODEL OF DALY AND HARLOW (1970).

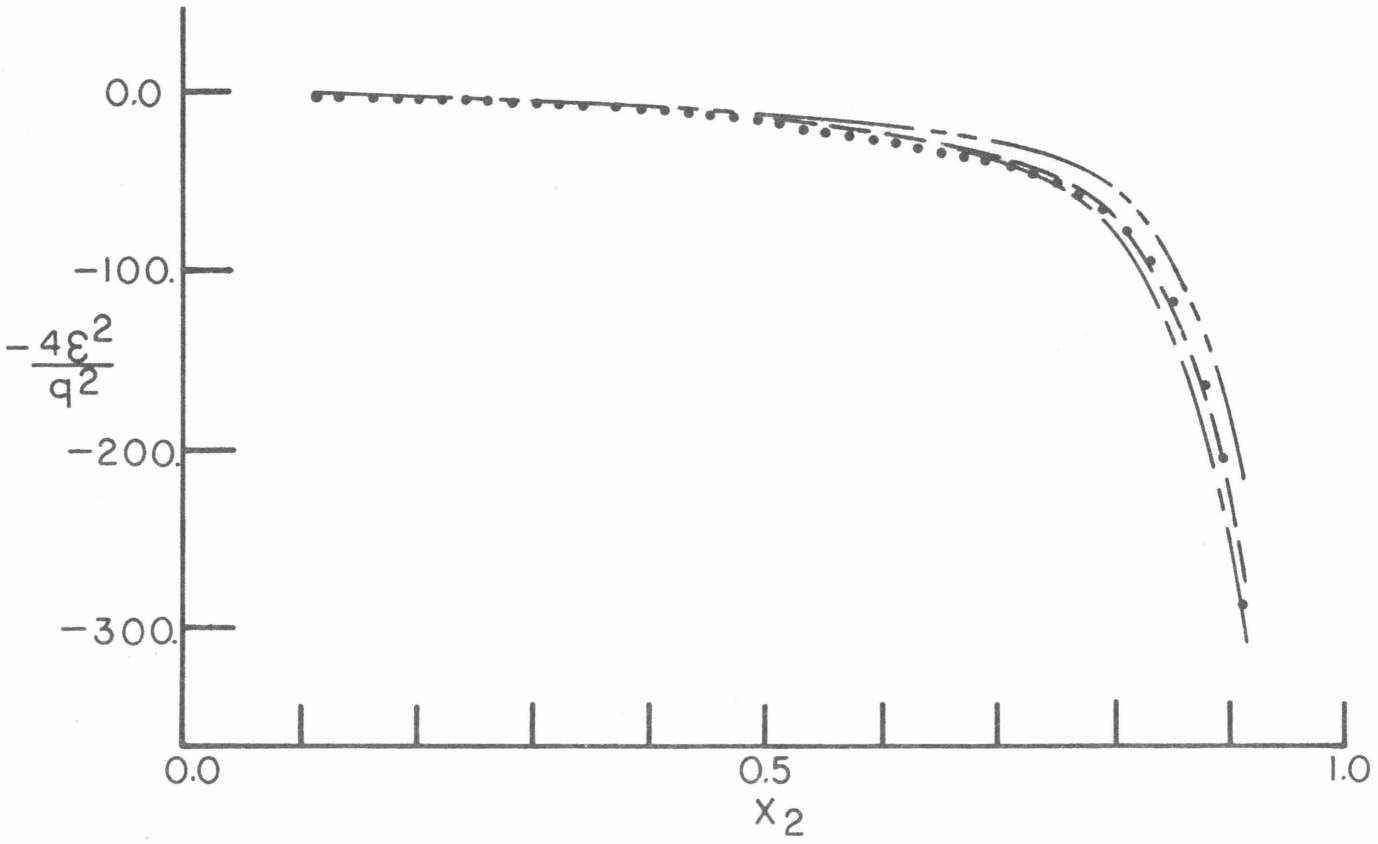

FIGURE 34: DISSIPATION BALANCE FOR PIPE FLOW; COMPARISON OF OTHER MODELS;
— — — MODEL OF HANJALIC AND LAUNDER (1972B),
—— - - —— MODEL OF SHIR (1973),
—— - —— MODEL OF DALY AND HARLOW (1970).

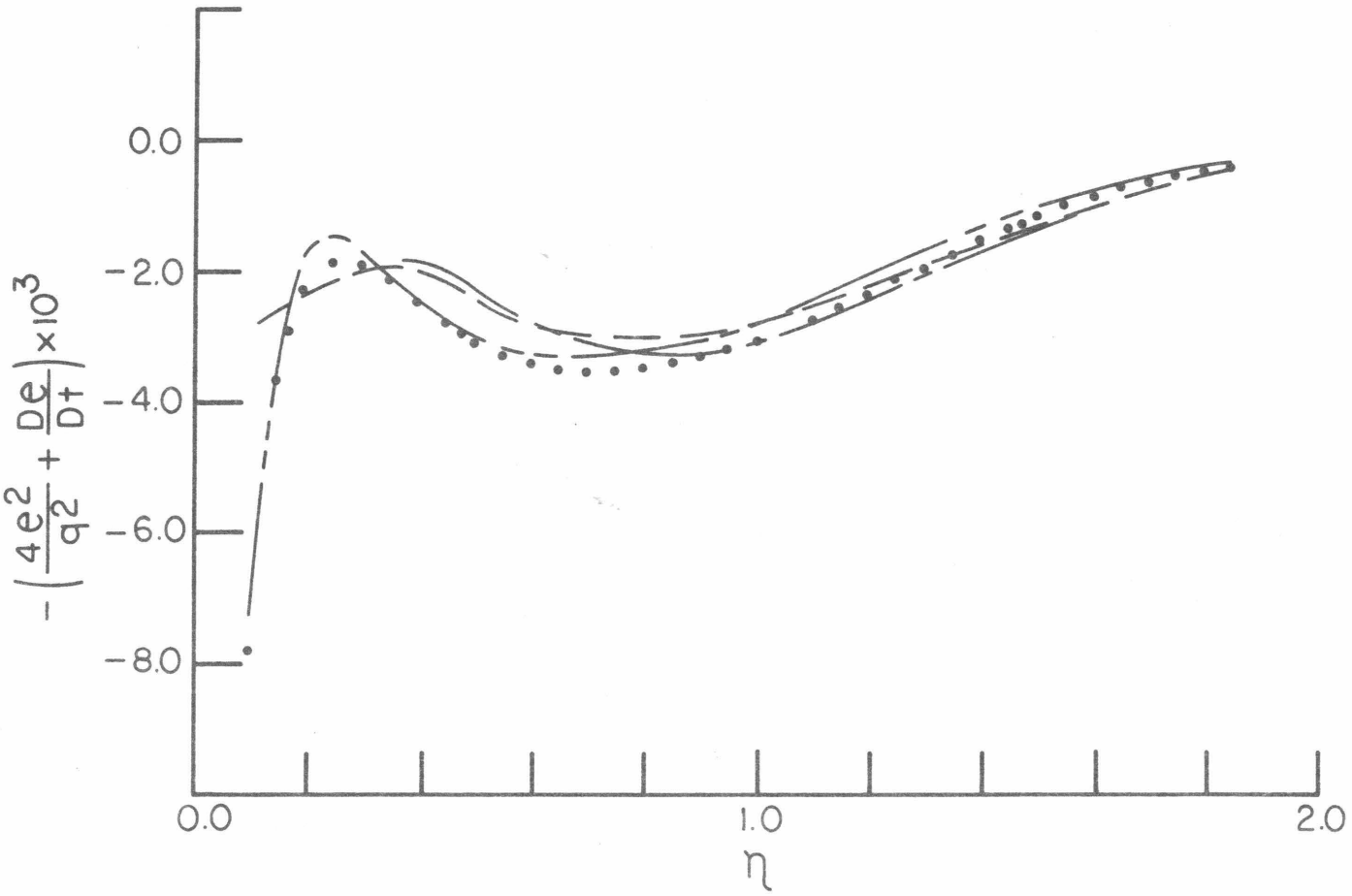

FIGURE 35: DISSIPATION BALANCE FOR WALL-JET; COMPARISON OF OTHER MODELS;
— — — MODEL OF HANJALIC AND LAUNDER (1972B),
—— - —— MODEL OF SHIR (1973),
—— - - —— MODEL OF DALY AND HARLOW (1970).

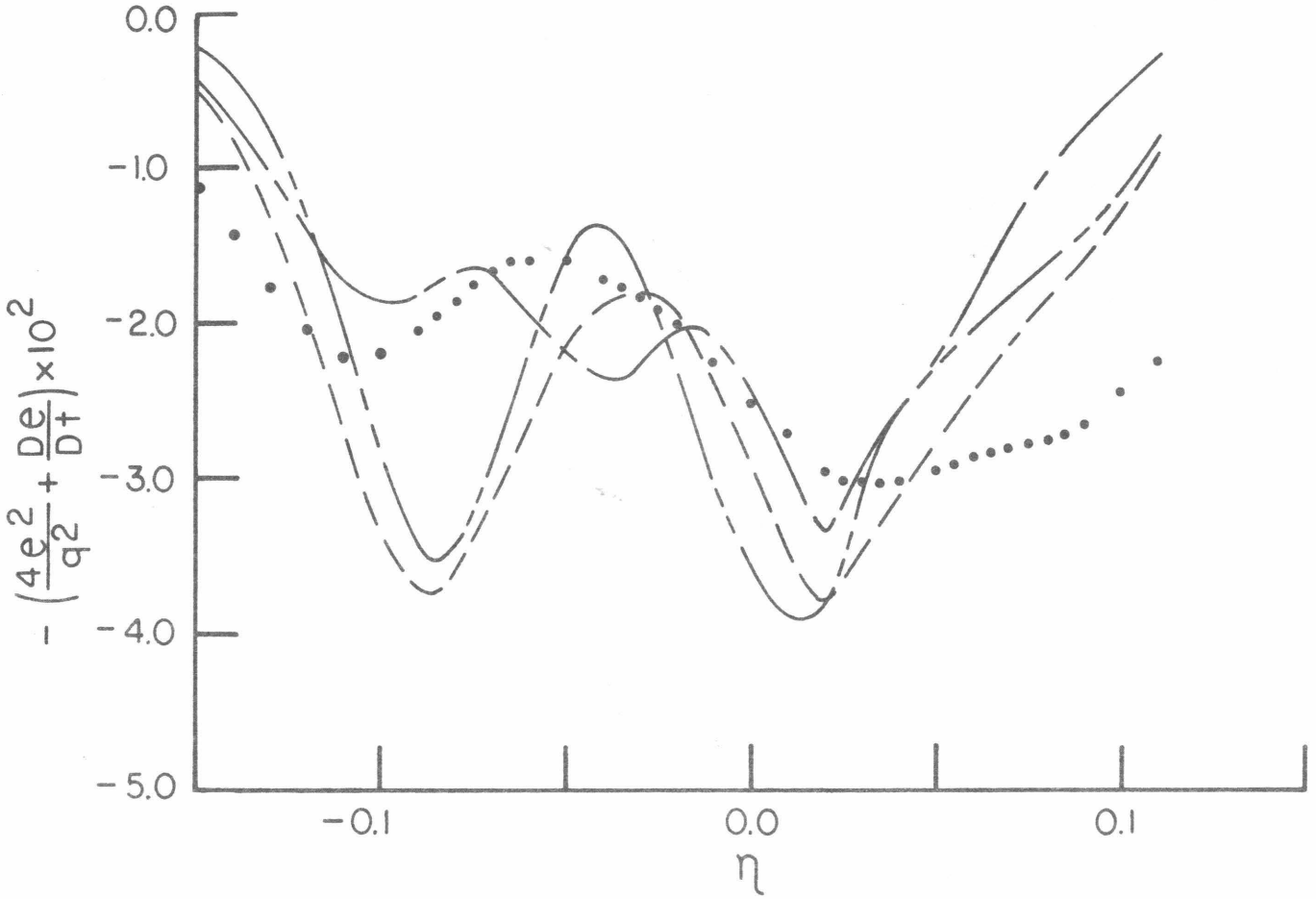

FIGURE 36: DISSIPATION BALANCE FOR MIXING-LAYER; COMPARISON OF OTHER MODELS;
— — — MODEL OF HANJALIC AND LAUNDER (1972B),
—— -- —— MODEL OF SHIR (1973),
—— - —— MODEL OF DALY AND HARLOW (1970).

present work give appreciably better overall agreement with the available experimental data.

5. CONCLUSIONS

The present work provides a much needed, unifying comparison of the second-order phenomenological turbulence models which have recently received the greatest attention in the literature. Although hampered by the extremely small body of experimental data (which has also been noted by previous authors, c.f. Daly (1974), and Lumley and Khajeh-Nouri (1973)), this comparison graphically demonstrates that at least one supposedly validated turbulence model is, in fact, *not even consistent with the experimental data that are available*. In particular, the values of certain model constants suggested by Daly and Harlow (1970), and used by Daly (1974), were shown to be in error by orders of magnitude when compared with the optimal values, calculated for the data examined in the present analysis. Of greater significance, however, is that even in the simple homogeneous flows (for which these incorrectly estimated coefficients do not enter), the Daly-Harlow model produces qualitatively unacceptable results.

In contrast to the Daly-Harlow model, the forms proposed by Hanjalic and Launder (1972b) and Shir (1973) were shown to be reasonably consistent with all of the inhomogeneous flow data which were examined. In particular, both Hanjalic and Launder's model and Shir's model of the tendency-toward-isotropy term were found to yield reasonable approximations for the four flows which we studied. However, even these models performed very poorly when applied to the simplest of turbulent flows, the homogeneous shear flow.

In addition to providing a comparison of turbulence models, the

present work also undertook the development of an improved turbulence model for isothermal flows. To this end, the rational closure technique proposed by Lumley and Khajeh-Nouri (1973) was adopted, and the systematic evaluation of the potentially numerous model constants was undertaken. Once again, the most significant handicap in carrying out this estimation was the dearth of totally documented experimental data, suitable for parameter estimation. This shortage ranges from the simplest of homogeneous decay flows which were considered in section 3.C, to the more complex inhomogeneous flows of the type examined in section 4. Notwithstanding this deficiency of data, however, our efforts to date have led to a preliminary estimate of the parameters for an isothermal turbulence model which shows promise as a widely applicable formulation. Although the parameters were estimated on the basis of a least-squares analysis of the experimental data, it is important that the estimates be viewed as *preliminary*, particularly for the non-homogeneous parameters. The 'fine-tuning' and ultimate verification of the universality of the model parameters must be established on the basis of *full solutions* of the equations of motion, and subsequent comparison with a broader cross-section of experimental flows.

REFERENCES

Arley, N. and K. R. Buch, Introduction to the Theory of Probability and Statistics, Wiley, New York, 1950.

Batchelor, G. K., "Energy Decay and Self-Preserving Correlation Functions in Isotropic Turbulence," Quart. Appl. Math., 6, 97 (1948).

Batchelor, G. K., The Theory of Homogeneous Turbulence, Cambridge Press, 1953.

Batchelor, G. K. and A. A. Townsend, "Decay of Vorticity in Isotropic Turbulence," Proc. Roy. Soc., A-190, 534 (1941).

Batchelor, G. K. and A. A. Townsend, "Decay of Isotropic Turbulence in the Initial Period," Proc. Roy. Soc., A-193, 539 (1948a).

Batchelor, G. K. and A. A. Townsend, "Decay of Turbulence in the Final Period," Proc. Roy. Soc., A-194, 527 (1948b).

Blake, W. K., J. Fluid Mech., 44, 637 (1970).

Blom, J. and L. Wartena, "The Influence of Changes in Surface Roughness on the Development of the Turbulent Boundary-Layer in the Lower Layers of the Atmosphere," J. Atmos. Sci., 26, 255 (1969).

Boussinesq, T. V., "Theorie analytique de la chaleur," Gantheir-Villars (1903).

Bradshaw, P., Ferris, D. H. and N. P. Atwell, "Calculation of Boundary-layer Development Using the Turbulent Energy Equation," J. Fluid Mech., 28, 593 (1967).

Businger, J. A., J. C. Wyngaard, Y. Izumi and E. F. Bradley, "Flux Profile Relationships in the Atmospheric Surface Layer," J. Atmos. Sci., 28, 181 (1971).

Champagne, F. H., V. G. Harris and S. Corrsin, "Experiments on Nearly Homogeneous Turbulent Shear Flow," J. Fluid Mech., 41, 81 (1970).

Chou, P. Y., "On the Velocity Correlations and the Solution of the Equations of Turbulent Fluctuations," Q. Appl. Math., 3, 31 (1945).

Coleman, B. D. and W. Noll, "Recent Results in the Continuum Theory of Viscoelastic Fluids," Ann. N. Y. Acad. Sci., 89, 672 (1961).

Comte-Bellot, G. and S. Corrsin, "Isotropy of Grid-Generated Turbulence," J. Fluid Mech., 25, 657 (1966).

Corrsin, S., Comment on 'Transport Equations in Turbulence', Phys. of Fluids, 16, 157 (1973).

Daly, B. J., "A Numerical Study of Turbulence Transitions in Convective Flow," J. Fluid Mech., 64, 129 (1974).

Daly, B. J. and F. H. Harlow, "Transport Equations in Turbulence," Phys. Fluids, 13, 2634 (1970).

Deardorff, J. W., "Counter Gradient Heat Transfer," J. Atmos. Sci., 23, 503 (1966).

Deardorff, J. W., "A Three-Dimensional Numerical Study of Turbulent Channel Flow at Large Reynolds Numbers," J. Fluid Mech., 41, 453 (1970a).

Deardorff, J. W., "A Three-Dimensional Numerical Investigation of the Idealized Planetary Boundary Layer," Geophysical Fluid Dynam., 1, 377 (1970b).

Deardorff, J. W., "Numerical Investigations of Neutral and Unstable Planetary Boundary Layers," J. Atmos. Sci., 29, 91 (1972).

Deardorff, J. W., "Three-Dimensional Numerical Study of the Height and Mean Structure of a Heated Planetary Boundary Layer," to appear Boundary Layer Met., (1974).

Deissler, R. G., "Counter Gradient Heat Transfer," Phys. Fluids, 11, 432 (1968).

Donaldson, C. du P., R. D. Sullivan and H. Rosenbaum, "A Theoretical Study of the Generation of Atmospheric Clear Air Turbulence," A.I.A.A.J., 10, 162 (1972).

Donaldson, C. du P., "Calculations of Turbulent Shear Flows for Atmospheric and Vortex Motions," A.I.A.A.J., 10, 4 (1972).

Donaldson, C. du P. and G. R. Hilst, "Effect of Inhomogeneous Mixing on Atmospheric Photochemical Reactions," Envir. Sci. Tech., 6, 812 (1972).

Elliot, J. A., "Microscale Pressure Fluctuations Measured Within the Lower Atmospheric Boundary Layer," J. Fluid Mech., 53, 351 (1972).

Emmons, H., "Critique of Numerical Modeling of Fluid Mechanics Phenomena," Annual Rev. Fluid Mech., 2, 15 (1970).

Gad-el-Hak, M., "Experiments on Nearly Isotropic Turbulence Behind a Jet Grid," Ph.D. Thesis, The Johns Hopkins University, 1972.

Gad-el-Hak, M. and S. Corrsin, "Measurements of the Nearly Isotropic Turbulence Behind a Uniform Jet Grid," J. Fluid Mech., 62, 115 (1974).

Gorshkov, N. F., Izv. Atmos. Oceanic Phys., 4, 460 (1968).

Hanjalic, K. and B. E. Launder, "Fully Developed Asymmetric Flows in a Plane Channel," J.F.M., 51, 301 (1972a).

Hanjalic, K. and B. E. Launder, "A Reynolds Stress Model of Turbulence and its Application to Thin Shear Flows," J.F.M., 52, 609 (1972b).

Harlow, F. H. and R. I. Nakayama, "Transport of Turbulence Energy Decay Rate," Los Alamos Report LA-3854 (1968).

Harlow, F. H. and R. I. Nakayama, "Turbulence Transport Equations," Phys. Fluids, 10, 2323 (1967).

Hinze, J. O., Turbulence, McGraw-Hill, New York, 1959.

Irwin, H. P. A. H., "Measurements in a Self-Preserving Plane Wall-Jet in a Positive Pressure Gradient," J. Fluid Mech., 61, 33 (1973).

Jones, W. P. and B. E. Launder, "The Prediction of Laminarization with a Two-Equation Model of Turbulence," Int. J. Heat Mass Trans., 15, 301 (1972).

Klebanoff, P. S., "Characteristics of Turbulence in a Boundary-Layer with Zero Pressure Gradient," Nat. Advis. Com. Aeronaut., Rep., 1247 (1955).

Ladyzhenskaya, O. A., The Mathematical Theory of Viscous Incompressible Flow, Gordon and Breach, New York, 1969.

Lamb, R. G., "Numerical Modeling of Air Pollution," Ph.D. Thesis, Department of Meteorology, University of California, Los Angeles (1971).

Lamb, R. G., "Statistics of Marked Particle Concentrations in Turbulent Fluid," J. Fluid Mech. submitted for publication (1974).

Lawn, C. J., "The Determination of the Rate of Dissipation in Turbulent Pipe Flow," J. Fluid Mech., 48, 477 (1971).

Lilly, D. K., "The Representation of Small Scale Turbulence in Numeri-

cal Simulation Experiments," IBM Report 320-1951, 195 (1967).

Lumley, J. L. "Rational Approach to Relations Between Motions of Differing Scales in Turbulent Flows," Phys. of Fluids, 10, 1405 (1967).

Lumley, J. L., "Toward a Turbulent Constitutive Relation," J. Fluid Mech., 41, 413 (1970).

Lumley, J. L. and B. Khajeh-Nouri, "Computational Modeling of Turbulent Transport," Second IUTAM-IUGG Symposium on Turbulent Diffusion and Environmental Pollution, Charlottesville, Va. (1973).

Monin, A. S. and A. M. Yaglom, Statistical Fluid Mechanics, MIT Press, Cambridge, 1971 .

Monin, A. S. and A. M. Obukhov, "Basic Turbulent Mixing Laws in the Atmospheric Surface Layer," Trudy Geofiz. Inst. AN SSSR, 24, 163 (1954).

Nee, V. W. and L. S. G. Kovasznay, "Simple Phenomenological Theory of Turbulent Shear Flows," Phys. Fluids, 12, 473 (1969).

Nickel, K., "Prandtl's Boundary-Layer Theory From the Viewpoint of a Mathematician," Ann. Rev. of Fluid Mech., 5, 405 (1973).

Nickerson, E. C., "Boundary-Layer Adjustment as an Initial Value Problem," J. Atmos. Sci., 25, 207 (1968).

Onishi, G. and M. A. Estoque, "Numerical Study on Atmospheric Boundary-Layer Flow Over Inhomogeneous Terrain," J. Meteor. Soc. Japan, 46, 280 (1968).

Orszag, S., "Numerical Methods for Simulation of Turbulence," Phys. Fluids, Suppl. II, 12, II-250 (1969).

Orszag, S., "Numerical Simulation of Turbulence," Proceedings of the Symposium on Statistical Models and Turbulence, San Diego, July 15-21 (1971a).

Orszag, S., "Spectral Calculations of Isotropic Turbulence: Efficient Removal of Aliasing Interactions," Phys. Fluids, 14, 2538 (1971b).

Orszag, S., "Numerical Simulation of Three-Dimensional Homogeneous Turbulence," Phys. Rev. Letters, 10, Jan. (1972).

Peterson, E. W., "On the Relation Between the Shear Stress and the Velocity Profile After a Change in Surface Roughness," J. Atmos. Sci., 26, 773 (1969a).

Rao, K. S., J. C. Wyngaard, and O. R. Coté, "The Structure of Two-Dimensional Internal Boundary Layer Over a Sudden Change in Surface Roughness," J. Atmos. Sci., to be published (1974).

Reynolds, C. W., "Computation of Turbulent Flows--State-of-the-Art, 1970," Report MD-27, Thermosciences Division, Dept. Mech. Eng., Stanford University, Stanford, California (1970).

Robertson, H. P., "The Invariant Theory of Isotropic Turbulence," Proc. Camb. Phil. Soc., 36, 209 (1940).

Rodi, W. and D. B. Spalding, "A Two-Parameter Model of Turbulence, and its Application to Free Jets," Warme-und Stoffubertragung, 3, 85 (1970).

Rosenbrock. H. H., "An Automatic Method for Finding the Greatest or Least Value of a Function," Comp. Journal, 3, 175 (1960).

Rotta, J., "Statistische Theorie Nichthomogener Turbulenz," Z. für Physik, 129, 547 (1951).

Shir, C. C., "A Numerical Computation of Airflow Over a Sudden Change in Surface Roughness," J. Atmos. Sci., 29, 304 (1972).

Shir, C. C., "A Preliminary Numerical Study of Atmospheric Turbulent Flows in the Idealized Planetary Boundary Layer," J. Atmos. Sci., 30, 1327 (1973).

Stewart, R. W., "Triple Velocity Correlations in Isotropic Turbulence," Proc. Cam. Phil. Soc., 41, 146 (1951).

Taylor, P. A., "On the Wind and Shear Stress Profiles Above a Change in Surface Roughness," Q. J. Roy. Met. Soc., 95, 77 (1969).

Taylor, P. A., "Model of Airflow Above Changes in Surface Heat Flux, Temperature and Roughness for Neutral and Unstable Conditions," Boundary-Layer Met., 1, 18 (1970).

Taylor, P. A., "Airflow Above Changes in Surface Heat Flux, Temperature and Roughness: An Extension to Include the Stable Case," Boundary-Layer Met., 1, 474 (1971).

Tennekes, H. and J. L. Lumley, "A First Course in Turbulence," The MIT Press, Cambridge, Massachusetts, 1972.

Tou, J. T., Modern Control Theory, McGraw-Hill, New York, 1964.

Townsend, A. A., "Mixed Convection Over a Heated Horizontal Plate," J.F.M., 55, 209 (1972).

Townsend, A. A., "On the Fine-Scale Structure of Turbulence," Proc. Roy. Soc., Series A, 208, 534 (1951).

Townsend, A. A., "The Uniform Distortion of Homogeneous Turbulence," Quart. J. Mech. and Applied Math., 7, 104 (1954).

Tucker, H. J. and A. J. Reynolds, "The Distortion of Turbulence by

Irrotational Plane Strain," J. Fluid Mech., 32, 657 (1968).

Uberoi, M. S., "The Effect of Wind-Tunnel Contraction on Free-Stream Turbulence," J. Aero. Sci., 23, 754 (1956).

Uberoi, M. S., "Equipartition of Energy and Local Isotropy in Turbulent Flows," J. App. Phys., 28, 1165 (1957).

Warsi, Z. U. A., "Uniqueness of Mean Turbulent Flows," Phys. of Fluids, 17, 34 (1974).

Wilson, D. J., "Turbulent Transport of Mean Kinetic Energy in Counter-gradient Shear Stress Regions," Phys. of Fluids, 17, 674 (1974).

Wygnanski, I. and H. E. Fiedler, "The Two-Dimensional Mixing Region," J. Fluid Mech., 41, 327 (1970).

Wyngaard, J. C., O. R. Coté and K. S. Rao, "Modeling the Atmospheric Boundary Layer," Second UTAM-IUGG Symposium on Turbulent Diffusion in Environmental Pollution, Charlottesville, Virginia, 1973.

Wyngaard, J. C. and O. R. Coté, "The Evolution of a Convective Planetary Boundary Layer - A Higher-Order-Closure Model Study," submitted to Boundary Layer Meteor., March (1974).

Wyngaard, J. C., S. P. S. Arya and O. R. Coté, "Some Aspects of the Structure of Convective Planetary Boundary Layers," J. Atmos. Sci. to be published (1974).

Appendix A: Correct Scaling of the 'Dissipation of ε' Term

It is well known (c.f. Hinze (1959), pp. 153) that the rate of turbulence energy dissipation is related to the two-point velocity correlation in the manner

$$\varepsilon = \nu \overline{\frac{\partial u_i}{\partial x_j} \frac{\partial u_i}{\partial x_j}} = \lim_{\substack{\bar{x}\to 0 \\ \bar{y}\to 0}} \nu \frac{\partial^2 \overline{u_i(\bar{r} + \bar{x})\ u_i\ (\bar{r} + \bar{y})}}{\partial x_j\ \partial y_j}$$

where $\bar{r}$ is a position vector. Similarly, the dissipation of ε term is related to the two-point velocity correlation in the manner

$$D \equiv \nu^2 \overline{\frac{\partial^2 u_i}{\partial x_k \partial x_\ell} \frac{\partial^2 u_i}{\partial x_k \partial x_\ell}} = \lim_{\substack{\bar{x}\to 0 \\ \bar{y}\to 0}} \nu^2 \frac{\partial^4 \overline{u_i(\bar{r} + \bar{x})\ u_i\ (\bar{r} + \bar{y})}}{\partial x_k \partial x_\ell \partial y_k \partial y_\ell}$$

At large Re_ℓ, the small scale (dissipative structure) is isotropic. Thus, at this scale the two-point velocity correlation can be described in terms of the single independent variable, $\bar{\xi} = \bar{x} - \bar{y}$ (the separation of the two points). Hence,

$$\overline{u_i(\bar{r} + \bar{x})\ u_i\ (\bar{r} + \bar{y})} = \overline{u_i(0)\ u_i(\bar{\xi})} = R_{ii}\ (\bar{\xi})\ ,$$

$$\varepsilon = - \lim_{\bar{\xi}\to 0} \nu \frac{\partial^2 R_{ii}(\bar{\xi})}{\partial \xi_j \partial \xi_j}$$

and

$$D = \lim_{\bar{\xi}\to 0} \nu^2 \frac{\partial^4 R_{ii}(\bar{\xi})}{\partial \xi_j \partial \xi_\ell \partial \xi_j \partial \xi_\ell}$$

if the three-dimensional energy spectrum is denoted by E(k), where

$$E(k) = \int_{|\bar{k}|=k} \frac{1}{8\pi^3} \int_{-\infty}^{\infty}\int_{-\infty}^{\infty}\int_{-\infty}^{\infty} R_{ii}(\bar{\xi}) \exp(-i\, \bar{k}\cdot\bar{\xi}) d\xi\, dA$$

(the integral over 'A' represents an integration over all shells of radius k) and k is the wave number, then

$$\varepsilon(k) = \nu k^2 E(k) \qquad \text{(A-1)}$$

and

$$D(k) = \nu^2 k^4 E(k) = \nu k^2 \varepsilon(k) \qquad \text{(A-2)}$$

Equation (A-1) indicates that the peak of the dissipation spectrum is shifted away from the peak of the energy spectrum, toward higher wave numbers, and smaller eddies. Similarly, (A-2) indicates that D(k) is shifted to even smaller eddies. However, $\varepsilon(k)$ has been found experimentally to peak at $k \sim 1/2\eta$. Since $1/\eta$ is the characteristic scale of the smallest eddies, D(k) must also peak at a value of k near $1/\eta$. Since these spectra reach their maxima at approximately the same wave number, we can make the estimate

$$D \sim \nu \int_0^{\infty} \frac{\varepsilon(k)}{\eta^2} dk = \nu \frac{\varepsilon}{\eta^2}$$

Appendix B: Discussion of Invariant Modeling

i) Invariant Basis for a Symmetric Second Order Tensor and Two Vectors

Consider the symmetric tensor and two vectors $\bar{\bar{A}}$, $\bar{\phi}$ and $\bar{\psi}$ where $\bar{\bar{A}}$ has zero trace. The number of independent 'invariants' (i.e. invariant under a general transformation of the coordinate system) needed to fully describe $\bar{\phi}, \bar{\psi}$ and $\bar{\bar{A}}$ are:

$\bar{\bar{A}}$: 5

$\bar{\psi}$: 3

$\bar{\phi}$: 3

11

As the principal invariants of $\bar{\bar{A}}$, the independent functions

$$\left.\begin{aligned} II &= A_{ij}A_{ij} \\ \text{and} \\ III &= A_{ik}A_{kj}A_{ji} \end{aligned}\right\} \quad (B\text{-}1)$$

are chosen. It is perhaps useful to note that these invariants are related to those (τ_i) which appear in the characteristic equation of $\bar{\bar{A}}$,

$$\lambda^3 - \tau_1\lambda^2 + \tau_2\lambda - \tau_3 = 0 \qquad (B\text{-}2)$$

where the three roots, λ_i, of equation (B-2) are the eigenvalues of $\bar{\bar{A}}$. It can be shown that since $\bar{\bar{A}}$ has zero trace and is symmetric,

τ_1 = trace of $\bar{\bar{A}}$ = 0,

τ_2 = sum of minors of diagonal elements = $\frac{II}{2}$,

and

$$\tau_3 = \text{determinant of } \overline{A} = \frac{III}{3}$$

The three additional invariants required to fully describe $\overline{A}$ may be constructed with the aid of the vectors $\overline{\phi}$ and $\overline{\psi}$. They are

$$A_{ij}\phi_i\psi_j,\ A_{ik}A_{kj}\phi_i\psi_j \text{ and } A_{ij}\psi_i\psi_j \tag{B-3}$$

Finally, to specify $\overline{\psi}$ and $\overline{\phi}$ to within a reflection requires six new invariants

$$\psi_i\psi_i,\ \phi_i\phi_i,\ A_{ij}\phi_i\phi_j,\ A_{ik}A_{kj}\phi_i\phi_j,\ A_{ik}A_{kj}\psi_i\psi_j \text{ and } \psi_i\phi_i \tag{B-4}$$

To resolve the sign ambiguity requires the additional invariant (which changes sign under a reflection of ψ_k)

$$\varepsilon_{ijk}\phi_i\phi_j\psi_k \tag{B-5}$$

where ε_{ijk} is the alternating tensor.

The scalars (B-1), (B-3), (B-4) and (B-5) constitute an invariant basis for the vectors and tensor $\overline{\phi}$, $\overline{\psi}$ and $\overline{A}$.

ii) Use of the Invariant Basis to Establish the Structure of a Second Order Tensor Function

It is desired to establish the most general form of the second order symmetric tensor function, T_{ij}, of the tensor $\overline{A}_{ij}$. The invariant of T_{ij}, formed with respect to two arbitrary vectors

$\bar{\phi}$ and $\bar{\psi}$ (i.e. $T_{ij}\phi_i\psi_j$) must be a function only of the invariants of $\bar{A}$, $\bar{\phi}$ and $\bar{\psi}$, listed in the previous section. However, since $T_{ij}\phi_i\psi_j$ is bilinear in ϕ_i and ψ_j, certain of these invariants may be eliminated since the functionality must be valid for arbitrary ϕ_i and ψ_j. Thus, $T_{ij}\phi_i\psi_j$ can be a function only of

$$\text{II, III} \tag{B-6}$$

$$\phi_i\psi_j,\ A_{ij}\phi_i\psi_j,\ A_{ik}A_{kj}\phi_i\psi_j \tag{B-7}$$

The invariants (B-6) do not contain ϕ_i or ψ_j, while the invariants (B-7) are bilinear in these variables. Thus $T_{ij}\phi_i\psi_j$ must be a linear function of (B-7) with coefficients that are functions of (B-6). Hence, the most general form for T_{ij} is

$$T_{ij} = a\delta_{ij} + bA_{ij} + cA_{ik}A_{kj} \tag{B-8}$$

If there are additional scalar variables, such as q^2 and ε, which are invariant under general coordinate transformations, these will also enter the functionality of (B-8) through the coefficients.

To emphasize that tensor products of $\bar{A}$, of higher than second order, need not be included in (B-8), it is useful to examine the Cayley-Hamilton Theorem (c.f. Tou (1964), pp. 43) which states that *every matrix satisfies its own characteristic equation*. Hence,

$$A_{ik}A_{k\ell}A_{\ell j} = -\frac{II}{2}A_{ij} + \frac{III}{3}\delta_{ij} \tag{B-9}$$

Furthermore, multiplication of (B-9) by A_{pi} gives

$$A_{pi}A_{ik}A_{k\ell}A_{\ell j} = -\frac{II}{2}A_{pi}A_{ij} + \frac{III}{3}A_{pj} \qquad \text{(B-10)}$$

If this process is continued, it can be shown that all tensor products of third and larger order can be expressed as a *linear* combination of A_{ij}, $A_{ik}A_{kj}$ and δ_{ij}, with coefficients which are polynomials in the invariants of A_{ij}. Due to this linearity, tensor products of third and higher order need not be included in (B-8).

Appendix C: Calculation of the Wall Effect Function for the Pipe Geometry

The scalar function in the wall-effect tensor used by Shir and Daly and Harlow, in cylindrical coordinates, takes the form

$$\psi(\bar{x}) = \psi(r) = \frac{1}{\pi} \oint \frac{1}{|\bar{x} - \bar{x}'|^4} \, d\theta \, dz \qquad \text{(C-1)}$$

where $\bar{x} = (r, \theta, z)$ is a vector in the cylindrical coordinate system, with z the axial coordinate. In (C-1) all lengths have been normalized by the pipe radius. This integral may be rewritten as an explicit function of r, θ, and z

$$\psi(r) = \frac{4}{\pi} \int_0^\infty \int_0^\pi \frac{d\theta \, dz}{(z^2 + 1 + 2r \sin \theta + r^2)^2}$$

$$= \frac{4}{\pi} \int_0^\infty \frac{1}{(z^2 + (1 + r^2))^2} \left(\frac{\pi - 2 \sin^{-1}(a)}{(1 - a^2)^{3/2}} \right.$$

$$\left. - \frac{2a}{1-a^2} \right) dz \qquad \text{(C-2)}$$

where

$$a = \frac{2r}{z^2 + 1 + r^2}$$

We were unable to integrate (C-2) analytically. Hence, for each r

of interest, the integral was evaluated numerically using Simpson's rule. The integral converged to its asymptotic limit for $z \gtrsim 10$.